TECHNISCHE UNIVERSITÄT DRESDEN

Leibniz-Institut für Festkörper- und Werkstoffforschung Dresden

IFW

Fakultät Maschinenwesen der Technischen Universität Dresden

DISSERTATION

Soft Ferromagnetic Bulk Metallic Glasses with Enhanced Mechanical Properties

Zur Erlangung des

akademischen Grades

Doktoringenieur (Dr.-Ing.)

von

Master of Technology

Parthiban Ramasamy

geboren am 15.05.1989 in Coimbatore, India

Contents

Abstract

In recent years Fe-based bulk metallic glasses (BMGs) have gained considerable interest due to their excellent soft magnetic properties with high saturation magnetization, high electrical resistivity, very good corrosion resistance, low materials cost, extremely high mechanical strength and hardness. Ever since the first Fe-based bulk glassy alloy was synthesized in the Fe-Al-Ga-P-C-B system by a copper mold technique, a very large number of Fe- based BMGs including Fe–Co-, Fe–Ni- and Fe–Co–Ni- based alloy systems have been developed.

Traditionally, BMGs are classified in to metal-metalloid and metal-metal types. In the metal-metalloid type, the metal content is typically ~ 80 at.% and metalloid content ~ 20 at.%. The metal can be just one or a combination of more than one element and similarly, the metalloid element can be just one or a combination of more than one element. Whereas, in metal-metal type there is no such requirement, the elements can be present in any proportion. Interestingly, all the ferromagnetic Fe-based BMGs developed so far are metal-metalloid type. Despite their relatively complicated chemical compositions, the low price of the constituent elements, as well as the possibility to use industrial pre-alloys, make the Fe-based BMGs very attractive for industrial applications

In spite of having excellent strength, Fe-based BMGs are not used as structural materials in service, so far. The major obstacle is their inherent brittleness under mechanical loading, once a crack is developed the material fails catastrophically. The ever growing industrial demand for the materials with outstanding properties, aside from exploring new alloy compositions, it is pertinent to understand why or why-not the existing system work and how to improve their properties. Recent years, much attention has been paid to improve the plasticity in the plasticity in BMGs. Recent reports suggested that the plastic deformability can be enhanced by introducing different microstructural heterogeneities such as free volume enhanced regions, separated phases, nano-crystals, atomic clusters caused by for instance additions of small amount of soft elements. Understanding the effect of addition of soft elements on thermal stability, structural evolution, magnetic and mechanical properties are the main point which this work addresses.

In this work, a study on two different soft ferromagnetic Fe-based glass forming alloys are presented, both of them known to have very high mechanical strength and excellent soft magnetic properties but so far have not been used in any industrial applications. The important issue is with the brittle behavior of this BMGs, particularly under mechanical loading. In each glass forming alloys, the aim was to find out the optimum quantity of the soft elements (Cu and Ga), which can be added to improve their room temperature plastic deformability without affecting the glass forming ability (GFA) and soft magnetic properties.

The first glass forming alloy that is studied is $Fe_{36}Co_{36}B_{19.2}Si_{4.8}Nb_4$. This glass forming alloy is highly sensitive to the impurities, only pure elements were used to form this alloy. The addition of only 0.5 at.% Cu completely changes the thermal stability and structural evolution but it also improves the mechanical properties. In case of Ga addition up to 1.5 at.% the crystallization behavior remains unaltered and the thermal stability improves marginally. The addition of Ga improves the plastic deformability of the glass by forming soft zones, whose melting point is much lower compared to rest of the alloy. These soft zones are responsible for the plastic deformation of this glass. Thus addition of Ga is very beneficial in improving the mechanical properties of this Fe-based BMG.

In the second part, $Fe_{74}Mo_4P_{10}C_{7.5}B_{2.5}Si_2$ glass forming alloy is studied. Unlike the aforementioned alloy, this glass forming alloy is not very sensitive to the impurities, industrial grade alloy elements can also be used to form this alloy. In this alloy addition of Cu is beneficial only up to 0.5 at.%, beyond that Cu addition deteriorates GFA and magnetic properties. In case of Ga addition up to 2 at.% the crystallization behavior remains unaltered and the thermal stability improves marginally Similar to the FeCoBSiNb glass, the addition of Ga in FeMoPCBSi glass also improves the plastic deformability of the glass by formation of soft zones.

Addition of small at.% Ga proved be an viable solution to improve the plastic deformability in the ferromagnetic Fe-based metallic glasses without compromising on thermal and magnetic properties of the glass.

In the final part we tried to cast the $Fe_{74}Mo_4P_{10}C_{7.5}B_{2.5}Si_2$ glass in a complex shape using an industrial high pressure die casting (HPDC) set up. The important issues were with the casting alloy temperature, casting speed and die material.

The aim of our work was to optimize the die material suitable for casting the BMGs and then address the issues with casting temperature and casting speed. We have thus attempted to gain a basic knowledge in casting the Fe-based BMG in industrial scale. Our effort was tremendously successful, we were able to produce fully amorphous complex shaped samples with excellent surface finish.

We have thus made a considerable advancement towards understanding the basics behind improving the room temperature plastic deformability in $Fe_{36}Co_{36}B_{19.2}Si_{4.8}Nb_4$ and $Fe_{74}Mo_4P_{10}C_{7.5}B_{2.5}Si_2$ ferromagnetic BMGs. We have also made a considerable progress in industrialization of bulk ferromagnetic BMGs.

Chapter 1

Theoretical background

1.1 Development of metallic glasses

In general glass is an amorphous (non-crystalline) solid material that lacks the long-range periodic arrangement like crystals [1, 2] mostly made up of silica (SiO_2) and oxides of other metals like Al, Ca, Mg, K, Na and etc. Among different type of glasses the most familiar type is soda-lime glass, which is hard, brittle and transparent, used widely in windows for both structural and decorative purpose. These oxide glasses are prepared by rapid cooling of the molten mixtures of silicates and metal oxides in order to prevent crystallization. During this dynamic transition from liquid to solid, which takes place at fast cooling rate, the atoms in the liquid do not rearrange themselves into regular periodic three dimensional structure i.e., crystalline solid [3]. Therefore, it is possible to say that the atomic arrangement in the glass is similar to that of the liquid with the same composition [4]. The glass-forming tendency varies widely depending upon the compositions, some oxide based mixtures form a glass at a normal Cooling rate of 1 K/min, whereas, the monoatomic metals with some impurities requires as the cooling rate as high as 10^{10} K/s [5]. By definition "Metallic glass" refers to an amorphous metallic alloy prepared by rapid solidification of molten alloy, hence it lacks the long range order symmetry and results in an amorphous structure [3]. Metallic glasses (MGs) are relatively young group of materials joined in the amorphous materials category [6-12]. Glasses have been found in every category of materials and of various bond type: covalent, ionic, van der Waals, hydrogen and metallic [13]. The first metallic glass, reported by Klement *et al.* [14], was produced at Caltech in 1960 by using a rapid quenching technique for cooling metallic melts at very high cooling rates of 10^5-10^6 K/s. The cooling rates required to produce these glasses are very high, thereby restricting the specimen geometry to thin ribbons, foils and powders [4]. During quenching, the nucleation and growth of crystalline phases are suppressed so that the structural configuration results in an amorphous liquid-like structure [6, 7, 15, 16].

After the discovery of $Au_{75}Si_{25}$ metallic glass in 1960, several researchers made a remarkable progress in developing new alloy compositions that can be amorphized easily [8], which indicates the scientific importance and the potential engineering applications of MGs [17-19]. The earliest

technique applied for the fabrication of MGs in the shape of wires or tapes for the technical applications was reported by Chen and Miller in 1970 [20]. The synthesis of first bulk metallic glass (BMG) with geometrical dimensions larger than 1mm was reported by Chen in 1974 [21], using suction casting method from Pd-Cu-Si alloy. Later, Turnbull *et al.* [22, 23] focused on Pd-based BMGs, however these Pd-based BMGs are too expensive for using in day to day life applications. Since the late 1980s, Inoue and his co-workers developed several new multicomponent alloy systems with the relatively high GFA in Mg-, Ln-, Zr-, Fe-, PdCu-, PdFe-, Ti- and Ni- based alloy systems using simple suction casting method [24-38].

The preparation of Fe-based metallic glass with good soft-magnetic properties from Fe-metalloid systems was first reported by Fujimori *et al.* [39] and Handely *et al.*[40]. Since then several alloys with excellent magnetic properties have been developed up to date. However, the shape and dimensions of the Fe- and Co- based amorphous magnetic alloys have been limited to wires and thin ribbons with thickness below 30 μm because of the necessity of a high cooling rate of almost 10^6 K/s for the formation of amorphous phase [41]. The first Fe-based bulk metallic glasses with large super cooled region was reported in Fe-Al-Ga-P-C-B alloy system by Inoue *et al.* [27, 42]. Subsequently, several Fe-based ferromagnetic bulk glassy forming alloys like Fe-(Co,Ni)-(Zr,Nb,Ta,Hf,Mo)-B [43], (Fe,Co,Ni)-Nb-B [44], Fe-Co-Ln-B [45], Fe-Co-Ni-Si-B [46], Fe-(Cr,Mo)-(P,C,B) [47], (Fe,Co,Ni)-(Zr,Nb,Ti,Ta)-B [48], Fe-Co-Ni-Zr-Mo-B [49], (Fe,Co)-Si-Nb-B [50], and (Fe,Co)-(Nb,Y)-B [51, 52] were developed because of their potential magnetic applications [53, 54]. Now, the development of Fe- and Co- based BMGs with high glass-forming ability (GFA) has gained more interest because of the soft magnetic properties [55, 56] and also because of their high mechanical strength [57-59].

1.2 Formation of metallic glasses

A glass may be considered as a solid with frozen-in liquid structure and sometimes referred to as "super-cooled liquid" [4]. Upon quenching of the melt [14], the supercooled liquid and crystalline phases compete with each other [13, 60, 61]. The variation of volume with temperature for a liquid is shown in Fig. 1.1. On cooling from initial state A, the change of volume with respect to

temperature decreases steadily along AB. If the rate of cooling is slow and nuclei are present, crystallization will take place at the melting temperature T_m.
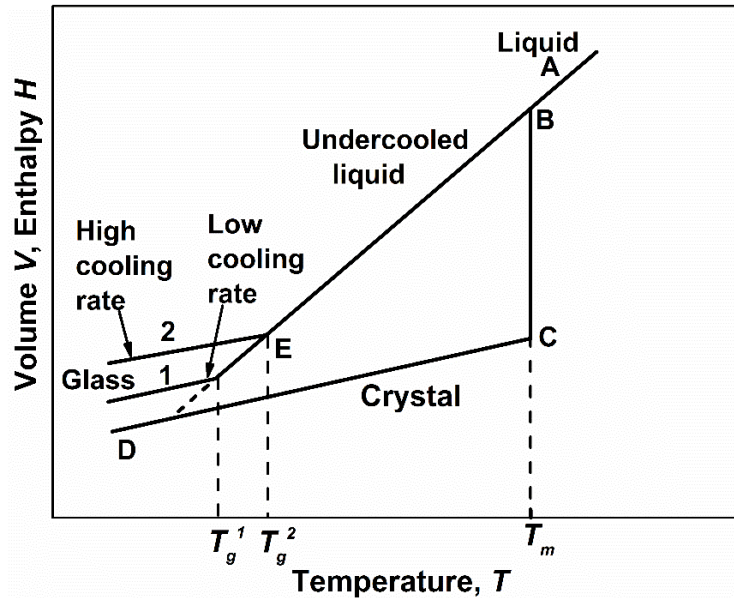
Figure 1.1: Change of volume as a function of temperature. Redrawn from [62]

The volume will decrease sharply from B to C; thereafter, the solid will contract with falling temperature along CD. If the rate of cooling is sufficiently rapid, crystallization does not take place at T_m. The volume of the supercooled liquid decreases along BE, which is a smooth continuation of AB. At a certain temperature T_g the volume undergoes a significant change in slope and continues to decrease with almost the same slope as the crystalline form (i.e. almost parallel with the CD curve). Only below T_g the material is a glass. As cooling rate increases from 1 to 2, T_g increases to a higher value, i.e. from T_g^1 to T_g^2 [63]. The temperature at which the viscosity of the undercooled liquid reaches a value of 10^{12} Pa.s is traditionally designated as the glass transition temperature T_g, [62]. In reality it is difficult to accurately measure the cooling rate (R_c) during quenching process. Therefore, the critical casting thickness (t_c), is often used to evaluate the R_c of BMGS [64, 65]. Moreover, other methods to predict or evaluate the GFA have also been proposed based on the constituent elements of the alloys [8].
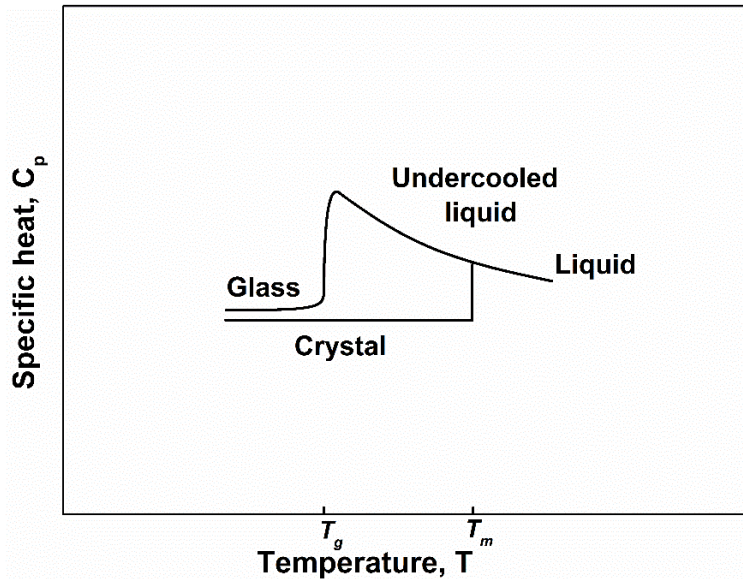
Figure 1.2: Variations of the specific heat with temperature for the crystal and glass-forming liquid. Redrawn from [62].

The variation of specific heat (C_p), with temperature is shown in Fig 1.2. On cooling from the liquid state the C_p of the undercooled liquid increases with decrease in temperature. The difference between the C_p of the undercooled liquid and the glass continuous to increase until T_g; at T_g the C_p of the undercooled liquid decreases suddenly, indicating the fewer degrees of freedom as a result of freezing of the liquid. Once glass is formed, the difference between the C_p of the glass and crystal is very less (see Fig. 1.2) [62].

During cooling from the liquid state, the viscosity of a metallic liquid increases slowly with decrease in temperature (Fig. 1.3). Close to the freezing temperature, the viscosity of the material increases suddenly up to 10^{15} Pa.s. However, the variation of viscosity in a glass-forming liquid is different, here the viscosity increases gradually in the liquid with decreases in temperature. But, this trend continues below the freezing point, even though the rate of increase is more rapid with a further decrease in temperature in the supercooled liquid. At T_g the viscosity is very high, there is no more flow of the liquid and the material is solid [62].
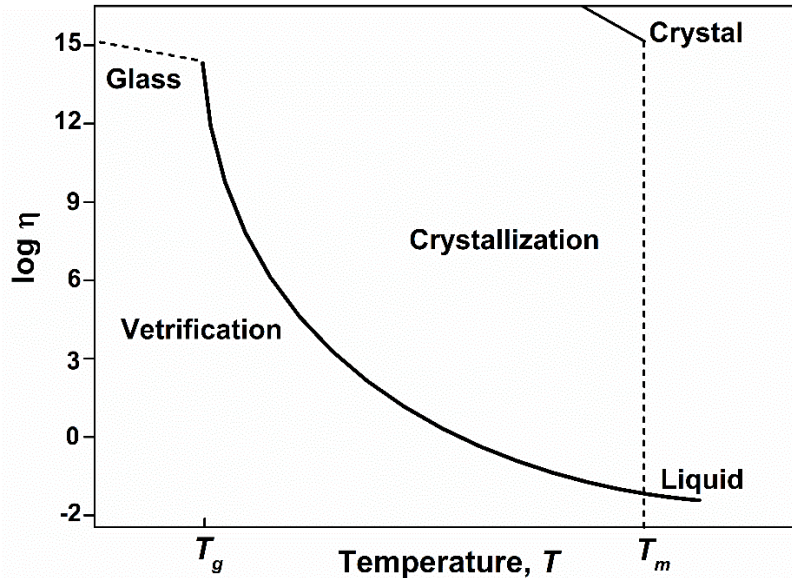
Figure 1.3: Variations of the viscosity with temperature for the crystal and glass-forming liquid. Redrawn from [62].

1.2 .1 Thermodynamic considerations in glass formation

The thermodynamic stability of a system at constant temperature and pressure is determined by its Gibbs free energy, *G*, defined as

$$G = H - TS \tag{1.1}$$

Where, *H* is the enthalpy, *T* is the absolute temperature, *S* is the entropy. Thermodynamically, a system will be in stable equilibrium only when it has attained the lowest possible value of Gibbs free energy. So in order to get the stable glass system the free energy should be as lowest or *ΔG* is negative*ΔG* = (G_{glass} - $G_{crystal}$). Mathematically it can be expressed as:

$$\Delta G = \Delta H_f - T\Delta S_f \tag{1.2}$$

where the *Δ* symbol represents the change in these quantities between the final and initial states, H_f and S_f represents the enthalpy of fusion and entropy of fusion, respectively [62]. The system becomes stable when the value of *G* is the lowest, or *ΔG* is negative. A negative value of *ΔG* can be obtained either by decreasing the value of ΔH_f or increase the value of ΔS_f or both. Since entropy is nothing but a measure of the different ways in which the constituent atoms can be arrange (microscopic sites), this value will increase with increase in number of components in the

alloy system. Thus, even if ΔH_f were to remain constant, the free energy will be lower because of the increased entropy when the alloys system consists of a large number of components.

The free energy of the system can also be lowered, at a constant temperature, in case of low chemical potential due to low enthalpy, and large interfacial energy between the liquid and solid phase. Since it will be difficult to intentionally control these parameters in an alloy system, the easiest way to decrease the free energy would be to increase the ΔS_f by having a large number of components in the alloy system. Increase in ΔS_f also results in an increase in the degree of dense random packing of atoms, which leads to decreases in ΔH_f and consequently increases the solid/liquid interfacial energy [8, 62]. Hence, it is easier to synthesize glassy phases in the multicomponent alloy system than in binary alloy systems [8, 62]. The three empirical rules suggested by Inoue [8] for the formation of good glass-forming alloys system are derived from both extensive experimental results and from thermodynamic point of view. The rules are: (1) Glass-forming alloys systems generally contain more than three elements; (2) Significant difference in atomic size ratios above about 12% among the three main constituent elements; (3) Negative heat of mixing among the three main constituent. Any metallic liquid, which satisfies the three empirical rules, is expected to have a denser randomly packed atomic configuration [6, 8, 13, 17]. Such kind of structure can effectively surpass the nucleation and growth of crystalline phase(s), which is equivalent to the increase in GFA of the glass-forming alloys [9]. Therefore, the competition between the liquid phase and crystalline phase plays an important role in the formation of metallic glasses [8, 9, 66]. Thus the glass formation depends purely on kinetics. According to the free volume model [67, 68] or the entropy model of the liquid state, it is expected that every liquid undergoes a transition to the glassy state, provided that crystallization could be by passed or avoided [62].

1.2.2 Kinetics of the glass formation

Volmer and Weber [69] made the first attempt to describe the nucleation process by considering the condensation of supersaturated vapour [3, 70]. Later Becker and Döring extended the same model [71]. Fisher and Turnbull applied the basic concepts of this theory to the liquid-solid phase transition [72]. According to Turnbull [13] nucleation in undercooled liquid is almost always

heterogeneous on seeds which are either present accidentally or deliberately injected into the system. These seeds may be crystals of the material itself or other solid materials, such as the container walls or particles suspended in the liquid. At a given cooling rate the undercooling required for the heterogeneous nucleation varies widely with composition and structure of the seed material [13]. Nucleation within the liquid and without the help of seeds is called homogeneous. Experimentally it is difficult to circumvent the effects of seeds and thereby realize homogeneous nucleation behavior [13].

In liquid metals, random fluctuations may create minute crystalline regions (clusters, embryos) even at temperatures above the melting point, but these will not be stable. They continue to be metastable also below the melting point because of the relatively large excess energy required for surface formation, which tends to weight the energy balance against their survival when they are small [3, 70].

Kinetic analysis based on simple nucleation theory leads to the following expression for the steady frequency of nucleus formation [13]:

$$I = \frac{k_n}{\eta} \exp\left[-\frac{b\alpha^3\beta}{T_r(\Delta T_r)^2}\right] \tag{1.3}$$

where k_n is a constant specified by the model, T_r is the reduced temperature (T/T_l), ΔT_r is the reduced supercooling (1- T/T_l), b is a constant determined by the shape of the nucleus, and α and β are dimensionless parameters defines as [13]:

$$\alpha = \frac{(N_A \bar{V}^2)^{1/3} \sigma}{\Delta H_m}, \tag{1.4}$$

$$\beta = \frac{\Delta H_m}{RT_m} = \frac{\Delta S_m}{R} \tag{1.5}$$

where N is Avagadro's number, R is universal gas constant, ΔH_m is the molar heat of fusion, $\Delta S_m = \Delta H_m/T_m$ is the entropy of fusion, ΔC_p is the molar difference in heat capacity between the crystal and the liquid and $\bar{V}$ is the molar volume of the crystal. The principal resistance of a fluid to nucleation is limited to α, which is proportional to the liquid-crystal interfacial energy σ. Physically α is the number of monolayers/area of a crystal, which would be melted at Tm by an enthalpy ΔH equal to σ [3, 13].

Figure 1.4. shows the calculated variation of the logarithm of the frequency of homogeneous nucleation of crystals in an undercooled liquid with reduced temperature for various values of $\alpha^3\beta$ [13]. For numerical modelling the number b was assigned its value for a sphere ($16\pi/3$), η was set equal to 10^{-3} Pa.s, independent of temperature, and k_n was given the value 10^{23} N.m [13].
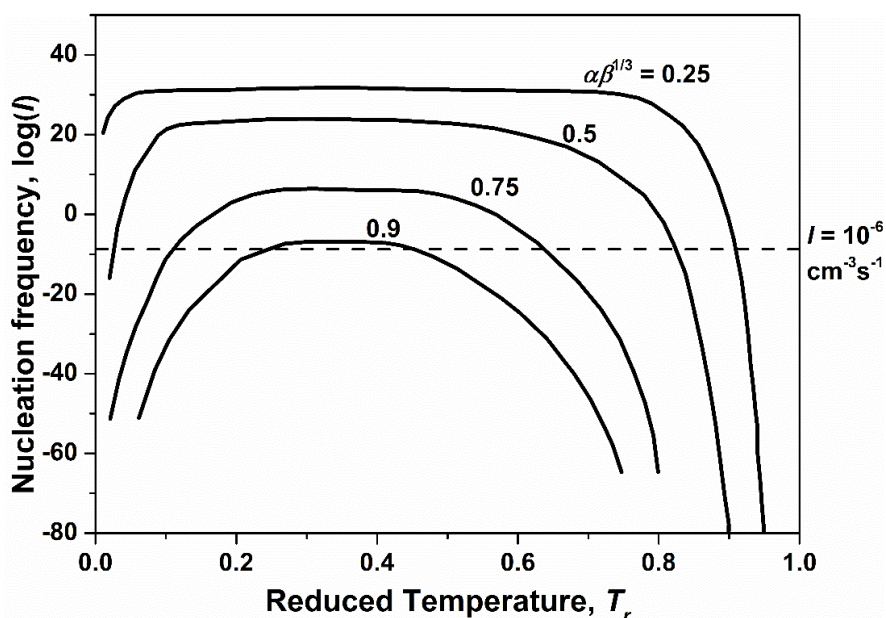
Figure 1.4: Calculated dependence of the logarithm of the frequency (in $1/cm^3s$) of homogeneous nucleation of crystals in an undercooled liquid as a function of the reduced temperature for various values of $\alpha\beta^{1/3}$ (computed with the equation 1.2) as indicated in [13]. Redrawn from [3]

It is possible to see that I is negligible at small undercooling. In fact, I must become 10^{-6} /cm^{3}s or larger in order to be observable under common experimental conditions. This indicates that I-ΔT_r relation closest to equilibrium where the simple theory is most valid is practically inaccessible to the experiment. With increasing ΔT_r, I increases to a broad maximum at $T_r = 1/3$ and falls to zero at $T = 0$ K. Liquids with $\alpha\beta^{1/3} > 0.9$ would practically not crystallize at any undercooling, unless they are seeded. Thus, they would form glasses for sufficient undercooling. In contrast, it should be practically impossible to suppress, upon cooling to 0 K, the crystallization of fluids with small $\alpha\beta^{1/3}$ (see Fig. 1.4.) [3]. From the knowledge gained so far β lies between 1 to 10 for most substances and it is near one for most simple monoatomic liquids [13]. Furthermore, α has been measured directly only in a few instances [73, 74] and there is no well accepted theory for

predicting it. Hence, it is reasonable to assume that it may be not greater than 1, i.e. one melted monolayer [3].

Further, Turnbull explained that the glass-forming tendency should increase with the reduced glass transition temperature $T_{rg} = T_g/T_m$ [13]. The effect of different assignments of T_{rg} on the nucleation frequency, calculated from the simple theory, with $\alpha\beta^{1/3} = 0.5$, is shown in Fig. 1.5. The viscosity was calculated from an equation of Fulcher form (1.2) with constant typical for a number of simple molecular liquids. The temperature at which η become 10^{14} Pa.s is considered as T_g [3].
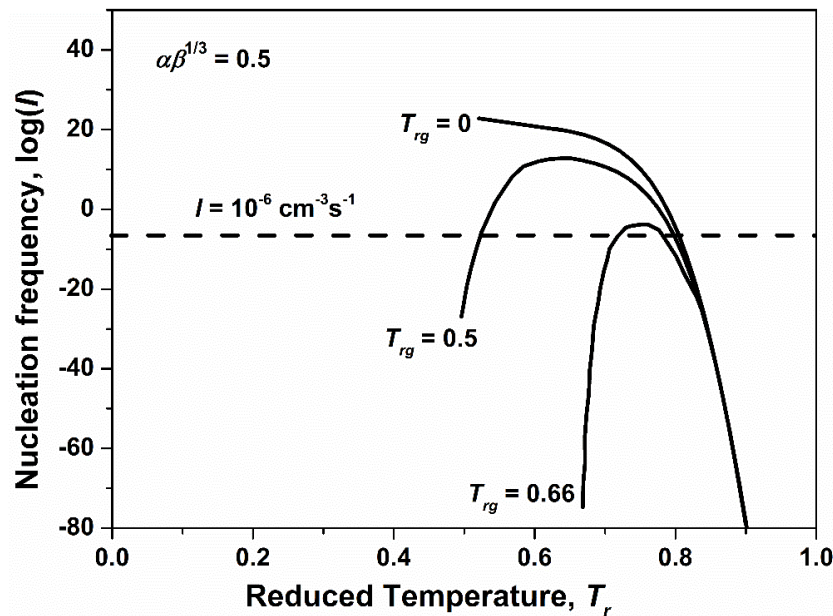
Figure 1.5: Variation of the logarithm of frequency (in 1/cm^{3}s) of homogeneous nucleation of crystals in liquids with reduced temperature calculates from eq. (1.2) as indicates in [13]. $\alpha\beta^{1/3}$ was set equal to ½ and the viscosity was calculated from the Fulcher equation. Redrawn from [3].

From Fig. 1.5 it possible to observe that the effect of increasing T_{rg} is to lower, sharpen and shift the peak in the I-T_r relation to higher T_r values. Liquids with a glass temperature as high as (2/3) T_m (i.e. $T_{rg} = 0.66$), if seed-free, would practically crystallize only within a narrow temperature range and then only slowly. Thus, they could be easily undercooled to glassy state. Liquids with a glass temperature $T_g = T_m/2$ (i.e. $T_{rg} = 0.5$) could be cooled to the glassy state only in a relative small volume and at high cooling rates, according to these relations [3].

1.3 Bulk metallic glasses developed so far

In the last two decades, several BMGs were developed. So far, the GFA of the non-ferrous BMGs is larger compared to the ferrous based BMGs. Typical alloy systems, which may form BMGs, reported up to date, are summarized in Table 1.1, together with the year when the first corresponding paper or patent of each alloy system was published. The first BMGs reported were based on non-ferrous systems, followed by the Fe-and Co- based alloy systems [3, 8, 75]. It can be observed that only in recent years Cu-based BMGs were developed.

Table 1.1: Typical bulk glassy alloy systems reported up to date together with the calendar year when the first paper or patent of each alloy system was published [3, 8, 62, 75].

1. Non-ferrous alloy systems		2. Ferrous alloy systems	
Mg-Ln-M (M = Ni, Cu, Zn)	1988	Fe-(Al,Ga)-(P,C,B,Si,Ge)	1995
Ln-Al-TM (TM = the VI- VIII group transition metal)	1989	Fe-(Nb,Mo)-(Al,Ga)-(P,B,Si)	1995
		Co-(Al,Ga)-(P,B,Si)	1996
Ln-Ga-TM	1989	Fe-(Zr,Hf,Nb)-B	1996
Zr-Al-TM	1990	Co-(Zr,Hf,Nb)-B	1996
Zr-Ti-TM-Be	1993	Ni-(Zr,Hf,Nb)-B	1996
Zr-(Ti,Nb,Pd)-Al-TM	1995	Fe-Co-Ln-B	1998
Pd-Cu-Ni-P	1996	Fe-(Nb,Cr,Mo)-(C,B)	1999
Pd-Ni-Fe-P	1996	Fe-(Cr,Mo,Ga)-(P,C,B)	1999
Pd-Cu-B-Si	1997	Co-Ta-B	1999
Ti-Ni-Cu-Sn	1998	Fe-Ga-(P,B)	2000
Cu-(Zr,Hf)-Ti	2001	Ni-Zr-Ti-Sn-Si	2001
Cu-(Zr,Hf)-Ti-(Y,Be)	2001	Fe-Cr-Mo-(Y,Ln)-C-B	2004
Cu-Zr	2004	Fe-Cr-Co-Mo-Mn-C-B-Y	2004
		Ni-Co-Nb-P-B-Si	2014

In general the bulk glass-forming alloys developed so far can be divided in to five groups based on their constituent elements, as summarized in Table 1.2. The transition metals belonging to the group numbers I to IV of the periodic table are named ETM (early transition metals), the group VIII metals are names LTM (late transition metals), simple metals are used for Mg and Be, and the metalloids are B,C,Si and P. The first group (i) of bulk glassy alloys consists of ETM (or Ln), Al and LTM, e.g. Zr-Al-Ni and Ln-Al-Ni systems. The second group (ii) is composed of LTM, ETM and metalloid, e.g. Fe-Zr-B and Co-Nb-B systems. The third group (iii) consists of LTM (Fe)-(Al,Ga)-metalloid systems. The fourth group (iv) consist of Mg-Ln-LTM and ETM (Zr,Ti)-simple metal (Be)-LTM alloys and the fifth group (v) consist of only LTM and metalloids, e.g. Pd-Cu-Ni-P and Pd-Ni-P, which is completely different from the first four groups (i-iv) [3, 8]. It is important to note that all first four group alloys are based on the three empirical rules summarized by Inoue [8] as mentioned in the earlier section 1.2.

Table 1.2: The five groups of composition able to form bulk metallic glasses [3, 8].

i	(Ln or ETM) - (Al or Ga) - LTM
ii	LTM – ETM - metalloid
iii	LTM - (Al and/or Ga) - metalloid
iv	Simple metal – Ln – LTM or Simple metal – ETM - LTM
v	LTM - metalloid

The composition summarized in Table 1.1 exhibit high reduced glass transition temperatures (T_{rg}) and a large extension of the supercooled liquid region. Up to date $Pd_{40}Cu_{30}Ni_{10}P_{20}$ is the BMG with the largest reported sample thickness of about 100 mm [29]. In case of Fe-based BMGs there are only few systems reported with large sample thickness. For e.g. Lu *et al*. [36] and Ponnnambalam *et al*. [76] reported a maximum diameter of 12 mm for $(Fe_{44.3}Cr_5Co_5Mo_{12.8}Mn_{11.2}C_{15.8}B_{5.9})_{98.5}Y_{1.5}$ and $Fe_{48}Cr_{15}Mo_{14}Er_2C_{15}B_6$ alloys respectively. However, these glasses are not magnetic and can only be used for structural applications [3].

1.4 Magnetic properties of metallic glasses

Magnetic properties are of fundamental importance for several applications in the electrical and electronic industries. Nowadays, significant efforts have been made on investigating the magnetic properties of the metallic glasses. Due to the development of many sophisticated devices, the soft magnetic materials are increasingly used in diverse applications like magnetic sensors, magnetic valves, transformers, magnetic clutches and magnetic shielding. In the last few decades, Fe-based glasses are widely investigated for their excellent soft magnetic properties [27, 31, 40, 50, 54, 77-89].

1.4.1 Origin of ferromagnetism in glassy state

The existence of long-range ferromagnetic ordering in a structurally disordered material could be due to the interactions between neighboring atomic moments, which make them to align parallel [70]. The quantum mechanical origin of the ferromagnetism by considering the interaction between electronic spins was described by Heisenberg [90]. It was shown that the coupling between neighboring electrons leads to the orientation of all the spins in one direction. This kind of parallel alignment of several spins in one direction give rise to a macroscopic moment. The coupling can be written as:

$$H = -\frac{1}{2} \sum_{<i,j>} J_{ij} . \vec{S}_i . \vec{S}_j \qquad (1.5)$$

where H is the Hamilton operator, J_{ij} the exchange integral and $\vec{S}_i$, $\vec{S}_j$ the spin operators of two neighboring electrons [90]. The summation counts all neighbor pairs. If the exchange integral is positive, the Hamilton operator takes a minimum value when the spins of the electrons are parallel and point into the same direction. This alignment is characteristic for ferromagnetic materials. When the exchange integral is negative, the arrangement of the spins parallel but pointing into opposite directions is energetically favorable. Such materials are called anti-ferromagnets. In the demagnetized state, ferromagnets show no net magnetization, but they are spontaneously decomposed in small regions/domains, within that regions the magnetic moments are ordered. The magnitude of the magnetization in all the domains are same but, the direction varies. The vectorial sum of all magnetic moments $\vec{m}$ relative to the entire volume of the ferromagnetic body is called

volume magnetization $\vec{M}_V$. In the demagnetised state, the magnetic moments are randomly oriented. The vectorial sum of the magnetic moments is zero and hence the total magnetization is zero [91].

1.4.2. Soft magnetic properties

The most desirable soft magnetic properties of the material includes high saturation magnetization, high relative permeability, low coercivity and high electrical resistivity [62, 82].

The addition of the non-magnetic elements for the increases of the glass-forming tendency decreases the exchange interactions and the number of nearest neighbor magnetic elements [82, 92]. Hence, in ferromagnetic glasses the addition of non-magnetic elements decreases the Curie temperature and saturation magnetization [82, 92].
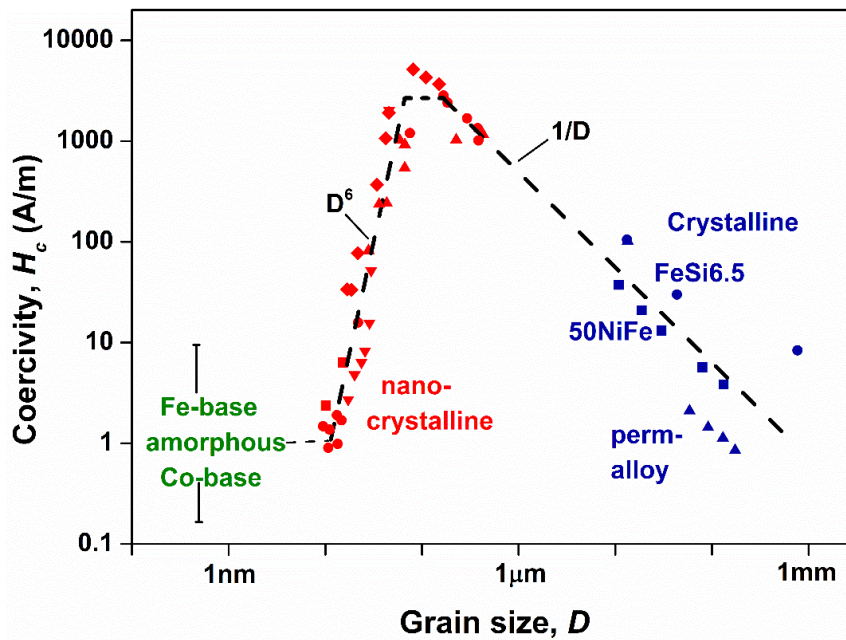
Figure 1.6: The evolution of the coercivity with crystallite size. Redrawn from [94].

In metallic glasses the absence of the domain wall pinning centers like dislocations and grain boundaries improves the soft magnetic behavior significantly. Also, the amorphous nature of the metallic glasses increases the electrical resistivity and this effect improves their high frequency

soft magnetic properties like magnetic permeability because of the reduction of the eddy current loss [82]. Generally, ferromagnetic metallic glasses exhibit very low coercivity < 10 A/m and high magnetic permeability up to 10^5 due to the absence of the magneto-crystalline anisotropy [82, 93]. According to random anisotropy model suggested by Herzer [94], the magneto-crystalline anisotropy is averaged out by the exchange interaction when the grain size is smaller than a critical length (L_0). Figure 1.6 depicts the influence of the crystallite size on the coercivity.

As it is seen in Fig. 1.6, below the critical crystallite size the coercivity significantly decreases with the 6th power of the crystallite size according to the following equation [82, 94]:

$$H_c = \frac{P_c k_1^4 D^6}{\mu_0 M_s A^3} \quad (1.6)$$

where A is the exchange stiffness constant, D is the average crystallite size, P_c is constant of unity, M_s is the saturation magnetization and μ_o is the permeability of free space. Therefore, when there are no grains, the theoretical value of the coercivity should approach zero.

Another important parameter which affects the coercivity is the elastic anisotropy. The existence of the residual stress $\Delta\sigma$ for a ferromagnetic sample with a saturation magnetostriction constant of λ_s contributes to the coercivity enhancement as [82]:

$$H_c \approx -\frac{3}{2}\pi \frac{\lambda_s \Delta\sigma \delta_w}{\mu_0 M_s l} \quad (1.7)$$

Where, δ_w denotes the magnetic domain wall thickness and l is the stress wavelength [82].

The rapid solidification may induce residual stress in the metallic glasses. Thermal annealing below the crystallization temperature decreases the residual stress and as result the coercivity will decrease.

Figure 1.7 shows a classification of the magnetic materials based on their coercivity, saturation polarization and remanence. The terms "hard" and "soft" magnets are used to distinguish ferromagnets based on their coercivity. As it can be seen, the soft magnetic materials have coercivity below 1 kA/m, while the hard magnets have the coercivity larger than 50 kA/m. The softest magnetic materials are the amorphous alloys [70, 95].
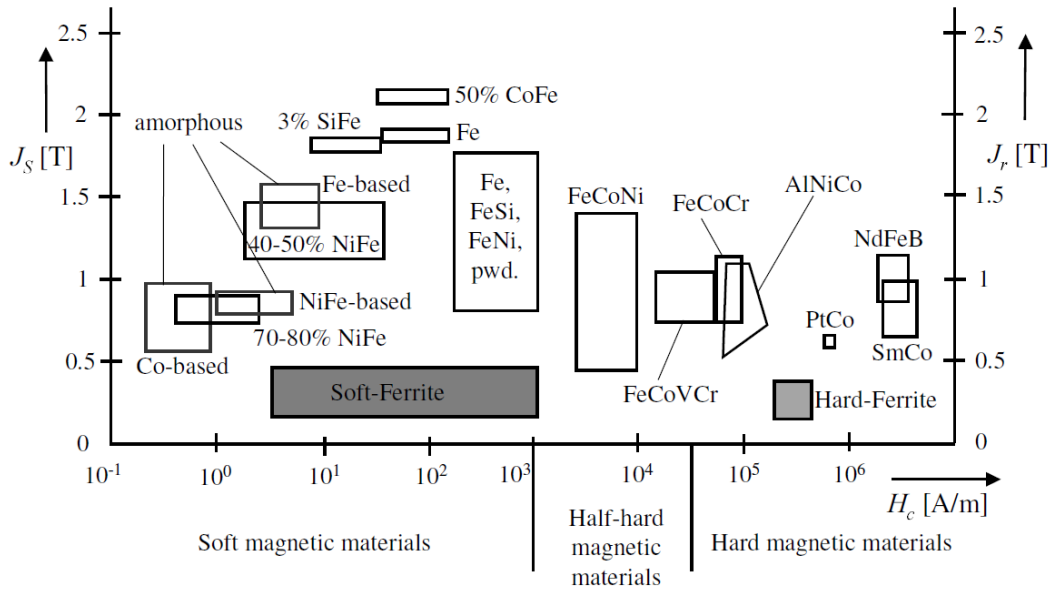
Figure 1.7: Classification of magnetic materials [95]

1.5 Mechanical properties of bulk glassy alloys

The mechanical and physical properties of the materials play a very important role for their applications. The completely disordered structure and metastable state of the metallic glasses possess some excellent mechanical, physical and chemical properties, which are promising for the current and future applications [10, 11, 75, 96-98]. The study of the mechanical behavior of these metallic glasses was first reported in 1971 by Masumoto *et al*. [99] in $Pd_{80}Si_{20}$ ribbons. Owing to development of several bulk metallic glass-forming systems in last few decades and availability of advanced characterization techniques, the research on mechanical behavior of materials has been quite active during the last few years. Generally, when a metallic glass is mechanically loaded, it first undergoes an elastic deformation followed either by fracture or by plastic deformation [98, 100]. Recently, Ashby *et al*. [101] collected mechanical properties for 1507 metals, alloys, metal-matrix composites and metallic glasses and they found that bulk metallic glasses can store more elastic energy per unit volume than other materials. It can be seen that the fracture stress σ_f has a clear linear relationship with Young's modulus E of all the studied materials,

i.e., $E/\sigma_f \approx 50$, further confirming the previous observations by other researchers [102, 103]. Fig. 1.8 shows the relationship between fracture strength and Young's modulus for some bulk glass-forming alloys along with the data of conventional crystalline alloys [8, 75]. The Fe-based bulk glasses exhibit a high fracture strength of 3000-4000 MPa and elastic strain of ~ 0.02, which are significantly higher than the corresponding values measured in the case of non-ferrous BMGs. Furthermore, these ferrous based metallic glass-forming alloys have a lower melting temperatures compared to the conventional Fe-based crystalline alloys, in spite of having much higher mechanical strength [75]. The Vickers hardness of the Fe-based glasses are also very high, usually from 800 to 1200 *HV*. Similar to the tensile fracture strength, the Vickers hardness keeps the same linear relation with Young's modulus [8].
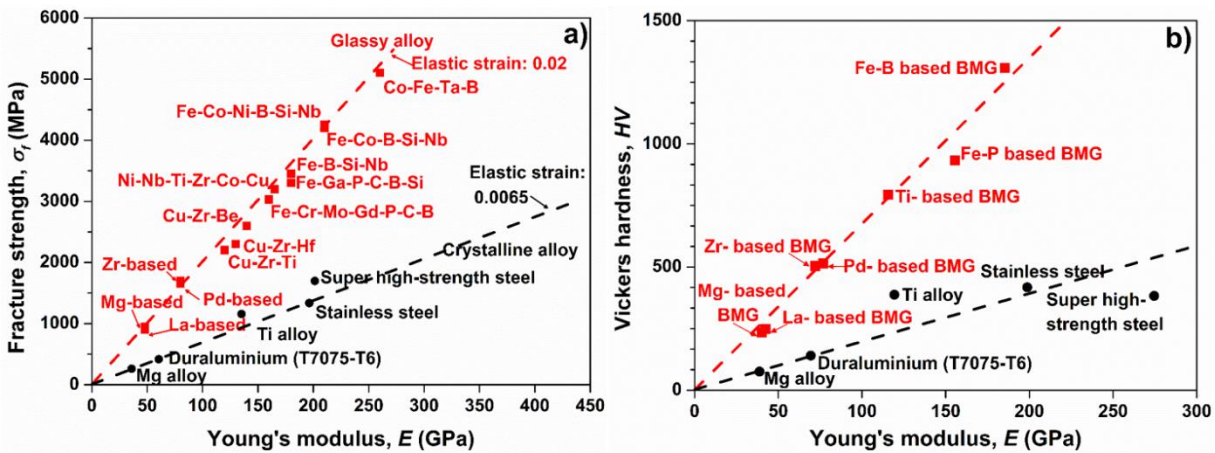
Figure 1.8: Relationship between (a) tensile fracture strength and Young's modulus; (b) Vickers hardness and Young's modulus for bulk glass-forming alloys. Redrawn from [8]

The slope of the linear relation for the bulk glassy alloys is much steeper than the ordinary crystalline alloys, indicating the fundamental mechanical properties of bulk glasses are significantly different from those crystalline alloys [70]. The difference in the tensile strength and hardness values between the glassy and crystalline alloys exceeds ~ 60%. The linear relation are also expressed as $\sigma_f/E = 0.02$ and $HV/E = 0.00061$[8].

Fig. 1.9 represent the relationship between the fracture strength and glass transition temperature for some of the bulk metallic glasses. Though small scatter is observed in the data, a general trend is observed in the σ_f *vs* T_g relationship, the strength increases with increase in the value of T_g Considering the fact that T_g is the reflection of atomic bonds between the constituent elements [104], the high bonding force between the constituting elements might be responsible for the higher glass transition temperature and higher strength.

Figure 1.9: Relationship between compressive fracture strength (σ_f) and glass transition temperature (T_g) for different bulk metallic glasses [105-107].
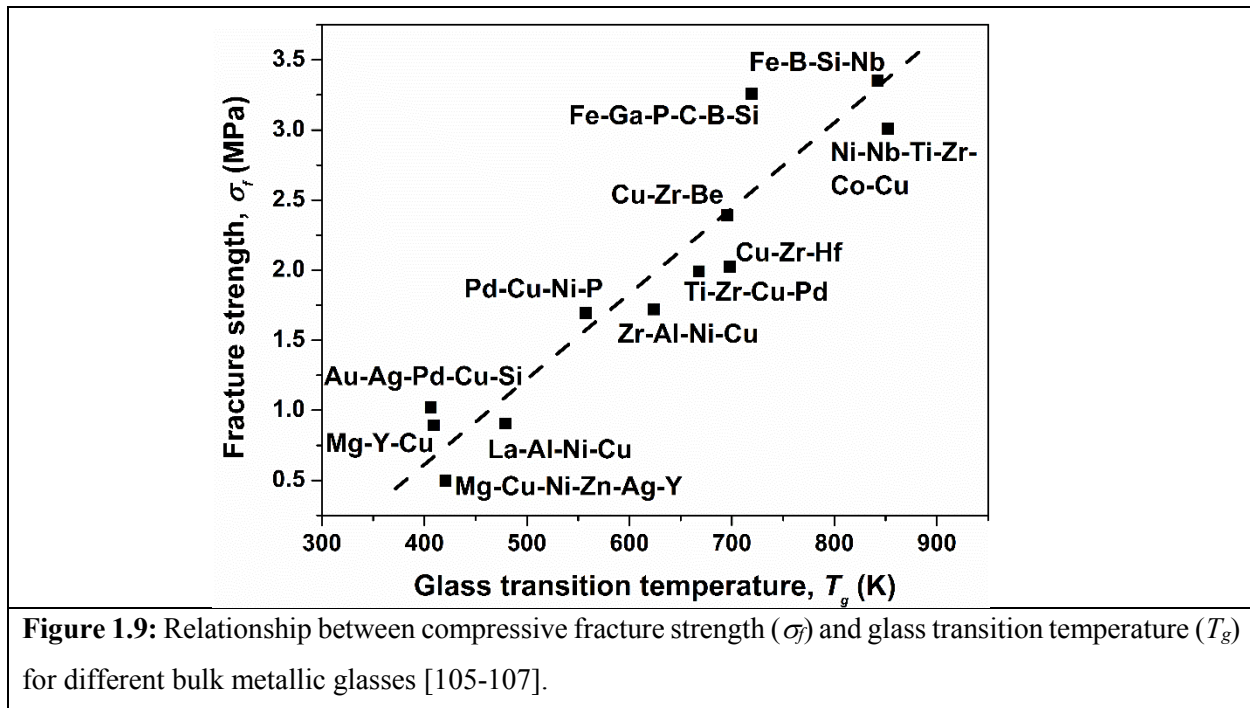
1.5.1 Deformation behavior of metallic glasses

The deformation behavior of metallic glasses including BMGs changes significantly at different temperature regimes. At lower temperatures, i.e. less than $0.5T_g$, the deformation is mostly concentrated in a few very thin shear bands that form approximately on the planes of maximum resolved shear stress. This localized deformation is referred to as inhomogeneous deformation. The inhomogeneous deformation in the metallic glass makes it mechanically unstable at high stresses, leading to catastrophic failures. On contrary, at slightly elevated temperatures, i.e. higher than $0.5T_g$, metallic glass undergoes viscous flow in which the plastic strain is distributed

continuously, not necessarily equally, between different volume elements within the material. In such case, each volume of the specimen contributes to the strain. This type of behavior is referred to as homogeneous deformation [62].

1.5.2 Inhomogeneous deformation

In general the crystalline materials undergoes strain hardening, when subjected to mechanical loading, as a result material becomes harder and therefore it is difficult to deform the materials beyond certain limit. In contrast, to the crystalline materials metallic glasses have been shown to exhibit the phenomenon of strain softening, i.e. an increase in strain makes the material softer and allows the material to be deformed at lower stresses and higher rates [62, 98, 100]. So far, several theories suggested for inhomogeneous deformation through formation of shear band.

Shear transformation zone theory

According to this theory the viscosity in the shear bands decreases during deformation due to the formation of free volume. This decreases the density of the glass and, consequently, decreases the resistance to deformation. Argon *et al*. [108, 109] suggested that during deformation small clusters of close-packed atoms spontaneously and co-operatively rearrange to accommodate the applied shear strain, which are termed as a shear transformation zone (STZ) as shown in Fig.1.10. [108, 110-114]. During shearing, STZ essentially involves a cluster of atoms that undergoes an inelastic shear distortion from one low energy configuration to another configuration with relatively low energy through an intermediate activated state with a high energy and a large volume [115, 116]. With further increase in the applied shear strain more STZs will be triggered, which results in the formation of shear bands [115].
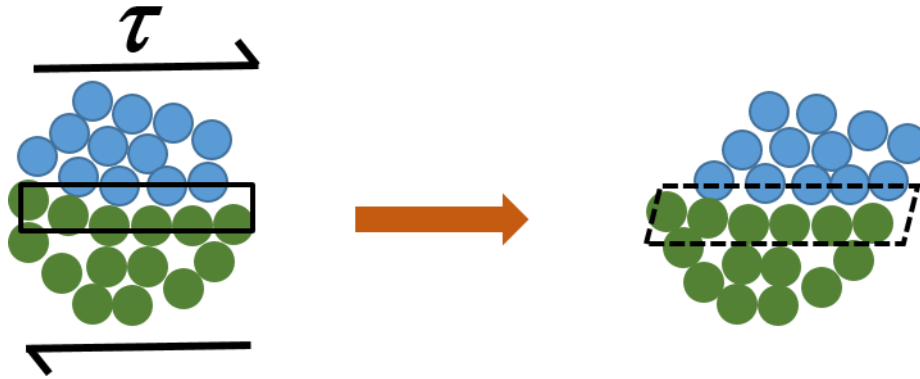
Figure 1.10: Two dimensional schematics of the atomistic deformation mechanisms proposed for amorphous metals, shear transformation zone (STZ) proposed by Argon [109]. Redrawn from [98]

The first quantitative model for the STZ was proposed by Argon in 1979 [109], indicating that the STZ operation is allied to the elastic confinement of the glass matrix and strain redistribution around the STZs. The free energy for the STZ activation in terms of the elastic constant of the glass is given by:

$$\Delta F_0 = \left[\frac{7-5v}{30(1-v)} + \frac{2(1+v)}{9(1-v)} \beta^2 + \frac{1}{2\gamma_0} \cdot \frac{\tau^0}{\mu(T)} \right] \cdot \mu(T) \cdot \gamma_0^2 \cdot \Omega_0 \qquad (1.8)$$

where v is Poisson's ratio, τ_0 is the athermal shear stress at which the STZ transforms, and $\mu(T)$ is the temperature dependent shear modulus. The second term in the bracket contains the dilatational energy related to STZ action, β is the ratio of the dilatation to shear strain, γ_0 is generally adopted to be of order ~ 0.1, and Ω_0 usually consists of a few to ~ 100 atoms [100, 109, 113, 117, 118]. Hence, the energy of an STZ is estimated to be on the order of 1-5 eV, or ~ 20-120$k_B T_g$, where k_B is the Boltzmann constant [100].

Free volume model

An alternative view on mechanism of plastic flow in metallic glasses is given by the classical "free-volume" model, as developed by Turnbull and co-workers [67, 119] and applied to the deformation of metallic glasses by Spaepen [120]. Free volume is defined that part of the thermal expansion or excess volume which is redistributed without energy change [121].

This model essentially views deformation as a series of discrete atomic jumps in the glass, as shown in Fig. 1.11.
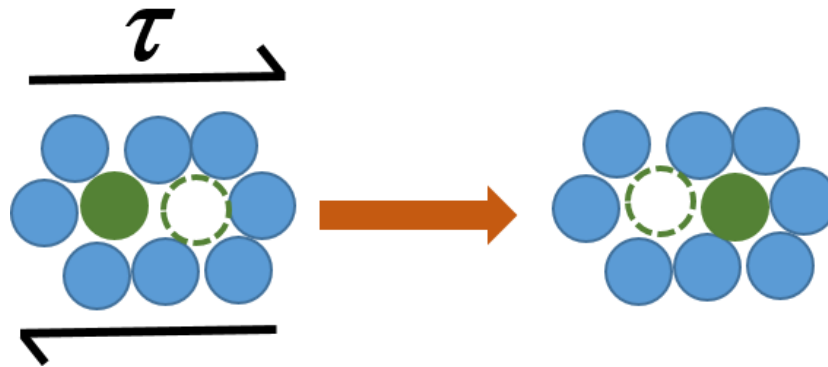
Figure 1.11: Two dimensional schematics of the atomistic deformation mechanisms proposed for amorphous metals, free volume model proposed by Spaepen [120]. Redrawn from [98].

The empty space around constituent atoms is called free volume and is assumed to be distributed statistically among all the atoms in metallic glasses [122-124]. Due to the weak mechanical coupling to the surroundings regions with large free volume, the inelastic relaxation is prone to occur by local atomic re-arrangements [19, 100, 115, 120]. These regions can act as a preferred sites where the destabilization of the glassy structure occurs with increase in applied stress. At low stresses, the annihilation rate of the free volume is exactly equal to its creation rate so that free volume keeps constant. At high stress, as the creation rate is larger than the annihilation rate, the softening occurs together with the increase of free volume. As the applied stress decreases the driving force for the creation of free volume decreases until the formation of new free volume achieves a steady state [19, 100, 115, 120].

1.5.3 Homogeneous deformation

Homogeneous deformation in metallic glasses occurs at high temperatures ($> 0.7T_g$) and also in the supercooled liquid state. This deformation could be thought as viscous flow of the supercooled liquid resulting in significant plasticity. It is possible to achieve net-shape forming capability by working with metallic glass in this temperature regime [125-128].

The homogeneous deformation is strongly dependent on the applied strain rate, suggesting that this could be is associated with a rate process [62]. The homogeneous deformation of the metallic glasses can also be understood using the concept of STZ proposed by Argon (see section 1.5.21.) [62, 109].

1.5.4 Temperature rise in the shear bands

As mentioned above (section 1.4.2), the local decrease in viscosity near the shear bands may aid the inhomogeneous flow in metallic glasses. Another theory suggested for this inhomogeneous deformation by Leamy *et al*. [129] was local adiabatic heating in the shear band. In his theory he proposed that shear banding in metallic glasses could occur due to adiabatic heating. Since it is difficult to measure directly the actual temperature rise in the shear band, alternative and indirect methods have been employed. The local temperature rise in shear bands estimated by different researches [130-139] is ranging from 0.1 to a few thousand degrees Kelvin. This large discrepancy is mainly due to the difficulty of direct measuring the temperature in extremely small distances of the shear band widths (~10-20 nm) [140-144] and short timescales (~10^{-5} s) for shear band propagation [114, 145]. Lately, different experimental techniques were used to measure the temperature rise in the shear bands. Yang *et al*. [137, 146] used a high speed infrared (IR) capture the dynamic shear band evaluation process in a Zr-based BMG alloy. In their work they have estimated that at the shear band initiation site the rise in temperature can be up to 650 K. Similarly, Bruck *et al*. [133] measured the temperature rise during dynamic testing of Zr-based BMG at a strain rates of 10^2-10^3 s^{-1}. From their measurement, they reported the rise in temperature was ~ 500 K near the shear bands. Recently, Yang *et al*. [147] used the STZ model proposed by Argon [109] to estimate the temperature rise in a shear band. In that model he balanced the mechanical work and heat generation with in an STZ unit, and also assumed that the whole process is adiabatic [62]. Based on his model, the shear band temperature of nine BMGs with six different alloys systems were calculated and the results are shown in Fig 1.12. Figure 1.12 shows the results of the temperature rise in the shear band at the time of fracture plotted against T_g. The temperature estimated in this method is limited only to the initial stage of shear banding [147]. From this result it was concluded that the catastrophic failure of BMGs is caused by the sudden drop in viscosity inside the shear band as a result if local heating to a level close to the glass transition temperature.
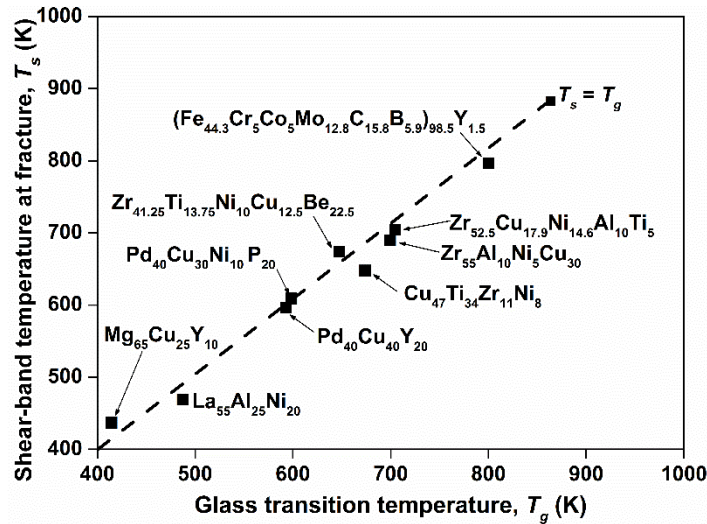
Figure 1.12: Temperature rise in the shear bands at the time of fracture for different BMG alloys plotted against the glass transition temperature [147].

1.6. Methods to improve the plasticity in metallic glasses

In general, most of the metallic glasses do not exhibit strain hardening and can sustain no plastic deformation. This brittle behavior under mechanical loading severely limits the applications of BMGs as engineering materials [98, 100]. So far, much attention has been paid to improve the plasticity in BMGs. Johnson and his group [117, 148] pointed out that plastic yielding of MGs at room temperature can be roughly described by an average shear strain limit of 0.0267±0.0020, implying that the elastic strain in required for the formation of a shear band nucleus in metallic glasses contains a collection of local STZs [149]. Therefore, the presence of a large STZ volume enables a smaller number of small STZs to be activated for the nucleation of a shear band. Moreover, these STZs result in the increase of the shear capability of the metallic glasses and facilitate the formation of multiple shear bands during plastic deformation. Hence the presence of large STZ volume in metallic glasses will aid in the improvement of plastic strain in metallic glasses.

It has been found that the plastic deformability can be largely enhanced by introducing different microstructural heterogeneities such as free volume, phase separation, nano-crystallization, short/medium-ranged clusters in to the glassy matrix by controlling the casting process [150-162]. In case of the phase separated BMGs, during deformation the second amorphous phase can act as a barrier for the crack propagation and thereby improving the room temperature plastic strain remarkably [163-167]. In case of Fe-based BMGs, the addition of small amounts of soft elements like Ni, Er and Cu can help in improving the room temperature plasticity [138, 168, 169].

Apart from addition of soft elements, phase separating elements and nano-crystals to alter the microstructure of the metallic glasses, pre-deformation methods such as cold-rolling, imprinting, ball milling or shot-peening can also introduce the heterogeneities in the glassy matrix. It has been demonstrated that pre-deformation can promote the plasticity of BMGs [170-180]. Improvement in the tensile plasticity of 0.5% was reported for $Zr_{50}Cu_{30}Ni_{10}Al_{10}$ BMG after cold-rolling with thickness reduction of 10 % [181].

Chapter 2

Experimental details and measurements

In this chapter, the experimental procedure involved in preparing the high quality glass-forming alloys, sample preparation techniques, sample characterization techniques, physical and functional property measurement techniques are discussed.

2.1 Sample preparation techniques

It is well known that, the quality of the starting master alloy, i.e. the absence of impurities like oxides or foreign inclusions, plays an important role in determining the GFA and reproducibility of the glassy samples [13]. For this reason, it is necessary to pay special attention to the preparation techniques.

In order to achieve a systematic understanding behind the improvement in mechanical and magnetic properties due to the addition of soft atoms like Cu and Ga in Fe-based glass-forming alloys, two different glass-forming systems $[(Fe_{0.5}Co_{0.5})_{0.75}B_{0.2}Si_{0.05}]_{96}Nb_4$ and $Fe_{74}Mo_4P_{10}C_{7.5}B_{2.5}Si_2$ were chosen [50, 89]. The master alloys $[(Fe_{0.5}Co_{0.5})_{0.75}B_{0.2}Si_{0.05}]_{96}Nb_4$, $\{[(Fe_{0.5}Co_{0.5})_{0.75}B_{0.2}Si_{0.05}]_{96}Nb_4\}_{100-x,y}$ (Cu_x, Ga_y) (x = 0.5), (y = 0.5, 1, 1.5, 2, 3, 4 and 5) , $Fe_{74}Mo_4P_{10}C_{7.5}B_{2.5}Si_2$ and $[Fe_{74}Mo_4P_{10}C_{7.5}B_{2.5}Si_2]_{100-x, y}$ (Cu_x, Ga_y) (x = 0.5 and 1), (y = 0.5, 1, 1.5 and 2) were prepared in several steps. In case of $[(Fe_{0.5}Co_{0.5})_{0.75}B_{0.2}Si_{0.05}]_{96}Nb_4$ alloy first the eutectic $Fe_{25}Nb_{75}$ (wt.%) pre-alloy was prepared by arc melting, followed by induction melting of the pre-alloy together with the rest of pure elements. The $Fe_{74}Mo_4P_{10}C_{7.5}B_{2.5}Si_2$ alloy was prepared through induction melting.

2.1.1 Arc melting

The eutectic $Fe_{25}Nb_{75}$ (wt.%) pre-alloy was produced by arc melting pure Fe (99.9 mass%) and pure Nb (99.9 mass%) lumps. The amounts of the constituting elements were weighed using a Mettler Toledo AT 200 scale and the accuracy is about 0.001 g.
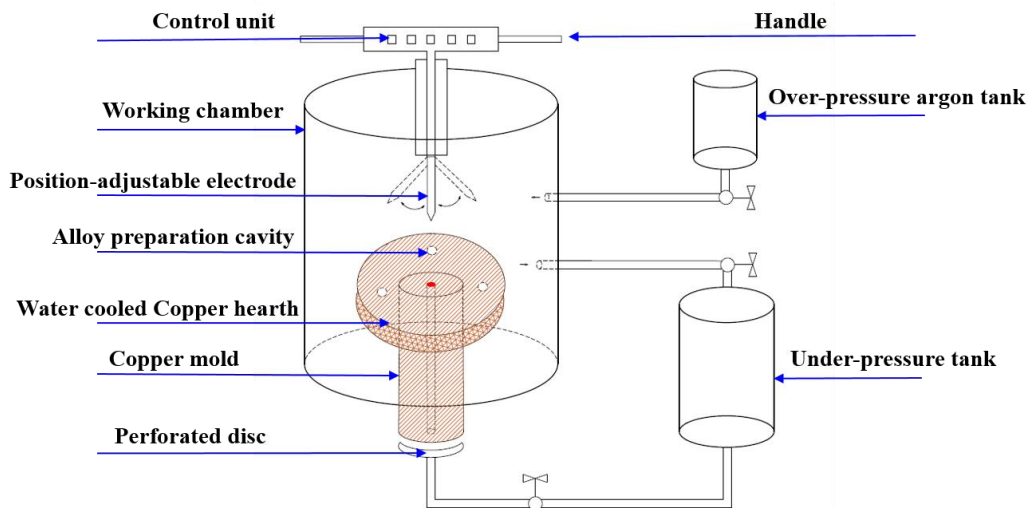
Figure 2.1: Schematic illustration of arc melting set-up.

This device consists of three important components: working chamber connected with vacuum pumps, tungsten electrode for melting and water cooled copper hearth, as shown in the Fig. 2.1. The working chamber is connected with a mechanical vacuum pump and a turbo-molecular vacuum pump in series; using these pumps it is possible to evacuate the chamber up to $10^{-5} – 10^{-6}$ mbar in 60-90 min. Tungsten electrode was used for producing the arc and the casting temperature was controlled by changing the melting current. The melting current can be varied from 0 to 400 A, while the melting time was controlled manually with a stop watch. The water cooled copper hearth has different cavities for both getter and alloy preparation; first the Ti getter was melted to remove the remaining traces of oxygen, followed by the melting of $Fe_{25}Nb_{75}$ pre-alloy. The pre-alloy was remelted at least three times to get the homogeneous composition.

2.1.2 Copper mold casting-master alloy preparation

The master alloy $[(Fe_{0.5}Co_{0.5})_{0.75}B_{0.2}Si_{0.05}]_{96}Nb_4$ were prepared by induction melting of the FeNb prealloy together with Fe and Co lumps (99.9 mass%), crystalline B (99.5 mass%) and crystalline Si (99.99 mass%), under protective argon (Ar) atmosphere. Similarly, the master alloy $Fe_{74}Mo_4P_{10}C_{7.5}B_{2.5}Si_2$ were prepared by the induction melting of Fe, Mo lumps (99.9 mass%), crystalline B (99.5 mass%) and crystalline Si (99.99 mass%), pure graphite as C, industrial Fe-P pre-alloy with P content of 14 at.%. Induction furnace with tilt casting facility made by EMA ELEKTRO MASCHINEN Schultze GmbH & Co. KG was used in order to produce the above mentioned master alloys. The experimental setup is shown in Fig. 2.2
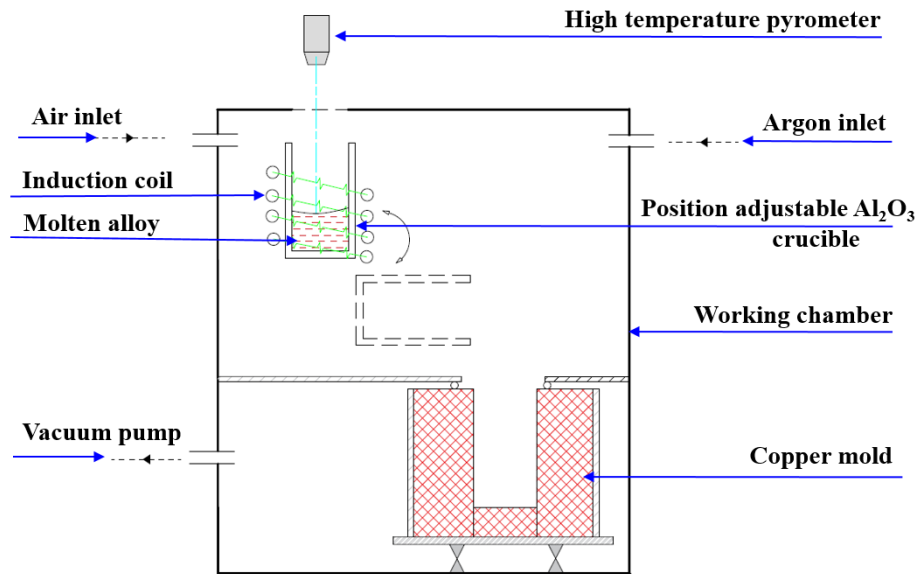
Figure 2.2: Schematic illustration of induction furnace set-up.

The device consist of two chambers: the melting chamber in which the induction coil and the working crucible are placed, and the mold chamber, which consist of copper mold. Both chambers can be evacuated up to 10^{-4} mbar using a vacuum pump and filled/flushed with 4N8 (i.e. 99.998%) pure Ar. For melting, ceramic (Al_2O_3) cylindrical crucible was used, with a diameter about 15 cm. The induction generator can deliver an adjustable power between 0 and 20 kW at a frequency of

20 kHz. The temperature was monitored by external infrared pyrometer visualizing the upper surface of the molten alloy through a glass window. The maximum achievable temperature was around 1800 °C. After melting all elements, the molten alloy was maintained at a temperature 200° C higher than its melting point for about 2 min, in order to get the homogeneous composition. The melting chamber can be tilted up to 90 degree to pouring the molten metal in to the casting chamber. The casting chamber may contain variable cylindrical copper molds, without cooling system. The copper molds with different internal channel sizes are used, depending upon quantity of the alloy melted.

Once the master alloys $[(Fe_{0.5}Co_{0.5})_{0.75}B_{0.2}Si_{0.05}]_{96}Nb_4$ and $Fe_{74}Mo_4P_{10}C_{7.5}B_{2.5}Si_2$ were produced, careful addition of Cu (99.99 mass %) and Ga (99.9 mass %) were done using the above mentioned arc melting technique. The above mentioned steps are followed to get master alloys of $\{[(Fe_{0.5}Co_{0.5})_{0.75}B_{0.2}Si_{0.05}]_{96}Nb_4\}_{100-x, y}$ (Cu_x, Ga_y) (x = 0.5), (y = 0.5, 1, 1.5, 2, 3, 4 and 5), and $[Fe_{74}Mo_4P_{10}C_{7.5}B_{2.5}Si_2]_{100-x, y}$ (Cu_x, Ga_y) (x = 0.5 and 1), (y = 0.5, 1, 1.5 and 2) respectively.

2.1.3 Melt-spinning

Melt spinning facility was used to produce the amorphous ribbons. In melt spinning, a molten metal is ejected by gas pressure on to a rapidly rotating wheel. Solidification occurs on the melt spinning wheel with a cooling rate of 10^5-10^6 K/s [182] and results in the formation of ribbons, the ribbons detach easily from the copper wheel due to differences in the thermal contraction.

Fig. 2.3 shows schematically the melt spinning device made by Edmund Bühler GmbH, which was used to produce the ribbons. This device consists of 2 chambers: the working chamber in which the induction coil and copper wheel are placed, and storage chamber, were the ribbons are collected after melt spinning. Both chambers can be evacuated up to 10^{-5}-10^{-6} mbar using rotary and turbo vacuum pumps and filled/flushed with 99.9% pure Ar.

Figure 2.3: Schematic illustration of melt spinning set-up.

The high-frequency induction generator can deliver an adjustable power between 0 to 30 kW at a frequency of 30 kHz. Pieces of the master alloys were inductively melted in a quartz tube, which has a circular nozzle tip of 5 mm length and 1 mm diameter. The position of the nozzle tip can be varied with respect to the wheel surface, the molten alloy was perpendicularly ejected onto the wheel surface from a distance of about 0.5 mm. An over-pressure of about 300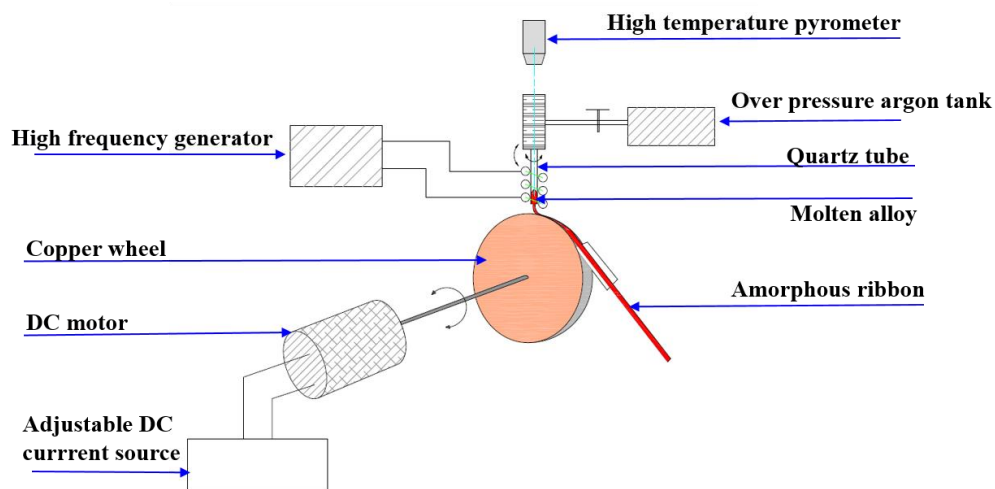 mbar of 99.998% pure argon was applied from the external tank. The temperature was monitored by an external infrared pyrometer visualizing the upper surface of the molten alloy through a quartz window. The maximum achievable temperature was limited to 1350 °C due to the working temperature limit of the quartz tube. The molten alloys were ejected at a temperature of about 150 to 200 K above the melting point of each alloy. The tangential velocity of the rotating copper wheel was precisely controlled with a specially built control system. In our work we used velocity of 25 m/s, to produce a homogeneous ribbons with an approximate width of 3-4 mm and a thickness of 35±5 μm respectively. The as-spun ribbons were directly guided in to the storage chamber, which was located in the same direction as that of the rotating copper wheel. The working parameters such as wheel velocity, ejection overpressure, distance between the nozzle and the wheel, ejection temperature, molten metal holding temperature were precisely controlled.

2.1.4 Injection casting

Injection casting facility was used to produce bulk amorphous samples. In this method, the molten alloy is injected in to a water-cooled copper mold by gas pressure. The cooling rates attained in this method are of the order of about 10^2-10^3 K/s [183].

Figure 2.4: Schematic illustration of injection casting set-up.

An in-house built injection casting device was used for the preparation of bulk glassy samples (Fig.2.4). This device consists of one working chamber in which the induction coil and copper mold are placed. The chamber can be evacuated up to 10^{-5}-10^{-6} mbar using rotary and turbo vacuum pumps and filled/flushed with 99.998% pure Ar. The High fr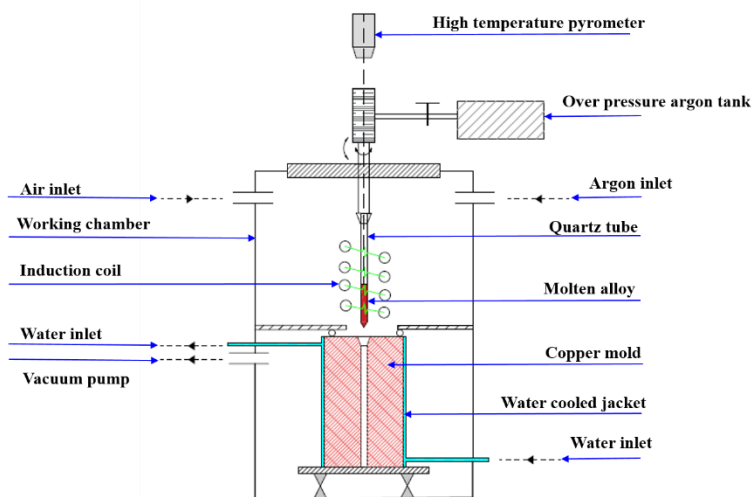equency induction generator can deliver an adjustable power between 0 to 30 kW at a frequency of 30 kHz. Pieces of the master alloy were inductively melted in a quartz tube, which has a circular nozzle tip of 5 mm length and 1 mm diameter. The distance between the nozzle tip and the inlet of the copper mold can be adjusted precisely, the mold entrance and the nozzle tip of the crucible are carefully aligned. The molten alloy was ejected onto the copper mold from a distance of about 0.5 mm. An over pressure of about 300 mbar of 99.998% pure argon was applied from the external tank. The temperature was monitored by an external infrared pyrometer visualizing the upper surface of the molten alloy

through a quartz window. The maximum achievable temperature was limit to 1350 °C due to the working temperature limit of the quartz tube. The molten alloys were ejected at a temperature about 150 to 200 K above the melting point of each alloy. The molds with an internal shape in the form of cylinder with 1, 1.5, 2, 2.5 and 3 mm diameter and 78 mm height, respectively, as well as a rectangular bar with 1x1mm and 2x2 mm and 78 mm height were used. The working parameters such as ejection overpressure, distance between the nozzle and the copper mold, ejection temperature, molten metal holding temperature were precisely controlled.

2.1.5 High pressure die casting

High pressure die casting method was chosen to obtain bulk amorphous alloys with large geometrical dimensions than those achieved by copper mold castings [184]. High pressure die casting (HPDC) has been widely used to manufacture a large variety of products with high dimensional accuracy and productivity [185]. HPDC is a single step process, in this method the casting defects such as gas pockets and shrink holes can be drastically reduced or controlled [184]. A schematic drawing of the high pressure die casting (HPDC) method used in our experiments is shown in Fig. 2.5 (a).

In our work the samples were cast in an industrial 'ÖGSZF110T' 100 t vertical high pressure die casting machine. For melting the alloy Kaloria GS/02 induction heating furnace was used. Typical HPDC machine is normally composed of two major sections: a fixed section (lower half of the die) and a movable section (upper half of the die and piston). The temperature during the whole casting process must be monitored and accurately controlled, as the quality of the casting is very sensitive to the variation in temperature. When the molten alloy is in the die cavity, the heat in the alloy should be removed to allow solidification and subsequent cooling to occur. However, the die temperature depends on a number of process variables such as cycle time, spray distribution and duration, water layout and flow rate, casting volume/geometry, as well as molten metal temperature and composition. In this work all the key-shaped samples were prepared at Breuckmann GmbH & Co KG Heiligenhaus, Germany, with the help of Dr. Attila Szabo and Dr. András Bárdos.
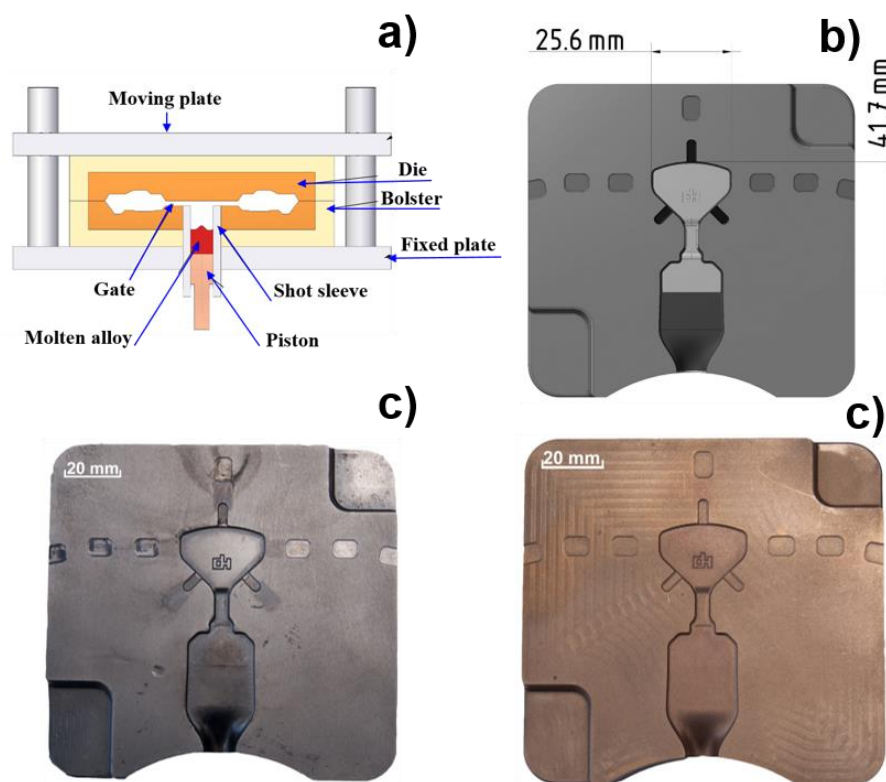
Figure 2.5: (a) Schematic illustration of high pressure die casting set-up; (b) 3D model of die. (c) Completed dies made from heat resistant steel and a copper alloy.

Figure 2.5 (b) show the 3D model of the die and Fig. 2.5 (c) and (d) the completed die made from a heat resistant steel and a copper alloy, respectively. Two different die materials were used for the casting purpose: heat resistant steel with a low heat conduction rate of 33 W/mK and a Cu alloy with high heat conduction rate of 230 W/mK respectively. The reason for the choice of the two different die materials was to test the influence of heat conduction on glass formation and on the die life.

2.2 Analysis techniques

2.2.1 Chemical composition analysis

The elemental composition analysis were done for all pre-alloys and master alloys after the preparation. Composition deviations due to the evaporation of some elements during the melting processes were carefully checked using Inductively Coupled Plasma with Optical Emission

Spectrometry (ICP-OES) technique. For analysis iCAP6500 DUO View instrument from Thermo Fisher Scientific GmbH was used.

In this technique, a piece of the sample is completely dissolved using a mixture of concentrated H_2SO_4 and concentrated HCl solutions. Then the analyte solution is sprayed as an aerosol into an argon plasma. At temperatures of 6500 K the elements are atomized and/or ionized. The temperature is high enough to excite atoms and ions so that they emit light. The resulting spectrum consisting of many emission lines is split up by an Echelle optics. The intensity of the emission lines is proportional to the concentration of the analyte. The accuracy of the device is 0.01-1 µg/l (depending on element).

2.2.2 Thermal analysis

A computer-controlled differential scanning calorimeter (NETZSCH 404) was used in order to determine glass transition, crystallization and melting point of the glassy samples. In our experiments we have used alumina (Al_2O_3) crucibles for the measurement, the camber was evacuated up to 10^{-5} mbar and then continuously flushed with 99.9% pure Ar. For all the measurements samples mass are maintained around 18-20 mg and heating rates of 5, 10, 15 and 20 K/min were used depending up on the measurements. The glass transition temperature T_g, the crystallization temperature T_x and the liquidus temperature T_{liq} were determined as the onsets of the respective events, using the two tangent method (for more details see the ref [186]). The accuracy of the measured data lies within ± 2 K.

2.3 Structural characterization techniques

2.3.1 X-ray diffraction

A standard X-ray diffraction (XRD) analysis was carried out to identify the phase formation of the samples. For our investigation we have used reflection and transmission configuration.

For reflection configuration (PANalytical X'Pert Pro Diffraction) Bragg-Brentano diffractometer using Co-K$_\alpha$ ($\lambda = 0.178897$ Å) was used. The diffractometer operated at a voltage of 40 kV and a current of 40 mA. In order to maintain the uniformity in the sample height, all the bulk samples were ground to 0.5 ± 0.01 mm. The diffraction intensities are recorded between 20 and 120 degrees (2θ) in a step mode, with a step size of $\Delta(2\theta) = 0.013°$ and data acquisition time per step 2.5 s.

2.3.2 Scanning electron microscopy (SEM)

Scanning electron microscopy (SEM) investigations were performed using Zeiss Gemini 1530 (Carl Zeiss AG) microscope. The fractured samples after compression tests were cleaned in ultrasonic bath using acetone as cleaning liquid. The samples are carefully mounted on special carbon tape for good electrical contact.

2.3.3 Transmission electron microscopy (TEM)

The investigations were performed using a Carl Zeiss Libra 200MC Ultra-High Resolution Transmission Microscope (UHR-TEM). The investigations were carried out at National Institute of Research and Development for Technical Physics (NIRDTP) Iasi, Romania, with the help of Dr. Gabriel Ababei, who operated the microscope. The samples were cut into slices with a thickness of about l mm from the as-cast rods. A further mechanical polishing, down to 100 μm thickness, was done using silicon carbide paper and diamond suspensions. The next thinning process, down to < 80 μm, was done using a dimple grinder. In order to obtain the final transparent area, a Focused Ion Beam (Carl Zeiss NEON 40 EsB Cross Beam) was used for FeCoBSiNb + Cu and FeMoPCBSi + Cu glasses and a GATAN Precision Ion Polishing System (PIPS) was used for FeCoBSiNb + Ga and FeMoPCBSi + Ga glasses. Ga added samples are relatively softer compared to the Cu added samples, therefore the two routes used for final thinning.

2.4 Magnetic measurements

2.4.1 Coercivity measurements

The coercivity (H_c) of the soft magnetic samples were directly measured using a DC Förster Coercimat, in which the magnetic field can be varied continuously from -250 mT to + 250 mT. The schematic view of the device is shown in the Fig 2.6.
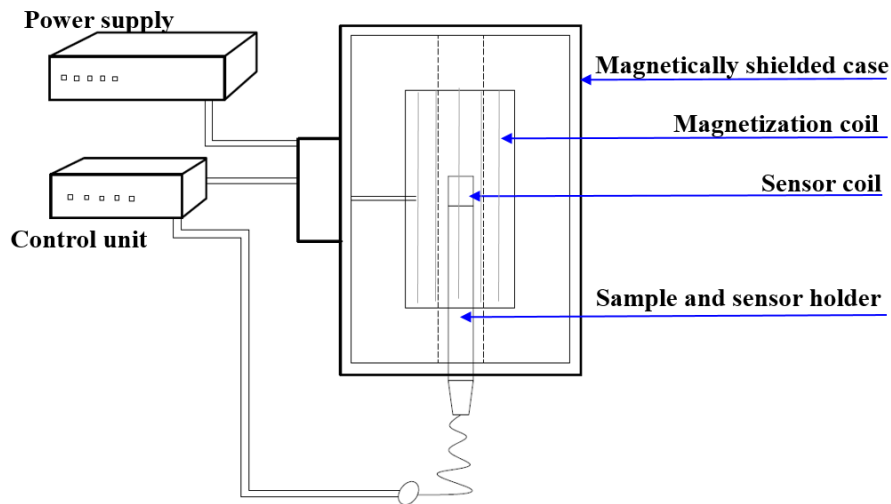
Figure 2.6: Schematic illustration of DC Förster Coercimat.

This device consist of one magnetizing coil and one pick up coil as shown in the above figure. For the H_c measurement the sample is placed over the pickup/sensor coil and the whole setup is positioned at the center of the magnetizing coil. Initially the sample is subjected to a high magnetizing field for few seconds and then the field is turned off. In the absence of the field the sample will have some residual magnetic field, which causes stray field proportional to the magnetization. This field can be reduced to zero by applying a magnetic field in the opposite direction compared to the magnetic field, the sensor coil will pick up the applied field and convert values directly it into A/m. This device can measure the values in both $+H_c$ and $-H_c$, the absolute value of the coercivity is the average of these two values: $H_c = (+H_c + (-H_c))/2$ [70].

For H_c measurements, in order to avoid the shape anisotropy due to different sizes of the samples, only cylindrical samples with the ratio of 1:10 (diameter : height) were used (i.e. minimum length for 2 mm diameter sample is 20 mm).

2.4.2 Saturation magnetization measurements

Physical property measurement system (PPMS) device was used to measure the magnetic properties of the magnetic properties of the soft magnetic materials. In our work, Quantum design PPMS 6500 device was used. In PPMS two different setups were used: The vibrating sample magnetometer (VSM) mode is designed to measure the saturation magnetization (M_s) of the soft magnetic samples and high temperature /furnace mode is designed to measure the saturation magnetization versus temperature for the magnetic samples. The PPMS in VSM mode is schematically shown in Fig. 2.7.
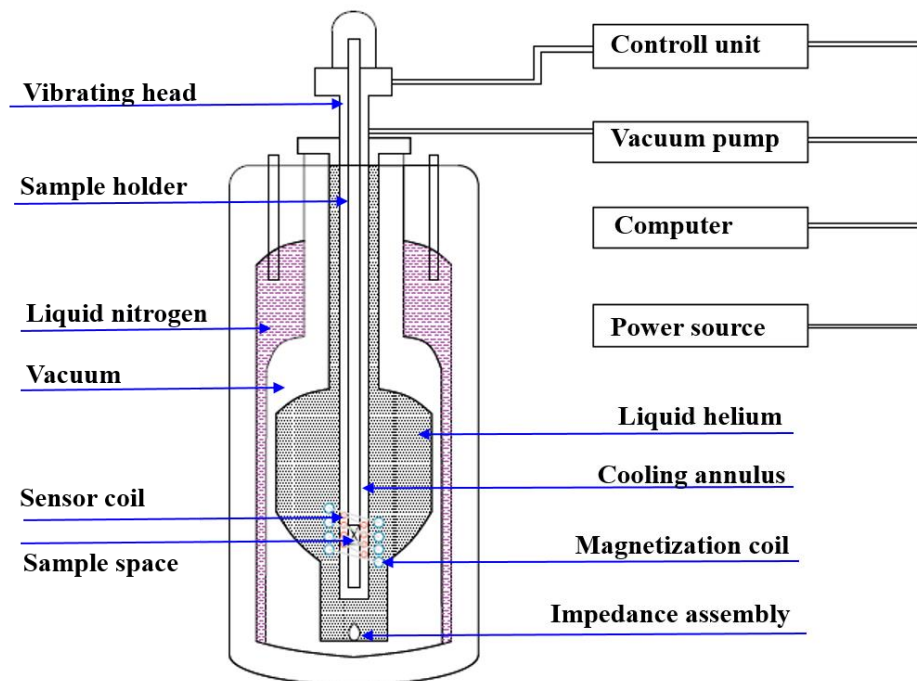
Figure 2.7: Schematic illustration of Physical Property Measurement System (PPMS).

In this system Magnetic DC fields up to 20 kOe ($\mu_0 H = 2$T) can be applied to the samples with a superconducting electromagnet. For saturation magnetization measurement the sample is mounted on a thin brass plate/tube. In VSM mode, the sample is vibrated continuously up and down inside the pickup coil, with a DC field varying between -10 kOe to 10 kOe. The magnetic sample is thus acting as a time-changing magnetic flux, varying inside a particular region of fixed area. From the Maxwell's law it is known that a time-varying magnetic flux is accompanied by an electric field [187] and the field induces a voltage in the pickup coils. This alternating voltage signal is processed by a lock-in amplifier. The result is a measure of the magnetization of the sample [70].

2.4.3 The Curie temperature measurements

In high temperature mode the magnetization of the sample is measured as a function of temperature. Before the measurements, the device was calibrated with pure Ni-samples. In this mode the sample is mounted on a thin heating plate (Rhodium heating coils), which can heat the samples up to 1000 K. the change in the sample temperature will modify the value of its magnetization [188].
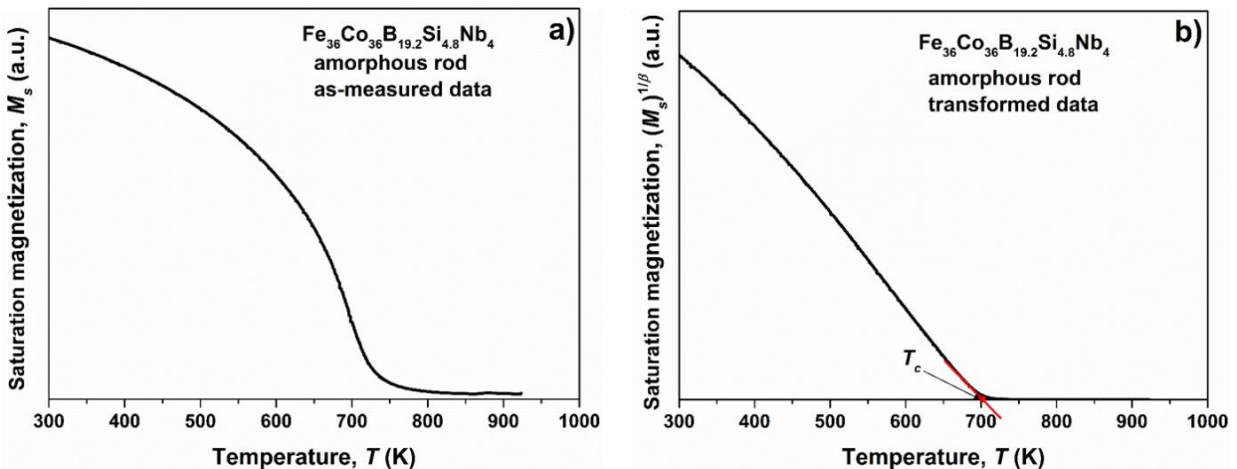
Figure 2.8: Saturation magnetization vs temperature (a) experimental data (b) transformed data used to determine the Curie temperature. The data corresponds to $Fe_{36}Co_{36}B_{19.2}Si_{4.8}Nb_4$ amorphous rod.

When the temperature approches T_c, the saturation magnetization can be described as [79]:

$$M_s(T) = M(0) \cdot \left[1 - \frac{T}{T_c}\right]^\beta,$$ (2.1)

where the exponent $\beta = 0.36$. In order to minimize the errors, the Curie temperature was considered as the temperature at which the $(M_s)^{1/\beta}$ deviated from the linearity. Fig. 2.8 shows the saturation magnetization as a function of temperature, (a) experimental data and (b) transformed data, i.e. $(Ms)^{1/\beta}$ vs temperature. The red dot in the image points the Curie temperature (T_c).

2.5 Mechanical characterization

2.5.1 Compression tests

The room temperature stress (σ) versus strain (ε) curves of the cylindrical samples in compression mode were determined using an INSTRON 8562 device, fitted with a laser-extensometer (Fiedler Optoelektronik GmbH). For compression tests the samples were prepared with an aspect ratio of 1:2 (diameter: height). The top and bottom faces were carefully polished and checked to be plane parallel. The machine was operated in constant strain rate mode, with a strain rate of 10^{-4} /s and the cross-head speed is 0.001 mm/s. The stress $\sigma = F/S$, where F is the applied force and S the cross-section area, was automatically calculated. From $\sigma = f(\varepsilon)$ plot the Young's modulus E can be calculated, as well as the yield stress (σ_y), the fracture stress (σ_f), the yield strain (ε_y) and the fracture strain (ε_f).

2.5.2 Hardness measurements

The hardness of the amorphous alloys was measured using a computer-controlled Struers Duramin 5 Vickers hardness tester. The device was equipped with a typical diamond indenter in the form of a pyramid with square base and an angle of 136 degrees between opposite faces. The Vickers hardness HV was calculated according to the following equation

$$HV = \frac{0.189F}{D^2}$$ (2.2)

where F is the applied load and D is the indentation diagonal. For each indentation, a load F of 0.980 N was applied for 10 seconds. The diagonal of the imprints as well as the hardness were calculated using a Digital Video Measuring System. Cross-section slice from the as-cast cylindrical bars were used for the investigation. The final hardness values were obtained after averaging 20 experimental data points.

2.5.3 Density measurements

The density measurements of the alloys were performed with Mettler Toledo instrument. Archimedes principle was utilized to find the density of the as-cast glasses. The sample was first weighed 60 times in air and then was soaked in water for an hour. The soaked sample was weighed again 60 times in the water. The density of the sample was then calculated by the ratio of the average weight of the sample in water to the average weight of the sample in air.

Chapter 3

Preparation and characterization of Fe-Co-B-Si-Nb-(Cu, Ga) bulk glassy samples

3.1 Introduction

The investigated compositions $[Fe_{36}Co_{36}B_{19.2}Si_{4.8}Nb_4]_{100-x,y}$ (Cu_x, Ga_y) (x = 0, 0.5)(y = 0, 0.5, 1, 2, 3, 4 and 5) are of metal-metalloid type. The basis for this alloy family is $Fe_{75}B_{15}Si_{10}$ alloy, first introduced by Hagiwara *et al*.[189]. The glass-forming ability of this glass-forming system was gradually increased by adding Nb at the expense of all elements [84]. Further, the GFA of this system may be increased by partially replacing Fe with Co or Ni or with both Co and Ni [50, 59]; as a result, a cast rod having 5 mm diameter was reported for the composition $[(Fe_{0.5}Co_{0.5})_{0.75}B_{0.2}Si_{0.05}]_{96}Nb_4$ [59, 190]. However, the replacement of Fe with Co or Ni decreases the saturation magnetization from 1.5 to 1.1 T depending on the percentage of substituting elements [50, 59, 84]. Bitoh *et al.* [191] reported a 7.7 mm diameter rod by melting the $[(Fe_{0.5}Co_{0.5})_{0.75}B_{0.2}Si_{0.05}]_{96}Nb_4$ master alloy together with a dehydrated B_2O_3 (fluxing agent) and then water quenching the whole melt. This bulk specimen is the thickest of any soft magnetic glass formed until now [3, 191]. From these recent works it is clear that $[(Fe_{0.5}Co_{0.5})_{0.75}B_{0.2}Si_{0.05}]_{96}Nb_4$ is the best glass former in its family. It is worth mentioning here, all the above mentioned 5 mm and 7.7 mm diameter samples are reported form the same Japanese group (i.e. Inoue's group in Sendai, Japan). In our lab the maximum achievable diameter upon injection casting was 3 mm for a length of 5 cm [3].

An important aspect, which limits the application of these bulk Fe-based metallic glass as an engineering materials, is the brittle behavior under mechanical loading [75]. In the last decade great efforts have been made to improve the plastic deformability of monolithic BMG or BMG composites. In our work we tried to improve the plastic deformability of the $[(Fe_{0.5}Co_{0.5})_{0.75}B_{0.2}Si_{0.05}]_{96}Nb_4$ glass by adding soft elements like Cu and Ga, in small percentage, at the expense of all elements. The concept of adding Cu to Fe-based glass was first introduced by Yoshizawa *et al*. [80] with the goal of improving the soft magnetic property of Fe-Si-B-Nb glass (FINEMET) through the precipitation upon annealing of nano α-Fe crystals in the amorphous

matrix. Since then Cu is added in several Fe-based metallic glass systems to improve their soft magnetic properties [81, 82, 85, 192-198]. Interesting to remark is that the nanocrystalline Fe-based alloys containing Cu are brittle [199], but, as it is also in our case, the as-cast samples may withstand a compressive plastic deformation. In the earlier works [53, 200, 201], Ga was used in several multicomponent Fe-based glasses to improve their GFA. In our work, Ga was chosen because of its low Young's modulus E of 9.8 GPa, large Poisson ratio ν of 0.47, low melting point $T_m \approx 303$ K [202] and its electronic structure, i.e. mainly s and p orbitals contribute to the metallic bonding [203]. The relatively large atomic radius of Ga (0.153 nm) also influences the atomic-level structure of the BMG.

For the compositions investigated in this work first $[(Fe_{0.5}Co_{0.5})_{0.75}B_{0.2}Si_{0.05}]_{96}Nb_4$ alloy was produced and then later Cu and Ga were added through arc melting. In this way $\{[(Fe_{0.5}Co_{0.5})_{0.75}B_{0.2}Si_{0.05}]_{96}Nb_4\}_{99.5}Cu_{0.5}$ and $\{[(Fe_{0.5}Co_{0.5})_{0.75}B_{0.2}Si_{0.05}]_{96}Nb_4\}_{100-y}Ga_y$ (y = 0.5, 1, 1.5, 2, 3, 4 and 5) alloys were obtained. This chapter presents the microstructure, mechanical and magnetic properties of the ribbons and rods produced from these alloys.

3.2 Characterization of amorphous ribbons and bulk samples

The addition of Cu to the $[(Fe_{0.5}Co_{0.5})_{0.75}B_{0.2}Si_{0.05}]_{96}Nb_4$ master alloy (for simplicity, this alloy will be further denoted as FeCoBSiNb) decreases the GFA drastically. For the addition of 0.5 at.% Cu the critical diameter (t_c) decreases to 2.5 mm and upon further increase of the Cu content it was possible to produce only amorphous ribbons [85, 195-198]. In the case of Ga addition up to 1.5 at.%, the GFA was not affected much; however further increase in Ga content decreases the GFA and its not possible to produce bulk samples when the Ga content is more than 5 at.%. Hence in our work we limited the addition of Cu and Ga to 0.5 at.% and 5 at.%, respectively.

3.2.1 Diffraction experiments using Co-$K\alpha$ radiation

The structure of the as-cast rods was investigated by X-ray diffraction using Co-K_α radiation ($\lambda=$ 0.17889 nm). Fig. 3.1 (a) and (b) depicts the XRD patterns of the as-cast $[FeCoBSiNb]_{100-x}(Cu)_x$ (x = 0, 0.5) and $[FeCoBSiNb]_{100-y}(Ga)_y$ (y =0, 0.5, 1, 1.5, 2, 3, 4 and 5) glassy samples with maximum achievable diameter.
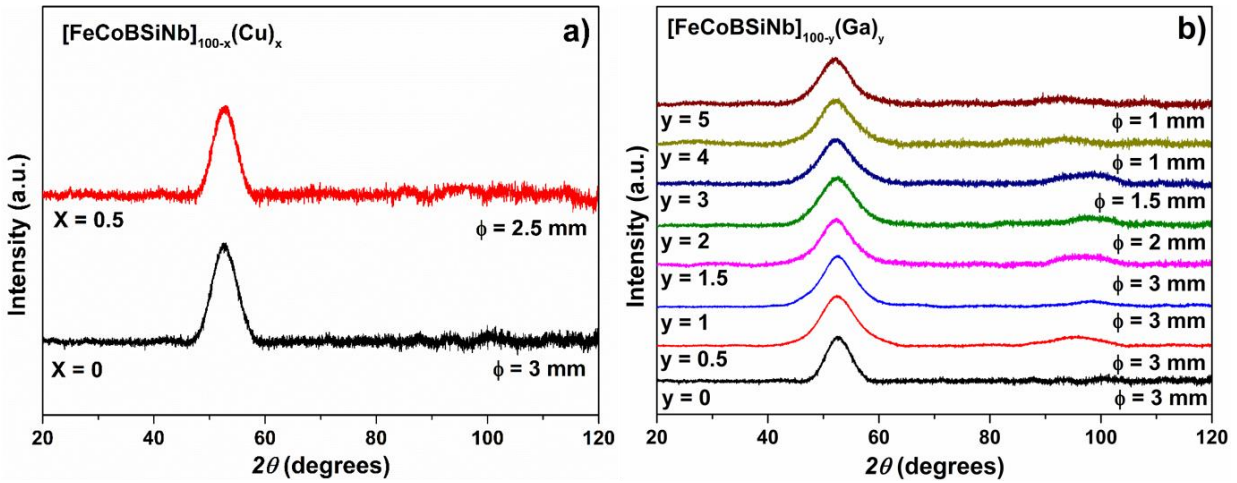
Figure 3.1: X-ray diffraction patterns of (a) as-cast [Fe$_{36}$Co$_{36}$B$_{19.2}$Si$_{4.8}$Nb$_4$]$_{100-x}$ (Cu)$_x$ (x = 0, 0.5) and (b) as-cast [Fe$_{36}$Co$_{36}$B$_{19.2}$Si$_{4.8}$Nb$_4$]$_{100-y}$ Ga$_y$ (y = 0, 0.5, 1, 1.5, 2, 3, 4 and 5) glassy rods.

The XRD patterns in Fig. 3.1 (a) and (b) exhibit characteristic broad diffraction maximum indicating the formation of a glassy structure. The first and second broad diffraction maxima for FeCoBSiNb glass are located at 2θ = 52.61° and 98.35°, respectively. However, the position of the broad maximum shifts slightly to lower diffraction angles with increase in Ga content. In case of the 0.5 at.% Cu addition, the peak shift is almost negligible (within the error bars). In order to avoid the errors in calculating the peak positons due to difference in the sample thickness, only ribbons were used for the peak position analysis. Fig. 3.2 (a) depicts the XRD patterns of [FeCoBSiNb]$_{100-y}$ (Ga)$_y$ (y =0, 0.5, 1, 1.5, 2, 3, 4 and 5) glassy ribbons. Fig. 3.2 (b) shows the shift of the first and second broad maxima of the XRD patterns presented in Fig. 3.2 (a) as a function of Ga content. The 2θ positions were obtained by fitting the broad diffraction maxima with symmetric Pseudo-Voigt function. The fitting errors are no larger than ± 0.03°. The first broad maxima shift continuously towards lower 2θ values with different slopes from 52.6° to 51.99° as the Ga content increases from 0 to 5 at.%, respectively. Similarly, the position of the second maxima also moves constantly with different slopes from 98.35° to 97.89° with the increase of Ga content.

For crystalline materials, where the Bragg's law for the first diffraction peak can be directly applied:

$$2d \cdot sin\theta = n\lambda \tag{3.1}$$

a shift of the diffraction angle 2θ towards lower values would mean an increase in the interplanar distance d:

$$d = \frac{n\lambda}{2 \sin \theta} \tag{3.2}$$
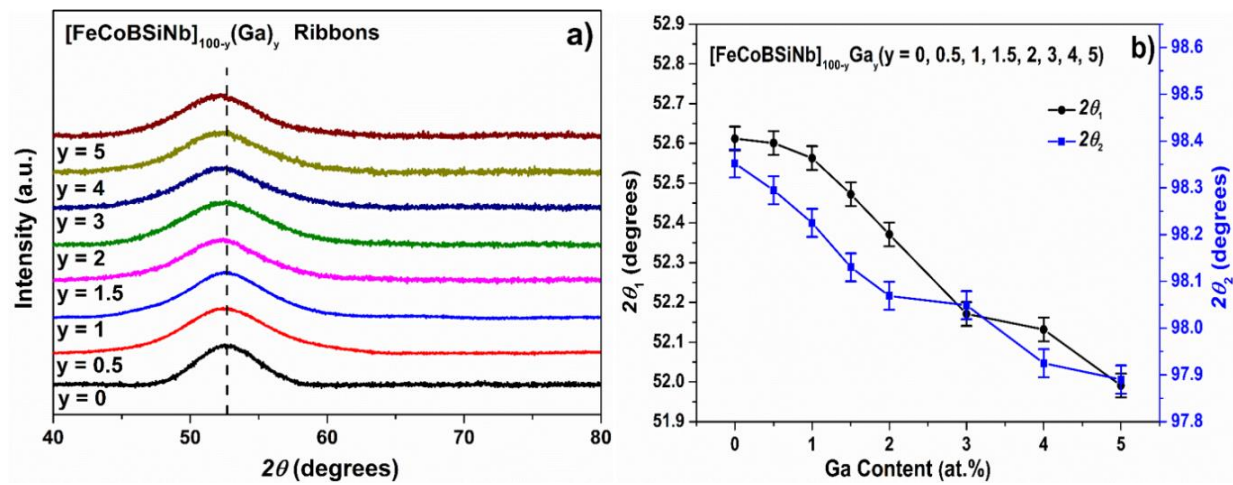
Figure 3.2: (a) X-ray diffraction patterns of as-spun $[Fe_{36}Co_{36}B_{19.2}Si_{4.8}Nb_4]_{100-y}Ga_y$ (y = 0, 0.5, 1, 1.5, 2, 3, 4 and 5) glassy ribbons and (b) changes in the position of first ($2\theta_1$) and second ($2\theta_2$) broad diffraction maxima center as a function of Ga content (at.%)

In case of amorphous alloys, because of the absence of any long-range order, the Bragg relations should be considered with restrictions. However, the position of the first broad diffraction maximum scales with the mean interatomic distance r_i through the Ehrenfest equation [204]:

$$Q = 1.23 \cdot \frac{2\pi}{r_i} \quad , \tag{3.3}$$

where Q is the wave vector:

$$Q = \frac{4\pi \cdot sin\theta}{\lambda} \quad . \tag{3.4}$$

Therefore,

$$sin\theta = \frac{1,23 \cdot \lambda}{2r_i} \tag{3.5}$$

The shift of first broad maximum towards lower $2\theta_1$ values indicates an increase in the mean atomic distance. The Ga atom has higher atomic radius (0.153 nm) when compared to B, Si, Fe and Co atoms (0.081 nm, 0.077 nm, 0.116 nm and 0.116 nm [202], respectively). The incorporation of the larger Ga atoms may result in such peak shifting, leading to structural changes (i.e. ordered zones/clusters) in these glassy alloys, which will be in detail discussed later. The slope of $2\theta_1$ changes as the Ga content reaches 1, 3 and 4 at.%, respectively. This indicates that more complex rearrangements are taking place at atomic level. However, the slope of $2\theta_2$ changes at a slightly different rate but the same trend was observed. According to Bernal's dense random packing hard-sphere model [205], metallic glasses can be conveniently described to a first order approximation, so that the position of the broad maxima are related to the different neighborhood shells and characterize the medium and short-range order (MRO, SRO). The position of the first broad peak scales with the mean interatomic distances and the second broad peak hold the information about MRO. Therefore it can be concluded that the substitution of Cu and Ga atoms increases the mean atomic distances but, at the same time, may provoke atomic level rearrangements. Therefore, it is expected that the Cu and Ga added glasses behave different compared to Cu and Ga free glass.

3.3 Characterization behavior, Thermal studies

The influence of the alloying elements on the GFA and thermal stability can be evaluated from the calorimetric measurements. DSC traces of the as-cast $[\text{FeCoBSiNb}]_{100-x}$ $(\text{Cu})_x$ (x = 0, 0.5) and $[\text{FeCoBSiNb}]_{100-y}$ Ga_y (y = 0, 0.5, 1, 1.5, 2, 3, 4 and 5) glassy samples are shown in Fig. 3 (a) and (b), (c), respectively. The DSC traces are measured at 20 K/min for bulk glassy 2 mm, 1.5 mm and 1 mm diameter samples depending on the compositions. For all compositions, the DSC traces show clearly the glass transition event, followed by the supercooled liquid region (SLR) and crystallization. The temperatures T_g, T_x, T_p and T_{liq} which are marked in the DSC curves are the glass transition temperature, the crystallization temperature, the crystallization peak temperatures and the liquidus temperature, respectively.
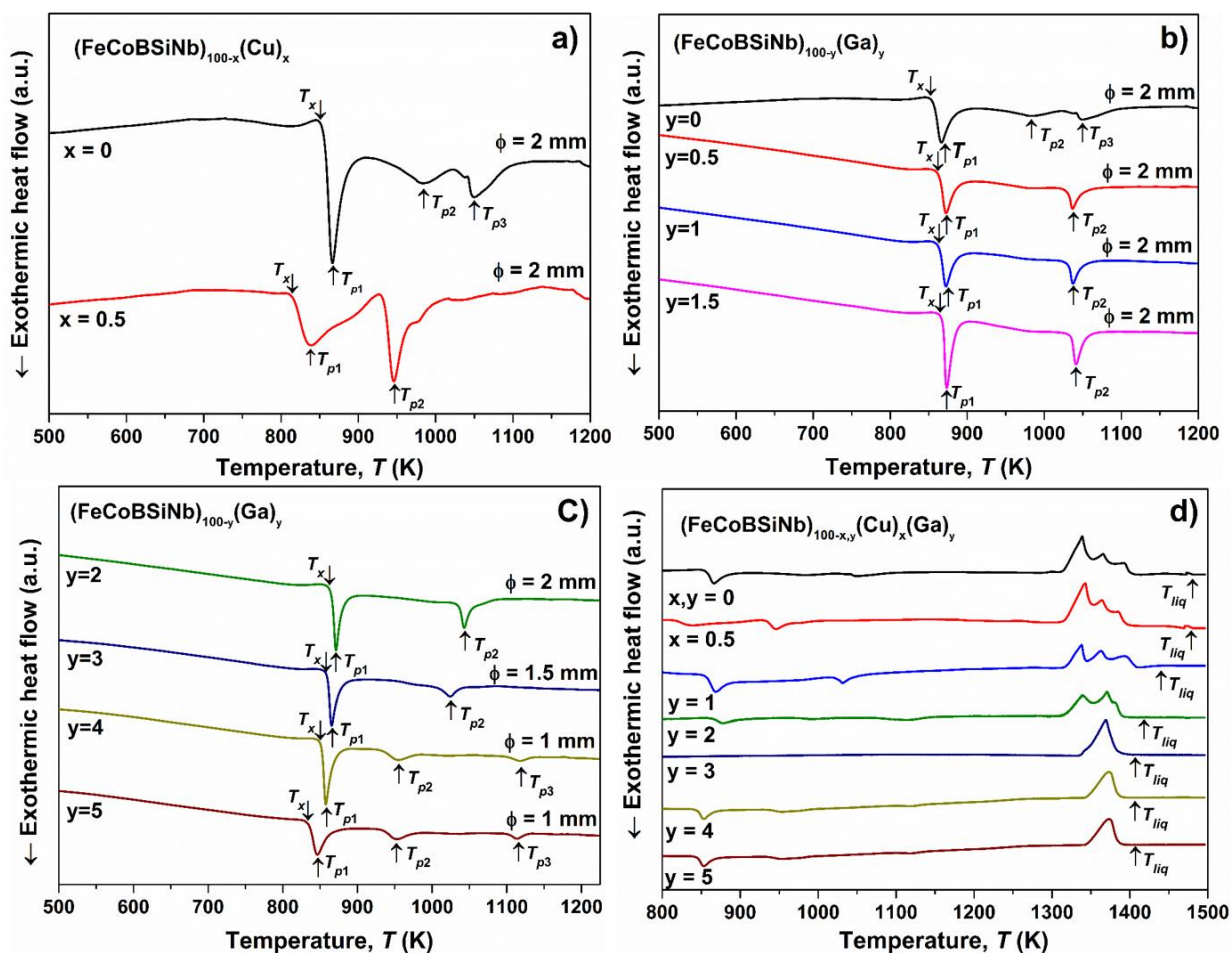
Figure 3.3: DSC traces for the as-cast (a) $[Fe_{36}Co_{36}B_{19.2}Si_{4.8}Nb_4]_{100-x}$ $(Cu)_x$ (x = 0, 0.5); (b) $[Fe_{36}Co_{36}B_{19.2}Si_{4.8}Nb_4]_{100-y}$ Ga_y (y = 0, 0.5, 1 and 1.5); (c) $[Fe_{36}Co_{36}B_{19.2}Si_{4.8}Nb_4]_{100-y}$ Ga_y (y = 2, 3, 4 and 5) glassy rods and (d) melting behavior of $[Fe_{36}Co_{36}B_{19.2}Si_{4.8}Nb_4]_{100-(x, y)}$ $(Cu)_x$ $(Ga)_y$ (x = 0, 0.5) (y = 0.5, 1, 1.5, 2, 3, 4 and 5) glassy rods. All the measurements are recorded at a heating rate of 20 K/min.

All these characteristic temperatures (except the peak temperature, which is directly the peak value) are measured as the onset of the corresponding events using the two-tangent method. The values for T_g, T_x, T_p and T_{liq} as a function of composition of the as-cast samples, measured at the same heating rate of 20 K/min, are given in Table 3.1. Using these values, the extension of the SLR ΔT_x ($\Delta T_x = T_x - T_g$), the reduced glass transition temperatures T_{rg} ($T_{rg} = T_g/T_{liq}$) [13] and the dimensionless parameter γ ($\gamma = T_x/(T_g+T_{liq})$) proposed by Lu *et al.*[64, 65] to predict the GFA, were also calculated.

From the DSC trace (Fig. 3.3 (a)) it is evident that FeCoBSiNb glass shows one main exothermic event at 867 K (T_{p1}) followed by two small events T_{p2} and T_{p3} at 985 K and 1050 K, respectively. The addition of only 0.5 at.% Cu completely changes the crystallization behavior (see Fig 3.3 (a)), leading to two main exothermic events at 838 K (T_{p1}) and 945 K (T_{p2}), respectively [199]. The addition of Cu shifts the primary crystallization process to lower temperatures and extends over a range of 100 K. The GFA of the alloy also decreases considerably, the critical diameter of the FeCoBSiNb+0.5Cu glass is $t_c = 2.5$mm.

In contrast to Cu addition, the addition of small atomic percentage of Ga (i.e. up to 1.5 at.% Ga) does not affect the glass transition event (see Fig 3.3 (b) and (c)), but the onset of crystallization temperature slightly increases from 858 K to 863 K for both 0.5 and 1 at.% Ga, and to 869 K for 1.5 at.% Ga-added glasses. On the other hand, the two small exothermic events T_{p2} and T_{p3} observed in FeCoBSiNb glass disappeared, instead a single strong exothermic event (T_{p2}) was observed at 1037, 1038 and 1042 K, for 0.5, 1 and 1.5 at.% Ga-added glasses, respectively. Interestingly, the GFA also remains same up to 1.5 at.% of Ga addition, and the critical diameter (t_c) remains 3 mm for all of these FeCoBSiNb+0.5Ga, FeCoBSiNb+1Ga and FeCoBSiNb+1.5Ga glasses. However, with further increase in Ga content from 2 to 5 at.% all characteristic temperatures T_g, T_x, T_p and T_{liq}, started to decrease gradually. Interestingly the BMG containing 4 and 5 at.% Ga shows secondary and tertiary exothermic events at 955 K , 953 K and 1118 K, 1114 K, respectively. Furthermore, the GFA of the alloys decreases when the Ga content was increased to more than 1.5 at.%. The critical diameter for the FeMoPCBSi+2Ga, FeMoPCBSi+3Ga, FeMoPCBSi+4Ga and FeMoPCBSi+5Ga glasses are $t_c = 2, 1.5, 1$ and 1 mm, respectively.

The melting behavior of all BMGs recorded by DSC at a heating rate of 20 K/min are shown in Fig. 3.3 (d). In case of the FeCoBSiNb alloy the presence of several melting peaks indicate the melting of different crystalline phases formed from the amorphous matrix upon heating. Though the melting starts at 1310 K it extends over 165 K and completely melts (T_{liq}) around 1475 K (see table 3.1) [199] indicating that this alloy is not eutectic. Moreover, the melting behavior and liquidus temperature remains almost unaffected with the addition of 0.5 at.% Cu and Ga, respectively. Similarly, for the alloys with 1 and 2 at.% Ga the melting behavior remains the same but the T_{liq} decreases to 1440 and 1420 K, respectively. The alloys containing 3, 4 and 5 at.% Ga shows a completely different melting behavior; all minor melting peaks disappeared and only one

main melting peak was observed, and also the melting range decreases from 165 K to 100 K. Furthermore, complete melting (T_{liq}) was observed at 1410 K for all the FeCoBSiNb+3Ga, FeCoBSiNb+4Ga and FeCoBSiNb+5Ga alloys.

Table 3.1: Glass transition temperatures (T_g), onsets (T_x) crystallization peak temperatures (T_{p1}, T_{p2} and T_{p3}) and liquidus temperatures (T_{liq}), as well as reduced glass transition temperatures T_{rg} ($T_{rg} = T_g/T_{liq}$), parameter γ ($\gamma = Tx/(T_g+T_{liq})$) and extension of the supercooled liquid region ΔT_x ($\Delta T_x = T_x - T_g$) for [Fe$_{36}$Co$_{36}$B$_{19.2}$Si$_{4.8}$Nb$_4$]$_{100-x,y}$ (Cu)$_x$ (Ga)$_y$ (x = 0, 0.5) (y = 0, 0.5, 1, 1.5, 2, 3, 4 and 5) glassy alloys measured at 20 K/min heating rate. The accuracy of the experimental data lies within ± 2 K. The literature data for Fe$_{36}$Co$_{36}$B$_{19.2}$Si$_{4.8}$Nb$_4$ [50] [206] glass are given for comparison purpose.

Composition	Rod φ (mm)	T_g (K)	T_x (K)	T_{p1} (K)	T_{p2} (K)	T_{p3} (K)	T_{liq} (K)	T_{rg}	γ	ΔT_x (K)
FeCoBSiNb [50]	5	820	870	-	-	-	1397	0.58	0.392	50
FeCoBSiNb [206]	2	827	860	-	-	-	1470	0.56	0.375	33
FeCoBSiNb	2	825	858	867	985	1050	1475	0.56	0.373	33
FeCoBSiNb+0.5Cu	2	793	818	838	945	-	1475	0.54	0.36	25
FeCoBSiNb+0.5Ga	2	825	863	873	1037	-	1475	0.56	0.375	38
FeCoBSiNb+1Ga	2	825	863	873	1038	-	1440	0.57	0.381	38
FeCoBSiNb+1.5Ga	2	825	869	873	1038	-	1440	0.57	0.383	41
FeCoBSiNb+2Ga	2	825	866	872	1043	-	1420	0.58	0.385	41
FeCoBSiNb+3Ga	1.5	824	858	865	1024	-	1410	0.58	0.384	34
FeCoBSiNb+4Ga	1.5	816	850	858	955	1118	1410	0.58	0.381	35
FeCoBSiNb+5Ga	1.5	800	830	846	953	1114	1410	0.56	0.375	30

The extension of the SLR (i.e. (ΔT_x) increases with the increase of Ga addition up to 2 at.% and then started to decrease with further increase of Ga content, indicating that T_x is more sensitive to

the Ga addition than T_g. The ΔT_x reaches a maximum value of 41 K for 1.5 and 2 at.% addition of Ga and a minimum value of 30 K for 5 at.% addition of Ga (see Fig. 3.4). The addition of 0.5 at.% Cu reduces the ΔT_x to as low as 25 K, also T_{rg} and γ to 0.54 and 0.360, respectively. For a good GFA, ΔT_x should be as large as possible [13]. The reduced glass transition temperature T_{rg} gradually increases from 0.56 to 0.58 with addition of Ga from 0 to 2 at.% and then remains constant up to 4 at.% Ga before decreasing to 0.56 for 5 at.% Ga addition. Similarly, the γ parameter reaches a maximum value of 0.385 for the glass having 2 at.% Ga, with further increase in Ga at.% γ starts to decrease. Usually, the γ values of BMGs range between 0.35 and 0.50 [65]. Lu *et al.*[65], also linked the γ parameter to the critical cooling rate R_c as well as to a maximum achievable thickness t_c by studying the data available on the literature for the representative non-ferrous BMGs.
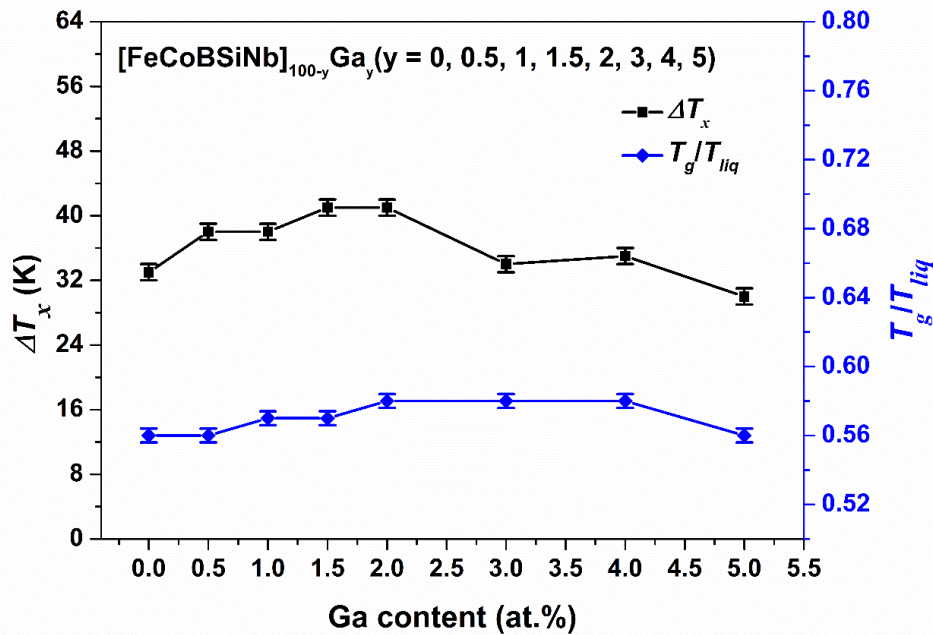
Figure 3.4: Extension of the supercooled liquid region ΔT_x and the reduced glass transition temperature T_{rg} as a function of Ga at.%.

The relationships can be expressed as follows:

$$R_c = 5.1 \text{ X } 10^{21} \exp(-117.19 \cdot \gamma), \tag{3.6}$$

and

$$t_c = 2.80 \text{ X } 10^{-7} \exp(41.70 \cdot \gamma), \tag{3.7}$$

where R_c is in K/s and t_c in mm. These theoretical relationship for critical diameter t_c and critical cooling rate R_c were calculated based on the already available literature data. If the above proposed relationship (eq. 3.7), is applied for our glasses the critical thickness (t_c) for FeCoBSiNb glass is around 1.5 mm and for FeMoPCBSi glass is around 2.22 mm. However, these values are in contradictory to the t_c obtained in our current work, in practical case it is very difficult to predict the GFA of the new alloys without actually casting the samples. Furthermore this calculation works well for only non-ferrous glass, Fe-based glasses hardly follow this rule [3].
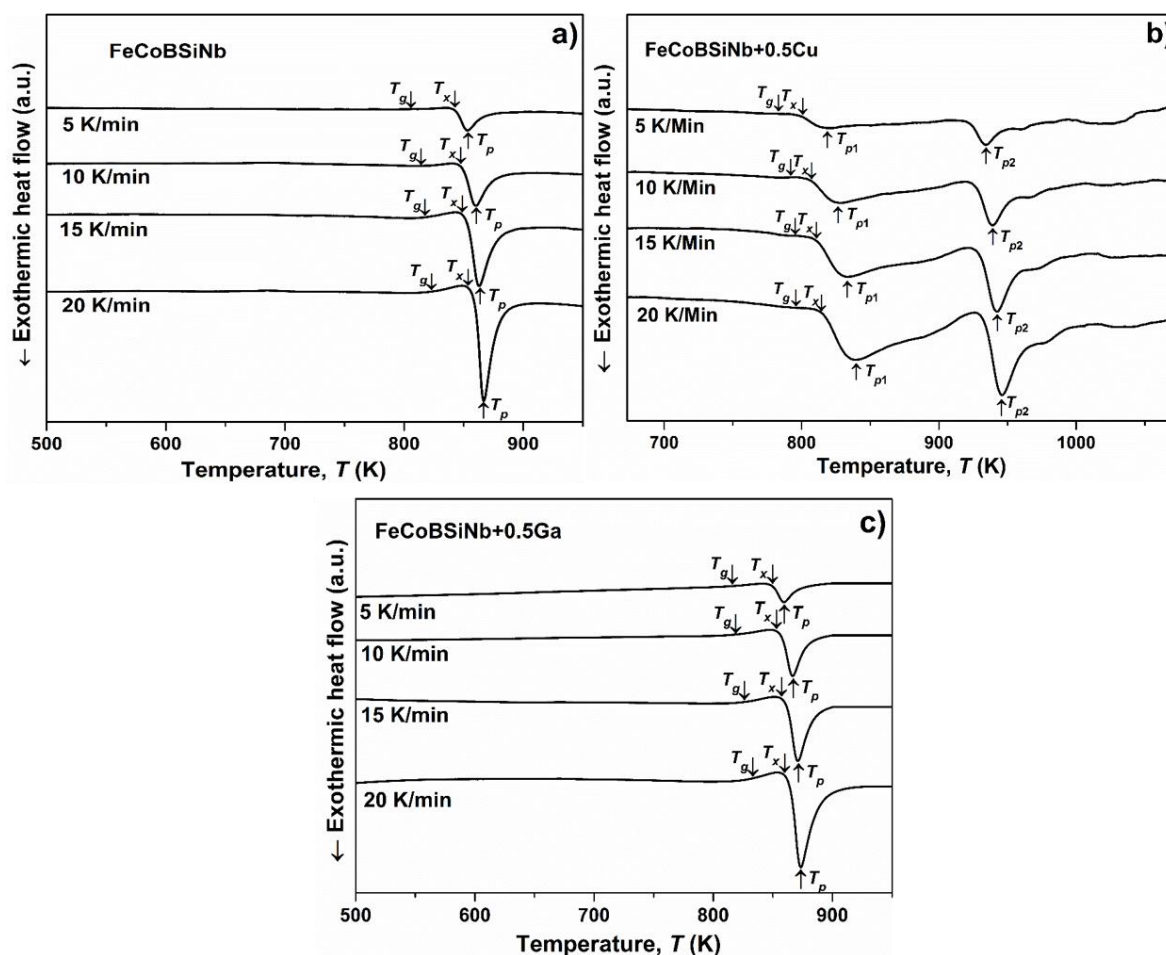
Figure 3.5: Isochronal DSC curves recorder at different heating rates for (a) $Fe_{36}Co_{36}B_{19.2}Si_{4.8}Nb_4$; (b) $[Fe_{36}Co_{36}B_{19.2}Si_{4.8}Nb_4]_{99.5}Cu_{0.5}$ and (c) $[Fe_{36}Co_{36}B_{19.2}Si_{4.8}Nb_4]_{99.5}Ga_{0.5}$ glassy samples.

Fig. 3.5 (a), (b) and (c) show the DSC traces measured at different heating rates of 5, 10, 15 and 20 K/min for the FeCoBSiNb, FeCoBSiNb+0.5Cu and FeCoBSiNb+0.5Ga glasses, respectively. Regardless of the heating rate, all curves clearly exhibit a distinct T_g and a supercooled liquid

region (SLR) followed by crystallization. From the DSC curves it is evident that all characteristic temperatures (T_g, T_x and T_p) shift to higher values with increasing heating rate (as shown in Table 3.2).

Table 3.2: Glass transition temperatures (T_g), onsets (T_x) crystallization peak temperatures (T_{p1}) for $Fe_{36}Co_{36}B_{19.2}Si_{4.8}Nb_4$, $[Fe_{36}Co_{36}B_{19.2}Si_{4.8}Nb_4]_{99.5}Cu_{0.5}$ and $[Fe_{36}Co_{36}B_{19.2}Si_{4.8}Nb_4]_{99.5}Ga_{0.5}$ glasses measured at 5, 10, 15 and 20 K/min. The accuracy of the experimental data lies within $\pm$ 2 K.

Compositions		5 K/min	10 K/min	15 K/min	20 K/min
FeCoBSiNb	T_g (K)	812	817	821	825
	T_x (K)	837	844	852	858
	ΔT_x (K)	25	27	31	33
	T_{p1} (K)	853	860	863	867
FeCoBSiNb+0.5Cu	T_g (K)	780	786	790	793
	T_x (K)	797	804	811	818
	ΔT_x (K)	17	18	21	25
	T_{p1} (K)	818	828	834	838
FeCoBSiNb+0.5Ga	T_g (K)	812	818	820	825
	T_x (K)	843	850	856	863
	ΔT_x (K)	31	32	34	38
	T_{p1} (K)	859	867	871	874

The apparent activation energy required for crystallization can be calculated using the Kissinger method [207]:

$$ln \frac{\beta}{T^2} = - \left(\frac{E}{RT}\right) + constant, \qquad (3.8)$$

where β is the heating rate, T is the characteristic temperature at that specific heating rate, E is the activation energy and R is the universal gas constant. The activation energy required for the crystallization event can be calculated by plotting $-ln(\beta/T_p^2)$ as a function of $1000/T_p$, where T_p is

the crystallization peak temperature, then the slope of the curve is proportional with the crystallization activation energy E_c. Fig. 3.6 presents the Kissinger plot calculated with the data presented in the Table 3.2. The good linear dependence of the measured data indicates the good reproducibility. The crystallization activation energies E_c for FeCoBSiNb, FeCoBSiNb+0.5Cu and FeCoBSiNb+0.5Ga glasses are E_c = 607 ± 14, 374 ± 8 and 557 ± 14 kJ/mol, respectively.
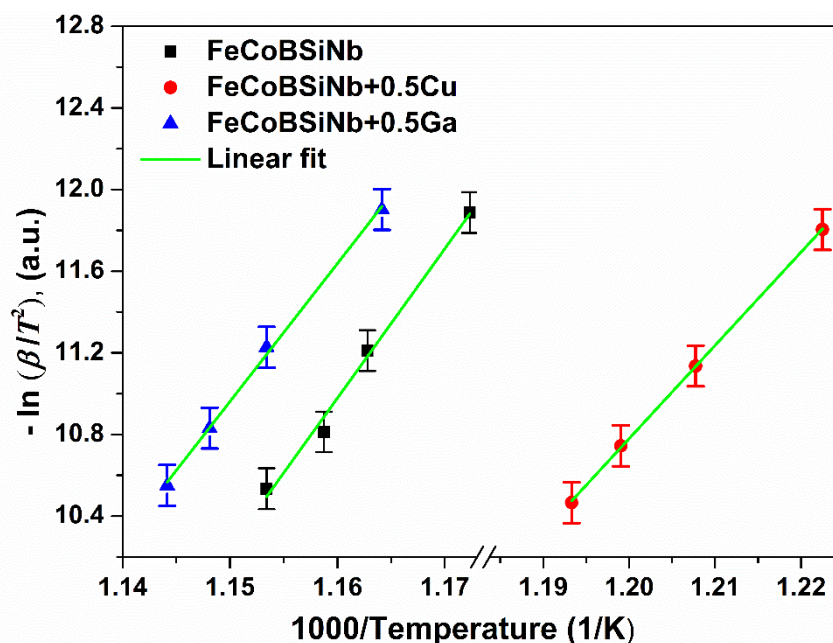
Figure 3.6: Kissinger plot for the calculation of activation energies required by crystallization event in $Fe_{36}Co_{36}B_{19.2}Si_{4.8}Nb_4$, $[Fe_{36}Co_{36}B_{19.2}Si_{4.8}Nb_4]_{99.5}Cu_{0.5}$ and $[Fe_{36}Co_{36}B_{19.2}Si_{4.8}Nb_4]_{99.5}Ga_{0.5}$ glasses.

The E_c of the FeCoBSiNb glass is higher than the previously reported values [206], this is mainly because Fe-based glasses are highly sensitive to the alloy compositions, even the presence of small impurities will greatly influence the T_g, T_x and T_p of the glasses [3]. The addition of 0.5 at.% of Ga slightly lowers the activation energy, still the E_c is very high compared to other well-known good glass formers in Zr- and Ti- based alloy systems [62]. High values of activation energy for crystallization indicates a very good thermal stability against crystallization. However, the Cu added glass has very low E_c, this is mainly because Fe and Cu have positive heat of mixing, though Fe and Cu mix above their melting point but during cooling the Cu atoms does not mix well with the system. This Cu atoms will act as a heterogeneous nucleation site, which in turn reduces the energy barrier required to reconstruct the atomic configuration [208].

3.4 Characterization behavior, X-ray diffraction studies

The structure evolution of the $[FeCoBSiNb]_{100-x,y}$ (Cu_x, Ga_y) (x = 0 and 0.5)(y = 0.5, 1, 2, 3, 4 and 5) glasses upon on annealing were studied using XRD. The investigated samples were cut from the as-cast rods and further annealed for 5 min at different characteristic temperatures (T_x and T_p) (see Fig. 3.3 (a), (b) and (c)) using same NETZSCH DSC 404 C under argon atmosphere. The heating and cooling were performed under constant heating and cooling rates of 20 K/min. Fig. 3.7 (a) depicts the structural evaluation of FeCoBSiNb glass from room temperature to 1273 K.
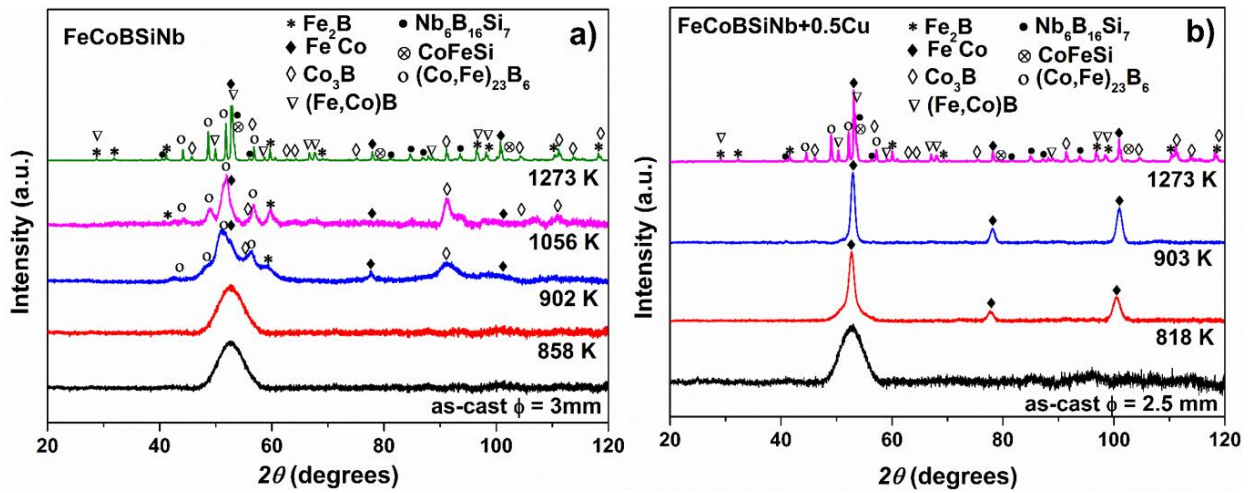
Figure 3.7: XRD patterns for (a) $Fe_{36}Co_{36}B_{19.2}Si_{4.8}Nb_4$ and (b) $[Fe_{36}Co_{36}B_{19.2}Si_{4.8}Nb_4]_{99.5}Cu_{0.5}$ glasses annealed up to their corresponding characteristic temperatures.

The as-cast FeCoBSiNb sample ($\phi = 3$ mm) was completely amorphous. The crystallization starts as soon as the sample reaches the onset of crystallization temperature T_x (i.e. 858 K), but it needs long time for fully crystallization [206]. The presence of broad diffraction maxima indicates that the glass remains amorphous even after annealing up to 858 K. Further, at 902 K i.e. after the end of first crystallization event, the $(Fe,Co)_{23}B_6$-type and bcc-(Fe,Co) peaks are clearly visible. Even at 902 K the first broad peak is still present, which indicates that some amorphous phase is not yet transformed. After the end of second exothermic event, at 1056 K other minor peaks corresponding to $(Fe,Co)_2 B$ and $(Fe,Co)_3 B$ are observed. Close to the melting point, at 1273 K, the glassy sample completely turned in to crystalline material.

The most probable crystalline sequence of this FeCoBSiNb glass is as follow: Amorphous→ $(Fe,Co)_{23}B_6$-type + bcc-(Fe,Co)+ residual amorphous →$(Fe,Co)_{23}B_6$-type + bcc-(Fe,Co)+ $(Fe,Co)_2B$ + $(Fe,Co)_3B$ + residual amorphous →$(Fe,Co)_{23}B_6$-type + bcc-(Fe,Co)+ $(Fe,Co)_2B$ + $(Fe,Co)_3B$+ $(Fe,Co)Si$+ $Nb_{16}B_6Si_7$. Similarly, the structural evolution of FeCoBSiNb+0.5Cu glass from room temperature to 1273 K is shown in Fig. 3.7 (b). As it can be observed from the DSC curve (see Fig. 3.3 (a)), the addition of Cu not only changes the thermal stability of the glass, but also the crystallization sequence of the glass. After heating to the first crystallization temperature (T_x = 818 K), bcc-(Fe,Co) phase starts to appear. The existence of a residual glassy matrix is confirmed by a broad diffraction maximum in the XRD pattern of the sample annealed at 818 K. The formation of the bcc-(Fe,Co) phase at lower temperatures may be attributed to the presence of a small amount of Cu atoms in the matrix (i.e. Fe and Cu have a positive heat of mixing), which can accelerate the initialization of the nanocrystals [78]. However, according to DSC (Fig. 3.3 (a)), Cu addition extends the time and temperature required for completion of crystallization. At 902 K, where the growth of (Fe,Co) is almost close to be complete, a second glass transition event is observed (i.e. an event associated most probably with the glass transition of the remaining glassy matrix). These results are in agreement with those recently presented by Stoica *et al.*[209], which indicates a completely different crystallization behavior of copper added glass compared to FeCoBSiNb alloy. However, close to the melting point i.e. at 1273 K, the crystalline pattern is almost same as that of the parent FeCoBSiNb alloy. The most probable crystalline sequence of this FeCoBSiNb+0.5Cu glass is as follow: Amorphous→ bcc-(Fe,Co)+ residual amorphous → bcc-(Fe,Co)+$(Fe,Co)_{23}B_6$-type + $(Fe,Co)_2B$ + residual amorphous →$(Fe,Co)_{23}B_6$-type + bcc-(Fe,Co)+ $(Fe,Co)_2B$ + $(Fe,Co)_3B$+ $(Fe,Co)Si$+ $Nb_{16}B_6Si_7$.

Unlike to the Cu addition, Ga addition in small at.% does not really affect the thermal stability as well as the crystallization sequence. Up to 1 at.% Ga, the thermal stability and crystallization sequence is almost as for the parent FeCoBSiNb glass (Fig. 3.3 (b) and (c)). However, with further increase in Ga content, the crystallization temperature decreases gradually. Fig. 3.8 (a) depicts the XRD patterns of the $[FeCoBSiNb]_{100-y}$ Ga_y (y =0, 0.5, 1, 2, 3, 4 and 5) glassy samples annealed up to the end of their first crystallization event, which is 902, 902, 902, 902, 898, 893 and 883 K, respectively. For good visibility the *2θ* range between 40 to 70 degrees is shown separately in Fig. 3.8 (b). The BMG with 1 at.% Ga shows distinguished bcc-(Fe,Co) peak along with $(Fe,Co)_{23}B_6$-type peaks at the end of first crystallization event. For the BMGs with 2 and 3 Ga at.% bcc-(Fe,Co)

phase started to form more instead of $(Fe,Co)_{23}B_6$-type phase. In case of FeCoBSiNb+4Ga and FeCoBSiNb+5Ga glasses only bcc-(Fe,Co) phase was observed after the first crystallization event, this effect is similar to that of the 0.5 at.% Cu. The formation of the bcc-(Fe,Co) phase for higher at.% Ga may be attributed to the presence of Ga atoms in the matrix, which may aid the nucleation of crystals even at lower temperatures.
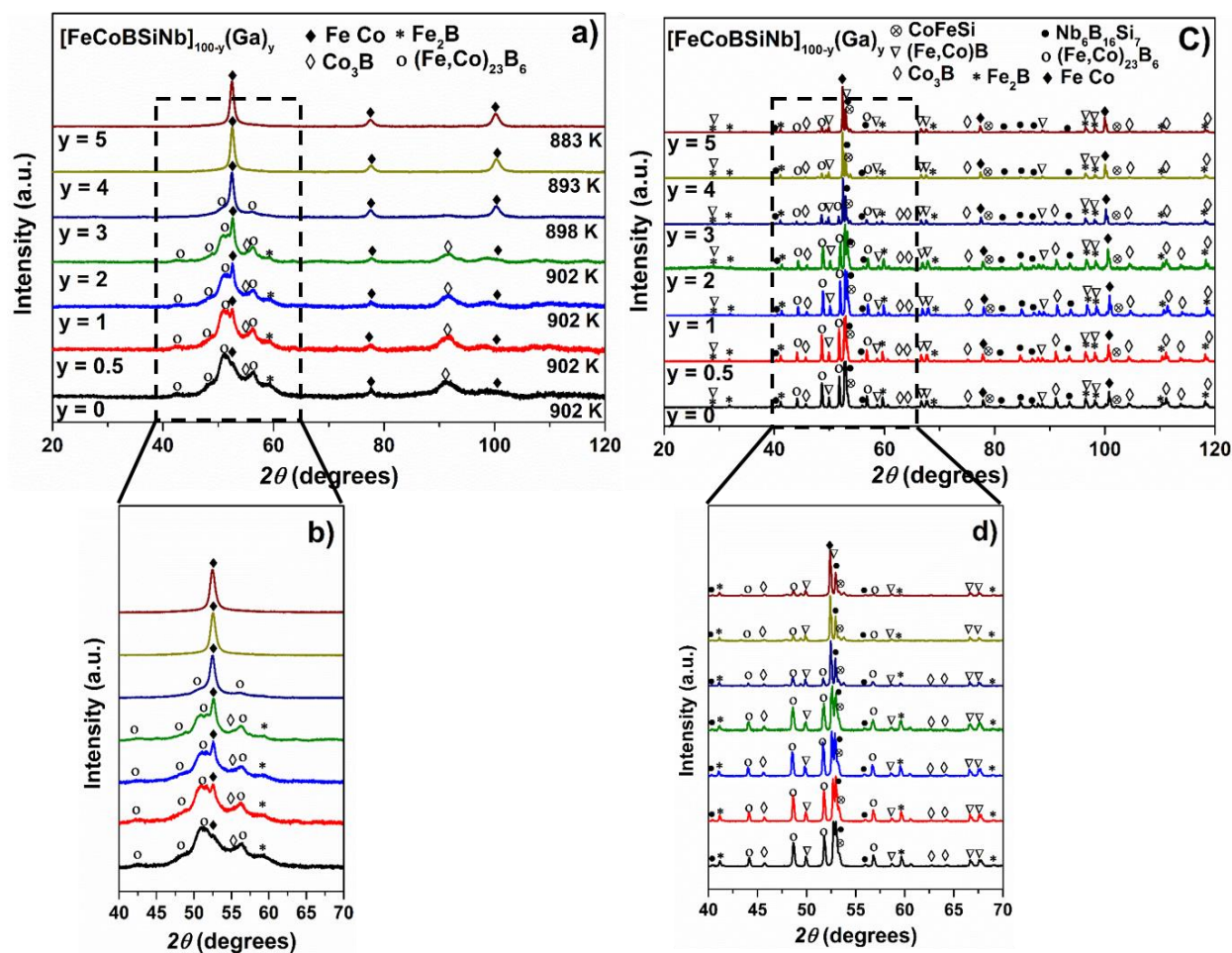
Figure 3.8: XRD patterns for the $[Fe_{36}Co_{36}B_{19.2}Si_{4.8}Nb_4]_{100-y}$ Ga_y (y =0, 0.5, 1, 2, 3, 4 and 5) glasses (a) annealed up to end of first crystallization event; (b) 2θ between 40 to 70 degrees (rectangle region from (a)); (c) annealed up to 1273 K and (d) 2θ between 40 to 70 degrees (rectangle region from (c)).

Fig. 3.8 (c) shows the XRD pattern of all samples annealed at 1273 K, again for good visibility the 2θ range between 40 to 70 degrees is shown separately in Fig. 3.8 (d). From the XRD patterns it

is evident that with increase in Ga content the $(Fe,Co)_{23}B_6$-type, $(Fe,Co)_2B$, $(Fe,Co)_3B$, $(Fe,Co)Si$, $Nb_{16}B_6Si_7$ phases decreases gradually and bcc-(Fe,Co) phase becomes more prominent.

3.5 Microstructural studies, STEM and HRTEM investigations

Scanning transmission electron microscopy (STEM) and high resolution transmission electron microscopy (HRTEM) investigations were carried out to investigate the structure of the as-cast samples. In order understand the effect of Cu and Ga addition in the FeCoBSiNb system only FeCoBSiNb+0.5Cu and FeCoBSiNb+0.5Ga glassy samples were chosen for studies. The samples were subjected to reflection X-ray diffraction before preparing for the STEM and HRTEM investigations and the samples were amorphous. STEM image of the as-cast FeCoBSiNb+0.5Cu and FeCoBSiNb+0.5Ga glassy samples are shown in Fig. 3.9 (a) and (b).
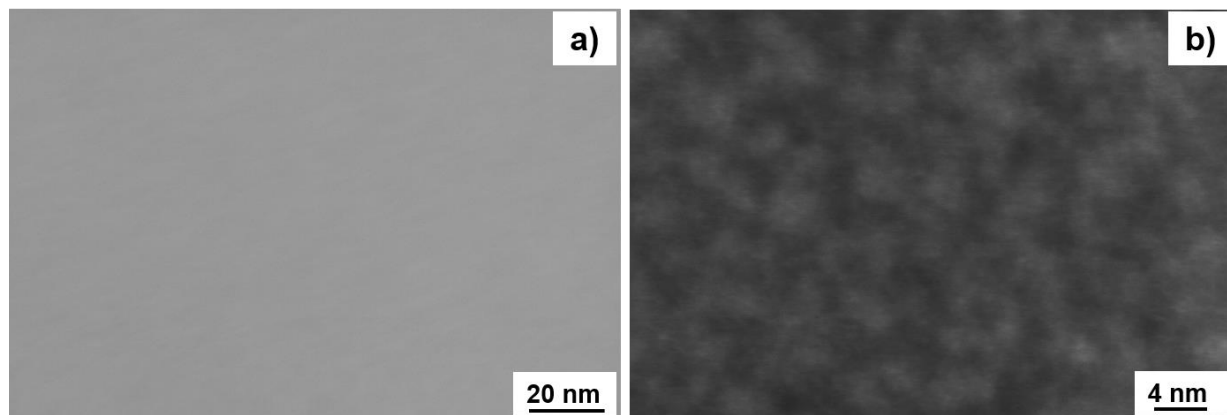
Figure 3.9: (a) STEM image of the as-cast (a) $[Fe_{36}Co_{36}B_{19.2}Si_{4.8}Nb_4]_{99.5}Cu_{0.5}$ and (b) $[Fe_{36}Co_{36}B_{19.2}Si_{4.8}Nb_4]_{99.5}Ga_{0.5}$ glassy samples.

From the STEM image it is evident that the 0.5 at.% Cu added glass was completely amorphous, but a cluster type structure was observed in 0.5 at.% Ga added glass. To verify the features observed in the STEM, bright field HRTEM observation were made on FeCoBSiNb+0.5Cu and FeCoBSiNb+0.5Ga glasses. The micrographs are shown in Fig. 3.10. (a), (b), together with their corresponding fast Fourier transformed (FFT) images (shown as inserts).

The as-cast FeCoBSiNb+0.5Cu glass shows some locally ordered regions, which are marked with the white circles in the image, but it is not evident if the Cu atoms form this ordering/cluster structure. The mixing enthalpies of Fe-Cu, Co-Cu, B-Cu, Si-Cu and Nb-Cu are 13, 6, 15, -2 and 3 kJ/mole, respectively [210]. These kind of repulsive enthalpies of mixing may influence the local chemical heterogeneity, producing ordered sites.
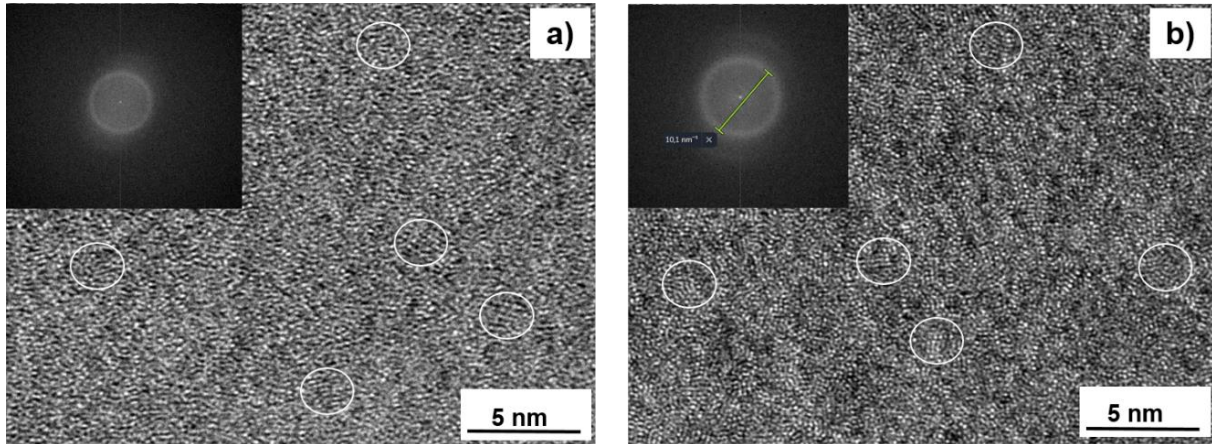
Figure 3.10: Bright field HRTEM image of the as-cast (a) $[Fe_{36}Co_{36}B_{19.2}Si_{4.8}Nb_4]_{99.5}Cu_{0.5}$ and (b) $[Fe_{36}Co_{36}B_{19.2}Si_{4.8}Nb_4]_{99.5}Ga_{0.5}$ glasses. Insert shows the fast Fourier transformed (FFT) image. Some features of local ordering are observed, which are marked by the white circles.

Compared to the Cu added glass, ordered zones are more frequently observed in the Ga added glass. The mixing enthalpies of Fe-Ga, Co-Ga, B-Ga, Si-Ga and Nb-Ga are -2, -11, 21, 0 and -8 kJ/mole, respectively [210]. Compared to the Cu atoms, the mixing enthalpies of the Ga with the rest of the elements are almost all negative but rather small. If this ordered zones is similar to those observed in the Cu added glass, then one could expect that they act as a nuclei for the formation of crystals of bcc-(Fe,Co) up on annealing. Instead, the annealing of the FeCoBSiNb+0.5Ga glass leads to formation of only small volume fraction of bcc-(Fe,Co) phase but large quantity of $(Fe,Co)_{23}B_6$-type phase (see fig. 3.8 (a)). Therefore it is to expect that the local ordering in the Cu-added and Ga-added glasses are different. However, it should be noted that the presence of ordered zones/clusters in the amorphous matrix does not necessarily imply that they act as a nucleation site for the crystal growth. The ordered embryos must be larger than the critical nucleus size in order for their growth to be thermodynamically favorable [211-213].
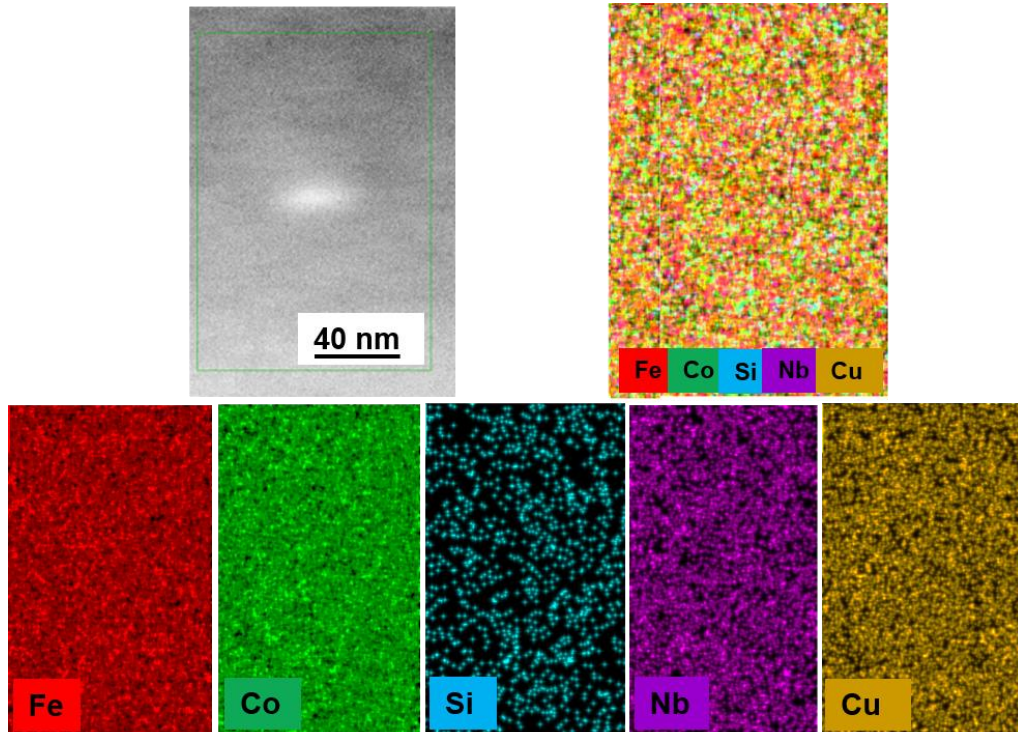
Figure 3.11: EDX mapping for the as-cast [Fe$_{36}$Co$_{36}$B$_{19.2}$Si$_{4.8}$Nb$_4$]$_{99.5}$Cu$_{0.5}$ glass
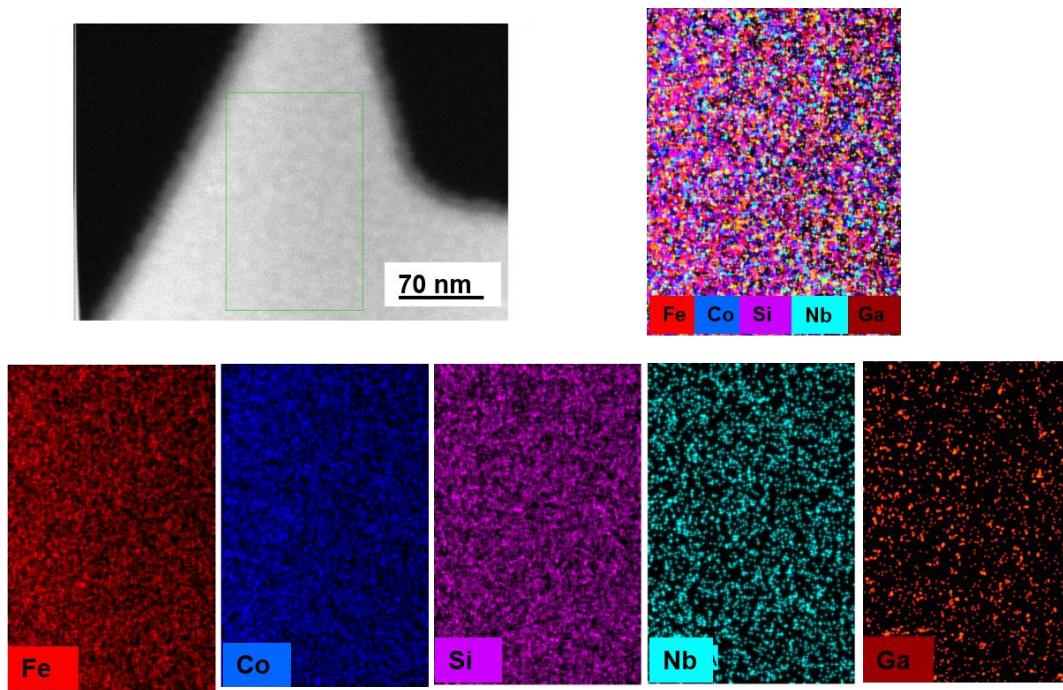
Figure 3.12: EDX mapping for the as-cast [Fe$_{36}$Co$_{36}$B$_{19.2}$Si$_{4.8}$Nb$_4$]$_{99.5}$Ga$_{0.5}$ glass

For a better understanding, energy-dispersive X-ray spectroscopy (EDX) mapping was done for both Cu- and Ga- added samples. The corresponding maps are shown in Fig. 3.11 and 3.12, respectively. In Cu-added samples no specific ordered zones/clusters were observed from the EDX mapping, but in case of Ga-added glass faint ordered zones/cluster behavior of the Ga atoms can be seen (see Fig. 3.12.). For the same atomic percentage addition of Cu and Ga, Ga atoms are showing higher tendency to form ordered zones/clusters compared to Cu atoms, which is in perfect agreement with the HRTEM results.

3.6 Magnetic properties of $[Fe_{36}Co_{36}B_{19.2}Si_{4.8}Nb_4]_{100-x, y}$ (Cu_x, Ga_y) $(x = 0$ and $0.5)$ $(y = 0.5, 1, 2, 3, 4$ and $5)$ glasses

The FeCoBSiNb glass is well known for its soft magnetic properties such as low coercivity $(H_c) \approx$ 2 A/m, saturation magnetization $(M_s) \approx 1$T and relative permeability $(\mu) \approx 12,000$ [50, 84, 214]. The soft magnetic properties of the ferromagnetic glasses are influenced by several factors, but some of the important factors are as follows: (1) presence of impurities, crystalline phases, short and medium range order, (2) anisotropies such as shape anisotropy and stress-induced anisotropy, caused by internal mechanical stress induced during the preparation of the samples, (3) addition of any non-magnetic elements. However, the stress-induced anisotropy can be reduced by annealing the samples below their onset of crystallization temperature.

3.6.1 Coercivity measurements

The coercivity values for the as-cast glassy samples of different compositions are listed in Table 3.3. In order to avoid the effects due to the sample geometry all coercivity measurements were done for cylindrical samples having the diameter-to-length ratio 1:20. The coercivity values of the FeCoBSiNb, FeCoBSiNb+0.5Cu, FeCoBSiNb+0.5Ga, FeCoBSiNb+1Ga glasses are almost identical. For Ga-added samples, further increase of Ga content increases the coercivity values. The increase in H_c with increase in Ga.% could be due to formation of large number of ordered zones/clusters (Fig. 3.9 and 3.10). The coercivity values of the 3 mm diameter rods are higher

compared to the 1.5 and 2 mm rods, this could be mainly due to geometry of the sample used for measurement or presence of few nuclei/clusters. For a completely amorphous samples with our any crystalline inclusions, the coercivity should be less than 10 A/m. [93].

The presence of any nano-crystals will increase the coercivity values over several orders of magnitude depending upon the volume fraction of the crystalline inclusions [87].

Table 3.3: Coercivity values for the as-cast $[Fe_{36}Co_{36}B_{19.2}Si_{4.8}Nb_4]_{100-x, y}$ (Cu_x, Ga_y) $(x = 0, 0.5)$ $(y = 0.5, 1, 2, 3, 4$ and $5)$ glassy samples. The accuracy of the experimental data lies within ± 0.1A/m.

Composition	Rod ϕ (mm)	H_c (A/m)	Composition	Rod ϕ (mm)	H_c (A/m)
FeCoBSiNb	1.5	2	FeCoBSiNb+1.5Ga	1.5	3
	2	2.7		2	5
	3	6		3	9
FeCoBSiNb+0.5Cu	1.5	2	FeCoBSiNb+2Ga	1.5	6
	2	2		2	7
FeCoBSiNb+0.5Ga	1.5	2	FeCoBSiNb+3Ga	1.5	4
	2	2			
	3	7	FeCoBSiNb+4Ga	1	6
FeCoBSiNb+1Ga	1.5	2			
	2	3	FeCoBSiNb+5Ga	1	7
	3	9			

The variation of coercivity as a function of annealing temperature for FeCoBSiNb, FeCoBSiNb+0.5Cu and FeCoBSiNb+0.5Ga glasses are shown in Fig. 3.13. The samples were annealed for 1 min at different characteristic temperatures such as T_g, T_x-5, T_x, T_x+5, T_{p1} and end of first crystallization event (see Fig. 3.3 (a), (b) and (c)) using the same NETZSCH DSC 404 C device working under argon atmosphere. The heating and cooling were performed under constant heating and cooling rates of 20 K/min. Due to the limited size of the DSC crucibles, cylindrical

samples having the diameter to length ratio 1:2 (i.e. 2 mm x 4 mm) were used for this measurements. In this case the absolute coercivity values will misguide us due to high demagnetizing factor, hence the coercivity after annealing (H_c-annealed) are normalized with the as cast coercivity (H_c-as-cast) to clearly see the effect of annealing on the H_c. All the normalized coercivity data measured for these samples after annealing at different temperatures are shown in Table 3.4. The H_c values remains almost constant for all glasses even they were annealed up to their respective T_g. Close to the crystallization start temperature i.e. $\approx$ 5 K before T_x the H_c decreases to half of the initial value for both FeCoBSiNb, FeCoBSiNb+0.5Ga glasses and for FeCoBSiNb+0.5Cu glass, the Hc decreases to almost $1/3^{rd}$ of the initial value. This initial decrease in coercivity close to the crystallization temperature may be due to the stress relaxation and a decreasing density of quasi-dislocation dipole-type (QDD) defects, which may pin the magnetic domain walls in the amorphous phase [215]. Upon further annealing until the end of their first crystallization event (i.e. 908, 908 and 918 K), the H_c increases to 3.8, 3.8 and 3.5 times the initial value for FeCoBSiNb, FeCoBSiNb+0.5Ga and FeCoBSiNb+0.5Cu glasses, respectively.

Table 3.4: Coercivity values for the $Fe_{36}Co_{36}B_{19.2}Si_{4.8}Nb_4$, $[Fe_{36}Co_{36}B_{19.2}Si_{4.8}Nb_4]_{99.5}Cu_{0.5}$ and $[Fe_{36}Co_{36}B_{19.2}Si_{4.8}Nb_4]_{99.5}Ga_{0.5}$ glasses in the as-cast state and after annealed to different temperatures. The accuracy of the experimental data lies within $\pm$ 0.1A/m.

FeCoBSiNb	Temperature (K)	303	827	853	868	888	908	
	H_c-annealed / H_c-as-cast	1	1	0.5	0.8	2	3.8	
FeCoBSiNb+0.5Ga	Temperature (K)	303	827	853	868	888	908	
	H_c-annealed / H_c-as-cast	1	1	0.5	0.8	2.4	3.8	
FeCoBSiNb+0.5Cu	Temperature (K)	303	793	813	828	838	888	918
	H_c-annealed / H_c-as-cast	1	1	0.3	0.6	0.8	1.5	3.5

The increase in H_c of the samples beyond their T_x can be attributed to the formation of crystals in their glassy matrix. It is worth noting that even after heating up to 918 K, the coercivity value for the Cu- added glass is still lower than that of FeCoBSiNb and FeCoBSiNb+0.5Ga glasses heated above their first crystallization event 908 K. Compared to FeCoBSiNb and FeCoBSiNb+0.5Ga glasses the H_c of the Cu- added glass increases slowly. The sudden increase in H_c of the devitrified FeCoBSiNb and FeCoBSiNb+0.5Ga glasses is most probably due to the formation of the $(Fe,Co)_{23}B_6$-type phase upon annealing, which is magnetically harder than the bcc-(Fe,Co) phase, [86].
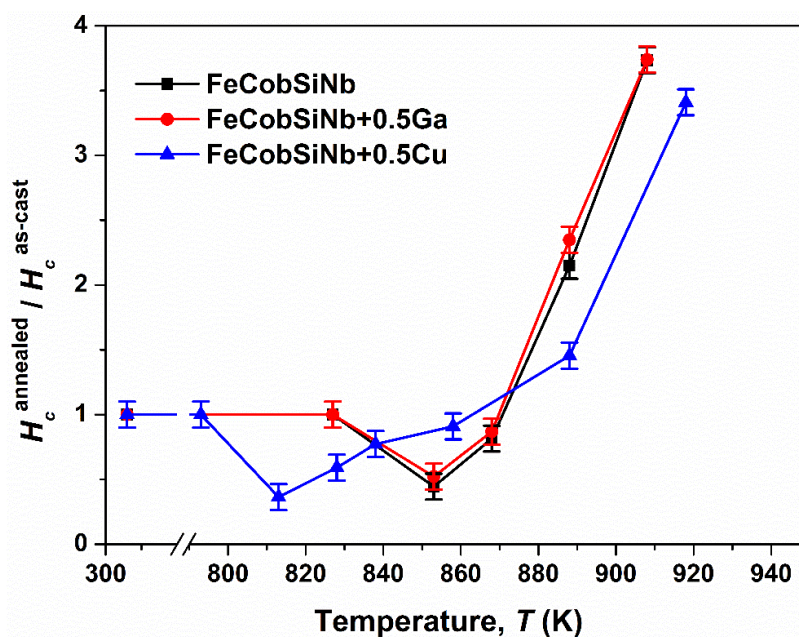
Figure 3.13: The variation of H_c-annealed / H_c-as-cast as a function of annealing temperature for $Fe_{36}Co_{36}B_{19.2}Si_{4.8}Nb_4$, $[Fe_{36}Co_{36}B_{19.2}Si_{4.8}Nb_4]_{99.5}Cu_{0.5}$ and $[Fe_{36}Co_{36}B_{19.2}Si_{4.8}Nb_4]_{99.5}Ga_{0.5}$ glasses. Annealing was done different characteristic temperatures such as T_g, T_x-5, T_x, T_x+5, T_{p1} and end of first crystallization event for each of these alloys.

According to the random anisotropy model [87, 216, 217] when the grain size is smaller than the magnetic exchange length (L_0) the exchange interaction will average out the magnetic anisotropy. L_0 represents the minimum length over which the direction of the magnetic moments can vary appreciably. If the grain size is lower than the L_0 the magnetization will not follow the randomly oriented easy axis of the individual grains, but increasingly it is forced to align parallel by the exchange interaction. As a result, the effective anisotropy is an average of several grains and, thus

considerably reduced. Further increase of crystal size enhances the anisotropy and, consequently, increases the coercivity. The magnetic exchange length for soft magnetic materials is $\approx$18 nm [218, 219]. Based on Table 3.4, the coercivity enhancement with increasing annealing temperature may be due to the increased magneto-crystalline anisotropy caused by growth of the (Fe,Co) and $(Fe,Co)_{23}B_6$-type crystals upon annealing. In order to prove above statement, the crystallite size of the devitrified FeCoBSiNb+0.5Cu glass was calculated at different annealed temperatures using Williamson-Hall method [220]. The crystallite sizes are 13 $\pm$ 4 nm, 18 $\pm$ 4 nm, and 22 $\pm$ 4 nm at 818 K, 863 K, and 903 K, respectively (see Fig. 3.7 (b)) [199]. When sample was annealed at 818 K for 1 min, size of the crystal formed is 13 $\pm$ 4 nm, which is below the magnetic exchange length for this material. As a result, the effective H_c (i.e., H_c-annealed / H_c-as-cast) of 0.3 is an average value of several crystals. At 863 K when the crystal size is approximately same as that of L_0 the H_c started to increase gradually. Beyond 863 K when the size of the crystallite are more than L_0 (> 18 nm) the H_c started to increase drastically (see Fig. 3.13). From this it is evident that with the increases in the crystallite size, the coercivity values also increase drastically.

3.6.2 Magnetization measurements

The saturation magnetization (M_s) of the glassy samples were measured using vibrating sample magnetometer (VSM). In order to avoid the effects due to the sample geometry all measurements were done for rod samples with 1 mm diameter and the length of 2 mm. Fig. 3.14 (a) and (b) show the typical room temperature DC hysteresis loops recorded with the VSM for the Cu- and Ga-added as-cast glassy samples. The behavior of the Ga- added samples close to the saturation region is shown as inset in the Fig. 3.14 (b).

From the hysteresis loops it is evident that the saturation occurs at relatively similar magnetic fields for all glasses. The addition of 0.5 at.% Cu marginally increases the M_s values from 108 to 109 Am^2/kg (Fig. 3.14 (a)). In contrast, for 0.5 at.% Ga the M_s remains almost the same, with further increase in Ga content M_s gradually decreases and reaches a value of 94 Am^2/kg for 5 at.% Ga-added glass. As discussed in the beginning (paragraph 3.6), with the addition of Ga (non-magnetic) M_s may decrease. The values of saturation magnetization for all Cu- and Ga- added samples, measured using the VSM, are summarized in Table 3.5.
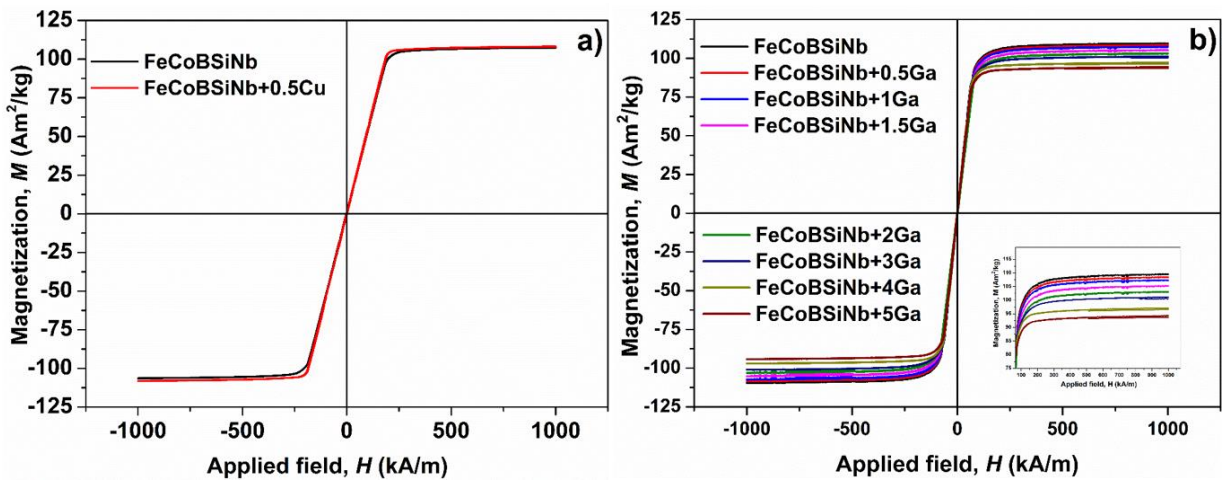
Figure 3.14: Hysteresis loops for the 1 mm diameter as-cast (a) $[FeCo_{36}B_{19.2}Si_{4.8}Nb_4]_{100-x}$ (Cu_x) (x = 0, 0.5); (b) $[Fe_{36}Co_{36}B_{19.2}Si_{4.8}Nb_4]_{100-y}$ (Ga_y) (y = 0, 0.5, 1, 2, 3, 4 and 5) glassy samples. Insert show the behavior of the Ga- added samples close to the saturation region i.e. between 80 and 100 Am^2/kg.

Fig. 3.15 shows the variation of the M_s with different annealed temperatures for FeCoBSiNb, FeCoBSiNb+0.5Cu and FeCoBSiNb+0.5Ga samples. The M_s of the FeCoBSiNb+0.5Cu glass increases after heat treatment, particularly above $T = 838$ K. The enhanced M_s after annealing up to $T = 918$K can be attributed to the formation of (Fe,Co) crystals with higher saturation magnetization than the amorphous phase [199] (Fig. 3.7 (b)). In contrast, upon annealing, the FeCoBSiNb and FeCoBSiNb+0.5Ga samples become more magnetically harder, with slight increase in M_s. This is due to the formation of (Fe,Co)$_{23}$B$_6$-type phase [206]. From these results, it can be concluded that the addition of 0.5 at.% Cu improves the soft magnetic properties in both as-cast and annealed conditions compared to the base FeCoBSiNb glass and 0.5 at.% Ga- added glass.
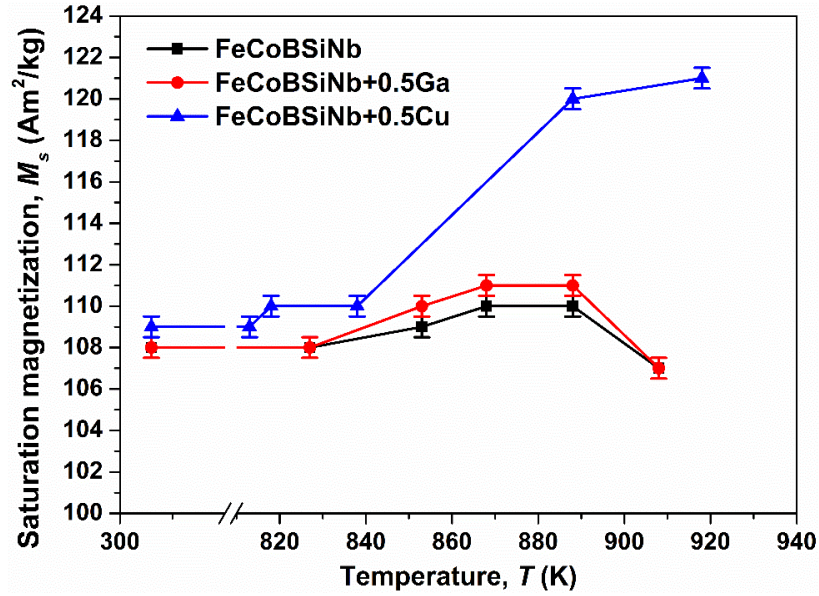
Figure 3.15: Variation of the saturation magnetization (M_s) with different annealing temperatures for $Fe_{36}Co_{36}B_{19.2}Si_{4.8}Nb_4$, $[Fe_{36}Co_{36}B_{19.2}Si_{4.8}Nb_4]_{99.5}Cu_{0.5}$ and $[Fe_{36}Co_{36}B_{19.2}Si_{4.8}Nb_4]_{99.5}Ga_{0.5}$ samples. Annealing was done different characteristic temperatures such as T_g, T_x-5, T_x, T_x+5, T_{p1} and end of first crystallization event for each of these alloys.

3.6.3 The Curie temperature measurements

The saturation magnetization versus temperature was measured using the same PPMS in high temperature mode and the Curie temperature (T_c) was calculated as described in paragraph 2.4.3. Fig. 3.16 (a), (b) and (c) shows the variation of M_s as a function of temperature for $[FeCoBSiNb]_{100-x, y}$ (Cu_x, Ga_y) (x = 0, 0.5) (y = 0, 0.5, 1, 2, 3, 4 and 5) glasses, respectively. From Fig. 3.16 (a) it can be observed that upon the addition of 0.5 at.% Cu the Curie temperature decreases from 701 to 698 K. This decrease in Curie temperature with only 3 K is lower than observed by Stoica *et al*. [209], but the trend is similar. Apart from the change in Curie temperature, the variation of M_s with temperature is also interesting. The near-zero magnetization value of the parent FeCoBSiNb alloy after the crystallization temperature (T_x = 858 K) indicates that the first phase which crystallizes is either non-magnetic or has the corresponding Curie temperature lower than the T_x. This confirms our XRD results (reported in the section 3.4) about the formation of the $(Fe,Co)_{23}B_6$-type phase; though this phase is magnetic, its Curie temperature depends strongly on the content of the magnetic atoms [209] and it is lower than the T_x. In case of the Cu added alloy the first T_x is 818 K and the primary phase is bcc-(Fe,Co), which is in perfect agreement with the thermomagnetic

65

behavior shown in Fig. 3.16 (a). The increase in M_s of the sample above 820 K clearly indicates that the crystallized phase has a high Curie temperature. However, due to the technical limitation the maximum temperature is limited to 923 K, with this temperature it is impossible to confirm the exact phase that formed during the crystallization. The room temperature M_s of the Cu added alloy becomes larger after cooling, and this is due to the presence of the bcc-(Fe,Co) crystals in ferromagnetic state.
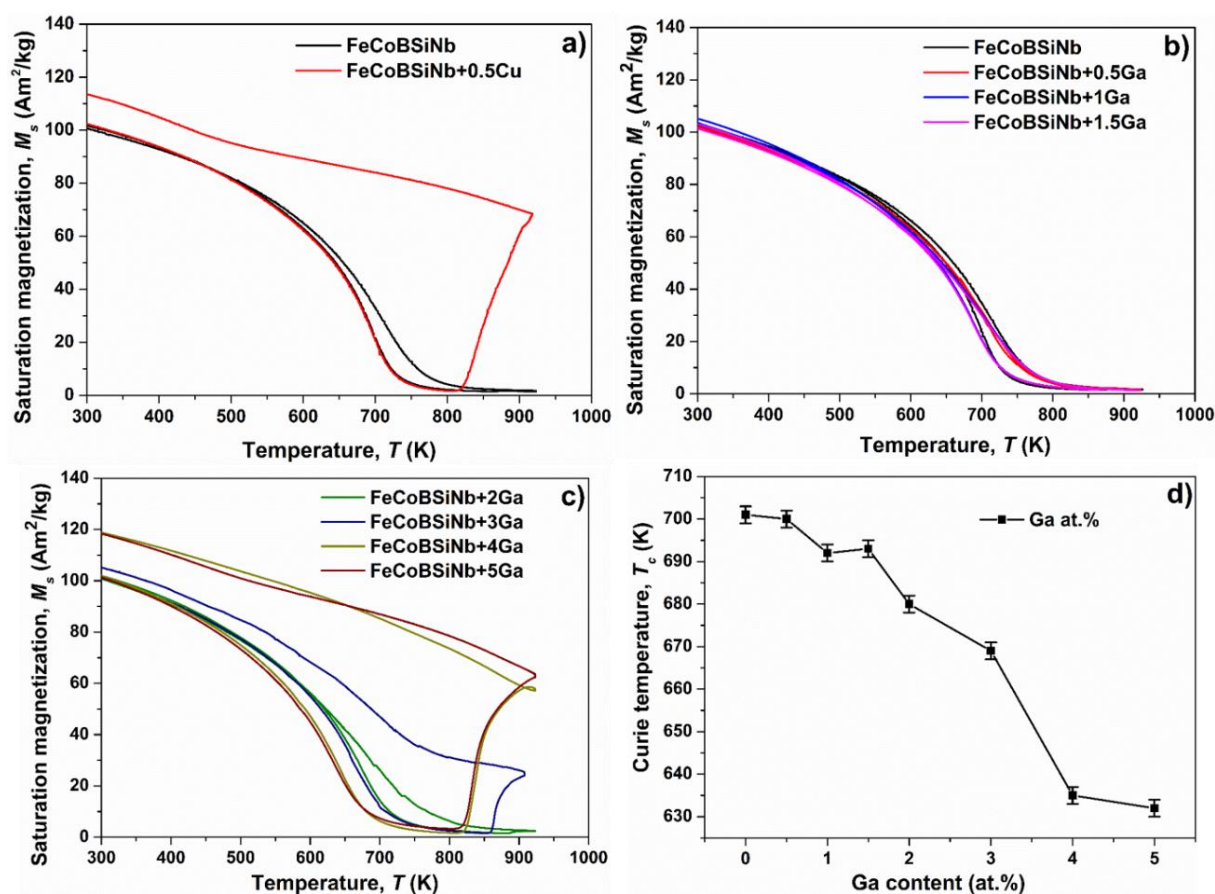
Figure 3.16: Variation of saturation magnetization (M_s) as a function of temperature for (a) $[Fe_{36}Co_{36}B_{19.2}Si_{4.8}Nb_4]_{100-x}$ (Cu_x) (x = 0, 0.5) and (b); (c) $[Fe_{36}Co_{36}B_{19.2}Si_{4.8}Nb_4]_{100-y}$ (Ga_y) (y = 0, 0.5, 1, 2, 3, 4 and 5) glasses; (d) variation of Curie temperature (T_c) as a function of Ga content (at.%).

Similar to the Cu addition, Ga addition also decreases the Curie temperature of the alloy; Fig. 3.16 (d) shows the variation of the Curie temperature as a function of Ga content. Up to 1 at.% Ga addition the T_c decreases marginally, beyond 1 at.% the T_c decreases drastically, and for the alloy with 5 at.% Ga the T_c is 632 K, which is almost 67 K lower than that of parent alloy (i.e.701 K).

The Curie temperatures for all Cu- and Ga-added samples, calculated as described in paragraph 2.4.3, are summarized in Table 3.5. The Curie temperature depends on the exchange interaction between the magnetic moments, which in turn depends on the distance between the magnetic atoms [92]. The addition of non-magnetic elements alters the distance between the magnetic atoms (i.e. Fe-Fe and Co-Co), hence the Curie temperature decreases with increase in Ga content.

Table 3.5: Saturation magnetization (M_s) and Curie temperature (T_c) values for $[Fe_{36}Co_{36}B_{19.2}Si_{4.8}Nb_4]_{100-x, y}$ (Cu_x, Ga_y) (x = 0, 0.5) (y = 0, 0.5, 1, 2, 3, 4 and 5) alloys. The accuracy of the measured date lies within ± 80 A/m (≈ 1 Oe) for saturation magnetization and ± 2 K for Curie temperature. The literature data for $Fe_{36}Co_{36}B_{19.2}Si_{4.8}Nb_4$ [221] is given for comparison.

Compositions	Rod ϕ (mm)	Saturation Magnetization M_s (Am^2/kg)	Curie temperature T_c (K)
FeCoBSiNb [221]	5	93	692
FeCoBSiNb	1	108	701
FeCoBSiNb+0.5Cu	1	109	698
FeCoBSiNb+0.5Ga	1	108	700
FeCoBSiNb+1Ga	1	107	692
1FeCoBSiNb+1.5 Ga	1	105	693
FeCoBSiNb+2Ga	1	103	680
FeCoBSiNb+3Ga	1	100	669
FeCoBSiNb+4Ga	1	97	635
FeCoBSiNb+5Ga	1	94	632

The magnetization as a function of temperature for all alloys containing less than 3 at.% Ga follows almost the same curve as the parent FeCoBSiNb alloy, i.e. the first phase formed after crystallization is either non-magnetic or has the corresponding Curie temperature less that the T_x.

The main phase which forms after the first crystallization is $(Fe,Co)_{23}B_6$-type phase. For the alloys having 3, 4 and 5 at.% Ga additions, the M_s values started to increase beyond their first crystallization event, indicating the formation of soft magnetic phase with a higher Curie temperature. The room temperature M_s of the 3, 4 and 5 at.% Ga added alloys are larger after cooling, this is due to the presence of the bcc-(Fe,Co) crystals in ferromagnetic state. All these results are in agreement with our DSC and XRD results presented in section 3.3 and 3.4.

3.7 Mechanical properties of $[Fe_{36}Co_{36}B_{19.2}Si_{4.8}Nb_4]_{100-x, y}$ (Cu_x, Ga_y) (x = 0 and 0.5) (y = 0.5, 1 and 1.5) glasses

As discussed earlier in section 1.5, the mechanical behavior of these glasses can be understand by performing compression tests and hardness measurements. In order to study and compare the effect of Cu and Ga additions on mechanical properties, all compression tests were performed on cylindrical samples with 1.5 mm diameter. The hardness measurements were performed on cross-sectional slice cut from rods with same geometry

3.7.1 Compression tests

The true stress-true strain curves for the as-cast $[FeCoBSiNb]_{100-x, y}$ (Cu_x, Ga_y) (x = 0, 0.5) (y = 0.5, 1 and 1.5) glassy samples are shown in Fig. 3.17 (a) and (b). All samples exhibit elastic deformation regime followed by a small compressive plastic regime. Fig. 3.17 (a) shows the true stress- true strain curves of 1.5 mm diameter as-cast FeCoBSiNb (black curve) and FeCoBSiNb+0.5Cu (red curve) samples. The FeCoBSiNb exhibits a very high yield strength of σ_y = 3.95 ± 0.020 GPa, an elastic strain of ε_y = 2.87%, a very high fracture strength of σ_f = 4.05 ± 0.02 GPa and a limited plastic strain ε_{pl} = 0.35%. The data are in agreement with earlier findings reported by other researchers [50]. In case of the Cu added sample the yield strength (σ_y) and fracture strength (σ_f) slightly decreases to 3.66 and 3.98 ± 0.02 GPa, respectively. Interestingly, the elastic strain (ε_y) and plastic strain (ε_{pl}) increases to 2.92 % and 0.77 % respectively, the improved plastic strain is almost twice of that of FeCoBSiNb. In addition, the Young's modulus, obtained upon linear fitting the stress-strain curve between 0.80 GPa and 3.0 GPa for both samples are 198 and 192 ± 5 GPa, respectively. The FeCoBSiNb+0.5Cu alloy shows the highest plastic

deformability reported for any other Fe-based BMG with a diameter of 2 mm, while keeping similar yield strength (σ_y) and fracture strength (σ_f), together with a plastic strain of 0.6% [199]. Similarly, for samples with 1 mm diameter a larger compressive yielding and maximum stress were reported for the FeCoBSiNb+0.5Cu glassy samples by Stoica *et al.* [138] i.e. 3.92 GPa and 4.14 GPa, respectively, together with a large plastic strain of 1.50%. It is well known that samples of smaller dimensions exhibit much higher plasticity [62]. The difference in the present σ_y, σ_f and ε_{pl} values and reported values [138, 199] are because of the differences in the sample geometry. However, it is seen here that the addition of 0.5% Cu improves the plastic deformability even for the 2 mm diameter glassy samples. Shen *et al.*[195] have found that the yielding of bulk samples with similar chemical composition (i.e. FeCoBSiNb with 0.25 at.% Cu) occurs at 3.70 GPa, and reported a maximum stress of 4.05 GPa and a plastic strain of 0.6%. They used rod samples with 2 mm diameter with a composite structure consisting of bcc-(Fe,Co) and $(Fe,Co)_{23}B_6$-type nanocrystalline grains embedded in an amorphous matrix. Table 3.6 summarizes the deformation data obtained from compression tests together with hardness and density values for all the composition studied in this work.
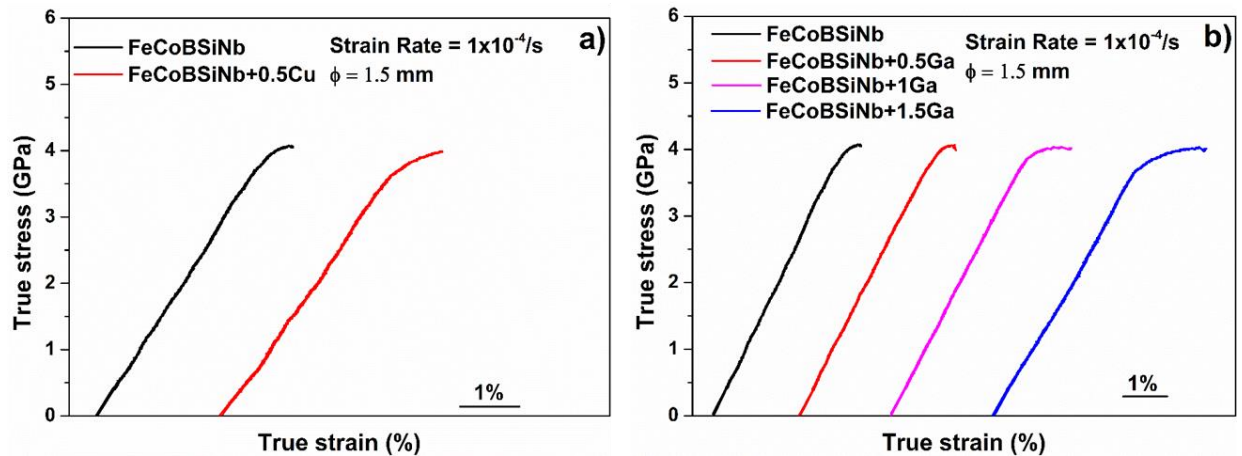
Figure 3.17: Compressive true stress-true strain curve for (a) $[Fe_{36}Co_{36}B_{19.2}Si_{4.8}Nb_4]_{100-x}$ (Cu_x) (x = 0, 0.5) and (b) $[Fe_{36}Co_{36}B_{19.2}Si_{4.8}Nb_4]_{100-y}$ (Ga_y) (y = 0, 0.5, 1, and 1.5) glasses measured at a strain rate of 1×10^{-4}/s.

The compressive behavior of the Ga added samples are shown in Fig. 3.18 (b), FeCoBSiNb (black curve), FeCoBSiNb+0.5Ga (red curve), FeCoBSiNb+1Ga (magenta curve) and FeCoBSiNb+1.5Ga (blue curve). It is evident that with increase in Ga content the plastic strain

increases gradually. For the 0.5at.% Ga- added sample the yield strength σ_y, elastic strain ε_y, fracture strength σ_f and plastic strain ε_{pl} are almost same as that of the FeCoBSiNb parent alloy i.e. 3.95 ± 0.02 GPa, 2.80%, 4.06 ± 0.02 GPa and 0.43%, respectively. It can be noted that unlike Cu, 0.5 at.% Ga does not improve the mechanical properties much, but for higher amount of Ga addition plastic deformation is improved (see Fig. 3.17 (b)). The yield stress is 3.71 and 3.62 ± 0.2 GPa for the 1 and 1.5 at.% Ga- added samples and their corresponding elastic strain are 2.73 % and 3.30 %, respectively.

Table 3.6: summarizes the Yield stress σ_y, yield strain ε_y, fracture stress σ_f, fracture strain ε_f, plastic strain ε_{pl}, Young's modulus E, Vickers hardness HV and density ρ for $[Fe_{36}Co_{36}B_{19.2}Si_{4.8}Nb_4]_{100\text{-x, y}}$ (Cu_x, Ga_y) (x = 0, 0.5) (y = 0.5, 1, 1.5, 2, 3, 4 and 5) alloys. The accuracy of the experimental data lies within ± 0.02 GPa for the stress-strain measurements, ± 10 HV for the hardness measurements and 0.5% for the density measurements. The literature data for $Fe_{36}Co_{36}B_{19.2}Si_{4.8}Nb_4$ [50] is given for reference.

Compositions	σ_y (GPa)	ε_y (%)	σ_f (GPa)	ε_f (%)	ε_{pl} (%)	E (GPa)	HV	ρ (g/cm^3)
FeCoBSiNb [50]	4.07	-	4.21	-	-	210	1220	-
FeCoBSiNb	3.95	2.87	4.05	3.22	0.35	198	1272	7.768
FeCoBSiNb+0.5Cu	3.66	2.92	3.98	3.69	0.77	192	1242	7.752
FeCoBSiNb+0.5Ga	3.82	2.80	4.06	3.23	0.43	186	1240	7.737
FeCoBSiNb+1Ga	3.71	2.73	4.01	3.87	1.07	178	1230	7.726
FeCoBSiNb+1.5Ga	3.62	3.3	4.01	4.83	1.53	167	1228	7.716
FeCoBSiNb+2Ga	-	-	-	-	-	-	1208	7.706
FeCoBSiNb+3Ga	-	-	-	-	-	-	1201	7.687
FeCoBSiNb+4Ga	-	-	-	-	-	-	1185	7.667
FeCoBSiNb+5Ga	-	-	-	-	-	-	1180	7.649

The fracture of first two Ga added samples occurs at nearly the same value of true stress, around 4 GPa, but the corresponding fracture strain is different: 3.87 % for 1 at.% Ga and 4.83 % for 1.5 at.% Ga- added samples. The plastic deformation of the samples extend up to 1.07 % and 1.53 % for 1 at.% and 1.5 at.% Ga- added samples. The fracture surface morphology of the samples after compression tests were investigated using SEM, as descried in the section 2.3.2. The observed fracture behavior is different from the observed results for Zr-, Cu-, Ni- and Ti based BMGs [222-225], where that fractures occurs only along the maximum shear plane, which is declined by 45° to the direction of applied load, and the fracture surface contains large numbers of a well-developed vein patterns.

The fracture surface of the FeCoBSiNb, FeCoBSiNb +0.5Cu and FeCoBSiNb +0.5Ga samples consists of a number of small fracture zones and their zone planes appear to be declined by about 70-90° to the direction of the applied load, which is similar to the previous results for FeCoBSiNb glass [50, 191]. This kind of failure is mainly due to the simultaneous generation of large no of small facture at many sites, at a very high stress level close to 4.0 GPa, upon fracture the samples shatter apart into many small fragments. The high fracture strength of these glasses are mainly because of their covalent bonding nature of their constituents [8, 50]. Though slight increase in plastic strain is observed for FeCoBSiNb +0.5Cu and FeCoBSiNb +0.5Ga samples, the overall appearance of the fracture surface is towards brittle fracture mode, with many shells indicating the generation and propagation of cracks.
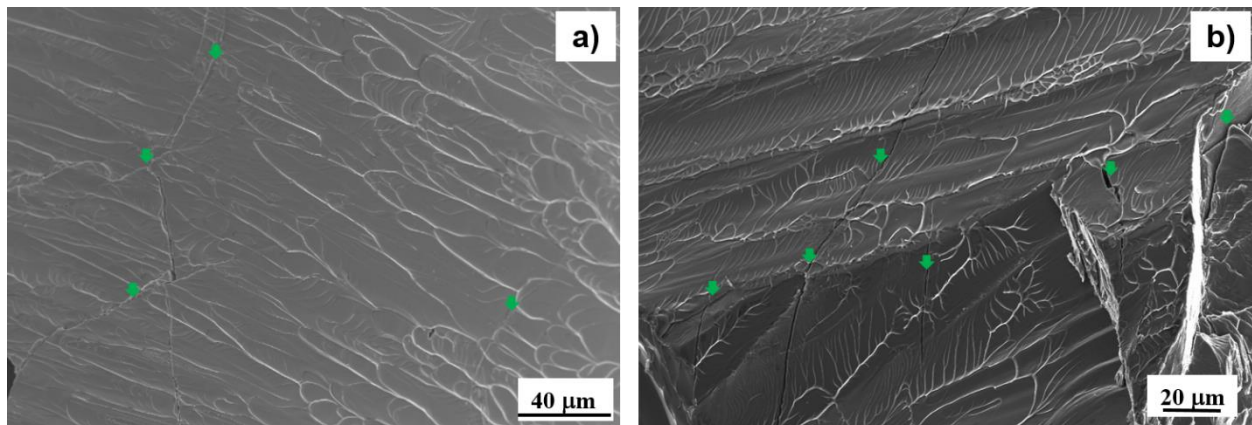
Figure 3.18: SEM micrographs of the $[Fe_{36}Co_{36}B_{19.2}Si_{4.8}Nb_4]_{99}Ga_1$ sample, showing fracture surface after compression test taken from different regions with different magnifications (a) and (b). Cracks are marked with green arrows.

Neither shear bands on the lateral surfaces nor typical vein patterns are observed on the fracture surface of these samples. However, more interesting features are observed in the FeCoBSiNb +1Ga and FeCoBSiNb +1.5Ga samples. Fig. 3.18 (a) and (b) shows the fracture surface of the FeCoBSiNb +1Ga samples after compression test taken from different regions with different magnifications. The fracture surfaces consists of large numbers of vein patterns combined with several micro cracks (indicated by green arrows in the image) At first the material starts to deform plastically; after a while the brittle fracture starts, because the cracks are super imposed on the vein patterns, indicating the combination of ductile and brittle failure mode.

Fig. 3.19 (a) represents the fracture surface of the FeCoBSiNb +1.5Ga samples taken from the center of the samples after compression test and Fig. 3.19 (b) shows the magnified image marked with dotted lines in the Fig 3.19 (a). The red arrow indicates the metal droplets, which are observed throughout the fracture surfaces. Compared to the 1 at.% Ga samples, the fracture surface of this 1.5 at.% Ga samples contains more vein patterns and less micro cracks, here also the micro cracks are superimposed on the vein patterns. The presence of metal droplets on the fracture surfaces suggests that, at very high stress level of 4.0 GPa the flowed layers must have been melted, as it is commonly observed in case of the deformable BMGs [226]. Lewandowski *et al*.[227] reported an increase temperature over 1000 K in the thermal diffusion zone near the shear bands in BMGs during bend test. In other works on Zr- based glasses [137, 228] even higher temperatures are reported for the specimens tested in compression and in tension.
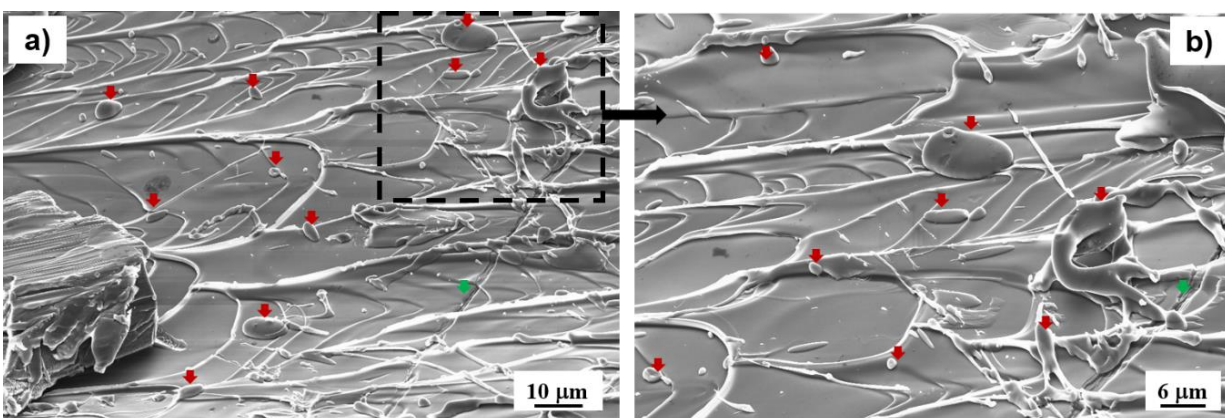
Figure 3.19: SEM micrographs of the $[Fe_{36}Co_{36}B_{19.2}Si_{4.8}Nb_4]_{98.5}Ga_{1.5}$ sample, (a) Fracture surface taken from the center of the sample after compression test and (b) Center region taken at higher magnification (square region from (a)). Droplets are marked with red arrows and cracks are marked with green arrows.

Greer e*t al.* [226] recently reviewed all the possible mechanisms and implications related to shear band heating and melting in bulk metallic glasses. In that review he concluded that tendency for the samples to fail at shear bands can readily be associated with thermal runaway and development of a liquid zone.

In a very recent work Stoica *et al.* [138] showed that during compression in FeCoBSiNb+0.5Cu glass the temperature in the shear plane can raise up to 1352 K. In his work the temperature raise in the shear plane was calculated based on two assumptions: (a) the speed of shear propagation in the sample is approximately $0.9V_s$ [229], where V_s is the velocity of a transverse sound wave through the sample and (b) the transverse speed of sound through FeCoBSiNb+0.5Cu sample was considered as 6100 m/s, as for carbon steels.

The most crucial part in calculating the temperature raise during the shear propagation is the shear time, i.e. the time necessary to for a shear band to start and stop operating and during which the heat flux Φ_q is released [138]. Though several researchers like Bengus *et al.*[229], Miracle *et al.*[230], Lewandowski *et al.*[227] and Georgarakis *et al.* [228] concluded different shear velocities for Zr based glasses there is no exact shear propagation data is available for Fe-based metallic glasses. Stoica *et al.* [138] in their work showed that maximum possible temperature raise in the shear plane is 1352 K by assuming maximum shear propagation rate (i.e. $0.9V_s$) which is just 30 K above the solidus temperature of the FeCoBSiNb+0.5Cu alloy and barely enough to melt very thin layers. Considering the fact that the solidus temperature of the both FeCoBSiNb+0.5Cu and FeCoBSiNb+1.5Ga alloys are ≈1310 K, no droplets are seen in the fracture surface of the FeCoBSiNb+0.5Cu glass [138] but in FeCoBSiNb+1.5Ga glass μm range molten droplets are observed throughout the fracture surfaces (see Fig. 3.19 (a) and (b)). From this results two conclusions can be drawn: (1) the shear propagation rate in FeCoBSiNb system should be higher than $0.9V_s$ (i. e., higher that V_s higher the temperature raise in the shear planes) or (2) the presence of Ga atoms leads to formation of soft zones, whose melting point is much lower compared to rest of the alloy. In either case more detailed study is required to get the exact conclusions, which is the future scope of this work. However, the addition of Ga improves the plastic deformation of the FeCoBSiNb glass to a great extent.

3.7.2 Hardness and density measurements

The Vickers hardness measurements were performed on cross-section slice from the as-cast cylindrical rods with 1.5 mm diameter as described in the section 2.5.2. In order to have more consistent result, more than 20 indentations were performed in each samples and the average value were obtained as the average of 20 indents. The hardness values of all glassy samples are listed in Table 3.6. The hardness value for the FeCoBSiNb glass is HV= 1272 ± 10 (12.47 GPa), the hardness of the 0.5 at.% Cu- and Ga- added glasses are almost same 1242 (12.18 GPa) and 1240 (12.16 GPa) HV.

The hardness decreases with increase in Ga % and reaches a minimum value of 1180 (11.57 GPa) HV for the 5 at.% Ga- added samples. This decrease in the hardness values are mainly due the presence of soft zones, which increases with increase in Ga content.

The density measurements were performed on master alloys for all compositions as described in the section 2.5.3. All density values are summarized in the Table 3.6. The density of the FeCoBSiNb alloy is ρ = 7.768 g/cm^3, which is lower than that of structural amorphous steel (i.e., 7.89 g/cm^3) [36] and ultrahigh strength maraging steels (i.e., ~8.12 g/cm^3) [231]. However, FeCoBSiNb glass is much stronger; hardness is more than twice that of the maraging steels [231].With addition of Cu and Ga the density decreases slightly and reaches a minimum value of ρ = 7.649 g/cm^3 for the alloy with 5 at.% Ga, which is obvious, because Ga has a low density compared to Cu, Fe and Co.

3.8 Discussion

Table 3.1 Summarizes all thermal stability values collected in this work compared with the values known from literature [50, 206]. The reported maximum achievable diameter was 5 mm for this FeCoBSiNb alloy [50], while in this work the maximum diameter produced was only 3 mm. The glass transition temperature obtained in this work is 825 K, which is higher than the value reported by Inoue *et al*. [50] but almost same with the values reported by Stoica *et al*. [206]. However, the extension of the supercooled liquid region is only 33K which is very low compared to the reported value of 50 K [50]. The reduced glass transition temperature is also smaller: 0.56 compared to

0.58. If the GFA of the current alloy is determined based on the extension of the SLR and the reduced glass transition as indicated by Inoue *et al*.[8], the current alloy has slightly lower GFA compared to the literature. These small differences in the thermal stability may arise due to small deviation in the overall composition, as shown by Stoica [3] in his very recent work.

The addition of Cu in the $Fe_{71.5-x}Co_xB_{13.5}Si_{10}Nb_4$ alloy was first reported by Inoue *et al*.[85], followed by Shen *et al*. [195] in his work he added only 0.25 at.% Cu in glass having same composition as our investigated $Fe_{36}Co_{36}B_{19.2}Si_{4.8}Nb_4$ alloy, but the thermal stability of the glass remains almost unaffected. Later, Li *et al*. [197] added 1, 1.5 and 2 at.% Cu in the same $Fe_{36}Co_{36}B_{19.2}Si_{4.8}Nb_4$ but they were able to produce only amorphous ribbons. Recently, Stoica *et al*. [138, 209] reported the preparation of bulk glassy samples having up to 2 mm in diameter with the addition of 0.5 at.% Cu. The extension of SLR reported there is 19 K, which is clearly lower than the 25 K reported in the current work; this may indicate that the current alloy has slightly better GFA.

The interesting ordered features observed in TEM (see Fig. 3.10) of this alloy may explain why the Cu free FeCoBSiNb alloy has wider SLR ($\Delta T_x = 33$ K) than the Cu containing alloy ($\Delta T_x = 25$ K). The wider SLR indicates longer incubation time for nucleation. For the alloy without Cu, crystallization requires the formation of complex $(Fe,Co)_{23}B_6$-type nuclei that are dissimilar to the ordered zones of the amorphous alloy. In case of the Cu- added alloy, the formation of the local order reduces the nucleation kinetics, there by easily promoting the formation of α-Fe from the amorphous matrix.

For the glass with 0.5 at.% Ga, there is 5 K increase in the crystallization temperature compared to the glass without Ga. The dissimilarities between the structures of the ordered zones observed in both Cu- and Ga- added samples may be one of the reason for the wide SLR of the FeCoBSiNb+0.5Ga alloys. The increase in crystallization temperature up on addition of Ga suggests that the degree of ordered zones/clusters formed due to the addition of Ga has no effect on the crystallization kinetics. This is not a surprising, given the fact that even after the addition of 0.5 at.% Ga the main precipitating phase is complex $(Fe,Co)_{23}B_6$-type phase. The crystallization activation energy (E_c) calculated in the section 3.3 clearly supports this claim, the addition of Cu reduces the E_c to almost half i.e. from 607 to 374 ±14 kJ/mol, but the Ga addition reduces the E_c to 557 ±14 kJ/mol. From this we can assume that, unlike the ordered zones/clusters formed due to

addition of Cu, ordered zones/clusters formed due to Ga addition does not influence in the thermal stability of the glass. It is well known that the presence of ordered zones/clusters in the amorphous matrix does not necessarily imply that they act as a nucleation site for the crystal growth. The ordered embryos must be larger than the critical nucleus size in order for their growth to be thermodynamically favorable [211-213].

However with increase in Ga content the first and second broad XRD maxima shifts to lower angles, indicating the formation of large number of ordered zones/clusters [205]. Up to 1 at.% addition of Ga the change slope of the $2\theta_1$ is very small and the GFA remains almost the same. The slope of $2\theta_1$ increase when the Ga content is more than 1 at.% and up to 3 at.% Ga, accordingly GFA decreases, the critical diameter for 2 and 3 at.% Ga-added alloys are 2 and 1.5 mm respectively. Further, for the 4 and 5 at.% Ga-added samples $2\theta_1$ decreases to 52.13° and 51.99°, respectively, similarly the GFA of these alloys also decreases to a critical diameter of 1 mm. From the thermal stability data it is evident that with increase in Ga content i.e. 3, 4 and 5 at.% the onset of crystallization temperature started to decrease and also only bcc-(Fe,Co) grows after the first crystallization event (see Fig. 3.8). At this point one can assume that the addition of Ga more than 2 at.% have similar effect like Cu addition and they are (i). decrease in onset of crystallization temperature and extension of supercooled liquid region ΔT_x; (ii) formation of the complex $(Fe,Co)_{23}B_6$-type phase is suppressed and only bcc-(Fe,Co) starts to grow after first crystallization event; (iii) the GFA decreases drastically t_c is merely 1.5 mm for 3 at.% and 1 mm for 4 and 5 at.% Ga addition respectively. All these changes could be because of the formation of ordered zones/clusters which are above the critical limit and hence started to grow with increase in temperature leading to decreases in the GFA of the alloys. From this we can conclude that the optimum quantity of Ga, which can be added without affecting the GFA as well as their thermal stability, is around 1.5 at.%.

The coercivity values reported in our work are comparable with the values reported by Shen *et al.* [221] and Stoica *et al.* [206] for the same $Fe_{36}Co_{36}B_{19.2}Si_{4.8}Nb_4$ alloy. However, the Curie temperature of this alloy is 19 K lower than the value reported by Stoica et al. and 9 K higher than the values reported by Shen et al. The differences in the coercivity is quite small, as mentioned earlier they may arise due to the small variation in the overall chemical composition. The magnetic properties of both the Cu- and Ga- (only up to 2 at.% Ga) added alloys are similar at the room

temperature; with increase in annealing temperature the Cu- added alloy has relatively better soft magnetic properties compared to the Ga- added. As mentioned earlier (section 3.6.2), the increase in M_s with increase in temperature is due to the formation of bcc-(Fe,Co) phase in the Cu added alloy, the growth of this bcc-(Fe,Co) phase can be clearly seen in the thermomagnetic curves shown in Fig. 3.16 (a). The M_s value starts to increase as soon as the bcc-(Fe,Co) crystal start to form, which is close to 820 K. In case of the Ga added alloys (i.e. up to 2 at.%) no such increase in M_s values were observed even after the completion of first crystallization event. However, for 3, 4 and 5 at.% Ga- added samples, one can clearly observe the increases in M_s values close to the respective crystallization start temperatures, indicating the formation of bcc-(Fe,Co) phase. This observation further confirms that when Ga is added beyond 2 at.%, then it will decrease GFA of the alloy by promoting the formation of large number of ordered zones.

The compression behavior of Cu and Ga added samples is very similar in the elastic regime. For the same amount of Cu and Ga addition (i.e. 0.5 at.%), the Cu- added sample shows slightly higher plastic strain ε_{pl} compared to the Ga- added samples (Table 3.6). Though the yield stress σ_y decreases with increase in Ga content, the fracture stress σ_f for all alloys are almost same ≈ 4.0 GPa. However, with increase in Ga content to 1.5 at.% the plastic strain ε_{pl} increases up to 1.53% and the Young's modulus decreases from 198 to 167 GPa. Table 3.7 summarizes the available data about the glass transition temperature T_g and compressive fracture stress σ_f for a number of Fe- and Co-based BMGs, which were developed in recent years.

Table 3.7: Glass transition temperature (T_g), fracture stress (σ_f), Young's modulus (E) and Vickers hardness (HV) data for Fe- and Co- based metallic glasses available in literature.

	Composition	T_g (K)	σ_f (GPa)	E (GPa)	HV
1	FC20+B+0.4wt% B [232]	640	3.48	125	970
2	$(Fe_{44.3}Cr_5Co_5Mo_{12.8}Mn_{11.2}C_{15.8}B_{5.9})_{98.5}Y_{1.5}$ [36]	804	3.0	257	1224
3	Fe48Cr15Mo14Er2C15B6 [76]	843	4.0	200	1200

4	$Fe_{72}B_{20}Si_4Nb_4$ [233]	829	4.0	200	995
5	$Fe_{74}Mo_4P_{10}C_{7.5}B_{2.5}Si_2$ [89]	729	3.28	-	-
6	$Fe_{40}Ni_{40}P_{14}B_6$ [234]	641	2.8	-	-
7	$Fe_{60}Co_8Zr_{10}Mo_5W_2B_{15}$ [235]	898	3.8	-	1360
8	$Fe_{63.5}Mo_{14}C_{15}B_6Er_{1.5}$ [236]	779	4.2	210	1142
9	$Fe_{75}Mo_5P_{10}C_{7.5}B_{2.5}$ [88]	708	3.28	-	-
10	$Fe_{66}Co_{10}Mo_4P_9C_4B_4Si_3$ [237]	744	3.37	-	-
11	$Fe_{71}Nb_6B_{23}$ [238]	840	4.85	-	-
12	$Fe_{58.5}Co_3Mo_{14}C_{15}B_6Er_{0.5}Ni_3$ [239]	757	3.98	-	-
13	$Fe_{53.25}Ni_{17.75}Nb_6B_{23}$ [240]	768	4.36	195	-
14	$Fe_{68.16}Dy_{3.84}B_{19.2}Si_{4.8}Nb_4$ [241]	873	3.77	-	1054
15	$Fe_{69.3}Ni_{7.7}Mo_5P_9C_{7.5}B_{1.5}$ [242]	667	3.26	-	-
16	$Co_{43}Fe_{20}Ta_{5.5}B_{31.5}$ [243]	910	5.18	268	-
17	$Co_{31}Fe_{31}Nb_6Dy_2B_{30}$ [244]	900	4.75	-	1258
18	$Co_{47.6}Fe_{20.42}B_{1.9}Si_{5.1}Nb_5$ [245]	853	4.34	-	-
19	$Co_{45.5}Fe_{2.5}Cr_{15}Mo_{14}C_{15}B_6Er_2$ [246]	844	5.0	217	-
20	$Co_{56}Ta_9B_{35}$ [247]	961	5.97	247	1621
21	$Co_{61}Nb_8B_{31}$ [248]	900	5.2	-	-
22	$Co_{69}Mo_{11}P_{14}B_6$ [249]	750	3.9	-	-

The relationship between compressive fracture strength (σ_f) and glass transition temperature (T_g) for the values listed in Table 3.7 are plotted in Fig. 3.20. The small region marked with blue circle illustrates the region corresponding to the present studied $[FeCoBSiNb]_{100-x, y}$ (Cu_x, Ga_y) (x = 0, 0.5) (y = 0, 0.5, 1 and 1.5) compositions.

The equation describing the linear fit can be written as:

$$\sigma_f = -1.54 \cdot 10^3 + 7.03 \cdot T_g \, , \tag{3.9}$$

where T_g is in K and σ_f is in MPa.

The relationship between the T_g and σ_f for non-ferrous BMGs (Cu-based) can be given as [250]:

$$\sigma_f = -3.35 \cdot 10^3 + 7.47 \cdot T_g \, , \tag{3.10}$$
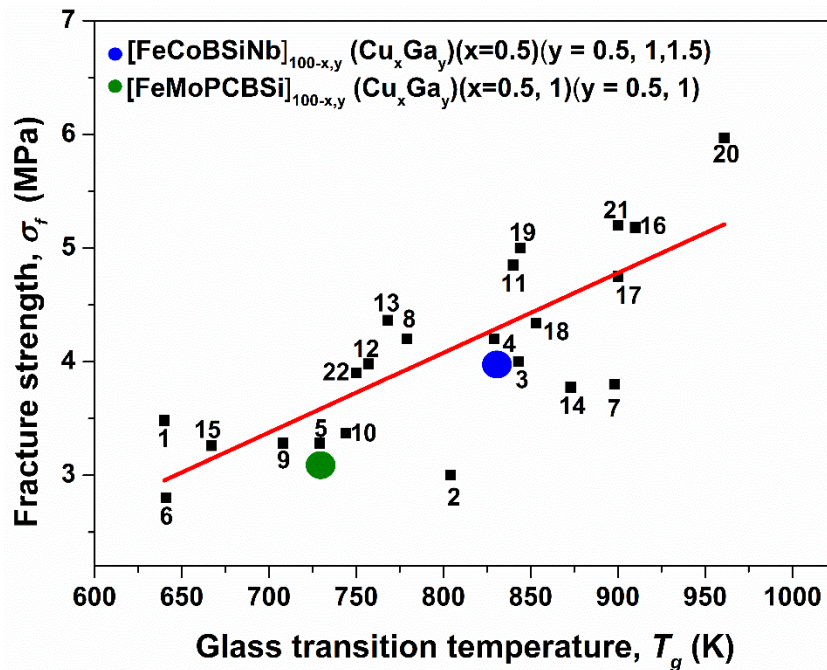
Figure 3.20: Relationship between compressive fracture strength (σ_f) and glass transition temperature (T_g) for the values summarized in Table 3.7. The number in the graphs is assigned to a composition, as presented in Table 3.7. Red line represents the linear fit. The small region marked with the Blue and Green circle represents the data measured for the [Fe$_{36}$Co$_{36}$B$_{19.2}$Si$_{4.8}$Nb$_4$] (Cu,Ga) and [Fe$_{74}$Mo$_4$P$_{10}$C$_{7.5}$B$_{2.5}$Si$_2$] (Cu,Ga) samples studied in this work.

It is interesting to compare the equations 3.9 and 3.10 written to describe Fe-, Co- based and non-ferrous based BMGs. It can be observed that the slopes of linear fit are almost similar for ferrous (7.0) and non-ferrous alloys (7.47). Though the slope is similar, a scattering could be observed in the data, this scatter could be due to the difference in the sample preparation and experimental

techniques. As observed in the Fig. 3.20 the fracture strength increases rapidly with increase in the T_g. Considering the fact that T_g is the reflection of atomic bonds between the constituent elements [104], the high bonding force between the constituting elements might be responsible for the high strength of Fe- and Co- based BMGs.

The Vickers hardness values measured for this alloys are comparable to the hardness value of the amorphous steels $Fe_{48}Cr_{15}Mo_{14}Er_2C_{15}B_6$ [76] and $(Fe_{44.3}Cr_5Co_5Mo_{12.8}Mn_{11.2}C_{15.8}B_{5.9})_{98.5}Y_{1.5}$ [36]. With the addition of Ga, the hardness values also decreases over 100 *HV* when Ga content is increased from 0 to 5 at.%. The σ_f/E, HV/σ_f and $HV/3E$ ratios for all the glasses are given in Table 3.8.

Table 3.8: σ_f/E, HV/σ_f and $HV/3E$ ratios for $[Fe_{36}Co_{36}B_{19.2}Si_{4.8}Nb_4]_{100-x, y}$ (Cu_x, Ga_y) $(x = 0, 0.5)$ $(y = 0, 0.5, 1$ and $1.5)$ glasses.

Compositions	σ_f/E	HV/σ_f	$HV/3E$
FeCoBSiNb	0.02	3.0	0.02
FeCoBSiNb+0.5Cu	0.02	3.0	0.02
FeCoBSiNb+0.5Ga	0.02	2.99	0.02
FeCoBSiNb+1Ga	0.02	3.0	0.02
FeCoBSiNb+1.5Ga	0.02	3.0	0.02

The σ_f/E, HV/σ_f and $HV/3E$ ratios for all the alloys are nearly fixed 0.02, 3.0 and 0.02, respectively. It can be concluded that the present Fe-based bulk glassy alloys have the same ratio in their properties like the previously reported BMGs [26, 50, 251]. The agreement also indicates that the Fe-based bulk glassy alloys have an elastic-plastic deformation mode without appreciable work hardening.

Chapter 4

Preparation and Characterization of Fe-Mo-P-C-B-Si-(Cu, Ga) bulk glassy samples

4.1 Introduction

The investigated composition $[Fe_{74}Mo_4P_{10}C_{7.5}B_{2.5}Si_2]_{100-x, y}$ $(Cu)_x$ $(Ga)_y$ (x = 0, 0.5, 1)(y = 0, 0.5, 1, 1.5 and 2) are of metal-metalloid type. The basis for this composition is $Fe_{75}Mo_5P_{10}C_{7.5}B_{2.5}$, first introduced by Zhang *et al*. [88]. The glass-forming ability and soft magnetic properties of this system was improved by addition of Si at the expense of Fe and Mo [89], as a result the maximum achievable diameter and saturation magnetization of this system increased to 5 mm and 1.34 T, respectively. Liu *et al*. [89] managed to cast rods with 5 mm diameter only after fluxing the master alloy with B_2O_3, however, without flux they may achieve already 4 mm. Again, in the line with what was mentioned in the previous chapter, the important aspect which limits the application of these bulk Fe-based metallic glass as an engineering materials is the brittle behavior under mechanical loading [75]. Therefore, in the last decade great efforts have been made to improve the plastic deformability of monolithic Fe-based BMGs

In our work we tried to improve the plastic deformability of the $Fe_{74}Mo_4P_{10}C_{7.5}B_{2.5}Si_2$ glass by adding soft elements like Cu, Ga in small percentage, at the expense of all elements. For the compositions investigated in this work first $Fe_{74}Mo_4P_{10}C_{7.5}B_{2.5}Si_2$ alloy was produced by induction melting and then Cu and Ga were added through arc melting. In this way $[Fe_{74}Mo_4P_{10}C_{7.5}B_{2.5}Si_2]_{100-x} Cu_x$ (x = 0.5 and 1) and $[Fe_{74}Mo_4P_{10}C_{7.5}B_{2.5}Si_2]_{100-y} Ga_y$ (y = 0.5, 1, 1.5, 2, 3, 4 and 5) alloys were obtained. In this chapter the microstructure, mechanical and magnetic properties of the ribbons and rods produced from these alloys were investigated.

4.2 Characterization of amorphous ribbons and bulk samples

The addition of Cu and Ga to the $Fe_{74}Mo_4P_{10}C_{7.5}B_{2.5}Si_2$ master alloy (for simplicity, this alloy will be further denoted as FeMoPCBSi) decreases the GFA drastically. Since we were interested only in the bulk samples we limited the Cu and Ga additions to 1 and 2 at.%, respectively.

4.2.1 Diffraction experiment using Co-$K\alpha$ radiation

The structure of the as-cast rods was investigated using X-ray diffraction using Co-K_α radiation (λ = 0.17889 nm). Fig. 4.1 (a) and (b) depicts the XRD patterns of the as-cast $[FeMoPCBSi]_{100-x}$ $(Cu)_x$ (x = 0, 0.5 and 1) and $[FeMoPCBSi]_{100-y}$ $(Ga)_y$ (y = 0, 0.5, 1, 1.5 and 2) glassy samples with maximum achievable diameter.
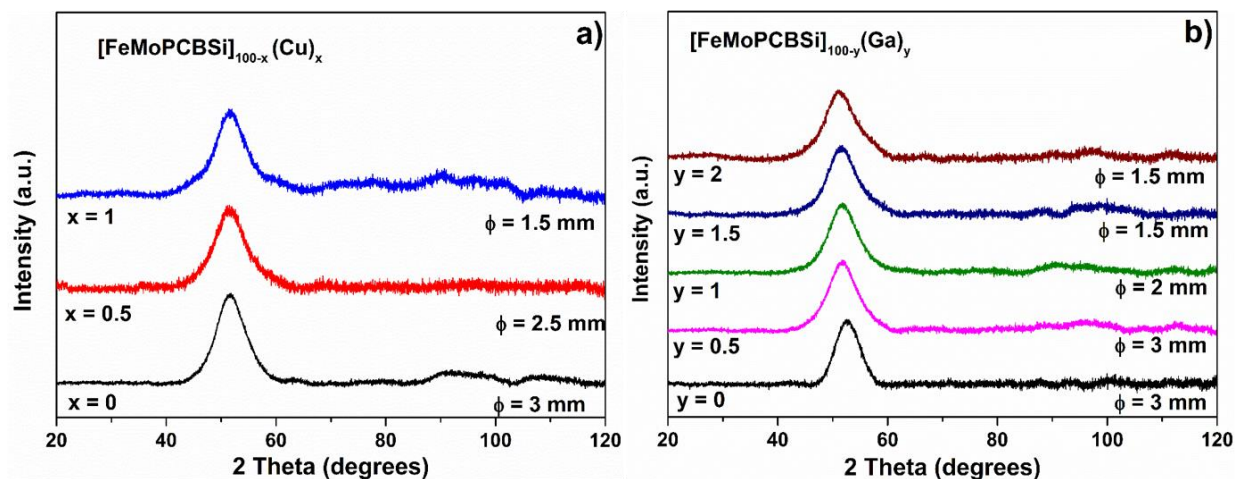
Figure 4.1: X-ray diffraction patterns of (a) as-cast $[Fe_{74}Mo_4P_{10}C_{7.5}B_{2.5}Si_2]_{100-x}$ $(Cu)_x$ (x = 0, 0.5 and 1) and (b) as-cast $[Fe_{74}Mo_4P_{10}C_{7.5}B_{2.5}Si_2]_{100-y}$ Ga_y (y = 0, 0.5, 1, 1.5 and 2) glassy rods.

The XRD patterns in Fig.4.1 (a) and (b) exhibits characteristic broad diffraction maxima indicating the formation of a glassy structure. The first and second broad diffraction maxima for FeMoPCBSi glass are located at 2θ = 51.70° and 93.98°, respectively. However, the position of the broad maxima shifts slightly to smaller diffraction angles with increase in Cu and Ga content.

In order to avoid the error in calculating the peak positons due to difference in the sample thickness, only ribbons were used for the peak position analysis. Fig. 4.2 (a) and (c) depicts the XRD patterns of [FeMoPCBSi]$_{100-x}$ (Cu)$_x$ (x = 0, 0.5 and 1) and [FeMoPCBSi]$_{100-y}$ (Ga)$_y$ (y =0, 0.5, 1, 1.5 and 2) glassy ribbons, respectively. Fig. 4.2 (b) and (d) shows the shift of the first and second broad maxima of the XRD patterns presented in Fig. 4.2 (a) and (c) as a function of Cu and Ga content, respectively.
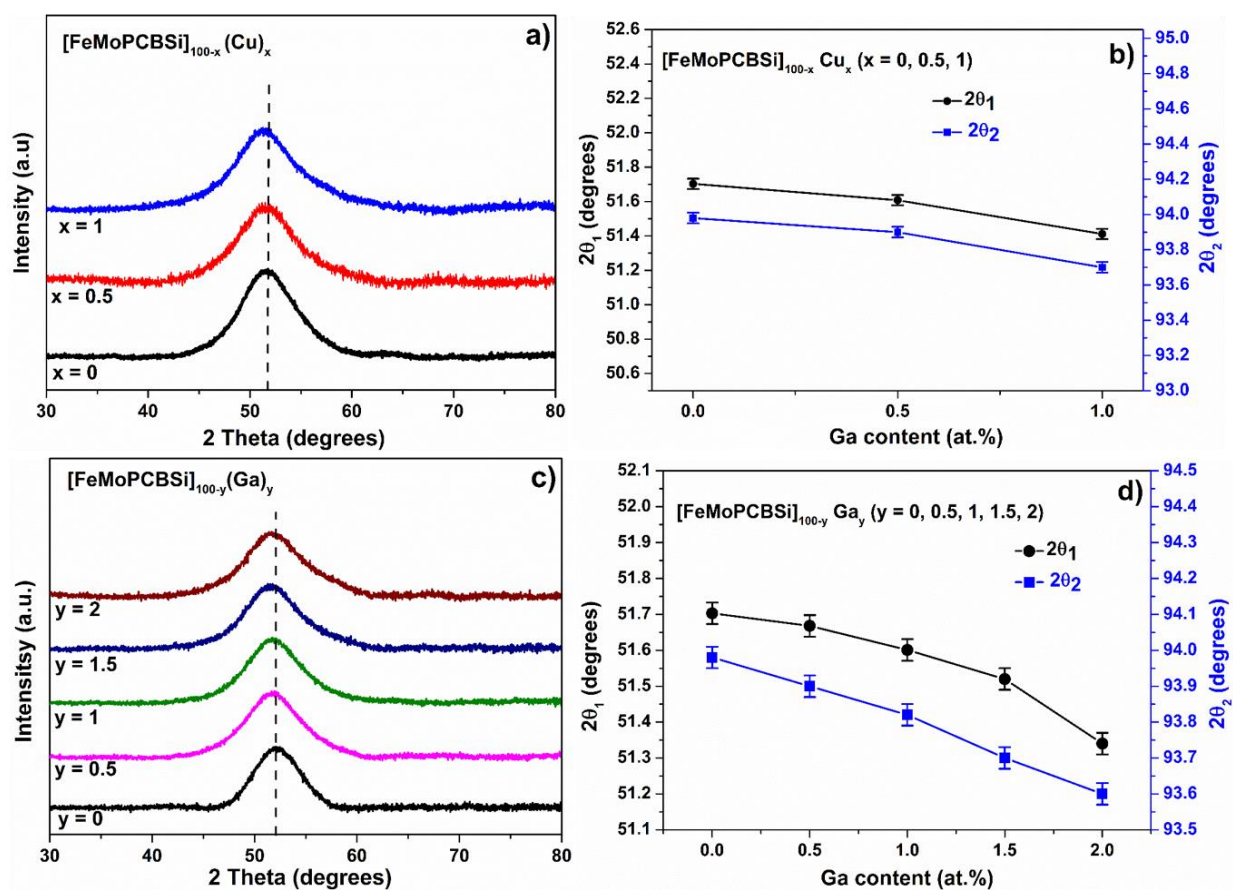
Figure 4.2: X-ray diffraction patterns of as-spun (a) [Fe$_{74}$Mo$_4$P$_{10}$C$_{7.5}$B$_{2.5}$Si$_2$]$_{100-x}$ (Cu)$_x$ (x = 0, 0.5 and 1), (c) [Fe$_{74}$Mo$_4$P$_{10}$C$_{7.5}$B$_{2.5}$Si$_2$]$_{100-y}$ Ga$_y$ (y = 0, 0.5, 1, 1.5 and 2) glassy ribbons and changes in the position of first ($2\theta_1$) and second ($2\theta_2$) broad diffraction maxima center as a function of (b) Cu content (at.%), (d) Ga content (at.%).

The 2θ positions were obtained by following the method described in the section 3.2.1. The first and second broad maxima of both Cu- and Ga- added samples shifts to smaller values with increase

in Cu and Ga at.%, respectively. The first and second broad maxima for the 0.5 and 1 at. % Cu added samples are $2\theta_1$ = 51.60°, 51.41° and $2\theta_2$ = 93.9°, 93.7°, respectively. Similarly, the first and second broad maxima for the 0.5 and 1 at.% Ga- added samples are $2\theta_1$ = 51.66°, 51.60° and $2\theta_2$ = 93.9°, 93.82°, respectively. For the addition of equal at.% of Cu and Ga (i.e., for 0.5 and 1 at.%), the shift in the first and second broad maxima to smaller 2θ values follows almost the same trend, however the shift is higher for the Cu- added samples compared to the Ga- added ones. With further increase in Ga content to 1.5 and 2 at.%, the shift in first and second broad maxima are more steep, i.e., $2\theta_1$ = 51.52°, 51.34° and $2\theta_2$ = 93.7°, 93.6°, respectively. As discussed earlier in section 3.2.1, this shift in the first and second broad maxima to smaller 2θ values with varying slopes for different at.% addition of Cu and Ga, indicates that complex rearrangements are happening at atomic levels. Therefore, it is expected that the Cu and Ga added glasses behave different compared to Cu and Ga free glass.

4.3 Characterization behavior, Thermal studies

The influence of the alloy additions on the GFA and thermal stability can be evaluated from the calorimetric measurements. Fig. 4.3 (a) and (b) depicts the DSC traces of the $[\text{FeMoPCBSi}]_{100-x}$ $(\text{Cu})_x$ (x = 0, 0.5 and 1) and $[\text{FeMoPCBSi}]_{100-y}$ $(\text{Ga})_y$ (y =0, 0.5, 1, 1.5 and 2) glassy rods, respectively. The DSC traces are measured at 20 K/min for bulk glassy 2 mm and 1.5 mm diameter samples depending up on the compositions. For all compositions the DSC traces clearly show the glass transition event, followed by the supercooled liquid region (SLR) and crystallization. The temperatures T_g, T_x, T_p and T_{liq} which are marked in the DSC curves are the glass transition temperature, the crystallization temperature, the crystallization peak temperatures and the liquidus temperature, respectively. All these characteristic temperatures (T_g, T_x, T_p and T_{liq}) were measured as the onset of the corresponding events using the two-tangent method. The values for T_g, T_x, T_p and T_{liq} as a function of composition of the as-cast samples, measured at the same heating rate of 20 K/min, are given in the Table 4.1. Using these values the extension of the SLR ΔT_x ($\Delta T_x = T_x - T_g$), the reduced glass transition temperatures T_{rg} ($T_{rg} = T_g/T_{liq}$) [13] and the dimensionless parameter γ ($\gamma = Tx/(T_g+T_{liq})$), proposed by Lu *et al.*[64, 65] to predict the GFA were also calculated.
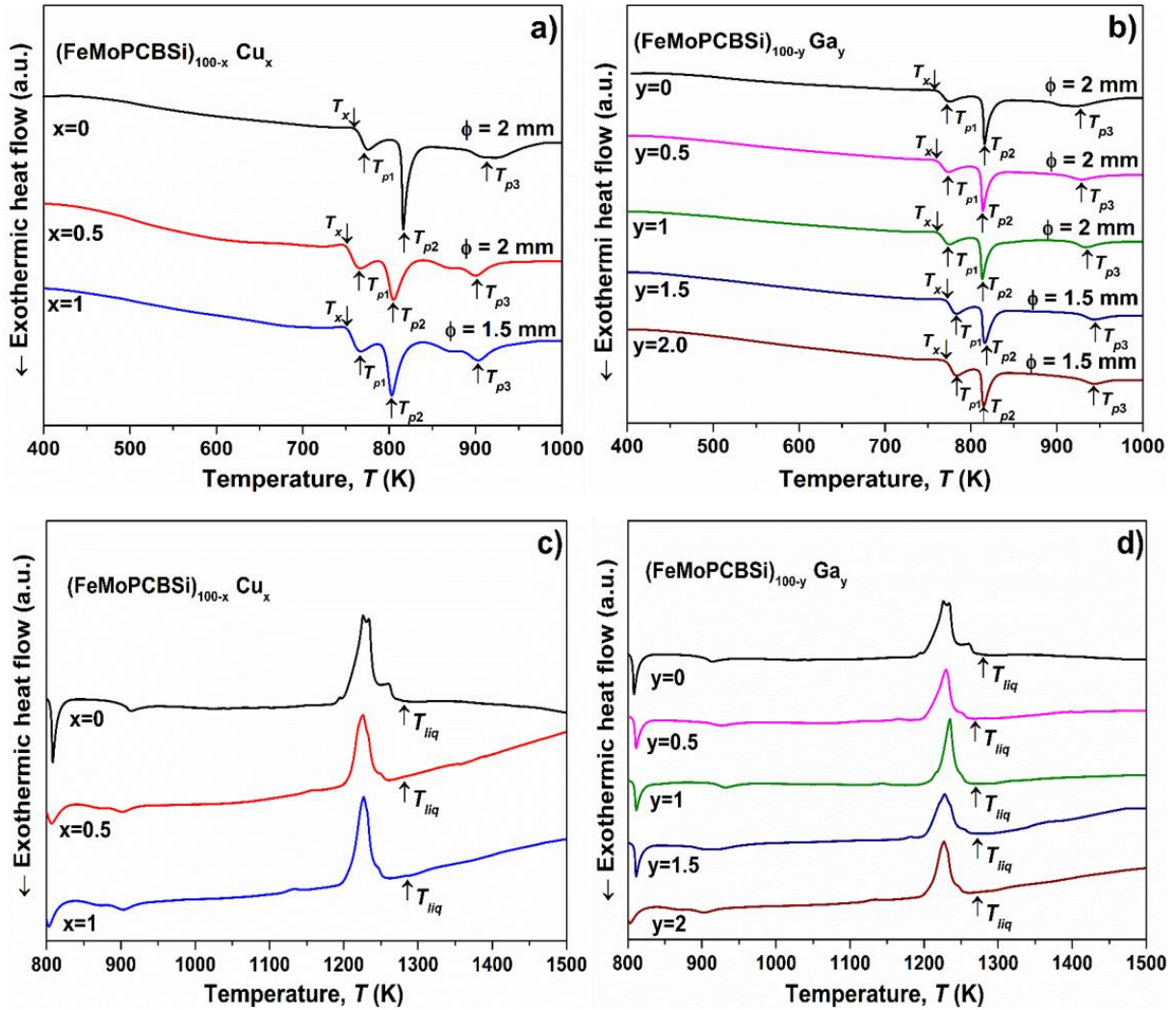
Figure 4.3: DSC traces for the as-cast (a) $[Fe_{74}Mo_4P_{10}C_{7.5}B_{2.5}Si_2]_{100-x}$ $(Cu)_x$ (x = 0, 0.5 and 1), (b) $[Fe_{74}Mo_4P_{10}C_{7.5}B_{2.5}Si_2]_{100-y}$ Ga_y (y = 0, 0.5, 1, 1.5 and 2) glassy rods and melting behavior of (c) $[Fe_{74}Mo_4P_{10}C_{7.5}B_{2.5}Si_2]_{100-x}$ $(Cu)_x$ (x = 0, 0.5 and 1), (d) $[Fe_{74}Mo_4P_{10}C_{7.5}B_{2.5}Si_2]_{100-y}$ Ga_y (y = 0, 0.5, 1, 1.5 and 2) glassy rods. All measurements are recorded at a heating rate of 20 K/min.

From the DSC trace (Fig 4.3 (a)) it is evident that FeMoPCBSi glass shows three distinct crystallization events at 777 K (T_{p1}), 815 K (T_{p2}) and 918 K (T_{p3}), respectively. Unlike the FeCoBSiNb glass (see Fig. 3.3 (a)) the addition of Cu does not alters the crystallization behavior of the FeMoPCBSi glass but lowers all characteristic temperatures such as T_g, T_x, T_{p1}, T_{p2} and T_{p3}. The T_g and T_x of FeMoPCBSi+0.5Cu and FeMoPCBSi+1Cu glasses are 726, 726 K and 757, 756 K, respectively (see Table 4.1).

The variation of ΔT_x and T_{rg} as a function of Cu content is shown in Fig. 4.4 (a). Though the addition of 0.5 and 1 at.% Cu reduces the T_g and T_x by 7 and 10 K, as a result ΔT_x reduces to 31 and 29, respectively. The T_{rg} and γ values for both alloys decreases to 0.56 and 0.376, which also indicates the decrease in GFA of the alloys. The critical diameter (t_c) of the FeMoPCBSi+0.5Cu and FeMoPCBSi+1Cu glasses are 2.5 and 1.5 mm, respectively. Fig. 4.3 (c) depicts the melting behavior of the Cu added glasses in comparison with the base FeMoPCBSi glass, no visible change in the melting behavior was observed for both the alloys.

Table 4.1: Glass transition temperatures (T_g), onsets (T_x) crystallization peak temperatures (T_{p1}, T_{p2} and T_{p3}) and liquidus temperatures (T_{liq}), as well as reduced glass transition temperatures T_{rg} ($T_{rg} = T_g/T_{liq}$), parameter γ ($\gamma = Tx/(T_g+T_{liq})$) and extension of the supercooled liquid region ΔT_x ($\Delta T_x = T_x-T_g$) for [Fe$_{74}$Mo$_4$P$_{10}$C$_{7.5}$B$_{2.5}$Si$_2$]$_{100-x, y}$ (Cu)$_x$ (Ga)$_y$ (x = 0, 0.5, 1)(y = 0, 0.5, 1, 1.5 and 2) glassy alloys measured at 20 K/min heating rate. The accuracy of the experimental data lies within ± 2 K. The literature data for Fe$_{74}$Mo$_4$P$_{10}$C$_{7.5}$B$_{2.5}$Si$_2$ [89] glass is given for reference purpose.

Composition	Rod ϕ (mm)	T_g (K)	T_x (K)	T_{p1} (K)	T_{p2} (K)	T_{p3} (K)	T_{liq} (K)	T_{rg}	γ	ΔT_x (K)
FeMoPCBSi [89]	5	729	766	-	-	-	1266	0.58	0.380	37
FeMoPCBSi	2	733	768	777	815	918	1283	0.57	0.381	35
FeMoPCBSi+0.5Cu	2	726	757	773	807	900	1283	0.56	0.376	31
FeMoPCBSi+1Cu	1.5	726	756	770	804	900	1283	0.56	0.376	29
FeMoPCBSi+0.5Ga	2	733	768	778	814	928	1283	0.57	0.381	35
FeMoPCBSi+1Ga	2	734	770	779	814	934	1283	0.57	0.381	36
FeMoPCBSi+1.5Ga	1.5	736	771	784	818	943	1270	0.58	0.384	36
FeMoPCBSi+2Ga	1.5	736	773	784	815	945	1270	0.58	0.385	37

Similar to FeCoBSiNb glass, the addition of Ga up to 2 at.% increases all characteristic temperatures such as T_g, T_x, T_{p1}, T_{p2} and T_{p3}. The T_g and T_x of FeMoPCBSi+0.5Ga, FeMoPCBSi+1Ga, FeMoPCBSi+1.5Ga and FeMoPCBSi+2Ga glasses are 733, 734, 736, 736 K and 768, 770, 771, 773 K respectively. For the addition of 0.5 and 1 at.% Ga T_g, T_x, ΔT_x, T_{rg} and γ remains almost the same as the base FeMoPCBSi glass, also the GFA remains the same .i.e., for both FeMoPCBSi+0.5Ga and FeMoPCBSi+1Ga glasses t_c = 3 mm. For the 1.5 and 2 at.% Ga added glass T_x increases to 771, 773 K, respectively, leading to increase in ΔT_x, T_{rg} and γ values. Fig. 4.4 (b) depicts the variation of ΔT_x and T_{rg} as a function of Ga content. Though the addition of Ga increases the ΔT_x and T_{rg} values gradually and reaches a maximum of 0.58 and 0.385, respectively, for 2 at.% Ga added alloy the GFA decreases drastically. The t_c for both FeMoPCBSi+1.5Ga and FeMoPCBSi+2Ga glasses reduced to 1.5 mm. The melting behavior of the Ga- added alloys is shown in Fig. 4.4 (d). Up to 1 at.% Ga the melting behavior and liquidus temperature (T_{liq}) remains the same. For the alloys having 1.5 and 2 at.% Ga T_{liq} decreases to 1270 K, but the melting behavior remains almost same as in the case of the parent FeMoPCBSi alloy.
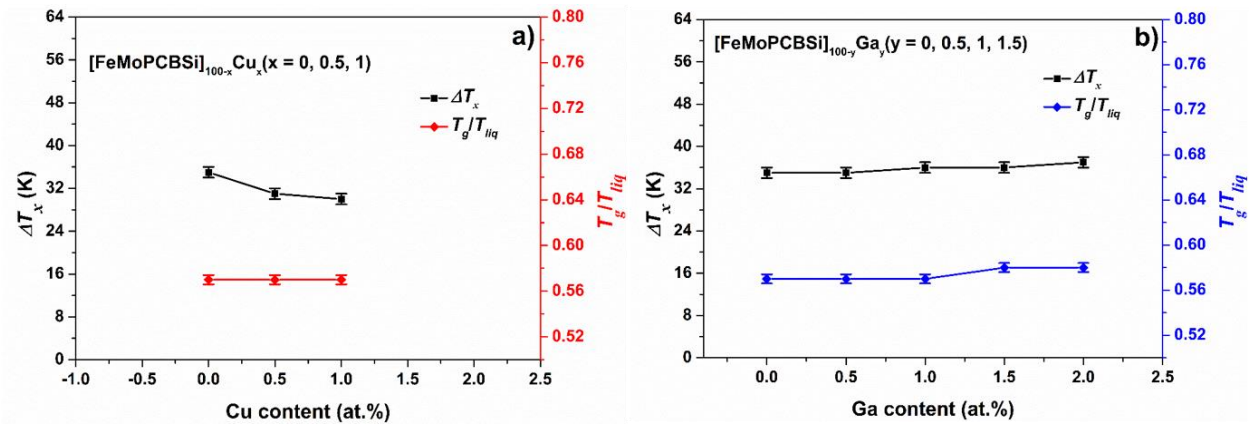
Figure 4.4: Extension of the supercooled liquid region ΔT_x and the reduced glass transition temperature T_{rg} as a function of (a) Cu content (at.%) (b) Ga content (at.%).

Fig. 4.5 (a), (b) and (c) show the DSC traces measured at different heating rates of 5, 10, 15 and 20 K/min for the FeMoPCBSi, FeMoPCBSi+0.5Cu and FeMoPCBSi+0.5Ga glasses, respectively. Regardless the heating rate, all curves clearly exhibit a distinct T_g and a SLR followed by crystallization. From the DSC curves it is evident that all the characteristic temperatures (T_g, T_x and T_p) shift to higher values with increasing heating rate (as shown in Table4.2).
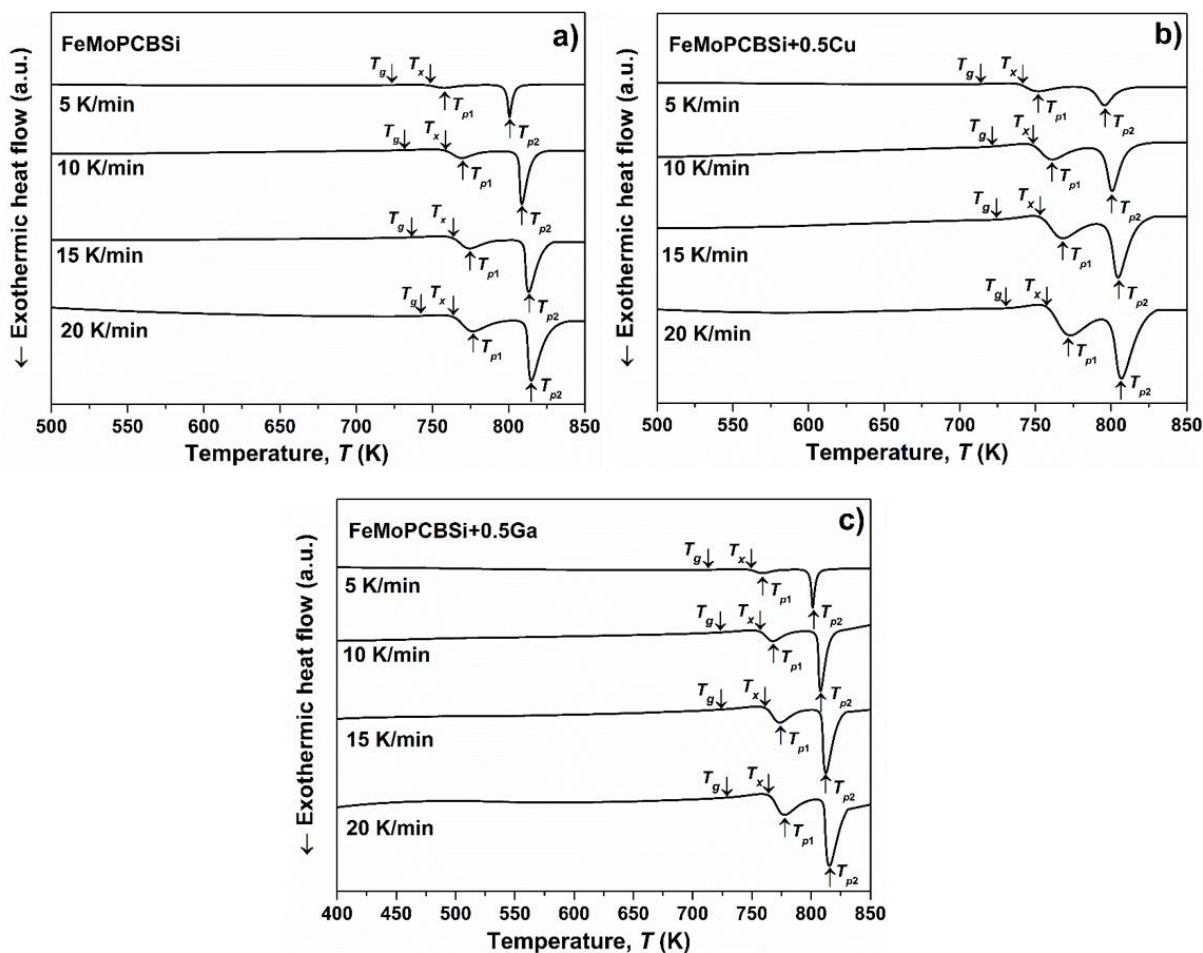
Figure 4.5: Isochronal DSC curves recorder at different heating rates for (a) $Fe_{74}Mo_4P_{10}C_{7.5}B_{2.5}Si_2$ (b) $[Fe_{74}Mo_4P_{10}C_{7.5}B_{2.5}Si_2]_{99.5}Cu_{0.5}$ and (c) $[Fe_{74}Mo_4P_{10}C_{7.5}B_{2.5}Si_2]_{99.5}Ga_{0.5}$ glassy samples.

The apparent activation energy required for the crystallization was calculated using the Kissinger method as described in the section 3.3 (paragraph 5). Fig. 4.6 presents the Kissinger plot calculated with the data presented in the Table 4.2.

Table 4.2: Glass transition temperatures (T_g), onsets (T_x) crystallization peak temperatures (T_{p1}) for $Fe_{74}Mo_4P_{10}C_{7.5}B_{2.5}Si_2$, $[Fe_{74}Mo_4P_{10}C_{7.5}B_{2.5}Si_2]_{99.5}Cu_{0.5}$ and $[Fe_{74}Mo_4P_{10}C_{7.5}B_{2.5}Si_2]_{99.5}Ga_{0.5}$ glasses measured at 5, 10, 15 and 20 K/min. The accuracy of the experimental data lies within ± 2 K.

Compositions		5 K/min	10 K/min	15 K/min	20 K/min
FeMoPCBSi	T_g (K)	713	725	730	733
	T_x (K)	745	757	763	768
	ΔT_x (K)	32	32	32	35
	T_{p1} (K)	757	769	774	777
FeMoPCBSi+0.5Cu	T_g (K)	710	721	726	726
	T_x (K)	738	749	754	757
	ΔT_x (K)	28	28	28	31
	T_{p1} (K)	752	761	768	773
FeMoPCBSi+0.5Ga	T_g (K)	713	722	727	733
	T_x (K)	749	758	763	768
	ΔT_x (K)	36	36	34	35
	T_{p1} (K)	759	768	773	778

The good linear dependence of the measured data indicates the good reproducibility. The crystallization activation energy E_c for FeMoPCBSi, FeMoPCBSi+0.5Cu and FeMoPCBSi+0.5Ga glasses are $E_c = 320 \pm 8$, 276 ± 8 and 341 ± 8 kJ/mol, respectively. The activation energy required for crystallization of this glass is almost half of the FeCoBSiNb glass and almost comparable to the good Zr- based glass formers [62]. Similar to the FeCoBSiNb glass the addition of Cu reduces the activation energy required for crystallization. However, addition of 0.5 at.% Ga increases the crystallization activation energy. This increase in value of E_c indicates the Ga addition improves the thermal stability against the crystallization.
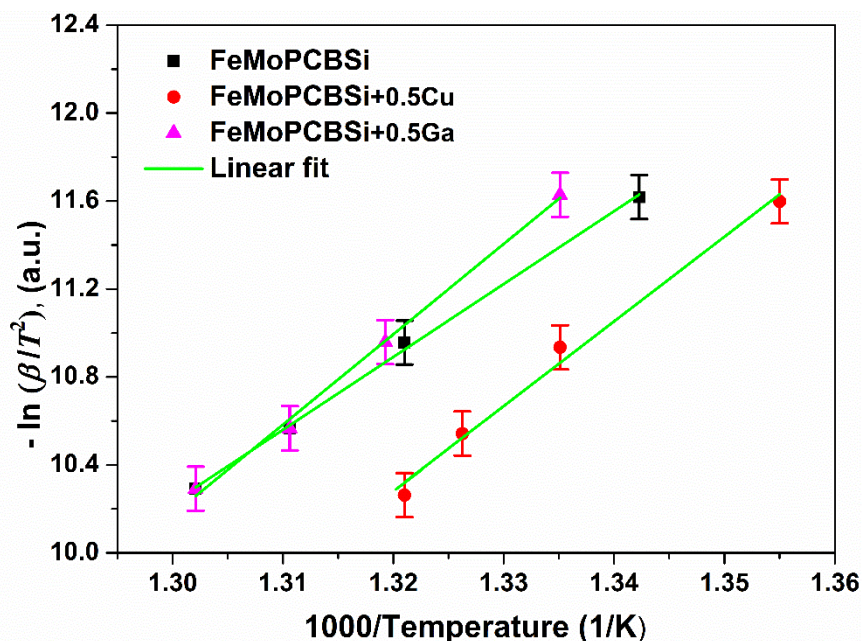
Figure 4.6: Kissinger plot for the calculation of activation energies required by crystallization event in $Fe_{74}Mo_4P_{10}C_{7.5}B_{2.5}Si_2$, $[Fe_{74}Mo_4P_{10}C_{7.5}B_{2.5}Si_2]_{99.5}Cu_{0.5}$ and $[Fe_{74}Mo_4P_{10}C_{7.5}B_{2.5}Si_2]_{99.5}Ga_{0.5}$ glasses.

4.4 Characterization behavior, X-ray diffraction studies

The structure evolution of the $[FeMoPCBSi]_{100-x,y}$ (Cu_x, Ga_y)(x = 0, 0.5 and 1)(y = 0.5, 1, 1.5 and 2) glasses upon on annealing was studied using XRD. The investigated samples were prepared from the as-cast rods. The samples were annealed for 5 min at different characteristic temperatures $(T_x$ and $T_p)$ (see Fig. 4.3 (a), (b) and (c)) using same NETZSCH DSC 404 C under argon atmosphere. The heating and cooling were performed under constant heating and cooling rates of 20 K/min. Fig. 4.7 (a) depicts the structural evaluation of FeMoPCBSi glass from room temperature to 1173 K.

The as-cast FeMoPCBSi sample (ϕ = 3mm) is completely amorphous and it remains completely amorphous even after annealing up to 763 K, which is 5 K below the onset of crystallization temperature T_x (.i.e., T_x -5 K). The crystallization starts as soon as the sample reaches T_x (.i.e. 768 K). The sample heated to 778 K, which is 10 K above T_x (.i.e., T_x +10 K), shows the presence of complex $Fe_{23}(B,C)_6$-type phase. At the end of first crystallization event only $Fe_{23}(B,C)_6$-type phase is observed along with the amorphous matrix.
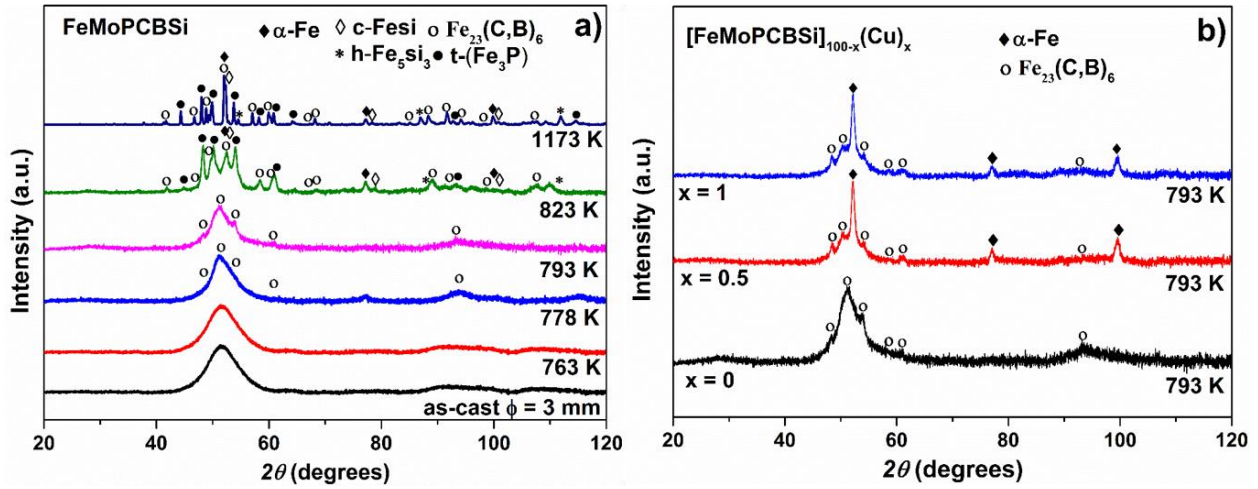
Figure 4.7: XRD patterns for (a) $Fe_{74}Mo_4P_{10}C_{7.5}B_{2.5}Si_2$ annealed up to the characteristic temperatures and (b) $[Fe_{74}Mo_4P_{10}C_{7.5}B_{2.5}Si_2]_{100-x}$ (Cu_x)(x = 0, 0.5 and 1)glasses annealed up to the end of first crystallization event.

During the second crystallization event, the $Fe_{23}(B,C)_6$-type phase starts to grow and several new phases form from the remaining amorphous matrix. The XRD pattern of the sample heated until the end of second crystallization event, i.e. 823 K, shows the formation of tetragonal Fe_3P, hexagonal Fe_5Si_3, cubic FeSi and α-Fe phases. Even at 823 K the first broad peak is still present, which indicates some amorphous phase is not yet transformed. Close to the melting point, at 1173 K, the glassy sample completely turns in to crystalline material. The most probable crystalline sequence of this FeMoPCBSi glass is as follow: Amorphous→ $Fe_{23}(B,C)_6$-type + residual amorphous → $Fe_{23}(B,C)_6$-type + t-(Fe_3P) + h-Fe_5Si_3 + c-FeSi + α-Fe + residual amorphous $Fe_{23}(B,C)_6$-type + t-(Fe_3P) + h-Fe_5Si_3 + c-FeSi + α-Fe. Compared to the FeCoBSiNb samples, which forms only one crystalline phase upon heating, i.e. the $Fe_{23}B_6$-type phase, the FeMoPCBSi alloy forms several different phases upon heating. This is not unusual and the concurrence of different crystalline phases in fact enhances the GFA. The formation of several types of crystalline phases requires high atomic mobility, the atoms should diffuse upon long distances there. Therefore higher temperatures are necessary to activate the diffusion process. As a result, the amorphous phase has enhanced thermal stability against crystallization and so higher GFA [3].

The structural evaluation of FeMoPCBSi+0.5Cu and FeMoPCBSi+1Cu glasses are shown in Fig. 4.7 (b). As it can be observed from the DSC curve (see Fig. 4.3 (a)), the addition of Cu decreases

the crystallization temperatures. After heating FeMoPCBSi+0.5Cu and FeMoPCBSi+1Cu glasses until the end of first crystallization event, i.e. 793 K, bcc-(Fe) phase start to form along with the $Fe_{23}(B,C)_6$-type phase. Upon heating to higher temperatures, t-Fe_3P, h-Fe_5S_3i, c-FeSi phases starts to form like in the FeMoPCBSi glass (image is not shown here). However close to melting point, i.e. at 1173 K, the crystalline patterns of both FeMoPCBSi+0.5Cu and FeMoPCBSi+1Cu glasses are almost same as that of the parent FeMoPCBSi alloy. The most probable crystalline sequence of the FeMoPCBSi+Cu glass is as follow: Amorphous→ $Fe_{23}(B,C)_6$-type + α-Fe + residual amorphous → $Fe_{23}(B,C)_6$-type + t-(Fe_3P) + h-Fe_5Si_3 + c-FeSi + α-Fe + residual amorphous $Fe_{23}(B,C)_6$-type + t-(Fe_3P) + h-FeSi + c-FeSi + α-Fe.

Fig. 4.8 shows the XRD patterns of the $[FeMoPCBSi]_{100-y}$ (Ga_y) (y = 0.5, 1, 1.5 and 2) glasses after annealing up to the end of their first crystallization event, i.e. 793 K. Similar to the Cu addition, the Ga addition also promotes the formation of α-Fe along with the $Fe_{23}(B,C)_6$-type phase. From the XRD patterns it is evident that for the small amount of Ga-, i.e. up to 1 at.%, small amount of α-Fe is seen, while in the case of the alloy with 1.5 at.% Ga a larger volume fraction of α-Fe appears at the end of the first crystallization event.
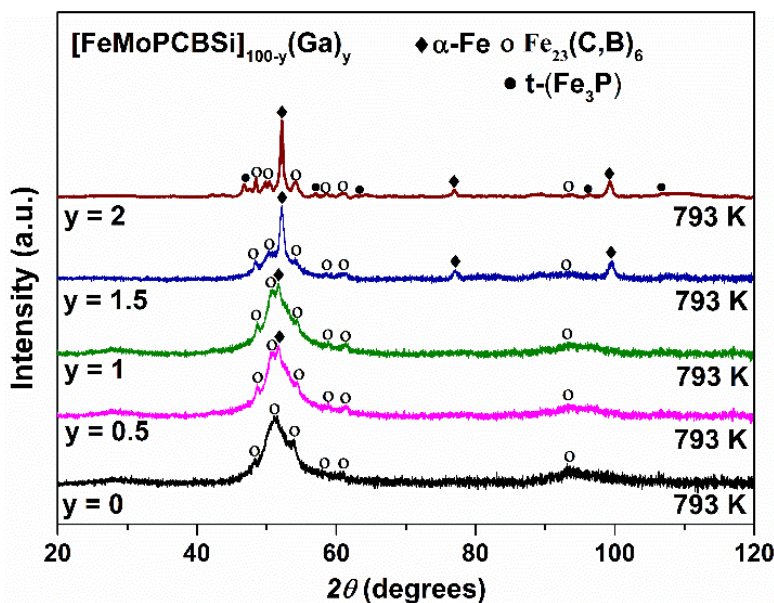
Figure 4.8: XRD patterns for the $[Fe_{74}Mo_4P_{10}C_{7.5}B_{2.5}Si_2]_{100-y}$ Ga_y (y =0, 0.5, 1, 1.5 and 2) glasses annealed up to end of first crystallization event.

The most probable crystallization sequence of the FeMoPCBSi + Ga glass up to 1.5 at.% Ga are as follow: Amorphous→ $Fe_{23}(B,C)_6$-type + α-Fe + residual amorphous → $Fe_{23}(B,C)_6$-type + t-(Fe_3P) + h-Fe_5Si_3 + c-FeSi + α-Fe + residual amorphous $Fe_{23}(B,C)_6$-type + t-(Fe_3P) + h-Fe_5Si_3 + c-FeSi + α-Fe. The addition of 2 at.% Ga promotes the formation of t-(Fe_3P) also along with α-Fe and $Fe_{23}(B,C)_6$-type phase. Up on heating to the higher temperatures t-Fe_3P, h-Fe_5Si_3, c-FeSi phases starts to form like in the FeMoPCBSi glass (image is not shown here). However, close to melting point, .i.e. at 1173 K, the crystalline pattern of all $[FeMoPCBSi]_{100-y}$ (Ga_y) (y = 0.5, 1, 1.5 and 2) glasses are almost same as that of the parent FeMoPCBSi alloy.

4.5 Microstructural studies, STEM and HRTEM investigations

Scanning transmission electron microscopy (STEM) and high resolution transmission electron microscopy (HRTEM) investigations were carried out to investigate the structure of as-cast samples. In order understand the effect of Cu and Ga addition in the FeMoPCBSi system only FeMoPCBSi+0.5Cu and FeMoPCBSi+0.5Ga glassy samples were chosen for studies. The samples were subjected to reflection X-ray diffraction before preparing for the STEM and HRTEM investigations and the samples were found to be amorphous. STEM image of the as-cast FeCoBSiNb+0.5Cu and FeCoBSiNb+0.5Ga glassy samples are shown in Fig. 4.9 (a) and (b). From the STEM image it is evident that faint clusters are observed in both 0.5 at.% Cu and 0.5 at.% Ga added glasses, which is similar to the clusters observed in the FeCoBSiNb+0.5Ga glass.
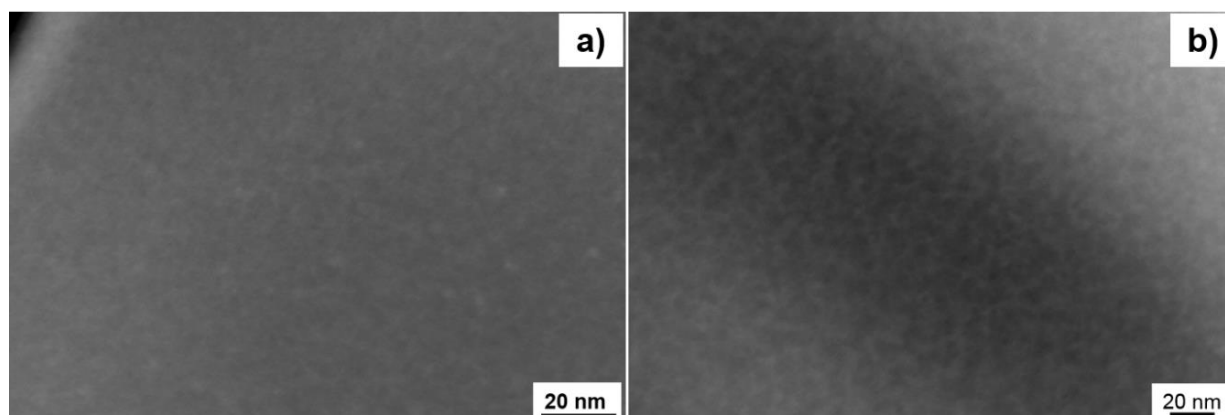
Figure 4.9: (a) STEM image of the as-cast (a) $[Fe_{74}Mo_4P_{10}C_{7.5}B_{2.5}Si_2]_{99.5}Cu_{0.5}$ and (b) $[Fe_{74}Mo_4P_{10}C_{7.5}B_{2.5}Si_2]_{99.5}Ga_{0.5}$ glassy samples.

In order to have a deeper understanding, bright field HRTEM observations were performed on as-cast FeMoPCBSi+0.5Cu and FeMoPCBSi+0.5Ga glassy samples and the micrographs are presented in Fig. 4.10 (a) and (b), respectively. Their corresponding fast Fourier transformed (FFT) images are shown as inserts.
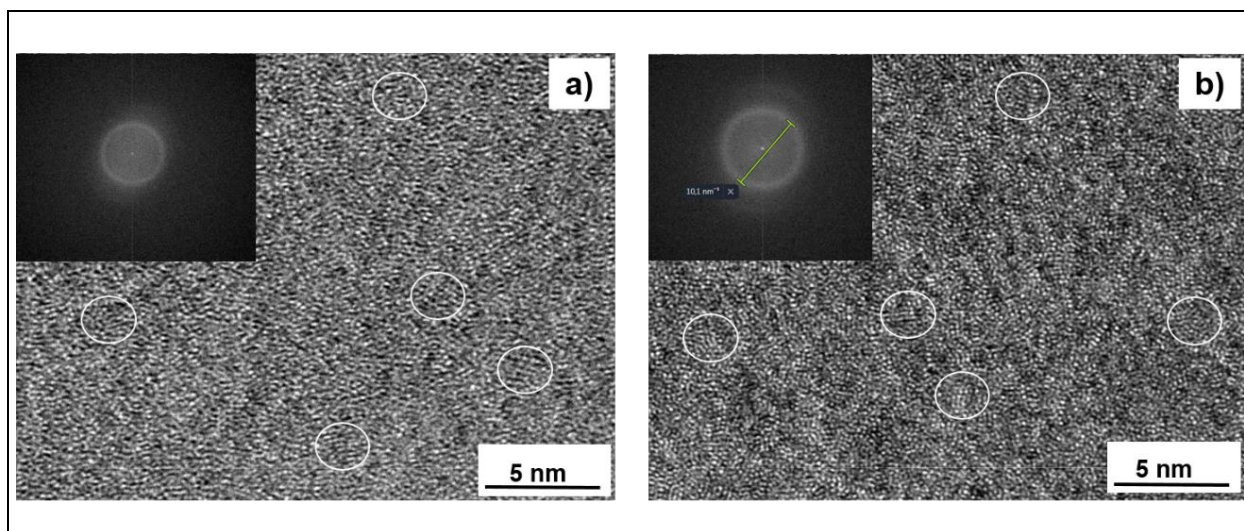
Figure 4.10: Bright field HRTEM image of the as-cast (a) $[Fe_{74}Mo_4P_{10}C_{7.5}B_{2.5}Si_2]_{99.5}Cu_{0.5}$ and (b) $[Fe_{74}Mo_4P_{10}C_{7.5}B_{2.5}Si_2]_{99.5}Ga_{0.5}$ glasses. Insert shows the fast Fourier transformed (FFT) image. Some features of local ordering are observed, which are marked in by the white circles.

Both Cu- and Ga- added glasses show features suggesting local ordering, which are marked with white circles in Fig. 4.10 (a) and (b). The mixing enthalpies of Fe-Cu, Mo-Cu, P-Cu, C-Cu, B-Cu, and Si-Cu are 13, 19, -9, 57, 15 and -2 kJ/mole, respectively [210]. Similar to the FeCoBSiNb system, the repulsive enthalpies of mixing in FeMoPCBSi glass also influence the local chemical heterogeneity, leading to ordered zones. Compared to the Cu- added glass the ordered zones are more frequently observed in the Ga- added glass. The mixing enthalpies of Fe-Ga, Mo-Ga, P-Ga, C-Ga, B-Ga and Si-Ga are -2, 7, -10, 57, 21 and 0 kJ/mole, respectively [210]. Compared to the Cu atoms the mixing enthalpies of the Ga are better but still they are weak. If this ordered zones/clusters were similar to those observed in the Cu added glass, then we expect that they act as a nuclei for the formation of crystals of α-Fe up on annealing. Instead, we observe that the annealing of the FeCoBSiNb+0.5Ga glass leads to formation of very small α-Fe precipitates and large quantity of $(Fe,Co)_{23}B_6$. From this it is to conclude that the ordering/clustering in the Cu-added and Ga- added glasses are different.
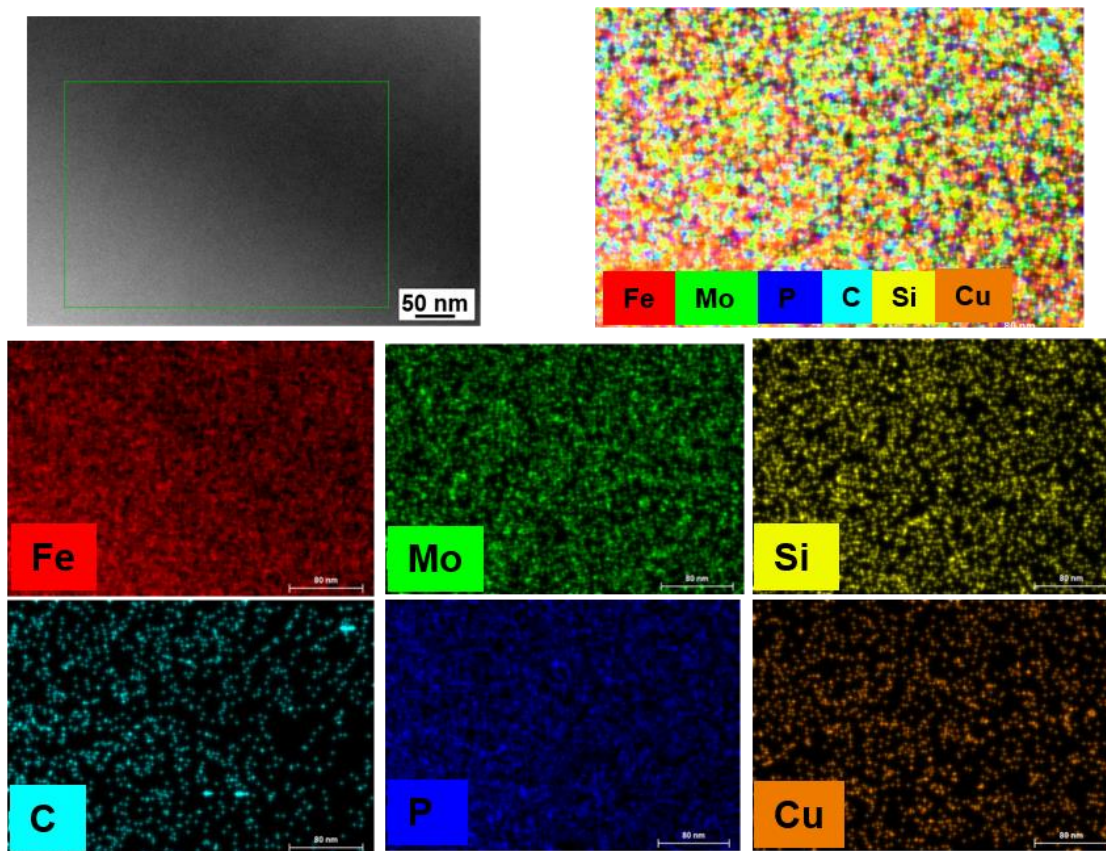
Figure 4.11: EDX mapping for the as-cast $[Fe_{74}Mo_4P_{10}C_{7.5}B_{2.5}Si_2]_{99.5}Cu_{0.5}$ glass

To determine the cluster type, energy-dispersive X-ray spectroscopy (EDX) mapping was done for both Cu- and Ga- added samples, and the corresponding maps are shown in Figs. 4.11 and 4.12, respectively. In Cu- added samples no Cu clusters were observed from the EDX mapping, while in the case of Ga- added glass also faint cluster behavior of the Ga atoms are observed (see Fig. 4.12.). For the same atomic percentage addition of Cu and Ga, Ga- atoms are showing higher tendency to form ordered zones/clusters as compared to Cu atoms, in perfect agreement to the HRTEM results.
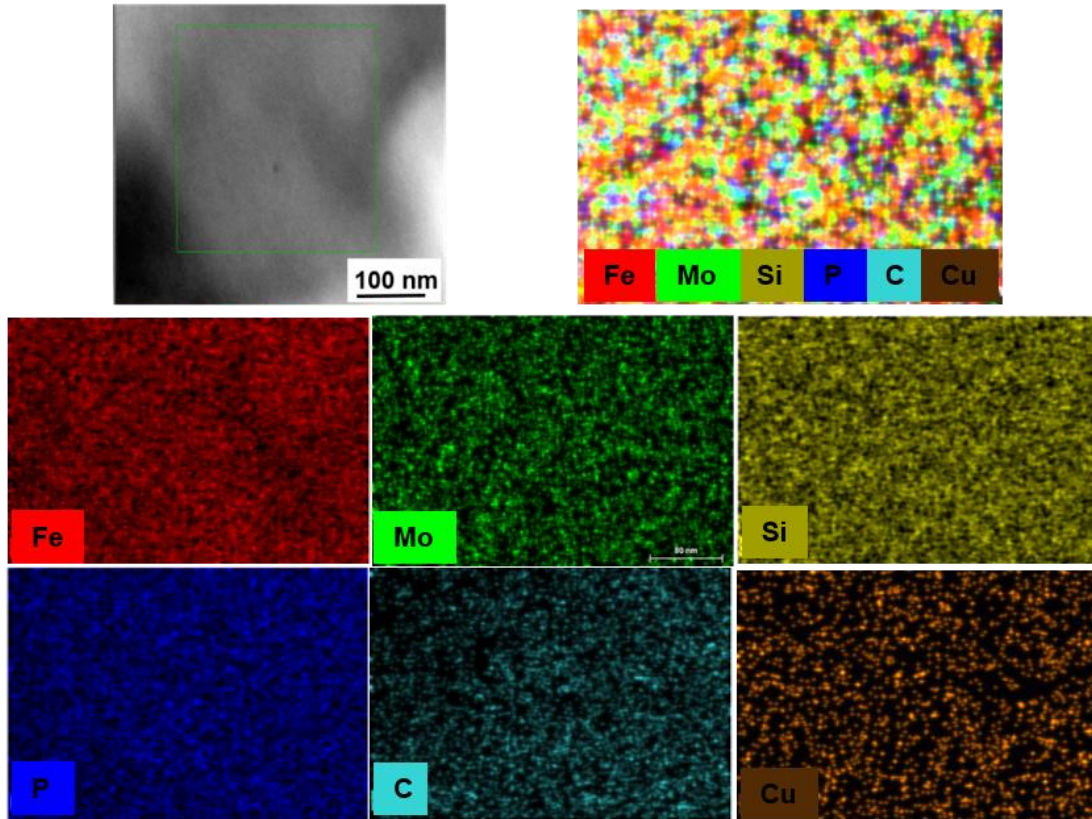
Figure 4.12: EDX mapping for the as-cast $[Fe_{74}Mo_4P_{10}C_{7.5}B_{2.5}Si_2]_{99.5}Ga_{0.5}$ glass

4.6 Magnetic properties of $[Fe_{74}Mo_4P_{10}C_{7.5}B_{2.5}Si_2]_{100-x, y}$ (Cu_x, Ga_y) (x = 0, 0.5 and 1) (y = 0.5, 1, 1.5 and 2) glasses

The FeMoPCBSi glass is well known for its soft magnetic properties such as low coercivity (H_c) ≈ 1.7 A/m, saturation magnetization (M_s) ≈ 1.34T, and AC permeability (μ_{AC}) $\approx 27,000$ [89]. To understand the effect of Cu and Ga addition on the FeMoPCBSi alloy some of the magnetic properties were studied.

4.6.1 Coercivity measurements

The coercivity values for the as-cast glassy samples of different compositions are listed in Table 4.3. In order to avoid the effects due to the sample geometry, all coercivity measurements were

done for cylindrical samples having the diameter to length ratio of 1:20. The coercivity values of the FeMoPCBSi, FeMoPCBSi+0.5Cu, FeMoPCBSi+0.5Ga, FeCoBSiNb+1Ga glasses are almost same, and gradually increases with increase in Cu and Ga at.%. The increase in H_c with increase in Cu and Ga.% could be due to formation of large numbers of short or medium range ordered zones (Figs. 4.10 and 4.11). The coercivity values of the 3 mm diameter rods are slightly higher compared to the 1.5 and 2 mm rods, this could be mainly due to geometry of the sample used for measurement or presence of few nuclei/clusters. The coercivity of all glasses in as-cast state are less than 6 A/m, indicating the absence of large nuclei/clusters [87, 211].

The variation of coercivity as a function of annealing temperature for FeMoPCBSi, FeMoPCBSi+0.5Cu and FeMoPCBSi+0.5Ga glasses are shown in Fig. 4.13. The samples were annealed for 1 min at different temperatures such as T_g, T_x-5, end of first crystallization event, end of second crystallization and end of second crystallization + 20 K (see Fig. 4.3 (a) and (b)) using the same NETZSCH DSC 404 C calorimeter under argon atmosphere. The heating and cooling were performed under constant heating and cooling rates of 20 K/min. Due to the limited size of the DSC crucibles, cylindrical samples having the diameter to length ratio 1:2 (.i.e., 2 mm x 4 mm) were used for this measurements.

Table 4.3: Coercivity values for the as-cast $[Fe_{74}Mo_4P_{10}C_{7.5}B_{2.5}Si_2]_{100-x, y}$ $(Cu)_x$ $(Ga)_y$ (x = 0, 0.5, 1)(y = 0, 0.5, 1, 1.5 and 2) glassy samples. The accuracy of the experimental data lies within ± 0.1A/m.

Composition	Rod φ (mm)	H_c (A/m)	Composition	Rod φ (mm)	H_c (A/m)
FeMoPCBSi	1.5	2	FeMoPCBSi+0.5Ga	1.5	2
	2	3		2	2
	3	5		3	6
FeMoPCBSi+0.5Cu	1.5	4	FeMoPCBSi+1Ga	1.5	2
	2	4.5		2	2.5
FeMoPCBSi +1Cu	1.5	4.5	FeMoPCBSi+1.5Ga	1.5	4
			FeMoPCBSi+2Ga	1.5	4

As mentioned earlier in section 3.6.1, in order to avoid the effect of demagnetizing factor the H_c of the annealed samples (H_c-annealed) are normalized with the H_c of the as-cast sample (H_c-as-cast). All the normalized coercivity data measured for these samples after annealing at different temperatures are shown in Table 4.4. Similar, to FeCoBSiNb glass the H_c values remains almost constant for all glasses even they were annealed up to their respective T_g, and attains a minimum value close to their crystallization start temperature (.i.e., $\approx$ 5 K). As discussed in the section 3.6.1, this initial decrease in coercivity close to the crystallization temperature may be due to stress relaxation and a decreasing density of quasi-dislocation dipole-type (QDD) defects pinning the magnetic domain walls in the amorphous phase [215].

Upon further annealing the samples until the end of their first crystallization event (i.e. 798, 785 and 798 K) the H_c increases to 6.4, 6.2 and 6.4 times the initial value for FeMoPCBSi, FeMoPCBSi+0.5Cu and FeMoPCBSi+0.5Ga glasses, respectively. The increase in H_c of the samples beyond their T_x can be attributed to the formation of $Fe_{23}(B,C)_6$-type crystals in their glassy matrix (see fig. 4.7 and 4.8). The coercivity starts to increase drastically when the samples were annealed above their first crystallization event, at the end of second crystallization event, the H_c increases to 63, 62 and 62 times the initial value for FeMoPCBSi, FeMoPCBSi+0.5Cu and FeMoPCBSi+0.5Ga glasses, respectively.
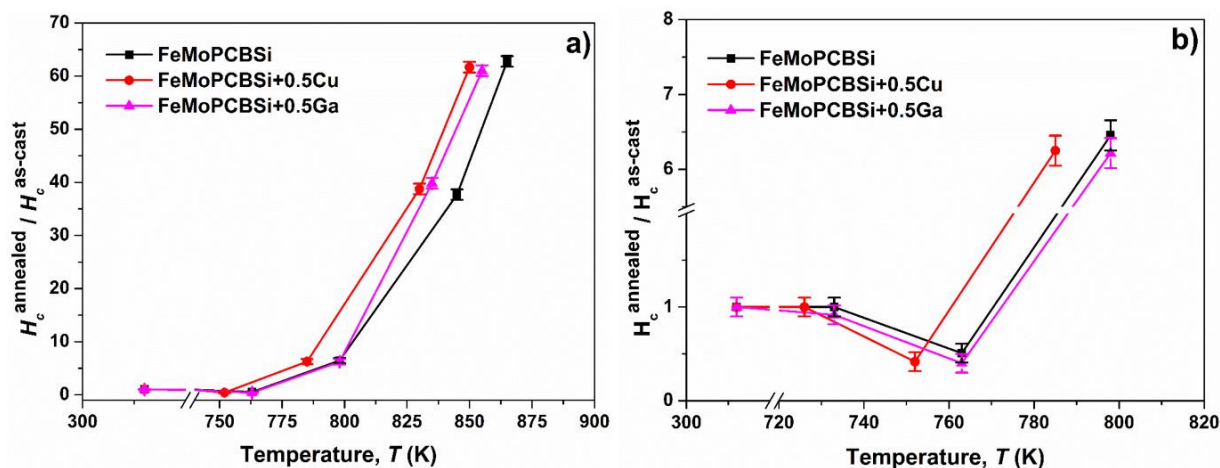
Figure 4.13: (a) The variation of H_c-annealed / H_c-as-cast as a function of annealing temperature for $Fe_{74}Mo_4P_{10}C_{7.5}B_{2.5}Si_2$, $[Fe_{74}Mo_4P_{10}C_{7.5}B_{2.5}Si_2]_{99.5}Cu_{0.5}$ and $[Fe_{74}Mo_4P_{10}C_{7.5}B_{2.5}Si_2]_{99.5}Ga_{0.5}$ glasses. Annealing was done different temperatures such as T_g, T_x-5, T_x, end of first crystallization (798 K), end of second crystallization (845 K) and end of second crystallization + 20 K for each of these alloys and (b) variation of H_c-annealed / H_c-as-cast from room temperature till end of first crystallization event.

Interestingly, the coercivity values of the Cu- added and Ga- added samples are slightly lower compared to the base FeMoPCBSi sample, this may be due to the formation of α-Fe, which is magnetically soft compared to the $Fe_{23}(B,C)_6$-type phase.

Table 4.4: Coercivity values for the $Fe_{74}Mo_4P_{10}C_{7.5}B_{2.5}Si_2$, $[Fe_{74}Mo_4P_{10}C_{7.5}B_{2.5}Si_2]_{99.5}Cu_{0.5}$ and $[Fe_{74}Mo_4P_{10}C_{7.5}B_{2.5}Si_2]_{99.5}Ga_{0.5}$ glasses in the as-cast state and after annealed to different temperatures. The accuracy of the experimental data lies within $\pm$ 0.1A/m.

FeMoPCBSi	Temperature (K)	303	733	763	798	845	865
	H_c-annealed / H_c-as-cast	1	1	0.5	6.4	38	63
FeMoPCBSi+0.5Cu	Temperature (K)	303	726	752	785	830	850
	H_c-annealed / H_c-as-cast	1	1	0.4	6.2	39	62
FeMoPCBSi+0.5Ga	Temperature (K)	303	733	763	798	835	855
	H_c-annealed / H_c-as-cast	1	1	0.4	6.2	40	62

4.6.2 Magnetization measurements

The saturation magnetization (M_s) of the glassy samples were measured using vibrating sample magnetometer (VSM). For all measurements the sample geometry were kept constant, as mentioned in section 3.6.2. Fig. 4.14 (a) and (b) shows the typical room temperature DC hysteresis loops recorded with VSM for the Cu- and Ga- added as-cast glassy samples. The insets in both figures show the behavior of the samples close their saturation region. From the hysteresis loops, it is evident that the saturation occurs at relatively similar magnetic fields for all glasses; also, the addition of 1 at.% Cu decreases the saturation magnetization (M_s) just marginally, from 115 to 113 Am^2/kg (Fig. 4.14 (a)).
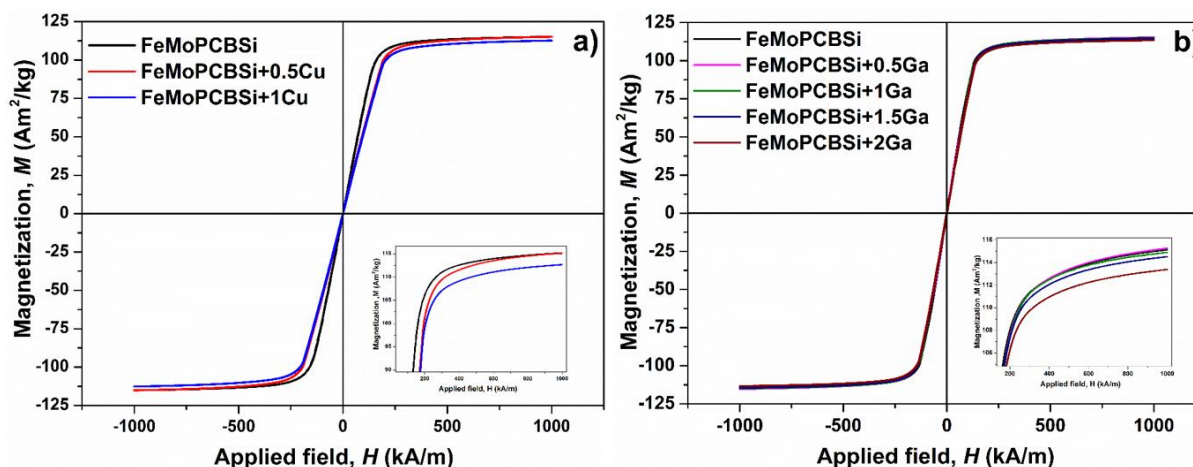
Figure 4.14: Hysteresis loops for the 1 mm diameter as-cast (a) $[Fe_{74}Mo_4P_{10}C_{7.5}B_{2.5}Si_2]_{100-x}$ (Cu_x) (x = 0, 0.5 and 1) (b) $[Fe_{74}Mo_4P_{10}C_{7.5}B_{2.5}Si_2]_{100-y}$ (Ga_y) (y = 0, 0.5, 1, 1.5 and 2) glassy samples. The insets show the behavior close to the saturation region i.e., between 100 and 115 Am^2/kg.

The values of saturation magnetization for all Cu- and Ga- added samples, measured using VSM, are summarized in Table 3.5. In contrast to the Cu additions, the M_s remains constant up to 1 at.% Ga addition, with further increase in Ga content M_s gradually decreases to 114 and 113 Am^2/kg for 1.5 and 2 at.% Ga- added glasses, respectively. As discussed in the beginning (section 3.6), with the addition of Cu and Ga (non-magnetic) the M_s decreases marginally. Fig. 4.15 shows the variation of the M_s function of annealing temperatures for FeMoPCBSi, FeMoPCBSi+0.5Cu and FeMoPCBSi+0.5Ga samples. The M_s of all alloys increases after heat treatment, particularly above their glass transition temperature T_g. The enhanced magnetic saturation after annealing above their T_g and below their crystallization start temperature can be attributed to the release of stress anisotropies resulting in better soft magnetic properties. The continuous increases in magnetic saturation of the Cu- added alloy up to 865 K can be attributed to the formation of α-Fe crystals with higher saturation magnetization than the amorphous phase. In case of the parent FeMoPCBSi and FeMoPCBSi+G.05Ga added alloys the saturation magnetization increases until the end of the first crystallization even and started to decrease after the second crystallization event. The initial increment can be attributed to the formation of fine $Fe_{23}(B,C)_6$ phase. Upon further annealing the crystals start to grow; also magnetically hard phases like Fe_3P and FeSi form, all together leading to decrease in saturation magnetization.

100
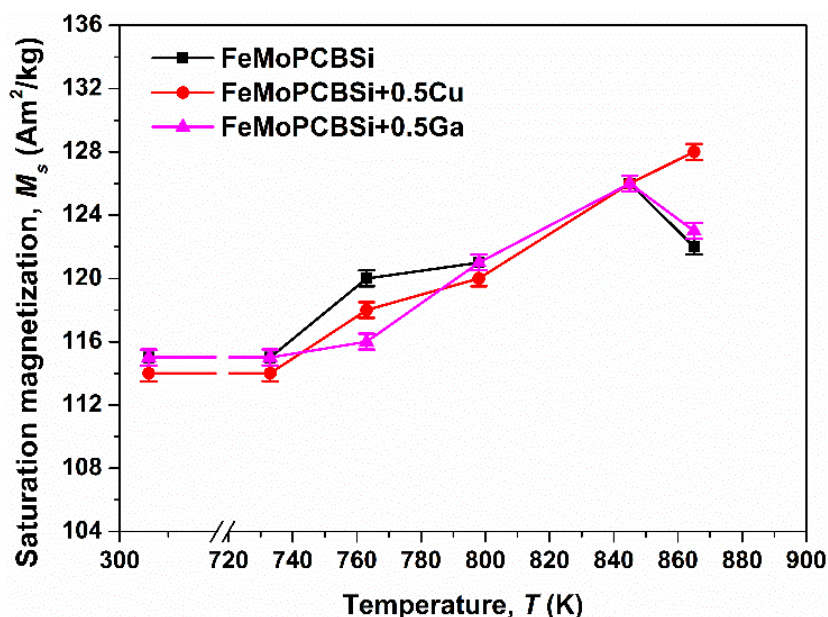
Figure 4.15: Variation of the saturation magnetization (M_s) with different annealed temperatures for $Fe_{74}Mo_4P_{10}C_{7.5}B_{2.5}Si_2$, $[Fe_{74}Mo_4P_{10}C_{7.5}B_{2.5}Si_2]_{99.5}Cu_{0.5}$ and $[Fe_{74}Mo_4P_{10}C_{7.5}B_{2.5}Si_2]_{99.5}Ga_{0.5}$ samples. Annealing was done different characteristic temperatures such as T_g, T_x-5, end of first crystallization event, end of second crystallization event and 20 K above the end of second crystallization event for each of these alloys.

4.6.3 The Curie temperature measurements

The saturation magnetization versus temperature was measured using the same PPMS in high temperature mode. Fig. 4.16 (a) and (c) shows the variation of M_s as a function of temperature for $[FeMoPCBSi]_{100-x}$ (Cu_x) (x = 0, 0.5 and 1) and $[FeMoPCBSi]_{100-y}$ (Ga_y) (y = 0, 0.5, 1, 1.5 and 2) glasses, respectively. The Curie temperature (T_c) was calculated as described in paragraph 2.4.3, the variation of the Curie temperature as a function of Cu and Ga content (at.%) are shown in Fig. 4.16 (b) and (d), respectively and their values are given in Table 4.5.
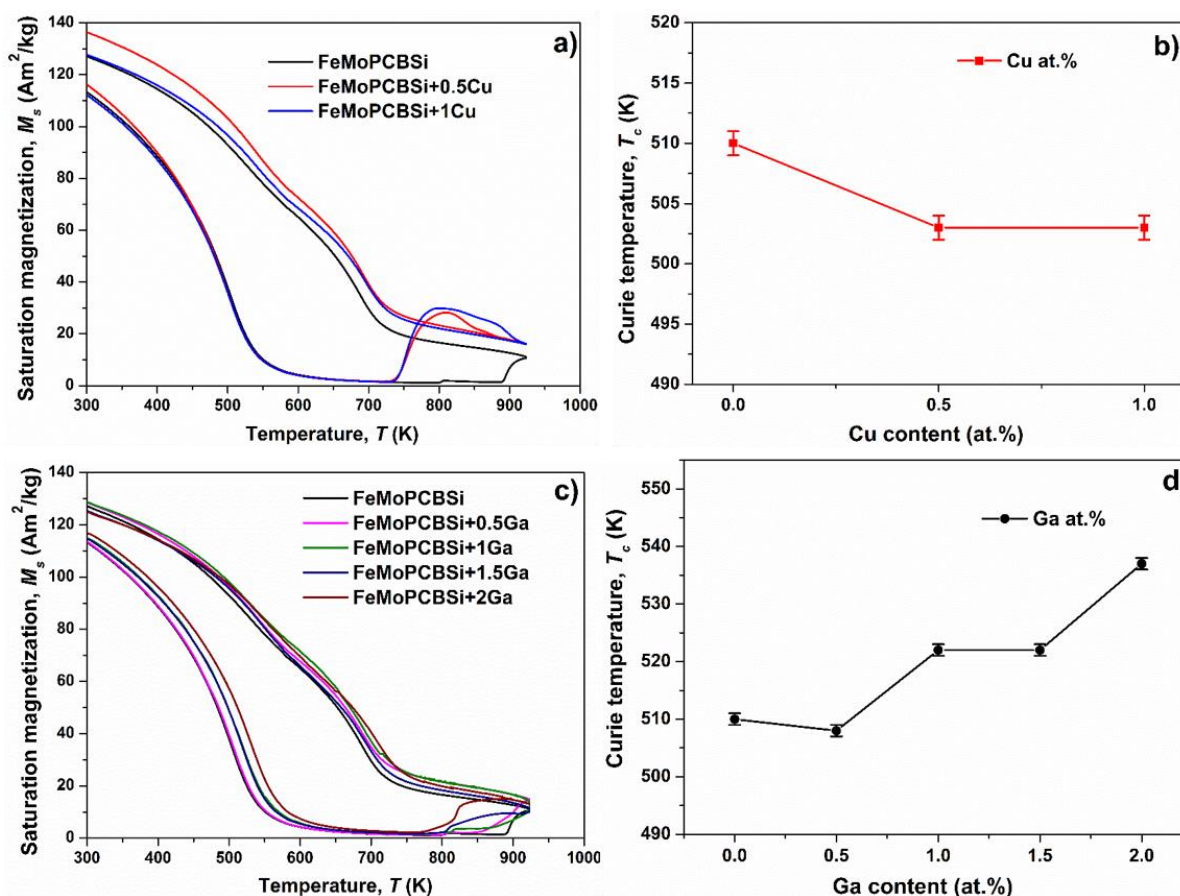
Figure 4.16: Variation of saturation magnetization (M_s) as a function of temperature for (a) $[Fe_{74}Mo_4P_{10}C_{7.5}B_{2.5}Si_2]_{100-x}$ (Cu_x) (x = 0, 0.5 and 1) and (c) $[Fe_{74}Mo_4P_{10}C_{7.5}B_{2.5}Si_2]_{100-y}$ (Ga_y) (y = 0, 0.5, 1, 1.5 and 2) glasses. Variation of Curie temperature as a function of (b) Cu content (at.%) and (d) Ga content (at.%).

The variation of M_s with temperature of the base alloy FeMoPCBSi is different from the FeCoBSiNb alloy, in this glassy sample the M_s increases in multiple steps. At first the M_s remains very low until the end of first crystallization event, implicating the formation of a non-magnetic phase or a phase with lower Curie temperature. In the beginning of second crystallization event (i.e. 800 K) the M_s value slightly increases and remains constant until 880 K and then increases continuously up to 923 K. The first phase forming during first crystallization event is $Fe_{23}(B,C)_6$-type phase, which has a lower Curie temperature. The increases in M_s value after 800 K is due to the formation of bcc-Fe phase (see Fig 4.7 (a)).

Table 4.5: Saturation magnetization (M_s) and Curie temperature (T_c) values for $[Fe_{74}Mo_4P_{10}C_{7.5}B_{2.5}Si_2]_{100-x,y}$ $(Cu)_x (Ga)_y$ (x = 0, 0.5, 1) (y = 0, 0.5, 1, 1.5 and 2) alloys. The accuracy of the measured date lies within ± 80 A/m (≈ 1 Oe) for saturation magnetization and ± 2 K for Curie temperature.

Compositions	Rod ϕ (mm)	Saturation Magnetization M_s (Am^2/kg)	Curie temperature T_c (K)
FeMoPCBSi	1	115	510
FeMoPCBSi+0.5Cu	1	115	503
FeMoPCBSi+1Cu	1	113	503
FeMoPCBSi+0.5Ga	1	115	508
FeMoPCBSi+1Ga	1	115	522
FeMoPCBSi+1.5Ga	1	114	522
FeMoPCBSi+2Ga	1	113	537

In the case of the Cu-added alloys the M_s starts to increase close to the onset of their first crystallization event, indicating the formation of a soft magnetic phase having higher Curie temperature, which is the bcc-Fe phase in this case. Unlike the Cu-added alloys, the Ga-added alloy does not show high increase in saturation magnetization values, only marginal increase is observed. This might be due to the concurrence of both $Fe_{23}(B,C)_6$-type and bcc-Fe phases having both low and high Curie temperature values. The room temperature M_s of the Cu- and Ga- added alloys are larger after cooling; this is due to the presence of the bcc-Fe crystals in ferromagnetic state. All these thermomagnetic curves are in agreement with previous DSC and XRD results reported in section 4.3 and 4.4 for both Cu- and Ga- added samples.

The Curie temperature of the FeMoPCBSi glass increases with the increase in Ga content. The T_c of the 2 at.% Ga- added alloy is 27 K higher than alloy without Ga, this significant increase in T_c could be due to the presence of large numbers of ordered zones/clusters. As mentioned earlier, the GFA of the alloys decreases as the Ga content increases; also, large amount of α-Fe precipitates appears when the Ga content increases [252].

4.7 Mechanical properties of $[Fe_{74}Mo_4P_{10}C_{7.5}B_{2.5}Si_2]_{100-x, y}$ (Cu_x, Ga_y) (x = 0, 0.5 and 1) (y = 0, 0.5 and 1) glasses

Similar to FeCoBSiNb system discussed in section 3.7, the mechanical behavior of these glasses were studied by performing compression tests and hardness measurements. In order to study the effect of Cu and Ga additions on the mechanical properties, all compression were performed on cylindrical samples having 1.5 mm diameter. The hardness measurements were performed on cross-sectional slice cut from rods with same geometry.

4.7.1 Compression tests

The true stress-true strain curves for the as-cast $[FeMoPCBSi]_{100-x, y}$ (Cu_x, Ga_y) (x = 0, 0.5 and 1) (y = 0, 0.5 and 1) glassy samples are shown in Fig. 4.17 (a) and (b). All samples exhibit elastic deformation regime followed by a small compressive plastic regime. Fig. 4.17 (a) shows the true stress-true strain curves for as-cast FeMoPCBSi (black line), FeMoPCBSi+0.5Cu (red line) and FeMoPCBSi+1Cu (blue line) cylindrical samples with 1.5 mm in diameter.
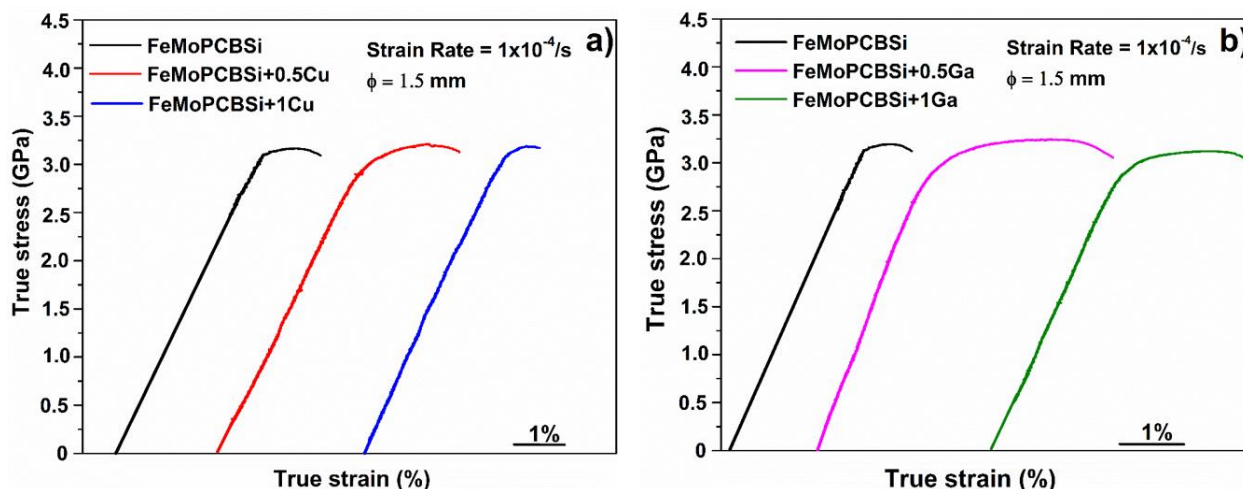
Figure 4.17: Compressive true stress-true strain curve for (a) $[Fe_{74}Mo_4P_{10}C_{7.5}B_{2.5}Si_2]_{100-x}$ (Cu_x) (x = 0, 0.5 and 1) and (b) $[Fe_{74}Mo_4P_{10}C_{7.5}B_{2.5}Si_2]_{100-y}$ (Ga_y) (y = 0, 0.5 and 1) glasses measured at a strain rate of 1×10^{-4}/s.

The FeMoPCBSi exhibits a high yield strength of $\sigma_y = 3.10 \pm 0.02$ GPa, an elastic strain of $\varepsilon_y = 2.1$ %, a high fracture strength of $\sigma_f = 3.12 \pm 0.02$ GPa and a limited plastic strain $\varepsilon_{pl} = 0.70$%. The fracture strength takes almost the same value as reported earlier by Liu *et al*. [89] for 1 mm diameter samples, but their plastic strain is around 4.3%. The difference in the present ε_{pl} and reported values [89] are because of the differences in the sample geometry, it is well known that samples of smaller dimensions exhibit higher plasticity [62]. The yield strength (σ_y) and fracture strength (σ_f) of the 0.5 and 1 at.% Cu- added samples are 2.83, 3.02 $\pm$ 0.02 GPa and 3.10, 3.18 $\pm$ 0.02 GPa respectively. Interestingly, for 0.5 at.% Cu the plastic strain (ε_{pl}) increases to 1.4 % and for 1 at.% the plastic strain (ε_{pl}) decreases to 0.5 % , this increases in plasticity due to the addition of small amount of Cu is similar to the FeCoBSiNb glass. Table 4.6 summarizes the deformation data obtained from compression tests together with hardness and density values for all the compositions studied in this work. The compressive behavior of the Ga added samples are shown in Fig. 4.17, FeMoPCBSi (black line), FeMoPCBSi+0.5Ga (magenta line) and FeMoPCBSi+1Ga (green line). Similar to the Cu addition, Ga addition also aids in improving the plastic strain. The yield stress (σ_y) and yield strain (ε_y) of 0.5 and 1 at.% Ga- added samples are 2.78, 2.79 $\pm$ 0.02 GPa and 1.4 and 1.9 %, respectively.

The fracture of both samples occurs at nearly the same value of true stress, 3.05 $\pm$ 0.02 GPa, but the corresponding fracture strain is different: 4.4 % for the 0.5 % Ga and .9 % for 1 % Ga added samples. The plastic deformation of the samples extend up to 3 % and 2% for 0.5 % and 1% Ga added samples. The fracture morphology of the samples after compression tests were investigated using SEM, as described in section 2.3.2. The sample consists of large number of small fracture zones and their zones appear to be declined by about 70-90° to the direction of the applied load, which is similar to the fracture behavior of FeCoBSiNb glass. This kind of failure is mainly due to the simultaneous generation of large number of small factures at many sites, at a high stress level close to 3.0 GPa and upon fracture the samples shatter apart into many small fragments. The high fracture strength of these glasses are mainly because of the covalent bonding nature of their constituents [8, 50]. Though slight increase in plastic strain is observed for FeMoPCBSi+0.5Cu and FeMoPCBSi +1Cu samples, the overall appearance of the fracture surface is towards brittle fracture mode, with many shells indicating the generation and propagation of cracks

Table 4.6: Yield stress σ_y, yield strain ε_y, fracture stress σ_f, fracture strain ε_f, plastic strain ε_{pl}, Young's modulus E, Vickers hardness *HV* and density ρ for $[Fe_{74}Mo_4P_{10}C_{7.5}B_{2.5}Si_2]_{100\text{-}x,\,y}\,(Cu)_x\,(Ga)_y$ (x = 0, 0.5, 1) (y = 0, 0.5, 1, 1.5 and 2) alloys. The accuracy of the experimental data lies within ± 0.02 GPa for the stress-strain measurements, ± 10 *HV* for the hardness measurements and 0.5% for the density measurements. The literature data for $Fe_{74}Mo_4P_{10}C_{7.5}B_{2.5}Si_2$ [89] glass is given for reference.

Compositions	σ_y (GPa)	ε_y (%)	σ_f (GPa)	ε_f (%)	ε_{pl} (%)	E (GPa)	*HV*	ρ (g/cm³)
FeMoPCBSi [89]	3.0	-	3.28	-	-	-	-	-
FeMoPCBSi	3.10	2.1	3.12	2.8	0.7	185	945	7.486
FeMoPCBSi+0.5Cu	2.83	1.7	3.10	3.1	1.4	177	930	7.478
FeMoPCBSi+1Cu	3.02	1.7	3.18	2.2	0.5	177	920	7.468
FeMoPCBSi+0.5Ga	2.78	1.4	3.05	4.4	3	175	930	7.465
FeMoPCBSi+1Ga	2.79	1.9	3.03	3.9	2	174	925	7.452
FeMoPCBSi+1.5Ga	-	-	-	-	-	-	910	7.445
FeMoPCBSi+2Ga	-	-	-	-	-	-	890	7.430
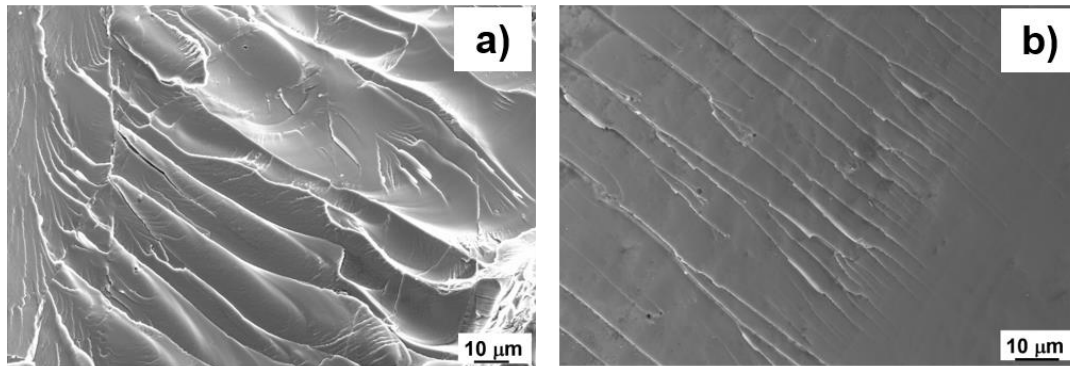
Figure 4.18: SEM micrographs of the $[Fe_{74}Mo_4P_{10}C_{7.5}B_{2.5}Si_2]_{99.5}Cu_{0.5}$ sample, showing fracture surface after compression test taken from different regions (a) and (b).

Fig. 4.18 (a) and (b) shows the fracture surface of the FeMoPCBSi+0.5Cu sample taken at different regions. No vein patterns can be observed on the fracture surface of these samples; instead several primary and secondary shear bands are observed throughout the samples.

Several secondary shear bands starts from the primary shear bands, but after propagating few μm they fail in a brittle manner. However, more interesting features are observed in the FeMoPCBSi+0.5Ga and FeMOPCBSi+1Ga samples. Figure 4.19 (a) and (b) shows the fracture surfaces of the FeMoPCBSi+0.5Ga samples after compression test taken from the center region. The fracture surfaces consists of large numbers of vein patterns combined with several micro cracks (indicated by green arrows in the image) At first the material starts to deform plastically, after a while the brittle fracture starts, the cracks (marked with green arrows) are super imposed on the vein patterns, indicating the combination of ductile and brittle failure mode.
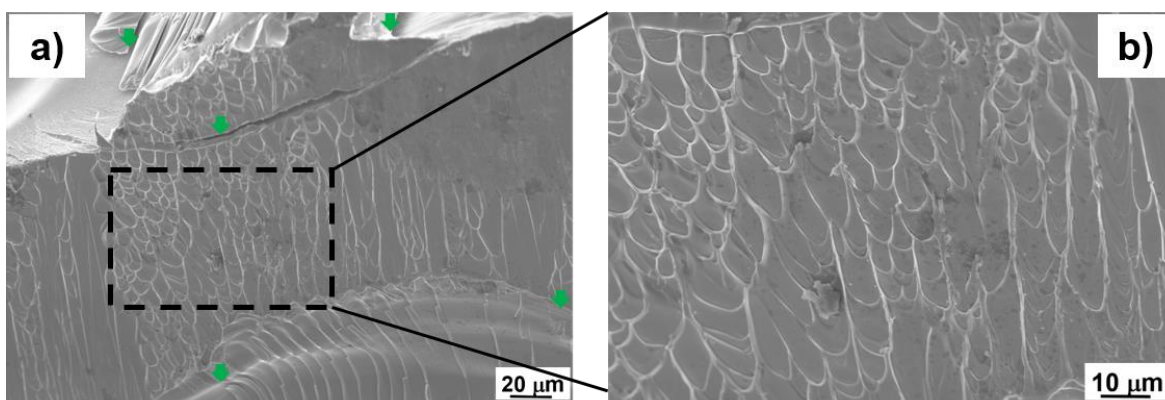
Figure 4.19: (a) SEM micrograph of the $[Fe_{74}Mo_4P_{10}C_{7.5}B_{2.5}Si_2]_{99.5}Ga_{0.5}$ sample, showing fracture surface after compression test and (b) center region taken at higher magnification (rectangular region marked in (a)). Cracks are marked with green arrows.

Figure 4.20(a) and (b) represents the fracture surface of the FeMoPCBSi+1Ga sample taken from the center of the sample after compression test, from different regions with different magnifications. In Fig. 4.20 (a) the red arrows indicate the metal droplets, which are observed throughout the fracture surfaces and the green arrows indicates the cracks. Compared to the 0.5 at.% Ga samples, the fracture surface of this 1 at.% Ga samples contains more vein patterns, less micro cracks and few molten droplets, here also the micro cracks are superimposed on the vein patterns. The presence of metal droplets on the fracture surfaces suggests that at high stress level of 3.0 GPa the flowed layers must have been melted, as it is commonly observed in case of the deformable BMGs [226].
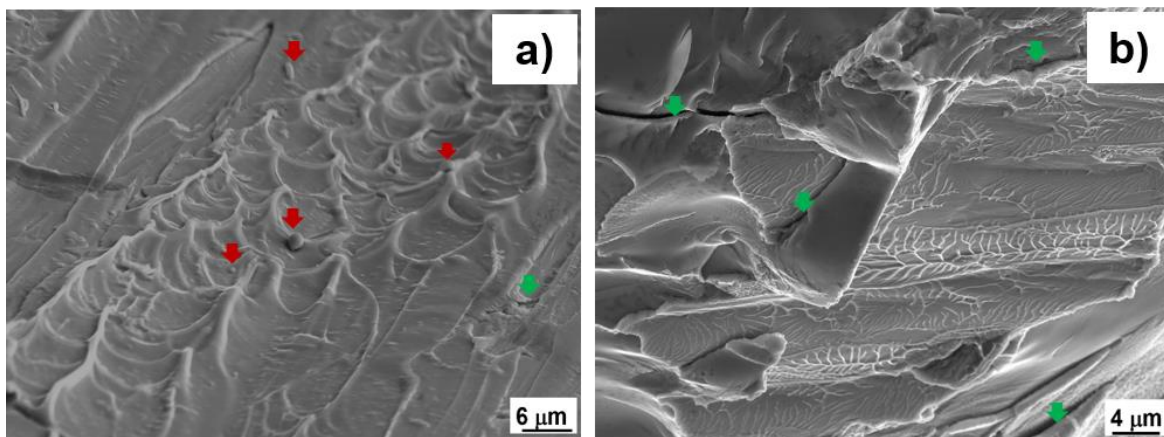
Figure 4.20: SEM micrographs of the $[Fe_{74}Mo_4P_{10}C_{7.5}B_{2.5}Si_2]_{99}Ga_1$ sample, showing fracture surface after compression test taken from different regions with different magnifications (a) and (b). Droplets are marked with red arrows and cracks are marked with green arrows.

Even at the low stress level, the formation of μm range molten droplets only in the Ga added sample indicates that the addition of Ga leads to the formation of low melting zones, whose melting point is much lower as compared to the rest of the alloy. However, the possibility of high shear propagation rate i.e. $> 0.9V_s$ [138, 227-230] cannot be rule out. In either case more detailed study is required to get the exact conclusions, which is future scope of this work. However, the addition of Ga improves the plastic deformation of the FeMoPCBSi glass to a great extent.

4.7.2 Hardness and density measurements

The Vickers hardness measurements were performed on cross-section slice from the as-cast cylindrical rods with 1.5 mm diameter as described in the section 2.5.2. In order to have consistent result, more than 20 indentations were performed in each samples and the final value is the average value of 20 indents. The hardness values of all glassy samples are summarized in Table 4.6. The hardness value for the FeMoPCBSi glass is $HV= 945 \pm 10$ (9.26 GPa). The hardness of the glass having up to 1 at.% Cu and Ga additions are almost unchanged: 920 (9.02 GPa) and 925 (9.07 GPa) HV, respectively. The hardness decreases with increase in Ga % and reaches a minimum value of 890 (8.72 GPa) HV for the 2% Ga-added samples, effect similar to the effect of Ga additions in FeCoBSiNb glass. This decrease in the hardness values are mainly due the presence of soft zones, which increases with increase in Ga content.

The density measurements were performed on the master alloys for all compositions as described in the section 2.5.3. All density values are summarized in the Table 4.6. The density of the FeMoPCBSi alloy is $\rho = 7.486$ g/cm^3, which is almost similar to that of the ductile Fe-Ni-Nb-B bulk glassy alloys [240]. Though the mechanical properties of Fe-Ni-Nb-B glassy alloys are better than FeMoPCBSi alloy, their GFA is very low compared to FeMoPCBSi alloy. With addition of Cu and Ga the density decreases and reaches a minimum value of $\rho = 7.468$ and 7.430 g/cm^3 for the alloys with 1 at.% Cu and 2 at.% Ga. The decrease in the density value with addition of Ga is obvious, because Ga has a low density compared to Cu, Fe and Mo.

4.8 Discussion

Table 4.1 Summarizes all the thermal stability values collected in this work comparing with the value known from literature [89]. The reported maximum achievable diameter is 5 mm for this FeMoPCBSi alloy [89], while in this work the maximum diameter produced is only 3 mm. The glass transition temperature and the onset of crystallization temperature values obtained are 733 and 768 K, which are slightly higher than the reported values 729 and 766 K, respectively. However, the extension of the supercooled liquid region is only 35K compared to the reported value of 37 K. The reduced glass transition temperature is also smaller 0.57 compared to 0.58. Considering the fact that GFA of the current alloy is determined based on the extension of the SLR and the reduced glass transition as indicated by Inoue *et al.*[8], the current alloy has slightly lower GFA compared to the literature data. As mentioned earlier (section 3.8), these small differences could be due a small deviation in the overall composition, as shown by Stoica [3] in his very recent work.

In contrast to FeCoBSiNb alloy, the addition of 0.5 and 1 at.% Cu does not alter the crystallization temperature of FeMoPCBSi alloy very much, however the GFA decreases drastically. Similar to the FeCoBSiNb glass, the addition Cu in this alloy also promotes the formation of some ordered features in the glassy matrix. The presence of ordered features (see Fig. 4.10) in this alloy may explain why the 0.5 and 1 at.% Cu- added FeMoPCBSi samples have narrower super cooled liquid region ($\Delta T_x = 31$ and 29 K) compared to the Cu free alloy ($\Delta T_x = 35$ K). Wider supercooled liquid region indicates longer incubation time for nucleation. For the alloy without Cu, crystallization requires the formation of complex $Fe_{23}(C,B)_6$ nuclei that are dissimilar to the ordered zones of the

amorphous alloy. In case of the Cu added alloy, the formation of the local order reduces the nucleation kinetics, there by easily promoting the formation of α-Fe from the amorphous matrix.

On the other hand, the addition of Ga slowly increases the crystallization temperature compared to the Ga free alloy. The dissimilarities between the structures of the ordered zones/clusters observed in both Cu- and Ga- added samples may be one of the reason for the wide supercooled liquid region of the Ga- added alloys. The increase in crystallization temperature upon addition of Ga suggests that the degree of ordered zones/clusters formed due to the addition of Ga has no effect on the crystallization kinetics. This is not a surprising event, given the fact that even after the addition of 1 at.% Ga the main precipitating phase is the complex $Fe_{23}(C,B)_6$. The activation energy for crystallization (E_c), calculated in the section 4.3, favors this claim, the addition of Cu reduces the E_c to a considerable amount i.e. from 320 to 276 $\pm$ 8 kJ/mol. Interestingly, the Ga addition increases the E_c to 341 $\pm$ 8 kJ/mol. From this we can assume that, unlike the ordered zones/clusters formed due to addition of Cu, ordered zones/clusters formed due to Ga addition does not influence in the thermal stability of the glass. On contrary, the addition of small amount of Ga improves the GFA, by hindering the formation of the $Fe_{23}(C,B)_6$-type phase. It is well known that the presence of ordered zones/clusters in the amorphous matrix does not necessarily imply that they act as a nucleation site for the crystal growth. The ordered embryos must be larger than the critical nucleus size in order for their growth to be thermodynamically favorable [211-213]. However, when the Ga is added more than 1 at.%, the GFA decreases drastically, the maximum castable diameter is only 1.5 mm, this could be because the ordered structures formed due to addition of Ga attains the critical limit, there by promoting the easy precipitation of the α-Fe.

The shifting of the first and second broad maxima in both Cu and Ga added samples also reflects the formation of ordered zones/clusters [205]. For the same amount of Cu and Ga additions, the shift in $2\theta_1$ and $2\theta_2$ positons of the Cu added samples are larger. Beyond 1 at.% Ga addition, the shift in $2\theta_1$ and $2\theta_2$ positions are even larger than in the Cu-added samples, indicating the formation of ordered zones/clusters. Furthermore, it is evident from the XRD patterns of the heat treated samples, beyond 1 at.% Ga addition, the formation of α-Fe is more dominating compared to the $Fe_{23}(C,B)_6$-type phase (see Fig. 4.8). At this point one can assume that the addition of Ga more than 1 at.% have similar effect like Cu addition and they are: (i) formation of the complex $Fe_{23}(C,B)_6$ phase is suppressed, more bcc-(Fe,Co) starts to grow after first crystallization event;

(ii) the GFA decreases drastically t_c is merely 1.5 for 1.5 and 2 at.% Ga addition respectively. All these changes could be because of the formation of ordered zones/clusters which are above the critical limit and hence start to grow as the temperature increases, leading to a decrease in the GFA of the alloys. From this we can conclude that the optimum quantity of Ga, which can be added without affecting the GFA as well as their thermal stability is around 1 at.%.

The coercivity values of 3 A/m reported in our work is almost comparable with the reported coercivity value of 1.7 A/m by Liu *et al*.[89] for the same alloy composition. The differences in the coercivity values are quite small, as mentioned earlier they may arise due to the small variation in the overall chemical composition. The saturation magnetization of all Ga-added samples remains almost the same, while in the case of Cu addition there is a gradual decrease in saturation magnetization. This decrease in the M_s values could be due the formation of more ordered non-magnetic structures. The magnetic properties of both Cu and Ga (i.e. up to 0.5 at.% Cu and 1 at.% Ga) added alloys are similar in as cast condition, upon annealing to higher temperatures the Cu-added alloy has relatively better soft magnetic properties compared to the Ga added. As mentioned earlier (section 4.6.2), the increase in M_s with increase in temperature is due to the formation of bcc-(Fe,Co) in the Cu added alloy, the growth of this bcc-(Fe,Co) can be clearly seen in the thermomagnetic curves shown in Fig. 4.16 (a). The M_s value starts to increase as soon as the bcc-(Fe,Co) starts to form around 730 K. The behavior of the Ga-added samples is similar to the Ga free alloys i.e. the magnetization values decreases after the first crystallization event due to the formation of $Fe_{23}(C,B)_6$ crystals. This observation further confirms that when the Ga addition is kept below 1 at.%, it will improve the thermal stability of the alloy. Beyond 1 at.%, Ga will decrease the GFA of the alloy by promoting the formation of large number of ordered zones/clusters. In contrast to the FeCoBSiNb alloy, the addition of Ga in FeMoPCBSi increases the Curie temperature of this alloy, this increase could be due to the formation of order zones [252].

The compression behavior of Cu and Ga added samples are similar in their elastic regime, for the same amount of Cu and Ga addition (i.e. 0.5 at.%) Cu- added sample shows slightly higher plastic strain ε_{pl} compared to the Ga- added samples (Table 4.6). Though the yield stress σ_y decreases with increase in Cu and Ga content, the fracture stress σ_f for Cu- added alloys are almost the same, i.e. $\approx$ 3.1 GPa and for the Ga samples the fracture stress decreases by $\approx$ 0.1 GPa. However, the maximum plastic strain ε_{pl} of 1.4% and 3%, respectively, are obtained only for 0.5 at.% Cu and

0.5 at% Ga added samples, respectively. The green circle in Fig. 3.20 shows the position of this FeMoPCBSi alloy compared to the other Fe-based glasses reported in the literatures. Therefore it can be concluded that in order to efficiently improve the mechanical property of this FeMoPCBSi glassy alloy it is desired to add only 0.5 at.% of Cu or Ga.

The Vickers hardness values measured for this alloys are lower as compared with the values of most of the Fe-based BMGs reported so far, even lower than FC20+0.4wt% B [232] or $Fe_{72}B_{20}Si_4Nb_4$ [233] glasses. With the addition of Ga, the hardness values also decreases over 50 HV when the Ga content from 0 to 2 at.%. The σ_f/E, HV/σ_f and $HV/3E$ ratios for all glasses are given in Table 4.7.

Table 4.7: σ_f/E, HV/σ_f and $HV/3E$ ratios for $[Fe_{74}Mo_4P_{10}C_{7.5}B_{2.5}Si_2]_{100-x,y}$ $(Cu_x\ Ga_y)$ (x = 0, 0.5 and 1) (y = 0.5 and 1) the glasses.

Compositions	σ_f/E	HV/σ_f	$HV/3E$
FeMoPCBSi	0.017	2.97	0.017
FeMoPCBSi+0.5Cu	0.017	2.94	0.017
FeMoPCBSi+1Cu	0.017	2.83	0.017
FeMoPCBSi+0.5Ga	0.017	2.99	0.017
FeMoPCBSi+1Ga	0.017	2.99	0.017

The σ_f/E, HV/σ_f and $HV/3E$ ratios for all the alloys are nearly fixed 0.017, $\approx$2.99 and 0.017, respectively. The σ_f/E and $HV/3E$ ratio of these bulk glassy alloys are lower compared to the previously reported BMGs [26, 50, 251]. This may indicate that the current glassy alloys shows some work hardening during the elastic-plastic deformation. This kind of alloys with appreciable work hardening during the deformation is very attractive for industrial applications.

Chapter 5

Scaling-up: High pressure die casting

5.1 Introduction

The current industry demands materials with low cost and improved mechanical properties: higher hardness, higher tensile strength and better surface qualities. As a general rule, a higher strength and hardness of the material brings along higher manufacturing costs and also higher manufacturing times, which limits their use. However, the abundant natural resources and low material cost of these Fe-based glasses, attracted the attention of the industries to look for an appropriate methods for producing these metallic glasses in an industrial scale. Fe-based glasses are very brittle and cannot withstand the industrial casting process, even if the material is a good glass former, hence their applications are limited to wires, ribbons and powder metallurgy (P/M) based products [253]. Hence, so far only a few reports are available on direct fabrication of bulk magnetic cores using casting techniques even in laboratory scale. Wu *et al.*[254] and Zhang *et al.*[255] reported on the direct fabrication of toroidal cores from $Fe_{66}Co_{10}Mo_{3.5}P_{10}C_4B_4Si_{2.5}$ BMG, having an inner diameter of 6 mm and an outer diameter of 10 mm. Similarly Bárdos et al. [256] fabricated a toroidal core with an outer diameter of 26 mm and inner diameter of 18 mm from $Fe_{70.7}C_{6.7}P_{10.4}B_5Si_{1.1}Mn_{0.1}Cr_2Mo_2Ga_2$ multicomponent alloy. The other methods commonly employed to produce bulk components other than casting is P/M, but this route involves hot pressing or sintering (spark plasma) which affects the soft magnetic properties of the Fe-based metallic glasses [83, 257]. Recently, thermoplastic forming (TPF) has been used to fabricate three dimensional BMG parts [128]. In TPF method the sample is heated to its super cooled liquid region (i.e. to the temperature in between the glass transition (T_g) and the crystallization temperature (T_x)) and then deformed plastically. In the supercooled liquid regime the glass becomes soft, due to the drastic decrease in viscosity of the glass [13, 15], which allows to deform the material without any defects. Even though TPF gives high surface quality and ability to reproduce very fine structures [96, 258-261], the processing time (t_p) must be short, in order to avoid crystallization. The short processing time limits the application of this technique for bigger and complex parts. Additive manufacturing techniques like selective laser melting (SLM), have also been used to produce BMG

parts with excellent properties [262-264]. However, it is very expensive and highly complicated to produce the uniform-sized multicomponent glass-forming alloy powders, which is used as a starting material for SLM process [262]. Another method, widely used in industries to produce large variety of products with high dimensional accuracy and good surface quality is high pressure die casting (HPDC) method [184]. HPDC offers the economical and efficient method for producing the component with low surface roughness and high dimensional accuracy and also this method has higher production rate, when compared with other casting techniques [265]. The characteristics of TPF, SLM and HPDC are summarized in Table 5.1.

Table 5.1: Comparison between thermoplastic forming (TPF), selective laser melting (SLM) and high pressure die casting (HPDC) process [185].

TPF method process	SLM method process	HPDC process
Multiple step process (depending on the shape two or more stages are involved in the processes)	Multiple step process (samples are built layer by layer in several steps)	Single step process
Final shape decides the processing time (since the processing time is limited, it may take several heating cycles to complete the product[96])	Processing time mainly depending on the shape and size of the final products. Several samples can be built simultaneously.	Casting process completes fast (high production rate)
Only few alloys were processed by this method (needs development of more novel techniques to establishing standards)	Standard parameters are available for few basic alloy systems only (standards are still in development stage [266])	Widely studied and casting parameters well established (standard casting parameters are readily available for several alloy systems)

Only very good glass formers with high SLR can be processed (Good glass formers often contains toxic (Be[267]) or expensive elements like Pt, Pd, Au et.[75, 268])	Only good glass formers with high thermal stability can be prepared by this method (during the addition of every new consecutive layer previous layer temperatures are subjected to increase in temperature, which leads to crystallization)	Marginal glass formers can also be produced by this method (Due to application of high pressure good contact is established between the mold and the molten metal, which increases the cooling rate)
Glassy plate, rod or granules serves as starting material (quality of the glassy sample decides the final product quality)	Difficult to get homogeneous multicomponent amorphous powder (SLM uses powder and the quality of the product depends on the quality of the powder[262])	Preparation of starting material is easy (normally induction melting or arc melting is preferred)
During the process micro-pores and micro-cracks will be closed	Very difficult to avoid micro-pores and micro cracks (initial powder particle size and scanning speed plays important role in controlling the micro-pores and micro-cracks [262, 264])	Casting defects such as gas pockets and shrink holes can be drastically reduced or controlled[269] (final product will have high density and low shrinkage)
TPF can be done in open atmosphere[270]	Needs high purity inert atmosphere to produce the samples (The fine powders will oxidize or explode if the working atmosphere has oxygen)	Casting environment can influence the crystallization kinetics (casting die temperature, casting speed and casting atmosphere affect the final product)
Internal stress can be relieved by slow cooling of the sample after final processing step[260]	By pre-heating the base plate the internal stress can be reduced	Samples have huge internal stress (the fast cooling results in large internal stress)

samples can be used after re - melting	Powders can be reused after an additional sieving (The whole process is carried under inert atmosphere)	Limited reusability of the material (repeated usage leads to absorption of more oxygen, which influences the heterogeneous nucleation sites)
Thin and micro sections can be produced easily and easier than thick sections	Any complex shape can be produced, powder size and the layer thickness are the only limiting factor, the technique has virtual no limitation	Thin sections and sections with interconnected holes cannot be produced (viscosity of the molten alloy determines the minimum section thickness)

5.2 Industrial scale casting

The purpose of current work was to design and to develop a high-pressure die casting method and suitable tools to directly cast Fe-based bulk metallic glasses [185]. For that, a high pressure die casting tool (key-shaped) for casting Fe-based BMG was designed. Also, the casting parameters of $Fe_{74}Mo_4P_{10}C_{7.5}B_{2.5}Si_2$ alloy (presented in Chapter 4), were optimized. This particular Fe-based composition was chosen because of its relatively low melting point of 1283 K, good glass-forming ability (GFA) and good soft magnetic properties [89]. Moreover, this alloy can be produced using industrial grade elements, which makes it cheap and a realistic candidate for applications. Another advantage is its relatively low affinity towards oxygen, which makes it much easier to handle compared to Ti-based or Zr-based alloys. In an industrial scale production, there are several factors which influences the quality, production rate as well as the cost of the final product. The tool life has a large impact on the manufacturing costs of the products in industrial casting processes. The tool life in HPDC process depends on several factors but the very important factors are casting temperatures and hardness of the casting material. In our initial approach to optimize the die life, two different die materials with different heat conductivity were used: hardened heat resistant steel with a low heat conduction rate of 33 W/mK and a mechanically soft copper-based alloy with high heat conduction rate of 230 W/mK respectively.
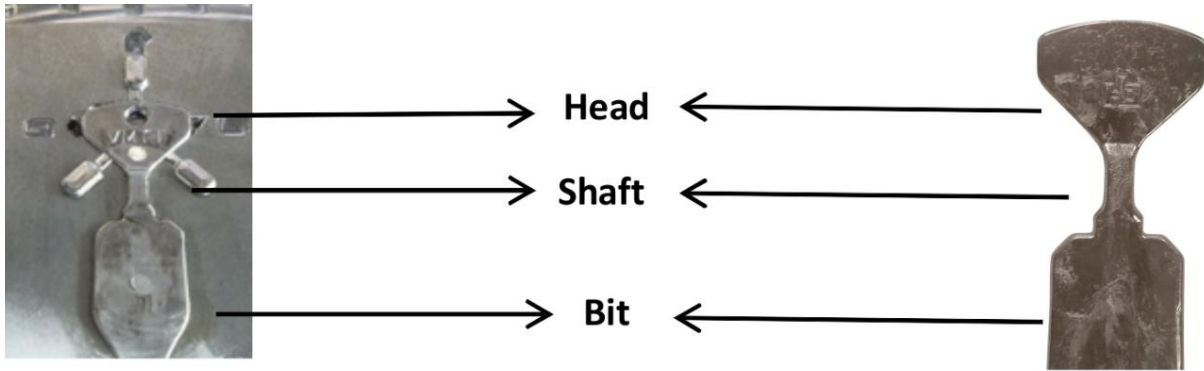
Figure 5.1: (a) Cast part (key) still in the die cavity (b) Cast part (key) separate from the die [185].

The key shaped sample produced from HPDC is shown in Fig. 5.1(a) and (b). The width and thickness of head, bit and stem regions are 25.6 mm x 3.5 mm (head, bit) and 5 mm x 3.5 mm (stem). The overall height of the sample is 41.7 mm.

5.2.1 Influence of alloy temperature during casting

It is well known that the alloy temperature during casting [271, 272] plays a vital role in determining the reproducibility as well as the quality of the bulk metallic glasses. In order to study the influence of the casting temperatures on the final product, an optimum material flow rate of 4 m/s was maintained and the samples were cast at 1353, 1393, 1453 and 1573 ± 10 K using both steel and copper die. These casting temperatures were fixed based on the liquidus temperature (T_{liq}) of the FeMoPCBSi alloy (T_{liq} =1283 K). For all characterization head of the key (see Fig 5.1 (a) and (b)) was used, because the melt travels maximum distance and also flows through different cross-sections, before reaching the key head. As a result head part has a maximum chance for crystallization; consequently this part is most critical and chosen for the analysis. The XRD patterns of the key samples produced at different casting temperatures 1353, 1393, 1453 and 1573 K with copper and steel die are shown in Fig. 5.2 (a) and (b), respectively. The keys cast at 1353 and 1393 k using both copper and steel die show relatively large crystalline peaks compared to the key cast at 1443 K, which is almost 160 K above the liquidus temperature (T_{liq} = 1283 K) of the

alloy. In case of the steel die the key cast at 1573 K is completely amorphous. However a small amount of crystalline peaks are observed in the core of the key cast using copper die even at the 1573 K.
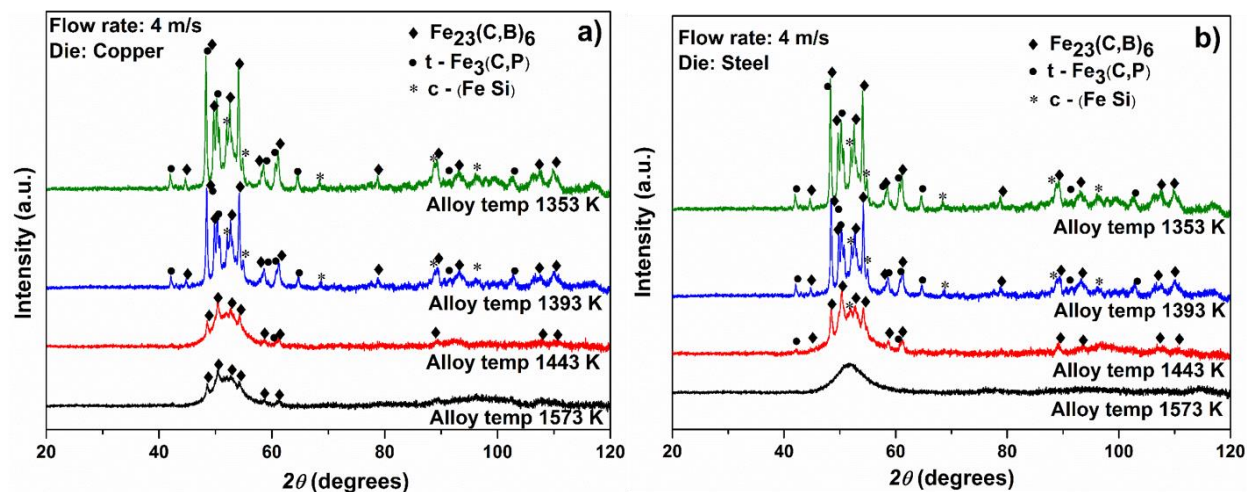
Figure 5.2: XRD patterns of the samples produced at different casting temperatures 1353, 1393, 1453 and 1573 K using (a) copper and (b) steel die, respectively [185].

This might be possibly due to the skin effect during HPDC [273]. The skin effect mostly occurs when the cooling rate of the cast part is very high; as a result the outer shell of the part solidifies very fast leading to a gap between the sample and the die surface. The gap between the die and cast part and amorphous outer shell hinders the heat transfer between the sample and die, leading to nucleation of the crystals in the core of the sample [274]. However, this shrinkage effect which is consistent in the case of crystalline materials is greatly reduced in the case of metallic glasses [128, 275]. Here a new effect may be present, which enhances the skin effect: the outer layer solidifies first, becoming amorphous, and in the amorphous state the alloy has far worse heat conductivity than the metallic mold [96]. The heat gradient become smaller and the heat transfer is worse and so the core may have enough time to crystallize.

Fig. 5.3 (a) and (b) depicts the DSC curves of the samples produced at different casting temperatures 1353, 1393, 1453 and 1573 K using copper and steel die, respectively. As it can be seen from the DSC curves the alloy temperature plays a vital role during casting process. If the alloy temperature is just 50-100K above the liquidus temperature, nucleation starts before

complete filling of the mold. The key-shaped samples cast at 1353 ± 10 K have the lowest first and second crystallization enthalpy values of -3.2 and -10.5 J/g, respectively (see Table 5.2). To achieve a homogeneous casting without flow lines and any other casting defects, the superheating of the alloy was slowly increased to over 250 K. The samples produced at 1573 K have the similar first and second crystallization enthalpy values -15.6 and -38.8 J/g compared to the sample produced in laboratory scale (see Table 5.2). Lin et al. [271] and Mukherjee et al. [272] systematically studied the effect of melt overheating on crystallization kinetics of Zr based metallic glasses. In their work they reported that for every alloy there exist an overheating threshold above which the crystallization time increases. The increase in crystallization time may be due to the dissolution of the heterogeneities acting as a nucleation sites; normally the heterogeneities may arise due to the minor traces of oxygen, high-temperature melting elements and oxides etc. If the overheating is less than the threshold limit the dissolution is incomplete and the nucleation starts quickly.

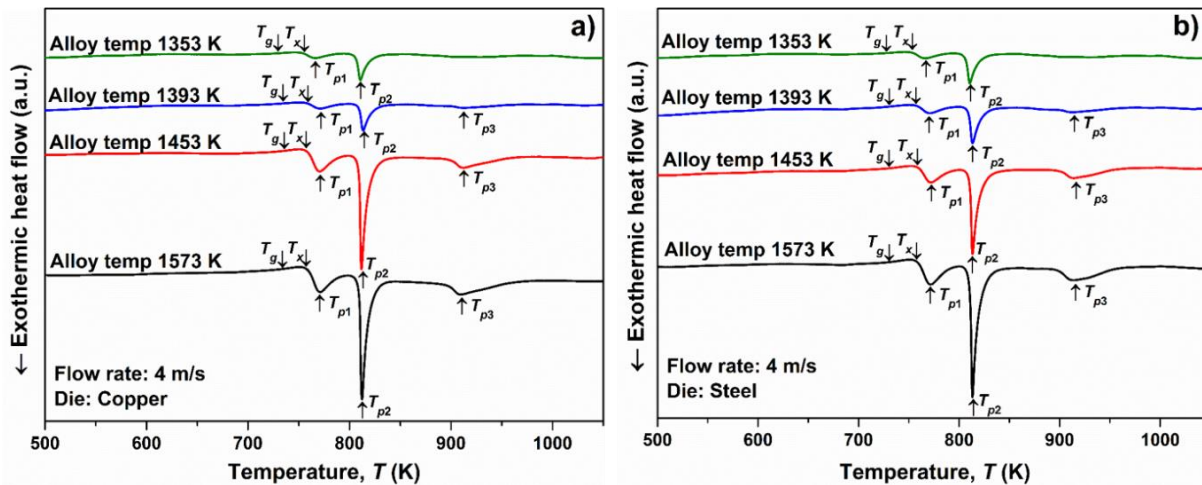**Figure 5.3:** DSC traces of the samples produced at different casting temperatures 1353, 1393, 1453 and 1573 K using (a) copper and (b) steel die, respectively [185].

This results is also supported by the XRD patterns (see Fig. 5.2 (a) and (b)). Hence in order to achieve completely amorphous key-shaped samples, the FeMoPCBSi glass should be overheated to at least 250 K above the melting point (i.e. 1573 K)

Table 5.2: Enthalpies of the first and second crystallization step for the key samples cast at different temperatures using copper and steel dies [185]. Enthalpies of the 3 mm rod cast in lab condition is given for reference purpose.

Sample cast conditions			First Crystallization enthalpy (J/g) ± 0.2	Second Crystallization enthalpy (J/g) ± 0.2
Die material	Flow rate (m/s)	Casting Temperature (K) ± 10		
Steel	4	1353	-3.8	-10.2
Steel	4	1393	-10.7	-27.5
Steel	4	1453	-12.4	-32.8
Steel	4	1573	-15.6	-38.8
Steel	12	1573	-13.1	-31.9
Steel	19	1573	-9.8	-26.7
Copper	4	1353	-3.2	-10.4
Copper	4	1393	-9.8	-28.7
Copper	4	1453	-11.8	-30.1
Copper	4	1573	-13.4	-32.8
Rod cast in lab - copper die	---	1523	-15.8	-39.1

5.2.2 Influence of metal flow rate during casting

The nature of metal flow in the die cavity plays a vital role in deciding the quality of the final product as well as the die life [184]. The molten metal flow rate mainly depends on the piston speed and physical properties of the fluid at that casting temperature. In order to elucidate the influence of the material flow speed on the key quality we decided to cast the samples at different flow rates, however due to the limited high temperature data on these glass-forming systems [276], the casting temperature was kept constant at 1573 K (see Fig. 5.2 (b)) and only the piston speed is varied. Three different flow rates 4, 12 and 19 m/s were chosen for our studies, by maintaining the

piston speed at low, intermediate and maximum points, respectively. The XRD patterns and DSC curves for the samples produced at different flow rates 4, 12 and 19 m/s are shown in Fig. 5.4 (a) and (b), respectively. From the XRD patterns it is evident that only the sample produced at low flow rate (i.e. 4 m/s) is completely amorphous, whereas the samples produced at higher flow rates (12 and 19 m/s) show some crystalline peaks. The crystallinity increases with the increase in the flow rate, the sample produced at a flow rate of 19 m/s shows relatively large crystalline peaks compared to the sample produced at 12 m/s. This increase in flow rate decreases the surface quality of the keys. The increase in the metal flow rate from 4 to 19 m/s causes the crystallization enthalpies of the first and second crystallization events to decrease from -15.6 and -38.8 J/g to -9.8 and -26.7 J/g, respectively (see Fig. 5.4 (b)). This increase in crystallinity of the samples with increase in flow rate is attributed to the nature of the fluid flow inside the die cavity [184].
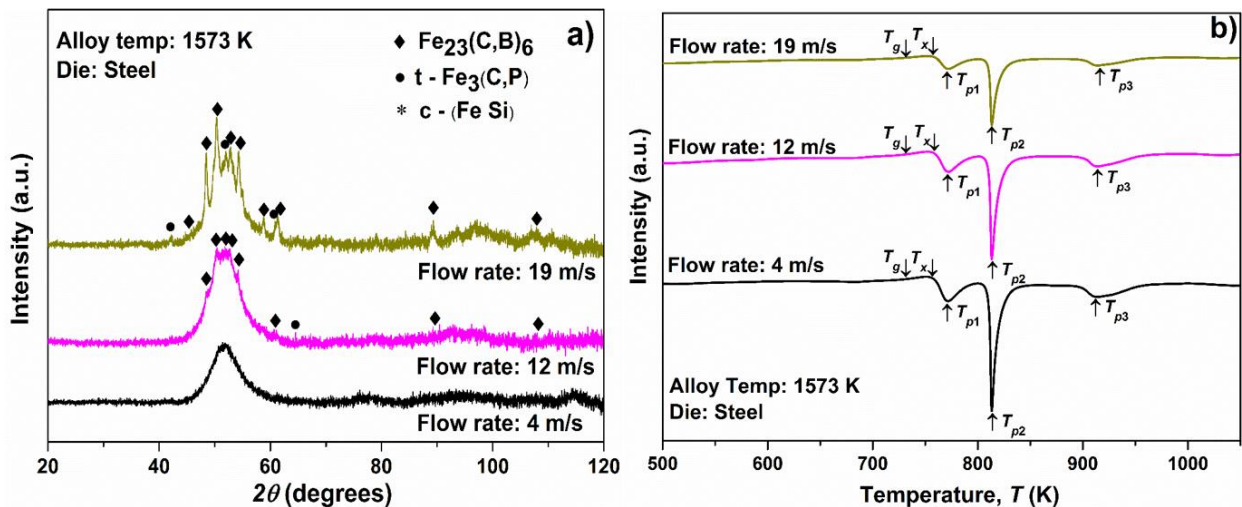
Figure 5.4: (a) XRD patterns and (b) DSC traces of the samples produced at different flow rates 4, 12 and 19 m/s, respectively using steel die.

At low flow rates, a fluid flow in a stable line with no mixing of the fluid, this phenomenon is known as laminar flow. On contrary, at higher flow rates, the stability of the fluid is compromised leading to macroscopic mixing, this phenomenon is known as turbulent flow. Moreover with increase in flow rate molten metal experiences increase in shear rate at different cross-sections. Shao *et al.* [277] showed that change in shear flow in SLR influences the local compositional

heterogeneities; with increase in the shear flow the magnitude of the heterogeneities also increases leading to drastic decrease in crystallization time. A similar trend was observed in our casting as well, the crystallization rate increases with the increase of the molten metal flow rate from 4 to 19 m/s. This may be because the molten metal undergoes sever strain while entering and exiting the shaft section, cross-section of the shaft is almost one fourth of the bit and head section (see Fig. 5.1 (a) and (b)). Moreover the repeated change in shear rate may induce several heterogeneous nucleation site, which further increases the fragility of the glass-forming liquid [278]. Hence, for steel die, 4 m/s is the optimum flow rate for obtaining a good key sample without any defects. Table 5.3 compares the glass transition temperature T_g, the onset of crystallization T_x and ΔT_x the extension of the supercooled liquid region (SLR) of the industrial cast key samples with the literature data [89] and also with the glassy samples produced in our laboratory (IFW Dresden). The maximum achievable diameter reported for this glass is 5 mm by Liu *et al*. [89], in our work we were able to cast key samples with maximum thickness of 3.5 mm. The reduced glass transition temperature $T_{rg} = T_g/T_{liq}$ (0.57) and extension of the supercooled liquid region (SLR, $\Delta T_x = T_x - T_g$) (35 K), are just slightly lower than the reported values of 0.58 and 37 K, respectively [89].

Table 5.3: Comparison between literature data [89] and our data for the $Fe_{74}Mo_4P_{10}C_{7.5}B_{2.5}Si_2$ glassy samples (3 mm rod and key sample). T_g is the glass transition temperature, T_x is the onset of crystallization, ΔT_x the extension of the supercooled liquid region (SLR), measured as the difference between crystallization and glass transition temperatures, T_{liq} is the liquidus temperature, T_{rg} the reduced glass transition temperature, measured as the ratio between the glass transition and liquidus temperatures [185].

$Fe_{74}Mo_4P_{10}C_{7.5}B_{2.5}Si_2$	D (mm)	T_g (K)	T_x (K)	ΔT_x (K)	T_{liq} (K)	T_{rg} (T_g/T_{liq})
Literature [89]	5	729	766	37	1266	0.58
Sample cast in lab - copper mold	3	730	765	35	1283	0.57
Key sample	--	725	760	35	1283	0.57

Though a small difference in T_x and T_g values between the industrial cast key sample and lab cast rod samples is observed, they are well within the experimental error range. The SLR and the reduced glass transition temperature are considered as an important criteria to evaluate the GFA of the alloy [8], in such case our alloy has slightly lower GFA compared to the data reported in literature. This small decrease in GFA is may be due the difference in the impurity and oxygen contents in the industrial raw materials. Besides, the differences in T_g and T_x between the lab cast samples and HPDC samples may arise from different cooling rates attained during casting.

It is known from literature that in the melt-spinning process, depending up on the composition of the glass, a steel wheel can outperform the copper wheel and vice versa. To cast the ribbons with low surface roughness, wheel materials with low thermal conductivity k is preferred [274]. Lower the k, longer the dwell time between the wheel and molten metal, leading to low surface roughness. Steel wheels are preferably used to prepare the amorphous ribbons of several binary alloys [20] as well as soft magnetic alloys [77]. Hence, steel die is the most suitable choice for production of glassy keys, because of the lower thermal conductivity k, better thermal contact, higher tool life and lower manufacturing cost.

The residual stress developed during the casting (thicker and thinner sections will have different stress because of the difference in their cooling rate) plays an important role in influencing the mechanical properties of the metallic glass [279, 280]. In Zr-based metallic glass a residual stress up to 900 MPa can be developed during cooling [279]. In case of the Fe-based metallic glasses, there is not enough data available on the magnitude of residual stress that can be developed during casting, but apparently the stress generated is large enough to initiate a crack between the regions having thermal mismatch [279] (e.g. glassy and crystalline parts) in the specimens. Once the crack is initiated it will try to reduce the stress concentration by propagating and splitting in to multiple branches [281]. The crack branching occurs predominately at all possible interfaces between the glassy and crystalline parts of the specimens due to the differences in their mechanical/elastic properties [280]. Figure 5.5 represents the SEM image (BSE mode) taken at different places over the cross-section of the key stem cast at 1353 K using copper mold.

Figure 5.5: SEM images of the key cast at 1353 K (a) taken close to the outer surface, showing a completely glassy part of the key (b) taken in between the core and the outer surface, revealing the interface between the glassy and crystalline parts and (c). taken at the core of the key, showing a completely crystalline region [185].
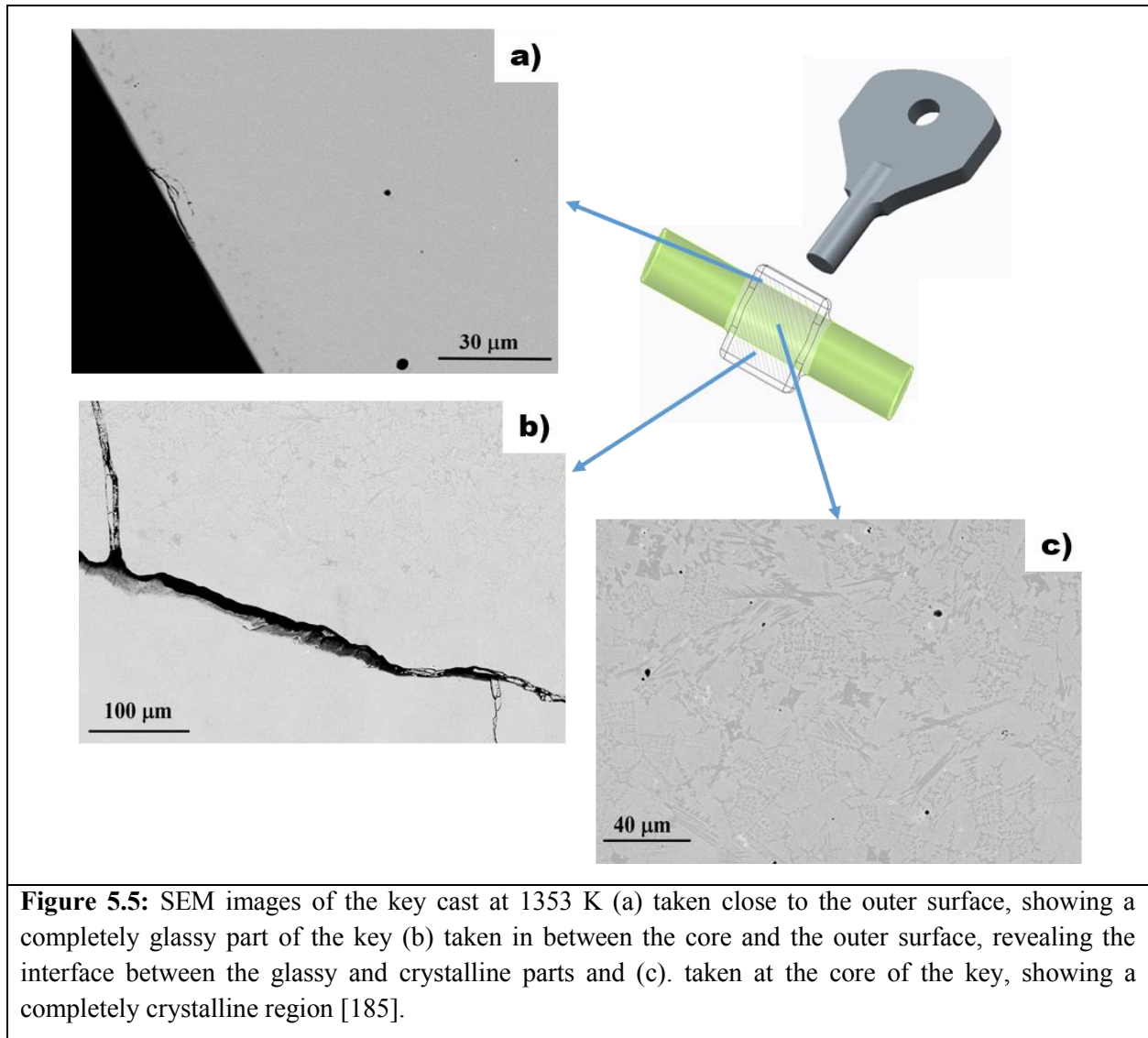
The image presented in Fig. 5.5 (a) taken close to the surface shows a completely glassy part of the sample. The image presented in Fig. 5.5 (b) was taken in between the core and surface shows the interface between the glassy matrix and crystalline part separated by a crack. The initial development of this crack may be due to the thermal mismatch strain developed during cooling [279]. This glassy and crystalline interface also reveals the skin effect. The image taken at the core of the stem reveals the presence of micron-size crystals and fine gas holes [184] in the glassy matrix. The skin effect are more visible in the keys cast at low temperature using copper mold, but also exist in the keys cast at high temperature where the cores are very small to detect.

5.2.3 Influence of HPDC parameters on magnetic properties

It is well known that during the casting of complex/critical parts with different cross-sections significant magnitude of residual stress will develop inside the specimens, in such cases presence of even very small crystals leads to the fracture of the samples (see Fig. 5.5 (b)). In order to ensure the quality of the key samples coercivity of the samples were measured. Table 5.4 lists the variation of the coercivity (H_c) of the key samples as a function of alloy temperature (K), flow rate (m/s) and die material along with the sample prepared in the laboratory condition. It is commonly accepted that soft magnetic BMG have very low values of coercivity [95].

Table 5.4: Coercivity of the keys as a function of casting speed (m/s), alloy temperature (K) and die material. Coercivity of the 3 mm rod cast in lab condition is given for reference purpose [185].

Die Material	Flow rate (m/s) ± 0.5	Alloy Temperature (K) ± 10	Coercivity H_c (A/m) ± 0.1
Steel	4	1573	7.8
Steel	4	1443	210
Steel	4	1393	>2000
Steel	4	1353	>2000
Steel	12	1573	9.8
Steel	19	1573	80
Copper	4	1573	57.9
Copper	4	1443	59.2
Copper	4	1393	>2000
Copper	4	1353	>2000
Rod cast in lab - copper die	---	1523	5

The presence of even small volume fraction of crystalline inclusions will significantly increases the coercivity due to domain pinning. Only if the size of the crystals are comparable or small than the size of the domain walls they have no influence on the coercivity [87, 217, 282]. Such small crystals or nuclei cannot be detected by X-ray diffraction.

In case of the steel die, the coercivity values of the keys cast at low flow rate (4 m/s) decreases from more than 2000 A/m to 7.8 A/m, as the casting temperature increases from 1353 K to 1573 K. However, even at high temperature (1573 K), upon increasing the flow rate from 4 m/s to 19 m/s the coercivity increases from 7.8 A/m to 80 A/m, indicating the presence of small crystals. The coercivity of the keys cast using copper die decreases from more than 2000 A/m to 57.9 A/m with increase in casting temperature for low rate. The high coercivity value 57.9 A/m for the key cast at 1573 K, indicates the presence of crystals in the sample, in agreement with the previous DSC and XRD findings.
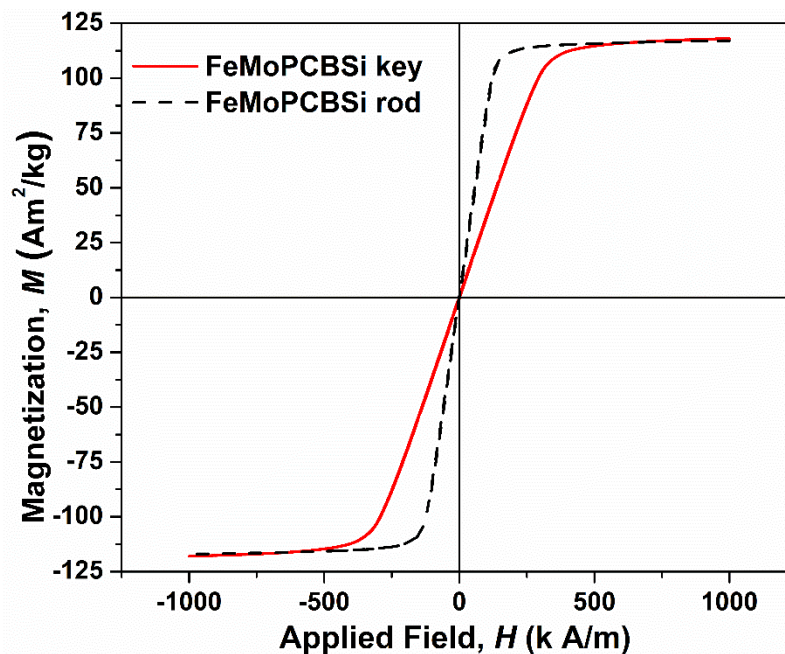
Figure 5.6: Hysteresis loops for the key cast by HPDC and a 2 mm rod cast under laboratory conditions.

The hysteresis loops for the glassy sample cast in laboratory condition (continuous red line) using copper die and the key cast with steel die (black dotted line) at 1573 K using the HPDC method are shown in Fig. 5.6. Although the samples cast under laboratory condition and HPDC exhibits the same saturation magnetization (118 Am^2/kg), there are some differences in the initial part of the loops. The coercivity and the shape of the hysteresis loops are greatly influenced by (a) the microstructure of the magnetic material (b) the geometry [282]. The geometry of the specimen also plays a major role in influencing the magnetic properties. With a proper geometry, the size and the shape effect could be reduced. Hence, with the above optimized parameters (casting temperature, flow rate and die material) the HPDC method can be used to produce soft ferromagnetic BMG parts in complex geometries.

Chapter 6

Summary

Ferromagnetic Fe-based bulk metallic glasses (BMGs) are very attractive for industrial application because of their high stability against crystallization, excellent soft magnetic properties and high mechanical strength. Although Fe-based glasses are moderate glass formers the important aspect which limits the application of Fe-based BMGs as engineering materials is the brittle behavior under mechanical loading. Improving the mechanical properties of Fe-based glasses without deteriorating their magnetic properties will help in improving the application of Fe-based glasses. The aim of this work is to improve the compressive plastic deformation in soft ferromagnetic Fe-based BMGs with the addition of soft elements like Cu and Ga.

The thesis focused on two soft ferromagnetic Fe-based BMGs: $Fe_{36}Co_{36}B_{19.2}Si_{4.8}Nb_4$ (FeCoBSiNb) and $Fe_{74}Mo_4P_{10}C_{7.5}B_{2.5}Si_2$ (FeMoPCBSi). Both glasses have good glass-forming ability (GFA) and excellent soft magnetic properties. In addition to the high corrosion resistance, the mechanical properties are also very good. Unfortunately, the plastic deformation behavior of these glasses is poor. In order to improve the plastic deformation of FeCoBSiNb and FeMoPCBSi glasses, small amounts of Cu and Ga are added and the resultant change in mechanical properties was investigated. It has been proven that the addition of small amounts of impurities will adversely affect the GFA and the soft magnetic properties of ferromagnetic BMGs. Hence, the microstructural evolution, as well as thermal and magnetic properties were studied. Furthermore, the effect of HPDC process parameters on microstructural evolution, thermal, and magnetic properties of $Fe_{74}Mo_4P_{10}C_{7.5}B_{2.5}Si_2$ BMG has also been investigated.

The FeCoBSiNb glass was investigated first; according to literature the critical diameter (t_c) for the FeCoBSiNb glass is 5 mm diameter, but in my experimental work t_c for this alloy was 3 mm diameter and 5 cm length. This difference in the t_c reported in the literature and in my work is could be due to the presence of impurity elements, which decreases the GFA of this alloy. In order to study the influence of Cu and Ga addition on FeCoBSiNb glass, at first a, FeCoBSiNb master alloy was prepared by adding pure elements and then systematically Cu and Ga elements were added through arc melting. From the [FeCoBSiNb] $_{100-x,y}$ (Cu_x, Ga_y)(x = 0, 0.5)(y = 0, 0.5, 1, 2, 3,

4 and 5) master alloys several amorphous ribbons and rods were prepared under the same conditions. The following results are achieved after microstructural characterization, thermal, magnetic and mechanical measurements of different samples in the current work:

➢ The addition of Cu is beneficial only up to 0.5 at.% for larger Cu additions the GFA decreases drastically. Addition of Cu decreases the thermal stability and completely changes the crystallization behavior of the glass. Upon crystallization a, $(Fe,Co)_{23}B_6$ – type phase forms as a primary phase in Cu- free glass, whereas the Cu addition leads to the formation of α-Fe as the primary phase.

➢ Only a marginal increase in saturation magnetization (M_s) values is observed for the Cu added glass, but the coercivity values remains almost same for both Cu free and Cu added glass.

➢ The addition of Cu proved to improve the plastic deformability of the glass. However no typical vein patterns are observed on the fracture surfaces. The absence of these vein patterns indicates that plastic deformation are takes place only on the atomic scale.

➢ Unlike Cu, the addition of Ga up to 1.5 at.% increases the thermal stability and the crystallization behavior remains unaltered. However, when more than 1.5 at.% Ga is added it decreases the thermal stability and also alters the crystallization behavior of the glass.

➢ Magnetic properties start to decrease marginally with increase in the Ga addition.

➢ The addition of Ga improves the plastic deformability of the glass. The presence of a large number of veins and μm size molten droplets on the vein patterns indicates that the presence of Ga atoms leads to formation of soft zones, whose melting point is much lower compared to the rest of the alloy. These soft zones are responsible for the plastic deformation of this glass.

In the second part of my work FeMoPCBSi glass was investigated. Similar to the FeCoBSiNb glass the t_c obtained in my experimental work for FeMoPCBSi glass is 3 mm, which is lower compared to the t_c of 5 mm reported in literature. However, due to the high content of Fe this glass is not very brittle, but shows some plastic deformability. Unlike the FeCoBSiNb alloy, the FeMoPCBSi alloy was prepared from a mixture of pure and industrial grade elements. The Cu and Ga elements were systematically added to the master alloy through arc melting. Several ribbons and rods were prepared from the $[FeMoPCBSi]_{100-x, y}$ $(Cu)_x$ $(Ga)_y$ (x = 0, 0.5, 1)(y = 0, 0.5, 1, 1.5

and 2) master alloys under same conditions. The results obtained from the detailed investigations can be summarized as below:

➢ The addition of Cu is beneficial only up to 0.5 at.%. For large amounts the GFA decreases drastically. Addition of Cu marginally decreases the thermal stability and significantly changes the crystallization behavior of the glass. Upon crystallization, a $Fe_{23}(C,B)_6$ – type phase forms as a primary phase in Cu- free glass, whereas the Cu addition leads to the simultaneous formation of α-Fe and $Fe_{23}(C,B)_6$ – type phase.

➢ The magnetic properties start to decrease marginally with increase in the Cu addition

➢ Addition of 0.5 at.% Cu significantly improves the plastic deformability of the glass, more than 0.5 at.% the plastic deformability decreases.

➢ Unlike Cu, the addition of up to 2 at.% Ga increases the thermal stability and the crystallization behavior remains unaltered. However, when more than 2 at.% Ga are added the GFA deteriorates drastically.

➢ The magnetic properties starts to decrease marginally with increase in the Ga addition.

➢ Similar to the FeCoBSiNb glass, the addition of Ga in FeMoPCBSi glass also improves the plastic deformability. The presence of a large number of vein patterns and μm size molten droplets on the vein patterns indicates that the Ga addition has the same effect for both glasses.

Addition of small amounts of Ga could be an viable solution to improve the plastic deformability in the ferromagnetic Fe-based metallic glasses without compromising on thermal and magnetic properties of the glass.

In the final part of my work I tried to produce FeMoPCBSi BMG on industrial scale using the high pressure die casting method (HPDC). The great advantage of HPDC is that even marginal glass formers can be used and complex geometries with high dimensional accuracy can be achieved. Compared to FeCoBSiNb, the FeMoPCBSi alloy has a lower melting point, a higher oxidation resistance and also better mechanical properties. Hence, I choose to start the industrial scale process with the FeMoPCBSi alloy.

The quality of the samples is strongly influenced by proper choice of die material, alloy temperature and flow rate of the material. A copper die with high thermal conductivity leads to the skin effect. Similarly, a high flow of 19 m/s rate influences the viscosity change due to the higher

shear rate leading to decrease in GFA of the glass. All samples produced under optimized conditions exhibit thermal stability and soft magnetic properties which are nearly the same as those of samples prepared under laboratory conditions. It should be mentioned here that the quality of the produced keys in the present work can be still optimized further by fine-tuning the casting parameters. This will improve the surface finish, reduce the porosity and hamper the formation of cracks during solidification. Nevertheless, these first results confirm that HPDC is useful for the production of bulk glassy alloys with good soft magnetic properties.

Through this work on HPDC process I have made a significant step towards the realization of Fe-based metallic glasses as an engineering materials.

Outlook

As demonstrated in the thesis, the addition of Ga in FeCoBSiNb and FeMoPCBSi glasses is very promising in improving the mechanical properties, however the mechanism behind this is yet to be understood clearly. We believe that in depth analysis using TEM and synchrotron radiation will shed more light to understand this mechanisms. I have already performed synchrotron studies on all the samples containing Ga, and the data is presently under analysis. I hope to extract more detailed information regarding the presence of any short/medium-range order (SRO/MRO). Additionally, in situ heating Synchrotron and TEM experiments are planned to understand the formation and growth of competing phases. More in depth analysis are planned to understand the reasons behind the formation of molten droplets in the fractured zones.

Although I have gained preliminary knowledge in improving the plastic deformation of ferromagnetic Fe-based BMGs, I believe, can be further improved. First and foremost, efforts are being made to choose different minor alloying elements, which will further help in improving the mechanical properties.

Regarding the production of Fe-based BMG in industrial scale, though this work clearly demonstrates that HPDC method can be successfully used for the production of ferromagnetic Fe-based BMGs, I believe, surface quality can be further improved. Several new experiments are planned in HPDC with new set of casting parameters to improve the surface quality of the samples. HPDC is a promising method to produce BMGs in large quantity, however very few studies are reported so far.

As a concluding remark, I strongly believe that the learnings from this work, from the point of view of improving the mechanical properties as well as producing the BMG in industrial scale in the aforementioned glass-forming alloys, may be directly extended to other similar ferromagnetic Fe-based glass-forming systems having poor mechanical properties.

Acknowledgements

I thank Dr. Thomas Gemming and all the members of IFW Dresden for the cooperation, help and the nice working environment.

During my work I had various collaboration with peoples from different countries and I visited other laboratories. I would like to thank all the peoples who helped me and who gave me opportunity to enlarge my research field: From Breuckmann GmbH & Co KG, Germany, Dr. András Bárdos and Mr. Volker Breuckmann for the High Pressure Die casting experiment and scientific discussions, as well as for his help and hospitality during my visit to the Industry. From University of Cambridge, United Kingdom, Prof. Dr. A. Lindsay Greer, From Institue National Polytechnique de Grenoble, France, Prof. Dr. Yannick Champion, From National Institute of Research and Development for Technical Physics, Romania, Dr. Nicoleta Lupu and Dr. Gabriel Ababei for TEM measurements, From Politehnica University Timisoara, Romania, Assoc. Prof. Dr. Mircea Nicoara. I would also like to acknowledge my project colleagues Maria, Carlos, Alexandra, Fabian, Pierre, Daria, Carolina, Sara, Victoria, Pablo, Attila, George, Yanpeng, Nicolas for the huge amount of right and wrong information about science as well as the life in Europe.

I thank my office colleagues Supriya, Lixia, Pei and Hans for the scientific discussions, creative collaborations, great memories and amazing time. Many thanks to Prashant, Raghu and Vamshi for their camaraderie. I wish to express my sincere thanks to all my flat mates Tamil and Minoj for the pleasant atmosphere at home. I also thank Eshwar, Nisha, Anamika, Mayukh, Mohul, Sudipa, Shreya, Tushar, Pranab, Vijay, Shankar, Madhuri and for the great company and the homely atmosphere outside work.

Finally, I would like to give my special thanks to my mother, father, brother and sister-in-law for their constant support and encouragement. Special thanks to my wife Priya, for her love and support. This thesis is dedicated to my brother Shanmugam Ramasamy, who have been my constant source of guidance and motivation.

Thanks to all family and friends and family, of near and far, for being part of this journey.

Dakeschön!

Publications

1. R. Parthiban, M. Stoica, I. Kaban, N. V. Ravikumar, J. Eckert, **Intermetallics**, 66 (2015) 48-55.

2. M. Stoica, R. Parthiban, I. Kaban, S. Scudino, M. Nicoara, Gavin B. M. Vaughan, J. Wright, Ravi Kumar, J. Eckert, **Acta Materialia**, 95 (2015) 335-342.

3. R. Parthiban, M. Stoica, A.H. Taghvaei, K. G. Prashanth, N.V. Ravikumar and J. Eckert, **Journal of Applied Physics**, 119 (2016) 073908.

4. M. Nicoara, A. Raduta, R. Parthiban, C. Locovei, J. Eckert, M. Stoica, **Acta Biomaterialia**, 36 (2016) 323-331.

5. Mircea Nicoara, Cosmin Locovei, Viorel Aurel Șerban, R. Parthiban, Mariana Calin and Mihai Stoica, **Materials**, 9 (2016) 331.

6. R. Parthiban, M. Stoica, M. Calin, J. Eckert, **Solid State Phenomena**, 254 (2016) 60-64.

7. Parthiban Ramasamy, Attila Szabo, Stefan Borzel, Jürgen Eckert, Mihai Stoica and András Bárdos, **Scientific Reports**, 6 (2016) 35258.

8. Parthiban Ramasamy, M. Stoica, S. Bera, M. Calin, J. Eckert, **Journal of Alloys and Compounds**, 707 (2017) 78-81.

9. Supriya Bera, Baran Sarac, Sascha Balakina, Parthiban Ramasamy, Mihai Stoica, Mariana Calin, Jürgen Eckert, **Materials and Design**, 120 (2017) 204-211.

10. Ramasamy Parthiban, Rub Nawaz Shahid, Sergio Scudino, Jürgen Eckert, Mihai Stoica, **Journal of alloys and Compounds**, 725 (2017) 227-236.

References

[1]   J. E. Shelby. Introduction to glass science and technology: Royal Society of Chemistry, 2005.

[2]   L. D. Pye, V. D. Fréchette, N. J. Kreidl. Borate glasses: structure, properties, applications: Springer Science & Business Media, 2012.

[3]   M. Stoica. Fe-Based Bulk Metallic Glasses: Understanding the Influence of Impurities on Glass Formation: Springer, 2017.

[4]   T. R. Anantharaman, C. Suryanarayana, Rapidly solidified metals: a technological overview, Key Eng. Mater. 17 (1987) 1-260.

[5]   H. Davies, J. Aucote, J. Hull, Amorphous nickel produced by splat quenching, Nature 246 (1973) 13-14.

[6]   A. L. Greer, Metallic glasses, Science 267 (1995) 1947-1953.

[7]   W. L. Johnson, Bulk glass-forming metallic alloys: Science and technology, MRS Bull. 24 (1999) 42-56.

[8]   A. Inoue, Stabilization of metallic supercooled liquid and bulk amorphous alloys, Acta Mater. 48 (2000) 279-306.

[9]   W.-H. Wang, C. Dong, C. Shek, Bulk metallic glasses, Mater. Sci. Eng., R 44 (2004) 45-89.

[10]   Y. Cheng, E. Ma, Atomic-level structure and structure–property relationship in metallic glasses, Prog. Mater Sci. 56 (2011) 379-473.

[11]   E. Axinte, Metallic glasses from "alchemy" to pure science: present and future of design, processing and applications of glassy metals, Mater. Des. 35 (2012) 518-556.

[12]   W. H. Wang, The elastic properties, elastic models and elastic perspectives of metallic glasses, Prog. Mater Sci. 57 (2012) 487-656.

[13]   D. Turnbull, Under what conditions can a glass be formed, Contemp. Phys. 10 (1969) 473-488.

[14]   W. Klement, R. Willens, P. Duwez, Non-crystalline structure in solidified gold–silicon alloys, Nature 187 (1960) 869-870.

[15]   C. A. Angell, Formation of Glasses from Liquids and Biopolymers, Science 267 (1995) 1924-1935.

[16]   J. C. Dyre, Colloquium: The glass transition and elastic models of glass-forming liquids, Rev. Mod. Phys. 78 (2006) 953-972.

[17]   M. Chen, A brief overview of bulk metallic glasses, NPG Asia Materials 3 (2011) 82-90.

[18]   A. Greer, E. Ma, Bulk metallic glasses: at the cutting edge of metals research, MRS Bull. 32 (2007) 611-619.

[19]   M. Chen, Mechanical behavior of metallic glasses: microscopic understanding of strength and ductility, Annu. Rev. Mater. Res. 38 (2008) 445-469.

[20]   H. Chen, C. Miller, A rapid quenching technique for the preparation of thin uniform films of amorphous solids, Rev. Sci. Instrum. 41 (1970) 1237-1238.

[21]   H. Chen, Thermodynamic considerations on the formation and stability of metallic glasses, Acta Metall. 22 (1974) 1505-1511.

[22]   A. Drehman, A. Greer, D. Turnbull, Bulk formation of a metallic glass: $Pd_{40}Ni_{40}P_{20}$, Appl. Phys. Lett. 41 (1982) 716-717.

[23]   H. Kui, A. L. Greer, D. Turnbull, Formation of bulk metallic glass by fluxing, Appl. Phys. Lett. 45 (1984) 615-616.

[24]   A. Inoue, K. Ohtera, K. Kita, T. Masumoto, New amorphous Mg-Ce-Ni alloys with high strength and good ductility, Jpn. J. Appl. Phys. 27 (1988) L2248-L2251.

[25]   A. Inoue, T. Zhang, T. Masumoto, Al–La–Ni amorphous alloys with a wide supercooled liquid region, Mater. Trans., JIM 30 (1989) 965-972.

[26]   A. Inoue, T. Zhang, T. Masumoto, Zr–Al–Ni amorphous alloys with high glass transition temperature and significant supercooled liquid region, Mater. Trans., JIM 31 (1990) 177-183.

[27]   A. Inoue, J. S. Gook, Fe-based ferromagnetic glassy alloys with wide supercooled liquid region, Mater. Trans., JIM 36 (1995) 1180-1183.

[28]   A. Inoue, N. Nishiyama, T. Matsuda, Preparation of bulk glassy $Pd_{40}Ni_{10}Cu_{30}P_{20}$ alloy of 40 mm in diameter by water quenching, Mater. Trans., JIM 37 (1996) 181-184.

[29]   A. Inoue, N. Nishiyama, H. Kimura, Preparation and thermal stability of bulk amorphous $Pd_{40}Cu_{30}Ni_{10}P_{20}$ alloy cylinder of 72 mm in diameter, Mater. Trans., JIM 38 (1997) 179-183.

[30]   A. Inoue, T. Zhang, Fabrication of bulk glassy $Zr_{55}Al_{10}Ni_5Cu_{30}$ alloy of 30 mm in diameter by a suction casting method, Mater. Trans., JIM 37 (1996) 185-187.

[31]   A. Inoue, T. Zhang, T. Itoi, A. Takeuchi, New Fe–Co–Ni–Zr–B amorphous alloys with wide supercooled liquid regions and good soft magnetic properties, Mater. Trans., JIM 38 (1997) 359-362.

[32]   T. Zhang, A. Inoue, Thermal and mechanical properties of Ti–Ni–Cu–Sn amorphous alloys with a wide supercooled liquid region before crystallization, Mater. Trans., JIM 39 (1998) 1001-1006.

[33]   T. Zhang, A. Inoue, Preparation of Ti–Cu–Ni–Si–B amorphous alloys with a large supercooled liquid region, Mater. Trans., JIM 40 (1999) 301-306.

[34]   F. Guo, S. J. Poon, G. J. Shiflet, Metallic glass ingots based on yttrium, Appl. Phys. Lett. 83 (2003) 2575-2577.

[35]   F. Guo, S. Poon, G. Shiflet, CaAl-based bulk metallic glasses with high thermal stability, Appl. Phys. Lett. 84 (2004) 37-39.

[36]   Z. P. Lu, C. T. Liu, J. R. Thompson, W. D. Porter, Structural Amorphous Steels, Phys. Rev. Lett. 92 (2004) 245503-4.

[37]   D. Xu, G. Duan, W. L. Johnson, Unusual glass-forming ability of bulk amorphous alloys based on ordinary metal copper, Phys. Rev. Lett. 92 (2004) 245504-4.

[38]   F. Guo, H.-J. Wang, S. J. Poon, G. J. Shiflet, Ductile titanium-based glassy alloy ingots, Appl. Phys. Lett. 86 (2005) 091907-3.

[39]   H. Fujimori, T. Masumoto, Y. Obi, M. Kikuchi, On the magnetization process in an iron-phosphorus-carbon amorphous ferromagnet, Jpn. J. Appl. Phys. 13 (1974) 1889-1890.

[40]   R. O'Handley, R. Hasegawa, R. Ray, C. P. Chou, Ferromagnetic properties of some new metallic glasses, Appl. Phys. Lett. 29 (1976) 330-332.

[41]   W. Chan. Rapidly solidifed alloys. edited by: H. H. Liebermann, Marcel Dekker. New York (1993) 1-15.

[42]   A. Inoue, Y. Shinohara, J. S. Gook, Thermal and magnetic properties of bulk Fe-based glassy alloys prepared by copper mold casting, Mater. Trans., JIM 36 (1995) 1427-1433.

[43]   A. Inoue, T. Zhang, H. Koshiba, A. Makino, New bulk amorphous Fe–(Co, Ni)–M–B (M= Zr, Hf, Nb, Ta, Mo, W) alloys with good soft magnetic properties, J. Appl. Phys. 83 (1998) 6326-6328.

[44]   T. Itoi, A. Inoue, High-frequency permeability of $(Fe, Co, Ni)_{62}Nb_8B_{30}$ amorphous alloys with a wide supercooled liquid region, Appl. Phys. Lett. 74 (1999) 2510-2512.

[45]   W. Zhang, A. Inoue, Thermal and Magnetic Properties of Fe–Co–Ln–B (Ln= Nd, Sm, Tb or Dy) Amorphous Alloys with High Magnetostriction, Mater. Trans., JIM 40 (1999) 78-81.

[46]   M. Trudeau, J. Huot, R. Schulz, D. Dussault, A. Van Neste, G. L'Espérance, Nanocrystalline Fe-(Co, Ni)-Si-B: The mechanical crystallization of amorphous alloys and the effects on electrocatalytic reactions, Phys. Rev. B 45 (1992) 4626-4636.

[47]   S. Pang, T. Zhang, K. Asami, A. Inoue, Synthesis of Fe–Cr–Mo–C–B–P bulk metallic glasses with high corrosion resistance, Acta Mater. 50 (2002) 489-497.

[48]   H. Chiriac, N. Lupu, Design and preparation of new soft magnetic bulk amorphous alloys for applications, Mater. Sci. Eng., A 375 (2004) 255-259.

[49]   D. Liu, W. Sun, H. Zhang, Z. Hu, Preparation, thermal stability and magnetic properties of Fe–Co–Ni–Zr–Mo–B bulk metallic glass, Intermetallics 12 (2004) 1149-1152.

[50]   A. Inoue, B. L. Shen, C. T. Chang, Super-high strength of over 4000 MPa for Fe-based bulk glassy alloys in $[(Fe_{1-x}Co_x)_{0.75}B_{0.2}Si_{0.05}]_{96}Nb_4$ system, Acta Mater. 52 (2004) 4093-4099.

[51]   S. Lee, H. Kato, T. Kubota, K. Yubuta, A. Makino, A. Inoue, Excellent thermal stability and bulk glass forming ability of Fe-B-Nb-Y soft magnetic metallic glass, Mater. Trans. 49 (2008) 506-512.

[52]   M. Stoica, V. Kolesar, J. Bednarčic, S. Roth, H. Franz, J. Eckert, Thermal stability and magnetic properties of partially Co-substituted $(Fe_{71.2}B_{24}Y_{4.8})_{96}Nb_4$ bulk metallic glasses, J. Appl. Phys. 109 (2011) 054901-6.

[53]   T. Shen, R. Schwarz, Bulk ferromagnetic glasses prepared by flux melting and water quenching, Appl. Phys. Lett. 75 (1999) 49-51.

[54]   B. Shen, A. Inoue, Bulk glassy Fe-Ga-PCB-Si alloys with high glass-forming ability, high saturation magnetization and good soft magnetic properties, Mater. Trans. 43 (2002) 1235-1239.

[55]   P. Pawlik, H. Davies, M. Gibbs, Magnetic properties and glass formability of $Fe_{61}Co_{10}Zr_5W_4B_{20}$ bulk metallic glassy alloy, Appl. Phys. Lett. 83 (2003) 2775-2777.

[56]   M. Stoica, S. Roth, J. Eckert, L. Schultz, M. Baro, Bulk amorphous FeCrMoGaPCB: Preparation and magnetic properties, J. Magn. Magn. Mater. 290 (2005) 1480-1482.

[57]   A. Inoue, B. L. Shen, H. Koshiba, H. Kato, A. R. Yavari, Cobalt-based bulk glassy alloy with ultrahigh strength and soft magnetic properties, Nat. Mater. 2 (2003) 661-663.

[58]   S. Sheng, C. Ma, S. Pang, T. Zhang, Glass-forming ability and mechanical properties of Sm-doped Fe–Cr–Mo–C–B glassy alloys, Mater. Trans. 46 (2005) 2949-2953.

[59]   A. Inoue, B. L. Shen, C. T. Chang, Fe- and Co-based bulk glassy alloys with ultrahigh strength of over 4000 MPa, Intermetallics 14 (2006) 936-944.

[60]   G. H. Fredrickson, Recent developments in dynamical theories of the liquid-glass transition, Annu. Rev. Phys. Chem. 39 (1988) 149-180.

[61]   J. C. Dyre, Source of non-Arrhenius average relaxation time in glass-forming liquids, J. Non-Cryst. Solids 235 (1998) 142-149.

[62]   C. Suryanarayana, A. Inoue. Bulk Metallic Glasses: CRC Press, Taylor & Francis Group, 2011.

[63]   C. A. Angell, K. L. Ngai, G. B. McKenna, P. F. McMillan, S. W. Martin, Relaxation in glassforming liquids and amorphous solids, J. Appl. Phys. 88 (2000) 3113-3157.

[64]   Z. Lu, C. Liu, Glass formation criterion for various glass-forming systems, Phys. Rev. Lett. 91 (2003) 115505-4.

[65]   Z. Lu, C. Liu, A new glass-forming ability criterion for bulk metallic glasses, Acta Mater. 50 (2002) 3501-3512.

[66]   A. L. Greer, Confusion by design, Nature 366 (1993) 303-304.

[67]   M. H. Cohen, D. Turnbull, Molecular transport in liquids and glasses, J. Chem. Phys. 31 (1959) 1164-1169.

[68]   G. Adam, J. H. Gibbs, On the temperature dependence of cooperative relaxation properties in glass-forming liquids, J. Chem. Phys. 43 (1965) 139-146.

[69]   M. Volmer, A. Weber, Keimbildung in übersättigten Gebilden, Z. phys. Chem. 119 (1926) 277-301.

[70]   M. Stoica. Casting and characterization of Fe-(Cr, Mo, Ga)-(P, C, B) soft magnetic bulk metallic glasses. Faculty of Mathematics and Natural Sciences, vol. Ph.D: Technischen Universität Dresden, 2005.

[71]   R. Becker, W. Doring, Kinetic treatment of the nucleation in supersaturated vapors, (1954).

[72]   D. Turnbull, J. C. Fisher, Rate of nucleation in condensed systems, J. Chem. Phys. 17 (1949) 71-73.

[73]   E. Buckle, A. Ubbelohde. Studies on the freezing of pure liquids. I. Critical supercooling in molten alkali halides. Proc. R. Soc. London, Ser. A, 259 (1960) 325-340.

[74]   M. Glicksman, C. Vold, Determination of absolute solid-liquid interfacial free energies in metals, Acta Metall. 17 (1969) 1-11.

[75]   A. Inoue, A. Takeuchi, Recent development and application products of bulk glassy alloys, Acta Mater. 59 (2011) 2243-2267.

[76]   V. Ponnambalam, S. J. Poon, G. J. Shiflet, Fe-based bulk metallic glasses with diameter thickness larger than one centimeter, J. Mater. Res. 19 (2004) 1320-1323.

[77]   M. Mitera, T. Masumoto, N. Kazama, Effect of silicon addition on the magnetic properties of Fe-B-C amorphous alloys, J. Appl. Phys. 50 (1979) 7609-7611.

[78]   Y. Yoshizawa, S. Oguma, K. Yamauchi, New Fe-based soft magnetic alloys composed of ultrafine grain structure, J. Appl. Phys. 64 (1988) 6044-6046.

[79]   G. Herzer, Grain structure and magnetism of nanocrystalline ferromagnets, IEEE Trans. Magn. 25 (1989) 3327-3329.

[80]   Y. Yoshizawa, K. Yamauchi, Fe-based soft magnetic alloys composed of ultrafine grain structure, Mater. Trans., JIM 31 (1990) 307-314.

[81]   K. Suzuki, A. Makino, N. Kataoka, A. Inoue, T. Masumoto, High saturation magnetization and soft magnetic properties of bcc Fe–Zr–B and Fe–Zr–B–M (M= transition metal) alloys with nanoscale grain size, Mater. Trans., JIM 32 (1991) 93-102.

[82]   M. E. McHenry, M. A. Willard, D. E. Laughlin, Amorphous and nanocrystalline materials for applications as soft magnets, Prog. Mater Sci. 44 (1999) 291-433.

[83]   S. Yoshida, T. Mizushima, A. Makino, A. Inoue, Structure and soft magnetic properties of bulk Fe-Al-Ga-P-C-B-Si glassy alloys prepared by consolidating amorphous powders, Mater. Sci. Eng., A 304 (2001) 1019-1022.

[84]   A. Inoue, B. Shen, Soft magnetic bulk glassy Fe-B-Si-Nb alloys with high saturation magnetization above 1.5 T, Mater. Trans. 43 (2002) 766-769.

[85]   A. Inoue, B. Shen, Soft magnetic properties of nanocrystalline Fe–Co–B–Si–Nb–Cu alloys in ribbon and bulk forms, J. Mater. Res. 18 (2003) 2799-2806.

[86]   R. Sundar, S. Deevi, Soft magnetic FeCo alloys: alloy development, processing, and properties, Int. Mater. Rev. 50 (2005) 157-192.

[87]   G. Herzer. Soft Magnetic Materials—Nanocrystalline Alloys. edited. Handbook of Magnetism and Advanced Magnetic Materials. John Wiley & Sons, Ltd (2007).

[88]   T. Zhang, F. Liu, S. Pang, R. Li, Ductile Fe-based bulk metallic glass with good soft-magnetic properties, Mater. Trans. 48 (2007) 1157-1160.

[89]   F. Liu, S. Pang, R. Li, T. Zhang, Ductile Fe–Mo–P–C–B–Si bulk metallic glasses with high saturation magnetization, J. Alloys Compd. 483 (2009) 613-615.

[90]   W. Heisenberg, Zur theorie des ferromagnetismus, Z. Phys. 49 (1928) 619-636.

[91]   S. Chikazumi, C. D. Graham. Physics of Ferromagnetism 2e: Oxford University Press on Demand, 2009.

[92]   N. Yamada, Atomic Magnetic Moment and Exchange Interaction between Mn Atoms in Intermetallic Compounds in Mn-Ge System, J. Phys. Soc. Jpn. 59 (1990) 273-288.

[93]   S. Roth, A. Ferchmin, S. Kobe. Landolt-Brnstein: Numerical Data and Functional Relationships in Science and Technology, vol. III/19 of Magnetic Properties of Metals, ed: HPJ Wijn. Springer-Verlag, Berlin Heidelberg, 1994.

[94]   G. Herzer, Grain size dependence of coercivity and permeability in nanocrystalline ferromagnets, IEEE Trans. Magn. 26 (1990) 1397-1402.

[95]   R. Boll, Soft magnetic metals and alloys, Mater. Sci. Technol. (1993).

[96]   J. Schroers, T. M. Hodges, G. Kumar, H. Raman, A. J. Barnes, Q. Pham, T. A. Waniuk, Thermoplastic blow molding of metals, Mater. Today 14 (2011) 14-19.

[97]   M. Carmo, R. C. Sekol, S. Ding, G. Kumar, J. Schroers, A. D. Taylor, Bulk metallic glass nanowire architecture for electrochemical applications, ACS Nano 5 (2011) 2979-2983.

[98]   M. M. Trexler, N. N. Thadhani, Mechanical properties of bulk metallic glasses, Prog. Mater Sci. 55 (2010) 759-839.

[99]   T. Masumoto, R. Maddin, The mechanical properties of palladium 20 a/o silicon alloy quenched from the liquid state, Acta Metall. 19 (1971) 725-741.

[100]   C. A. Schuh, T. C. Hufnagel, U. Ramamurty, Mechanical behavior of amorphous alloys, Acta Mater. 55 (2007) 4067-4109.

[101]   M. Ashby, A. Greer, Metallic glasses as structural materials, Scripta Mater. 54 (2006) 321-326.

[102]   M. Telford, The case for bulk metallic glass, Mater. Today 7 (2004) 36-43.

[103]   L. Tian, Y.-Q. Cheng, Z.-W. Shan, J. Li, C.-C. Wang, X.-D. Han, J. Sun, E. Ma, Approaching the ideal elastic limit of metallic glasses, Nat. Commun. 3 (2012) 609-6.

[104]   F. R. De Boer, W. Mattens, R. Boom, A. Miedema, A. Niessen, Cohesion in metals, (1988) 774-781.

[105]   A. Inoue, B. Shen, A. Yavari, A. Greer, Mechanical properties of Fe-based bulk glassy alloys in Fe–B–Si–Nb and Fe–Ga–P–C–B–Si systems, J. Mater. Res. 18 (2003) 1487-1492.

[106]   L. YH, T. CW, H. JC, Mechanical Behavior of Au-Based Metallic Glass in Micro-Scale at Ambient and Elevated Temperatures, Mater. Trans. 50 (2009) 2795-2800.

[107]   H. Ma, J. Xu, E. Ma, Mg-based bulk metallic glass composites with plasticity and high strength, Appl. Phys. Lett. 83 (2003) 2793-2795.

[108]   A. Argon, H. Kuo, Plastic flow in a disordered bubble raft (an analog of a metallic glass), Mater. Sci. Eng. 39 (1979) 101-109.

[109]   A. Argon, Plastic deformation in metallic glasses, Acta Metall. 27 (1979) 47-58.

[110]   V. Bulatov, A. Argon, A stochastic model for continuum elasto-plastic behavior. I. Numerical approach and strain localization, Modell. Simul. Mater. Sci. Eng. 2 (1994) 167-184.

[111]   V. Bulatov, A. Argon, A stochastic model for continuum elasto-plastic behavior. II. a study of the glass transition and structural relaxation, Modell. Simul. Mater. Sci. Eng. 2 (1994) 185-202.

[112]   V. Bulatov, A. Argon, A stochastic model for continuum elasto-plastic behavior. III. Plasticity in ordered versus disordered solids, Modell. Simul. Mater. Sci. Eng. 2 (1994) 203-222.

[113]   D. Srolovitz, V. Vitek, T. Egami, An atomistic study of deformation of amorphous metals, Acta Metall. 31 (1983) 335-352.

[114]   C. A. Schuh, A. C. Lund, Atomistic basis for the plastic yield criterion of metallic glass, Nat. Mater. 2 (2003) 449-452.

[115]   J. Langer, Shear-transformation-zone theory of deformation in metallic glasses, Scripta Mater. 54 (2006) 375-379.

[116]   M. Falk, J. Langer, Dynamics of viscoplastic deformation in amorphous solids, Phys. Rev. E 57 (1998) 7192-7205.

[117]   W. Johnson, K. Samwer, A universal criterion for plastic yielding of metallic glasses with a $(T/T_g)^{2/3}$ temperature dependence, Phys. Rev. Lett. 95 (2005) 195501-4.

[118]   A. Argon, L. Shi, Analysis of plastic flow in an amorphous soap bubble raft by the use of an inter-bubble potential, Philos. Mag. A 46 (1982) 275-294.

[119]   D. Polk, D. Turnbull, Flow of melt and glass forms of metallic alloys, Acta Metall. 20 (1972) 493-498.

[120]   F. Spaepen, A microscopic mechanism for steady state inhomogeneous flow in metallic glasses, Acta Metall. 25 (1977) 407-415.

[121]   D. Turnbull, M. H. Cohen, Free-volume model of the amorphous phase: glass transition, J. Chem. Phys. 34 (1961) 120-125.

[122]   R. Busch, A. Masuhr, W. Johnson, Thermodynamics and kinetics of Zr–Ti–Cu–Ni–Be bulk metallic glass forming liquids, Mater. Sci. Eng., A 304 (2001) 97-102.

[123]   P. Steif, F. Spaepen, J. Hutchinson, Strain localization in amorphous metals, Acta Metall. 30 (1982) 447-455.

[124]   V. Khonik, The kinetics of irreversible structural relaxation and homogeneous plastic flow of metallic glasses, Phys. Status Solidi A 177 (2000) 173-189.

[125]   Y. Kawamura, T. Shibata, A. Inoue, T. Masumoto, Workability of the supercooled liquid in the $Zr_{65} Al_{10}Ni_{10}Cu_{15}$ bulk metallic glass, Acta Mater. 46 (1998) 253-263.

[126]   G. Wang, S. Fang, X. Xiao, Q. Hua, J. Gu, Y. Dong, Microstructure and properties of Zr 65 Al 10 Ni 10 Cu 15 amorphous plates rolled in the supercooled liquid region, Mater. Sci. Eng., A 373 (2004) 217-220.

[127]   J. J. Lewandowski, M. Shazly, A. S. Nouri, Intrinsic and extrinsic toughening of metallic glasses, Scripta Mater. 54 (2006) 337-341.

[128]   J. Schroers, N. Paton, Amorphous metal alloys form like plastics, Adv. Mater. Processes 164 (2006) 61-63.

[129]   H. Leamy, T. Wang, H. Chen, Plastic flow and fracture of metallic glass, Metall. Mater. Trans. B 3 (1972) 699-708.

[130]   K. M. Flores, R. H. Dauskardt, Local heating associated with crack tip plasticity in Zr–Ti–Ni–Cu–Be bulk amorphous metals, J. Mater. Res. 14 (1999) 638-643.

[131]   C. Liu, L. Heatherly, J. Horton, D. Easton, C. Carmichael, J. Wright, J. Schneibel, M. Yoo, C. Chen, A. Inoue, Test environments and mechanical properties of Zr-base bulk amorphous alloys, Metall. Mater. Trans. A 29 (1998) 1811-1820.

[132]   T. Masumoto, R. Maddin, Structural stability and mechanical properties of amorphous metals, Mater. Sci. Eng. 19 (1975) 1-24.

[133]   H. A. Bruck, A. J. Rosakis, W. L. Johnson, The dynamic compressive behavior of beryllium bearing bulk metallic glasses, J. Mater. Res. 11 (1996) 503-511.

[134]   J.-J. Kim, Y. Choi, S. Suresh, A. Argon, Nanocrystallization during nanoindentation of a bulk amorphous metal alloy at room temperature, Science 295 (2002) 654-657.

[135]   W. J. Wright, R. B. Schwarz, W. D. Nix, Localized heating during serrated plastic flow in bulk metallic glasses, Mater. Sci. Eng., A 319 (2001) 229-232.

[136]   P. Donovan, A yield criterion for Pd40Ni40P20 metallic glass, Acta Metall. 37 (1989) 445-456.

[137]   B. Yang, P. Liaw, G. Wang, M. Morrison, C. Liu, R. Buchanan, Y. Yokoyama, In-situ thermographic observation of mechanical damage in bulk-metallic glasses during fatigue and tensile experiments, Intermetallics 12 (2004) 1265-1274.

[138]   M. Stoica, S. Scudino, J. Bednarčik, I. Kaban, J. Eckert, FeCoSiBNbCu bulk metallic glass with large compressive deformability studied by time-resolved synchrotron X-ray diffraction, J. Appl. Phys. 115 (2014) 053520-053529.

[139]   P. Thurnheer, F. Haag, J. Löffler, Time-resolved measurement of shear-band temperature during serrated flow in a Zr-based metallic glass, Acta Mater. 115 (2016) 468-474.

[140]   P. Donovan, W. Stobbs, The structure of shear bands in metallic glasses, Acta Metall. 29 (1981) 1419-1436.

[141]   E. Pekarskaya, C. Kim, W. Johnson, In situ transmission electron microscopy studies of shear bands in a bulk metallic glass based composite, J. Mater. Res. 16 (2001) 2513-2518.

[142]   P. Lowhaphandu, S. Montgomery, J. J. Lewandowski, Effects of superimposed hydrostatic pressure on flow and fracture of a Zr-Ti-Ni-Cu-Be bulk amorphous alloy, Scripta Mater. 41 (1999) 19-24.

[143]   T. Mukai, T. Nieh, Y. Kawamura, A. Inoue, K. Higashi, Dynamic response of a $Pd_{40}Ni_{40}P_{20}$ bulk metallic glass in tension, Scripta Mater. 46 (2002) 43-47.

[144]   Y. Zhang, A. Greer, Thickness of shear bands in metallic glasses, Appl. Phys. Lett. 89 (2006) 071907-3.

[145]   T. Hufnagel, T. Jiao, Y. Li, L. Xing, K. Ramesh, Deformation and failure of $Zr_{57}Ti_5Cu_{20}Ni_8Al_{10}$ bulk metallic glass under quasi-static and dynamic compression, J. Mater. Res. 17 (2002) 1441-1445.

[146]   B. Yang, M. L. Morrison, P. K. Liaw, R. A. Buchanan, G. Wang, C. T. Liu, M. Denda, Dynamic evolution of nanoscale shear bands in a bulk-metallic glass, Appl. Phys. Lett. 86 (2005) 141904-3.

[147]   B. Yang, C. Liu, T. Nieh, M. Morrison, P. Liaw, R. Buchanan, Localized heating and fracture criterion for bulk metallic glasses, J. Mater. Res. 21 (2006) 915-922.

[148]   M. D. Demetriou, J. S. Harmon, M. Tao, G. Duan, K. Samwer, W. L. Johnson, Cooperative shear model for the rheology of glass-forming metallic liquids, Phys. Rev. Lett. 97 (2006) 065502-3.

[149]   D. Pan, A. Inoue, T. Sakurai, M. W. Chen, Experimental characterization of shear transformation zones for plastic flow of bulk metallic glasses, Proc. Natl. Acad. Sci. U. S. A. 105 (2008) 14769-14772.

[150]   J. Schroers, W. L. Johnson, Ductile Bulk Metallic Glass, Phys. Rev. Lett. 93 (2004) 255506-4.

[151]   E. S. Park, H. J. Chang, D. H. Kim, Effect of addition of Be on glass-forming ability, plasticity and structural change in Cu–Zr bulk metallic glasses, Acta Mater. 56 (2008) 3120-3131.

[152]   X. Hui, S. Liu, S. Pang, L. Zhuo, T. Zhang, G. Chen, Z. Liu, High-zirconium-based bulk metallic glasses with large plasticity, Scripta Mater. 63 (2010) 239-242.

[153]   M. Calin, J. Eckert, L. Schultz, Improved mechanical behavior of Cu–Ti-based bulk metallic glass by in situ formation of nanoscale precipitates, Scripta Mater. 48 (2003) 653-658.

[154]   K. Yao, F. Ruan, Y. Yang, N. Chen, Superductile bulk metallic glass, Appl. Phys. Lett. 88 (2006) 122106-3.

[155]   Y. C. Kim, J. H. Na, J. M. Park, D. H. Kim, J. K. Lee, W. T. Kim, Role of nanometer-scale quasicrystals in improving the mechanical behavior of Ti-based bulk metallic glasses, Appl. Phys. Lett. 83 (2003) 3093-3095.

[156]   C. Fan, A. Inoue, Ductility of bulk nanocrystalline composites and metallic glasses at room temperature, Appl. Phys. Lett. 77 (2000) 46-48.

[157]   Z. Zhu, L. Gu, G. Xie, W. Zhang, A. Inoue, H. Zhang, Z. Hu, Relation between icosahedral short-range ordering and plastic deformation in Zr–Nb–Cu–Ni–Al bulk metallic glasses, Acta Mater. 59 (2011) 2814-2822.

[158]   L. Zhang, Y.-Q. Cheng, A.-J. Cao, J. Xu, E. Ma, Bulk metallic glasses with large plasticity: Composition design from the structural perspective, Acta Mater. 57 (2009) 1154-1164.

[159]   D. Qu, K.-D. Liss, Y. Sun, M. Reid, J. Almer, K. Yan, Y. Wang, X. Liao, J. Shen, Structural origins for the high plasticity of a Zr–Cu–Ni–Al bulk metallic glass, Acta Mater. 61 (2013) 321-330.

[160]   K. Song, S. Pauly, Z. Wang, U. Kühn, J. Eckert, Effect of TaW particles on the microstructure and mechanical properties of metastable $Cu_{47.5}Zr_{47.5}Al_5$ alloys, Mater. Sci. Eng., A 587 (2013) 372-380.

[161]   K. Song, S. Pauly, Y. Zhang, R. Li, S. Gorantla, N. Narayanan, U. Kühn, T. Gemming, J. Eckert, Triple yielding and deformation mechanisms in metastable $Cu_{47.5}Zr_{47.5}Al_5$ composites, Acta Mater. 60 (2012) 6000-6012.

[162]   K. Song, S. Pauly, B. Sun, Y. Zhang, J. Tan, U. Kühn, M. Stoica, J. Eckert, Formation of Cu–Zr–Al–Er bulk metallic glass composites with enhanced deformability, Intermetallics 30 (2012) 132-138.

[163]   E. Park, D. Kim, Phase separation and enhancement of plasticity in Cu–Zr–Al–Y bulk metallic glasses, Acta Mater. 54 (2006) 2597-2604.

[164]   Q. Cao, J. Li, Y. Zhou, J. Jiang, Mechanically driven phase separation and corresponding microhardness change in $Cu_{60}Zr_{20}Ti_{20}$ bulk metallic glass, Appl. Phys. Lett. 86 (2005) 081913.

[165]   X. Du, J. Huang, K. Hsieh, Y. Lai, H. Chen, J. Jang, P. Liaw, Two-glassy-phase bulk metallic glass with remarkable plasticity, Appl. Phys. Lett. 91 (2007) 131901-3.

[166]   J. Oh, T. Ohkubo, Y. Kim, E. Fleury, K. Hono, Phase separation in $Cu_{43}Zr_{43}Al_7Ag_7$ bulk metallic glass, Scripta Mater. 53 (2005) 165-169.

[167]   E. S. Park, D. H. Kim, Phase separation and enhancement of plasticity in Cu–Zr–Al–Y bulk metallic glasses, Acta Mater. 54 (2006) 2597-2604.

[168]   A. Inoue, B. L. Shen, A New Fe-based Bulk Glassy Alloy with Outstanding Mechanical Properties, Adv. Mater. 16 (2004) 2189-2192.

[169]   X. J. Gu, A. G. McDermott, S. J. Poon, G. J. Shiflet, Critical Poisson's ratio for plasticity in Fe–Mo–C–B–Ln bulk amorphous steel, Appl. Phys. Lett. 88 (2006) 211905-3.

[170]   K. Song, S. Pauly, Y. Zhang, S. Scudino, P. Gargarella, K. Surreddi, U. Kühn, J. Eckert, Significant tensile ductility induced by cold rolling in $Cu_{47.5}Zr_{47.5}Al_5$ bulk metallic glass, Intermetallics 19 (2011) 1394-1398.

[171]   S. Scudino, B. Jerliu, S. Pauly, K. Surreddi, U. Kühn, J. Eckert, Ductile bulk metallic glasses produced through designed heterogeneities, Scripta Mater. 65 (2011) 815-818.

[172]   R. Raghavan, R. Ayer, H. Jin, C. Marzinsky, U. Ramamurty, Effect of shot peening on the fatigue life of a Zr-based bulk metallic glass, Scripta Mater. 59 (2008) 167-170.

[173]   F. Méar, B. Lenk, Y. Zhang, A. Greer, Structural relaxation in a heavily cold-worked metallic glass, Scripta Mater. 59 (2008) 1243-1246.

[174]   M. Lee, K. Lee, J. Das, J. Thomas, U. Kühn, J. Eckert, Improved plasticity of bulk metallic glasses upon cold rolling, Scripta Mater. 62 (2010) 678-681.

[175]   Y. Zhang, W. Wang, A. Greer, Making metallic glasses plastic by control of residual stress, Nat. Mater. 5 (2006) 857-860.

[176]   J. Zhao, F. Wu, R. Qu, S. Li, Z. Zhang, Plastic deformability of metallic glass by artificial macroscopic notches, Acta Mater. 58 (2010) 5420-5432.

[177]   Y. Wang, D. Qu, X. Wang, Y. Cao, X. Liao, M. Kawasaki, S. Ringer, Z. Shan, T. Langdon, J. Shen, Introducing a strain-hardening capability to improve the ductility of bulk metallic glasses via severe plastic deformation, Acta Mater. 60 (2012) 253-260.

[178]   W. Dmowski, Y. Yokoyama, A. Chuang, Y. Ren, M. Umemoto, K. Tsuchiya, A. Inoue, T. Egami, Structural rejuvenation in a bulk metallic glass induced by severe plastic deformation, Acta Mater. 58 (2010) 429-438.

[179]   Q. Cao, J. Liu, K. Yang, F. Xu, Z. Yao, A. Minkow, H. Fecht, J. Ivanisenko, L. Chen, X. Wang, Effect of pre-existing shear bands on the tensile mechanical properties of a bulk metallic glass, Acta Mater. 58 (2010) 1276-1292.

[180]   Q. Cao, J. Li, Y. Zhou, A. Horsewell, J. Jiang, Effect of rolling deformation on the microstructure of bulk $Cu_{60}Zr_{20}Ti_{20}$ metallic glass and its crystallization, Acta Mater. 54 (2006) 4373-4383.

[181]   Y. Yokoyama, T. Yamasaki, A. Inoue, Significant Tensile Plasticity of Cold Rolled $Zr_{50}Cu_{30}Ni_{10}Al_{10}$ Bulk Glassy Alloys, Rev. Adv. Mater. Sci 18 (2008) 131-136.

[182]   V. I. Tkatch, A. I. Limanovskii, S. N. Denisenko, S. G. Rassolov, The effect of the melt-spinning processing parameters on the rate of cooling, Mater. Sci. Eng., A 323 (2002) 91-96.

[183]   T. Kozieł, Estimation Of Cooling Rates In Suction Casting And Copper-Mould Casting Processes, Arch. Metall. Mater. 60 (2015) 767-771.

[184]   E. J. Vinarcik. High integrity die casting processes: John Wiley & Sons, 2002.

[185]   P. Ramasamy, A. Szabo, S. Borzel, J. Eckert, M. Stoica, A. Bárdos, High pressure die casting of Fe-based metallic glass, Sci. Rep. 6 (2016) 35258-11.

[186]   R. Speyer. Thermal analysis of materials: CRC Press, 1993.

[187]   E. Kneller. Ferromagnetismus. Germany: Springer-Verlag Berlin, 1962.

[188]   B. D. Cullity, C. D. Graham. Introduction to magnetic materials: John Wiley & Sons, 2011.

[189]   M. Hagiwara, A. Inoue, T. Masumoto, Mechanical properties of Fe-Si-B amorphous wires produced by in-rotating-water spinning method, Metall. Trans. A 13 (1982) 373-382.

[190]   B. Shen, Y. Zhou, C. Chang, A. Inoue, Effect of B to Si concentration ratio on glass-forming ability and soft-magnetic properties in $(Co_{0.705}Fe_{0.045}B_{0.25-x}Si_x)_{96}Nb_4$ glassy alloys, J. Appl. Phys. 101 (2007) 09N101-3.

[191]   T. Bitoh, A. Makino, A. Inoue, A. Greer, Large bulk soft magnetic $[(Fe_{0.5}Co_{0.5})_{0.75}B_{0.20}Si_{0.05}]$ $_{96}Nb_4$ glassy alloy prepared by B_2O_3 flux melting and water quenching, Appl. Phys. Lett. 88 (2006) 182510-3.

[192]   T. Kubota, A. Makino, A. Inoue, Low core loss of $Fe_{85}Si_2B_8P_4Cu_1$ nanocrystalline alloys with high B s and B 800, J. Alloys Compd. 509 (2011) S416-S419.

[193]   A. Urata, H. Matsumoto, S. Yoshida, A. Makino, Fe–B–P–Cu nanocrystalline soft magnetic alloys with high B s, J. Alloys Compd. 509 (2011) S431-S433.

[194]   H. Jung, S. Yi, Effect of Cu addition on nanocrystallization behaviors and magnetic properties of the $Fe_{76.5-x}C_{6.0}Si_{3.3}B_{5.5}P_{8.7}Cu_x$ (x= 0-3at.%) bulk metallic glass, J. Alloys Compd. 561 (2013) 76-81.

[195]   B. Shen, H. Men, A. Inoue, Fe-based bulk glassy alloy composite containing in situ formed α-(Fe,Co) and $(Fe,Co)_{23}B_6$ microcrystalline grains, Appl. Phys. Lett. 89 (2006) 101915-3.

[196]   Y. Jia, S. Zeng, S. Shan, L. Zhang, C. Fan, B. Zhang, Z. Zhan, R. Liu, W. Wang, Effect of copper addition on the glass forming ability of a Fe–Co based alloy, J. Alloys Compd. 440 (2007) 113-116.

[197]   R. Li, S. Kumar, S. Ram, M. Stoica, S. Roth, J. Eckert, Crystallization and magnetic properties of $[(Fe, Co)_{0.75}Si_{0.05}B_{0.20}]_{94}Nb_6$ metallic glasses, J. Phys. D: Appl. Phys. 42 (2009) 085006-6.

[198]   M. Stoica, S. Roth, J. Eckert, T. Karan, S. Ram, G. Vaughan, A. R. Yavari, FeCoBSiNb bulk metallic glasses with Cu additions, Phys. Status Solidi C 7 (2010) 1331-1335.

[199]   P. Ramasamy, M. Stoica, A. Taghvaei, K. Prashanth, R. Kumar, J. Eckert, Kinetic analysis of the non-isothermal crystallization process, magnetic and mechanical properties of FeCoBSiNb and FeCoBSiNbCu bulk metallic glasses, J. Appl. Phys. 119 (2016) 073908-9.

[200]   M. Stoica, J. Eckert, S. Roth, L. Schultz, Preparation of bulk amorphous Fe–Cr–Mo–Ga–P–C–B alloys by copper mold casting, Mater. Sci. Eng., A 375 (2004) 399-402.

[201]   A. Inoue, Bulk amorphous alloys with soft and hard magnetic properties, Mater. Sci. Eng., A 226 (1997) 357-363.

[202]   W. Martienssen, H. Warlimont. Springer handbook of condensed matter and materials data: Springer Science & Business Media, 2006.

[203]   N. Zheng, R. Qu, S. Pauly, M. Calin, T. Gemming, Z. Zhang, J. Eckert, Design of ductile bulk metallic glasses by adding "soft" atoms, Appl. Phys. Lett. 100 (2012) 141901-141904.

[204]   P. Ehrenfest. On interference phenomena to be expected when Roentgen rays pass through a di-atomic gas. KNAW, Proceedings, 17 (1915) 1914-1915.

[205]   J. Bernal, Geometry of the structure of monatomic liquids, Nature 185 (1960) 68-70.

[206]   M. Stoica, R. Li, A. R. Yavari, G. Vaughan, J. Eckert, N. Van Steenberge, D. R. Romera, Thermal stability and magnetic properties of FeCoBSiNb bulk metallic glasses, J. Alloys Compd. 504, Supplement 1 (2010) S123-S128.

[207]   H. E. Kissinger, Variation of Peak Temperature With Heating Rate in Differential Thermal Analysis, J. Res. Natl. Bur. Stand. 57 (1956) 217-221.

[208]   M. Ohnuma, K. Hono, H. Onodera, J. S. Pedersen, S. Linderoth, Cu clustering stage before the crystallization in Fe-Si-B-Nb-Cu amorphous alloys, Nanostruct. Mater. 12 (1999) 693-696.

[209]   M. Stoica, P. Ramasamy, I. Kaban, S. Scudino, M. Nicoara, G. B. M. Vaughan, J. Wright, R. Kumar, J. Eckert, Structure evolution of soft magnetic $(Fe_{36}Co_{36}B_{19.2}Si_{4.8}Nb_4)_{100-x}Cu_x$ (x =0 and 0.5) bulk glassy alloys, Acta Mater. 95 (2015) 335-342.

[210]   A. Takeuchi, A. Inoue, Classification of bulk metallic glasses by atomic size difference, heat of mixing and period of constituent elements and its application to characterization of the main alloying element, Mater. Trans. 46 (2005) 2817-2829.

[211]   D. M. Herlach, Non-equilibrium solidification of undercooled metallic metls, Mater. Sci. Eng., R 12 (1994) 177-272.

[212]   D. Turnbull, Kinetics of solidification of supercooled liquid mercury droplets, J. Chem. Phys. 20 (1952) 411-424.

[213]   J. W. Christian. The theory of transformations in metals and alloys: Pergamon, 2002.

[214]   M. Aykol, M. V. Akdeniz, A. O. Mekhrabov, Solidification behavior, glass forming ability and thermal characteristics of soft magnetic Fe–Co–B–Si–Nb–Cu bulk amorphous alloys, Intermetallics 19 (2011) 1330-1337.

[215]   T. Bitoh, A. Makino, A. Inoue, Origin of low coercivity of $(Fe_{0.75}B_{0.15}Si_{0.10})_{(100-x)}$Nb-x (x=1-4) glassy alloys, J. Appl. Phys. 99 (2006) 08F102-3.

[216]   G. Herzer. Random anisotropy model: Springer Netherlands, 2005.

[217]   R. Harris, D. Zobin, The random anisotropy model for amorphous metallic alloys: generalized molecular field calculations, J. Phys. F 7 (1977) 337-350.

[218]   G. S. Abo, Y.-K. Hong, J. Park, J. Lee, W. Lee, B.-C. Choi, Definition of magnetic exchange length, IEEE Trans. Magn. 49 (2013) 4937-4939.

[219]   M. E. Schabes, H. N. Bertram, Magnetization processes in ferromagnetic cubes, J. Appl. Phys. 64 (1988) 1347-1357.

[220]   G. K. Williamson, W. H. Hall, X-ray line broadening from filed aluminium and wolfram, Acta Metall. 1 (1953) 22-31.

[221]   B. Shen, A. Inoue, C. Chang, Superhigh strength and good soft-magnetic properties of (Fe, Co)–B–Si–Nb bulk glassy alloys with high glass-forming ability, Appl. Phys. Lett. 85 (2004) 4911-4913.

[222]   A. Inoue, T. Zhang, Fabrication of bulky Zr-based glassy alloys by suction casting into copper mold, Mater. Trans., JIM 36 (1995) 1184-1187.

[223]   A. Inoue, W. Zhang, T. Zhang, K. Kurosaka, High-strength Cu-based bulk glassy alloys in Cu–Zr–Ti and Cu–Hf–Ti ternary systems, Acta Mater. 49 (2001) 2645-2652.

[224]   T. Zhang, A. Inoue, New bulk glassy Ni-based alloys with high strength of 3000 MPa, Mater. Trans. 43 (2002) 708-711.

[225]   S. Zhu, X. Wang, A. Inoue, Glass-forming ability and mechanical properties of Ti-based bulk glassy alloys with large diameters of up to 1cm, Intermetallics 16 (2008) 1031-1035.

[226]   A. Greer, Y. Cheng, E. Ma, Shear bands in metallic glasses, Mater. Sci. Eng., R 74 (2013) 71-132.

[227]   J. Lewandowski, A. Greer, Temperature rise at shear bands in metallic glasses, Nat. Mater. 5 (2006) 15-18.

[228]   K. Georgarakis, M. Aljerf, Y. Li, A. LeMoulec, F. Charlot, A. Yavari, K. Chornokhvostenko, E. Tabachnikova, G. Evangelakis, D. Miracle, Shear band melting and serrated flow in metallic glasses, Appl. Phys. Lett. 93 (2008) 031907-3.

[229]   V. Bengus, E. Tabachnikova, S. Shumilin, Y. I. Golovin, M. Makarov, A. Shibhov, J. Miskuf, K. Csach, V. Ocelik, Some peculiarities of ductile shear failure of amorphous alloy ribbons, Int. J. Rapid Solidif. 8 (1993) 21-31.

[230]   D. Miracle, A. Concustell, Y. Zhang, A. Yavari, A. Greer, Shear bands in metallic glasses: size effects on thermal profiles, Acta Mater. 59 (2011) 2831-2840.

[231]   W. Sha. Ultra High-Strength Maraging Steel. edited. Steels: From Materials Science to Structural Engineering. London: Springer London (2013) 141-161.

[232]   A. Inoue, X. M. Wang, Bulk amorphous FC20(Fe–C–Si) alloys with small amounts of B and their crystallized structure and mechanical properties, Acta Mater. 48 (2000) 1383-1395.

[233]   K. Amiya, A. Urata, N. Nishiyama, A. Inoue, Fe-B-Si-Nb bulk metallic glasses with high strength above 4000 MPa and distinct plastic elongation, Mater. Trans. 45 (2004) 1214-1218.

[234]   K. Yao, C. Zhang, Fe-based bulk metallic glass with high plasticity, Appl. Phys. Lett. 90 (2007) 061901-3.

[235]   A. Inoue, T. Zhang, A. Takeuchi, Bulk amorphous alloys with high mechanical strength and good soft magnetic properties in Fe–TM–B (TM= IV–VIII group transition metal) system, Appl. Phys. Lett. 71 (1997) 464-466.

[236]   X. Gu, A. McDermott, S. J. Poon, G. J. Shiflet, Critical Poisson's ratio for plasticity in Fe–Mo–C–B–Ln bulk amorphous steel, Appl. Phys. Lett. 88 (2006) 211905-3.

[237]   F. Li, B. Shen, A. Makino, A. Inoue, Excellent soft-magnetic properties of (Fe, Co)–Mo–(P, C, B, Si) bulk glassy alloys with ductile deformation behavior, Appl. Phys. Lett. 91 (2007) 234101-3.

[238]   J. Yao, J. Wang, Y. Li, Ductile Fe–Nb–B bulk metallic glass with ultrahigh strength, Appl. Phys. Lett. 92 (2008) 251906-3.

[239]   K. Qiu, J. Pang, Y. Ren, H. Zhang, C. Ma, T. Zhang, Fe-based bulk metallic glasses with a larger supercooled liquid region and high ductility, Mater. Sci. Eng., A 498 (2008) 464-467.

[240]   J. Park, G. Wang, R. Li, N. Mattern, J. Eckert, D. Kim, Enhancement of plastic deformability in Fe–Ni–Nb–B bulk glassy alloys by controlling the Ni-to-Fe concentration ratio, Appl. Phys. Lett. 96 (2010) 031905-3.

[241]   J. Li, H. Men, B. Shen, Soft-ferromagnetic bulk glassy alloys with large magnetostriction and high glass-forming ability, AIP Adv. 1 (2011) 042110-7.

[242]   A. Seifoddini, M. Stoica, M. Nili-Ahmadabadi, S. Heshmati-Manesh, U. Kühn, J. Eckert, New $(Fe_{0.9}Ni_{0.1})_{77}Mo_5P9C_{7.5}B_{1.5}$ glassy alloys with enhanced glass-forming ability and large compressive strain, Mater. Sci. Eng., A 560 (2013) 575-582.

[243]   A. Inoue, B. Shen, H. Koshiba, H. Kato, A. R. Yavari, Cobalt-based bulk glassy alloy with ultrahigh strength and soft magnetic properties, Nat. Mater. 2 (2003) 661-663.

[244]   Q. Man, A. Inoue, Y. Dong, J. Qiang, C. Zhao, B. Shen, A new CoFe-based bulk metallic glasses with high thermoplastic forming ability, Scripta Mater. 69 (2013) 553-556.

[245]   Y. Dong, A. Wang, Q. Man, B. Shen, $(Co_{1-x}Fe_x)_{68}B_{21.9}Si_{5.1}Nb_5$ bulk glassy alloys with high glass-forming ability, excellent soft-magnetic properties and superhigh fracture strength, Intermetallics 23 (2012) 63-67.

[246]   T. Zhang, Q. Yang, Y. Ji, R. Li, S. Pang, J. Wang, T. Xu, Centimeter-scale-diameter Co-based bulk metallic glasses with fracture strength exceeding 5000 MPa, Chin. Sci. Bull. 56 (2011) 3972-3977.

[247]   J. Wang, R. Li, N. Hua, T. Zhang, Co-based ternary bulk metallic glasses with ultrahigh strength and plasticity, J. Mater. Res. 26 (2011) 2072-2079.

[248]   C. Dun, H. Liu, L. Hou, L. Xue, L. Dou, W. Yang, Y. Zhao, B. Shen, Ductile Co–Nb–B bulk metallic glass with ultrahigh strength, J. Non-Cryst. Solids 386 (2014) 121-123.

[249]   L. Bie, Q. Li, D. Cao, H. Li, J. Zhang, C. Chang, Y. Sun, Preparation and properties of quaternary CoMoPB bulk metallic glasses, Intermetallics 71 (2016) 7-11.

[250]   A. Inoue, A. Takeuchi, Recent progress in bulk glassy alloys, Mater. Trans. 43 (2002) 1892-1906.

[251]   H. Chen, Glassy metals, Rep. Prog. Phys. 43 (1980) 353-432.

[252]   C. Conde, A. Conde, D. Janičkovič, P. Švec, Composition dependence of Curie temperature and microstructure in amorphous Fe–Co–Mo–Cu–B metallic glasses, J. Magn. Magn. Mater. 304 (2006) e739-e742.

[253]   A. Inoue, F. L. Kong, Q. K. Man, B. L. Shen, R. W. Li, F. Al-Marzouki, Development and applications of Fe- and Co-based bulk glassy alloys and their prospects, J. Alloys Compd. 615, Supplement 1 (2014) S2-S8.

[254]   S. S. Wu, B. L. Shen, A. Inoue, Preparation and properties study of bulk $Fe_{75.5}Ga_3P_{10.5}C_4B_4Si_3$ metallic glass ring by copper mold casting, Intermetallics 12 (2004) 1261-1264.

[255]   M. Zhang, F. Kong, A. Wang, C. Chang, B. Shen, Soft magnetic properties of bulk FeCoMoPCBSi glassy core prepared by copper mold casting, J. Appl. Phys. 111 (2012) 07A312-3.

[256]   A. Bardos, A. Lovas, S. Roth, M. Stoica, L. K. Varga, Multicomponent magnetically soft alloy with high glass-forming ability and improved castability, Czech J. Phys. 55 (2005) 593-599.

[257]   S. Ishihara, W. Zhang, H. Kimura, M. Omori, A. Inoue, Consolidation of Fe-Co-Nd-Dy-B glassy powders by spark-plasma sintering and magnetic properties of the consolidated alloys, Mater. Trans. 44 (2003) 138-143.

[258]   J. P. Chu, H. Wijaya, C. W. Wu, T. R. Tsai, C. S. Wei, T. G. Nieh, J. Wadsworth, Nanoimprint of gratings on a bulk metallic glass, Appl. Phys. Lett. 90 (2007) 034101-3.

[259]   N. Zhang, C. J. Byrne, D. J. Browne, M. D. Gilchrist, Towards nano-injection molding, Mater. Today 15 (2012) 216-221.

[260]   J. Schroers, Processing of Bulk Metallic Glass, Adv. Mater. 22 (2010) 1566-1597.

[261]   G. Duan, A. Wiest, M. L. Lind, J. Li, W. K. Rhim, W. L. Johnson, Bulk Metallic Glass with Benchmark Thermoplastic Processability, Adv. Mater. 19 (2007) 4272-4275.

[262]   S. Pauly, L. Löber, R. Petters, M. Stoica, S. Scudino, U. Kühn, J. Eckert, Processing metallic glasses by selective laser melting, Mater. Today 16 (2013) 37-41.

[263]   H. Meier, C. Haberland, Experimental studies on selective laser melting of metallic parts, Materialwiss. Werkstofftech. 39 (2008) 665-670.

[264]   H. Y. Jung, S. J. Choi, K. G. Prashanth, M. Stoica, S. Scudino, S. Yi, U. Kühn, D. H. Kim, K. B. Kim, J. Eckert, Fabrication of Fe-based bulk metallic glass by selective laser melting: A parameter study, Mater. Des. 86 (2015) 703-708.

[265]   L. X. Kong, F. H. She, W. M. Gao, S. Nahavandi, P. D. Hodgson, Integrated optimization system for high pressure die casting processes, J. Mater. Process. Tech. 201 (2008) 629-634.

[266]   D. L. Bourell, M. C. Leu, D. W. Rosen, Roadmap for additive manufacturing: identifying the future of freeform processing, The University of Texas at Austin, Austin, TX (2009).

[267]   A. Peker, W. L. Johnson, A highly processable metallic glass: $Zr_{41.2}Ti_{13.8}Cu_{12.5}Ni_{10.0}Be_{22.5}$, Appl. Phys. Lett. 63 (1993) 2342-2344.

[268]   N. Nishiyama, K. Takenaka, H. Miura, N. Saidoh, Y. Zeng, A. Inoue, The world's biggest glassy alloy ever made, Intermetallics 30 (2012) 19-24.

[269]   A. Inoue, T. Nakamura, N. Nishiyama, T. Sugita, T. Masumoto, Bulky Amorphous Alloys Produced by a High-Pressure Die Casting Process, Key Eng. Mater. 81-83 (1993) 147-152.

[270]   J. Schroers, The superplastic forming of bulk metallic glasses, JOM 57 (2005) 35-39.

[271]   X. Lin, W. Johnson, W. Rhim, Effect of oxygen impurity on crystallization of an undercooled bulk glass forming Zr–Ti–Cu–Ni–Al alloy, Mater. Trans., JIM 38 (1997) 473-477.

[272]   S. Mukherjee, Z. Zhou, J. Schroers, W. Johnson, W. Rhim, Overheating threshold and its effect on time–temperature-transformation diagrams of zirconium based bulk metallic glasses, Appl. Phys. Lett. 84 (2004) 5010-5012.

[273]   Z. W. Chen, Skin solidification during high pressure die casting of Al–11Si–2Cu–1Fe alloy, Mater. Sci. Eng., A 348 (2003) 145-153.

[274]   A. D. Setyawan, H. Kato, J. Saida, A. Inoue, Glass formation dependence on casting-atmosphere pressure in $Zr_{65}Al_{7.5}Ni_{10}Cu_{17.5-x}Pd_x$ (x= 0-17.5) alloy system: A resultant effect of quasicrystalline phase transformation and cooling mechanism during mold-casting process, J. Appl. Phys. 103 (2008) 044907-8.

[275]   J. F. Löffler, Bulk metallic glasses, Intermetallics 11 (2003) 529-540.

[276]   R. Parthiban, M. Stoica, I. Kaban, K. Ravi, J. Eckert, Viscosity and fragility of the supercooled liquids and melts from the Fe–Co–B–Si–Nb and Fe–Mo–P–C–B–Si glass-forming alloy systems, Intermetallics 66 (2015) 48-55.

[277]   Z. Shao, J. P. Singer, Y. Liu, Z. Liu, H. Li, M. Gopinadhan, C. S. O'Hern, J. Schroers, C. O. Osuji, Shear-accelerated crystallization in a supercooled atomic liquid, Phys. Rev. E 91 (2015) 020301-8.

[278]   C. Way, P. Wadhwa, R. Busch, The influence of shear rate and temperature on the viscosity and fragility of the $Zr_{41.2}Ti_{13.8}Cu_{12.5}Ni_{10.0}Be_{22.5}$ metallic-glass-forming liquid, Acta Mater. 55 (2007) 2977-2983.

[279]   E. Ustundag, B. Clausen, J. C. Hanan, M. A. M. Bourke, A. Winholtz, A. Pekers, Residual stresses in bulk metallic glasses due to differential cooling or thermal tempering, MRS Online Proceedings Library Archive 554 (1998) 431-436.

[280]   B. A. Sun, W. H. Wang, The fracture of bulk metallic glasses, Prog. Mater Sci. 74 (2015) 211-307.

[281]   Z. F. Zhang, F. F. Wu, W. Gao, J. Tan, Z. G. Wang, M. Stoica, J. Das, J. Eckert, B. L. Shen, A. Inoue, Wavy cleavage fracture of bulk metallic glass, Appl. Phys. Lett. 89 (2006) 251917-3.

[282]   G. Herzer. The random anisotropy model. edited. Properties and Applications of Nanocrystalline Alloys from Amorphous Precursors. Springer (2005) 15-34.